

1 LEVERAGING MULTI-MESSENGER ASTROPHYSICS FOR DARK MATTER SEARCHES

By

Daniel Nicholas Salazar-Gallegos

A DISSERTATION

Submitted to  
Michigan State University  
in partial fulfillment of the requirements  
for the degree of

Physics—Doctor of Philosophy  
Computational Mathematics in Science and Engineering—Dual Major

Today

**ABSTRACT**

3 I did Dark Matter with HAWC and IceCube. I also used Graph Neural Networks

<sup>4</sup> Copyright by

<sup>5</sup> DANIEL NICHOLAS SALAZAR-GALLEGOS

<sup>6</sup> Today

## ACKNOWLEDGMENTS

8 I love my friends. Thanks to everyone that helped me figure this out. Amazing thanks to the people  
9 at LANL who supported me. Eames, etc Dinner Parties Jenny and her child Kaydince Kirsten, Pat,  
10 Andrea Family. You're so far but so critical to my formation. Unconditional love. Roommate

## TABLE OF CONTENTS

|    |   |      |
|----|---|------|
| 12 | LIST OF TABLES . . . . .  | vii  |
| 13 | LIST OF FIGURES . . . . .   | viii |
| 14 | LIST OF ABBREVIATIONS . . . . .   | xvii |
| 15 | CHAPTER 1      INTRODUCTION . . . . .   | 1    |
| 16 | CHAPTER 2      DARK MATTER IN THE COSMOS . . . . .  | 2    |
| 17 | 2.1 Introduction . . . . .  | 2    |
| 18 | 2.2 Dark Matter Basics . . . . .  | 3    |
| 19 | 2.3 Evidence for Dark Matter . . . . .  | 4    |
| 20 | 2.4 Searching for Dark Matter: Particle DM . . . . .  | 11   |
| 21 | 2.5 Sources for Indirect Dark Matter Searches . . . . .   | 16   |
| 22 | 2.6 Multi-Messenger Dark Matter . . . . .   | 18   |
| 23 | CHAPTER 3      HIGH ALTITUDE WATER CHERENKOV (HAWC) OBSERVATORY . . . . .   | 21   |
| 24 | 3.1 The Detector . . . . .  | 21   |
| 25 | 3.2 Events Reconstruction and Data Acquisition . . . . .  | 21   |
| 26 | 3.3 Remote Monitoring . . . . .   | 21   |
| 27 | CHAPTER 4      ICECUBE NEUTRINO OBSERVATORY . . . . .   | 22   |
| 28 | 4.1 The Detector . . . . .  | 22   |
| 29 | 4.2 Events Reconstruction and Data Acquisition . . . . .  | 22   |
| 30 | 4.3 Northern Test Site . . . . .  | 22   |
| 31 | CHAPTER 5      GLORY DUCK: MULTI-WAVELENGTH SEARCH FOR DARK MATTER ANNIHILATION TOWARDS DWARF SPHEROIDAL GALAXIES . . . . . | 23   |
| 32 | 5.1 Introduction . . . . .  | 23   |
| 33 | 5.2 Dataset and Background . . . . .  | 25   |
| 34 | 5.3 Analysis . . . . .  | 27   |
| 35 | 5.4 Likelihood Methods . . . . .  | 31   |
| 36 | 5.5 HAWC Results . . . . .  | 38   |
| 37 | 5.6 Glory Duck Combined Results . . . . .   | 40   |
| 38 | 5.7 HAWC Systematics . . . . .  | 45   |
| 39 | 5.8 $J$ -factor distributions . . . . .   | 47   |
| 40 | 5.9 Discussion and Conclusions . . . . .  | 53   |
| 43 | CHAPTER 6      MULTITHREADING HAWC ANALYSES FOR DARK MATTER SEARCHES . . . . .  | 57   |
| 44 | 6.1 Introduction . . . . .  | 57   |
| 45 | 6.2 Dataset and Background . . . . .  | 57   |
| 46 | 6.3 Analysis . . . . .  | 59   |

|    |   |            |
|----|---|------------|
| 48 | 6.4 Likelihood Methods . . . . .  | 63         |
| 49 | 6.5 Computational Methods: Multithreading . . . . .   | 63         |
| 50 | 6.6 Analysis Results . . . . .  | 69         |
| 51 | 6.7 Systematics . . . . .   | 74         |
| 52 | 6.8 Conclusion and Discussion . . . . .   | 74         |
| 53 | <b>CHAPTER 7 HEAVY DARK MATTER ANNIHILATION SEARCH WITH ICE-CUBE'S NORTH SKY TRACK DATA . . . . .</b> | <b>76</b>  |
| 55 | 7.1 Introduction . . . . .  | 76         |
| 56 | 7.2 Dataset and Background . . . . .  | 77         |
| 57 | 7.3 Analysis . . . . .  | 78         |
| 58 | 7.4 Likelihood Methods . . . . .  | 86         |
| 59 | 7.5 Background Simulation . . . . .   | 87         |
| 60 | 7.6 Signal Recovery . . . . .   | 88         |
| 61 | 7.7 Systematics . . . . .   | 89         |
| 62 | 7.8 Conclusions . . . . .   | 89         |
| 63 | <b>CHAPTER 8 NU DUCK . . . . .</b>  | <b>111</b> |
| 64 | <b>APPENDIX A MULTI-EXPERIMENT SUPPLEMENTARY FIGURES . . . . .</b>                                    | <b>112</b> |
| 65 | <b>APPENDIX B MULTITHREADING DARK MATTER ANALYSES SUPPLEMENTARY MATERIAL . . . . .</b>                | <b>113</b> |
| 67 | B.1 Remaining Spectral Models . . . . .   | 113        |
| 68 | B.2 <code>mpu_analysis.py</code> . . . . .  | 114        |
| 69 | B.3 Comparison with Glory Duck . . . . .  | 123        |
| 70 | <b>APPENDIX C ICECUBE HEAVY DARK MATTER ANALYSIS SUPPLEMENTARY MATERIAL . . . . .</b>                 | <b>126</b> |
| 72 | C.1 Docker Image for Oscillating Neutrino Spectra . . . . .   | 126        |
| 73 | C.2 Spline Fitting Statuses . . . . .   | 129        |
| 74 | C.3 Segue 1 And Ursa Major II Signal Recovery . . . . .   | 130        |
| 75 | <b>BIBLIOGRAPHY . . . . .</b>   | <b>131</b> |

## LIST OF TABLES

|   |   |
|---|---|
| <p>77    Table 5.1    Summary of the relevant properties of the dSphs used in the present work. Column 1 lists the dSphs. Columns 2 and 3 present their heliocentric distance and galactic coordinates, respectively. Columns 4 and 5 report the <math>J</math>-factors of each source given from the <math>\mathcal{GS}</math> and <math>\mathcal{B}</math> independent studies and their estimated <math>\pm 1\sigma</math> uncertainties. The values <math>\log_{10} J</math> (<math>\mathcal{GS}</math> set) [45] correspond to the mean <math>J</math>-factor values for a source extension truncated at the outermost observed star. The values <math>\log_{10} J</math> (<math>\mathcal{B}</math> set) [49] are provided for a source extension at the tidal radius of each dSph. <b>Bolded sources are within HAWC's field of view and provided to the Glory Duck analysis.</b> . . . . .</p> <p>86    Table 5.2    Summary of dSph observations by each experiment used in this work. A ‘-’ indicates the experiment did not observe the dSph for this study. For Fermi-LAT, the exposure at 1 GeV is given. For HAWC, <math> \Delta\theta </math> is the absolute difference between the source declination and HAWC latitude. HAWC is more sensitive to sources with smaller <math> \Delta\theta </math>. For IACTs, we show the zenith angle range, the total exposure, the energy range, the angular radius <math>\theta</math> of the signal or ON region, the ratio of exposures between the background-control (OFF) and signal (ON) regions (<math>\tau</math>), and the significance of gamma-ray excess in standard deviations, <math>\sigma</math>. . . . .</p> <p>95    Table 6.1    Summary of the relevant properties of the dSphs used in the present work. Column 1 lists the dSphs. Columns 2 and 3 present their heliocentric distance and galactic coordinates, respectively. Column 4 reports the <math>J</math>-factors of each source given from the <math>\mathcal{LS}</math> studies and estimated <math>\pm 1\sigma</math> uncertainties. The values <math>\log_{10} J</math> (<math>\mathcal{LS}</math> set) [66] correspond to the mean <math>J</math>-factor values for a source extension truncated at <math>0.5^\circ</math>. . . . .</p> <p>101    Table 6.2    Timing summaries for analyses for serial and multithreaded processes. <math>M</math> tasks is the number of functional-parallel tasks ran for the computation. <math>T_{p,c}</math> is a single run time in hours:minutes:seconds for runs utilizing <math>p</math> nodes and <math>c</math> threads. Runs are run interactively on the same computer to maximize consistency. Empty entries are indicated with ‘-’. (.) entries are estimated entries extrapolated from data earlier in the column. . . . .</p> <p>107    Table 6.3    Speed up summaries for analyses for serial and multithreaded processes. <math>M</math> tasks is the number of functional-parallel tasks ran for the computation. <math>S_{p,c}</math> is a single speedup comparison for runs utilizing <math>p</math> nodes and <math>c</math> threads. <math>[\cdot]</math> are the estimated speedups calculated from Tab. 6.2, Eq. (6.7), and Eq. (6.4). Empty entries are indicated with ‘-’. . . . .</p> <p>112    Table 7.1    <b>TODO: fill me daddy</b> . . . . .</p> <p>113         Proof I know how to include</p> | <p>32</p> <p>33</p> <p>63</p> <p>67</p> <p>69</p> <p>84</p> |
|---|---|

## LIST OF FIGURES

|     |            |   |    |
|-----|------------|---|----|
| 115 | Figure 2.1 | Rotation curve fit to NGC 6503 from [7]. Dashed line is the contribution from visible matter. Dotted curves are from gas. Dash-dot curves are from dark matter (DM). Solid line is the composite contribution from all matter and DM sources. Data are indicated with bold dots with error bars. Data agree strongly with a matter + DM composite prediction. . . . .   | 5  |
| 120 | Figure 2.2 | Light from distant galaxy is bent in unique ways depending on the distribution of mass between the galaxy and Earth. Yellow dashed lines indicate where the light would have gone if the matter were not present [8]. . . . .   | 7  |
| 123 | Figure 2.3 | (left) Optical image of galactic cluster 1E0657-558. (right) X-ray image of the cluster with redder meaning hotter and higher baryon density. (both) Green contours are reconstruction of gravity contours from weak lensing. White rings are the best fit mass maxima at 68.3%, 95.5%, and 99.7% confidence. The matter maxima of the clusters are clearly separated from x-ray maxima. [9]  | 8  |
| 128 | Figure 2.4 | Plank CMB sky. Sky map features small variations in temperature in primordial light. These anisotropies are used to make inferences about the universe's energy budget and developmental history. [10] . . . . .  | 9  |
| 131 | Figure 2.5 | Observed Cosmic Microwave Background power spectrum as a function of multipole moment from Plank [10]. Blue line is best fit model from $\Lambda$ CDM. Red points and lines are data and error, respectively. . . . .   | 10 |
| 134 | Figure 2.6 | Predicted power spectra of CMB for different $\Omega_m h^2$ values for fixed baryon density from [11]. (left) Low $\Omega_m h^2$ increases the prominence of first and second peaks. (middle) $\Omega_m h^2$ is most similar to the observed power spectrum. The second and third peaks are similar in height. (right) $\Omega_m h^2$ is large which suppresses the first peak and raises the prominence of the third peak. . . . .   | 10 |
| 139 | Figure 2.7 | The Standard Model (SM) of particle physics. Figure taken from <a href="http://www.quantumdiaries.org/2014/03/14/the-standard-model-a-beautiful-but-flawed-theory/">http://www.quantumdiaries.org/2014/03/14/the-standard-model-a-beautiful-but-flawed-theory/</a> . . . . .  | 12 |
| 142 | Figure 2.8 | Simplified Feynman diagram demonstrating with different ways DM can interact with SM particles. The 'X's refer to the DM particles whereas the SM refer to fundamental particles in the SM. The large circle in the center indicates the vertex of interaction and is purposely left vague. The colored arrows refer to different directions of time as well as their respective labels. The arrows indicate the initial and final state of the DM -SM interaction in time. | 13 |

|     |  |    |
|-----|--|----|
| 148 | Figure 2.9 A single jet event in ATLAS detector from 2017 [16]. Jet momentum was<br>149 observed to be 1.9 TeV. Missing transverse momentum was observed to be<br>150 1.9 TeV compared to the initial transverse momentum of the event was 0.<br>151 Implied MET is traced by a red dashed line in event display. . . . .  | 14 |
| 152 | Figure 2.10 More detailed pseudo-Feynman diagram of particle cascade from dark matter<br>153 annihilation into 2 quarks. The quarks hadronize and down to stable particles<br>154 like $\gamma$ or the anti-proton ( $p^-$ ). Diagram pulled from ICRC 2021 presentation<br>155 on DM annihilation search [17]. . . . .  | 15 |
| 156 | Figure 2.11 Dark Matter (DM) decay spectrum for $b\bar{b}$ initial state and $\gamma$ final state. Redder<br>157 spectra are for larger DM masses. Bluer spectra are light DM masses. $x$ is a<br>158 unitless factor defined as the ratio of the mass of DM, $m_\chi$ , and the final state<br>159 particle energy $E_\gamma$ . Figure from [19]. . . . .   | 17 |
| 160 | Figure 2.12 Different dark matter density profiles compared. Some models produce ex-<br>161 ceptionally large densities at small r [20]. . . . .   | 18 |
| 162 | Figure 2.13 The Milky Way Galaxy in photons ( $\gamma$ ) and neutrinos ( $\nu$ ) [22]. The Galactic<br>163 center is at $l=0^\circ$ and is the brightest region in all panels. (top) An Optical<br>164 color image of the Milky Way galaxy seen from Earth. Clouds of gas and dust<br>165 obscure some light from stars. (2nd down) Integrated flux of $\gamma$ -rays observed<br>166 by the Fermi-LAT telescope [23]. (middle) Expected neutrino emission<br>167 that corresponds with Fermi-LAT observations. (2nd up) Expected neutrino<br>168 emission profile after considering detector systematics of IceCube. (bottom)<br>169 Observed neutrino emission from region of the galactic plane. Substantial<br>170 neutrino emission was detected. . . . .   | 19 |
| 171 | Figure 2.14 Dark Matter annihilation spectra for different final state particle and standard<br>172 model annihilation channels [24]. Photons (red), $e^\pm$ (green), $\bar{p}$ (blue), $\nu$ (black). . . . .   | 20 |
| 173 | Figure 5.1 Sensitivities of five gamma-ray experiments compared to percentages of the<br>174 Crab nebula's emission and dark matter annihilation. Solid lines present<br>175 estimated sensitivities to power law spectra [FACT CHECK THIS]for each<br>176 experiment. Green lines are Fermi-LAT sensitivities where lighter green is<br>177 the sensitivity to the galactic center and dark green is its sensitivity to higher<br>178 declinations. Orange, red, and purple solid lines represent the MAGIC, HESS,<br>179 and VERITAS 50 hour sensitivities respectively. The maroon and brown lines<br>180 are the HAWC 1 year and 5 year sensitivities. Across four decades of gamma-<br>181 ray energy, these experiments have similar sensitivities on the order $10^{-12}$<br>182 $\text{erg cm}^{-2}\text{s}^{-1}$ . The dotted lines are estimated dark matter fluxes assuming<br>183 $m_\chi = 5 \text{ TeV}$ DM annihilating to bottom quarks (red), tau leptons (blue),<br>184 and W bosons (green). Faded gray lines outline percentage flux of the Crab<br>185 nebula. Figure is an augmented version of [25] . . . . . | 24 |

|     |            |   |    |
|-----|------------|---|----|
| 186 | Figure 5.2 | Effect of Electroweak (EW) corrections on expected DM annihilation spectrum for $\chi\chi \rightarrow W^-W^+$ . Solid lines are spectral models that consider EW corrections. Dash-dot lines are spectral models without EW corrections. Red lines are models for $M_\chi = 1$ TeV. Blue lines represent models for $M_\chi = 100$ TeV. All models are sourced from the PPPC4DMID [44]. . . . .   | 28 |
| 191 | Figure 5.3 | $\frac{dJ}{d\Omega}$ maps for Segue1 (top) and Coma Berenices (bottom). Origin is centered on the specific dwarf spheroidal galaxies (dSph). X and Y axes are the angular separation from the center of the dwarf. Profile is truncated at the scale radius. Plots of the remaining 11 dSph HAWC studied are linked in Fig. A.1. . . . .  | 30 |
| 195 | Figure 5.4 | Illustration of the combination technique showing a comparison between $-2 \ln \lambda$ provided by four instruments (colored lines) from the observation of the same dSph without any $J$ nuisance and their sum, <i>i.e.</i> the resulting combined likelihood (thin black line). According to the test statistics of Equation (5.7), the intersection of the likelihood profiles with the line $-2 \ln \lambda = 2.71$ indicates the 95% C.L. upper limit on $\langle \sigma v \rangle$ . The combined likelihood (thin black line) shows a smaller value of upper limit on $\langle \sigma v \rangle$ than those derived by individual instruments. We also show how the uncertainties on the $J$ factor effects the combined likelihood and degrade the upper limit on $\langle \sigma v \rangle$ (thick black line). All likelihood profiles are normalized so that the global minimum $\widehat{\langle \sigma v \rangle}$ is 0. We note that each profile depends on the observational conditions in which a target object was observed. The sensitivity of a given instrument can be degraded and the upper limits less constraining if the observations are performed in non-optimal conditions such as a high zenith angle or a short exposure time. . . . . | 36 |
| 210 | Figure 5.5 | . . . . .   | 39 |
| 211 | Figure 5.6 | HAWC TS values for best fit $\langle \sigma v \rangle$ versus $m_\chi$ for seven SM annihilation channels with $J$ factors from $\mathcal{GS}$ . The solid black line shows the combined best fit TS values. The colored, dashed lines are the TS values for each of the 13 sources HAWC studied. . . . .   | 40 |
| 215 | Figure 5.7 | HAWC Brazil bands at 95% confidence level on $\langle \sigma v \rangle$ versus DM mass for seven annihilation channels with $J$ -factors from $\mathcal{GS}$ [55]. The solid line represents the combined limit from 13 dSphs. The dashed line is the expected limit. The green band is the 68% containment. The yellow band is the 95% containment. . . . .  | 41 |

|     |             |  |    |
|-----|-------------|--|----|
| 220 | Figure 5.8  | Upper limits at 95% confidence level on $\langle \sigma v \rangle$ in function of the DM mass for<br>221 eight annihilation channels, using the set of $J$ factors from Ref. [55] ( $\mathcal{GS}$ set<br>222 in Table 5.1). The black solid line represents the observed combined limit,<br>223 the black dashed line is the median of the null hypothesis corresponding<br>224 to the expected limit, while the green and yellow bands show the 68% and<br>225 95% containment bands. Combined upper limits for each individual detector<br>226 are also indicated as solid, colored lines. The value of the thermal relic<br>227 cross-section in function of the DM mass is given as the red dotted-dashed<br>228 line [56]. . . . . | 42 |
| 229 | Figure 5.9  | Same as Fig. 5.8, using the set of $J$ factors from Ref. [49, 57] ( $\mathcal{B}$ set in Table 5.1). . . . .   | 43 |
| 230 | Figure 5.10 | Comparisons of the combined limits at 95% confidence level for each of the<br>231 eight annihilation channels when using the $J$ factors from Ref. [55] ( $\mathcal{GS}$ set in<br>232 Table 5.1), plain lines, and the $J$ factor from Ref. [49, 57] ( $\mathcal{B}$ set in Table 5.1),<br>233 dashed lines. The cross-section given by the thermal relic is also indicated [56]. . . . .   | 45 |
| 234 | Figure 5.11 | Comparisons of the combined limits at 95% confidence level for a point source<br>235 analysis and extended source using [55] $\mathcal{GS}$ J-factor distributions and PPPC<br>236 [44] annihilation spectra. Shown are the limits for Segue1 which will have<br>237 the most significant impact on the combined limit. 6 of the 7 DM annihilation<br>238 channels are shown. Solid lines are extended source studies. Dashed lines<br>239 are point source studies. Overall, the extended source analysis improves the<br>240 limit by a factor of 2. . . . .   | 47 |
| 241 | Figure 5.12 | Same as Fig. 5.11 on Coma Berenices. This dSph also contributes signifi-<br>242 cantly to the limit. The limits are identical in this case. . . . .  | 48 |
| 243 | Figure 5.13 | Comparison of combined limits when correcting for HAWC's pointing sys-<br>244 tematic. All DM annihilation channels are shown. The solid black line is the<br>245 ratio between published limit to the declination corrected limit. The blue solid<br>246 line or "Combined_og" represented the limits computed for Glory Duck. The<br>247 solid orange line or "Combined_ad" represented the limits computed after<br>248 correcting for the pointing systematic. . . . .   | 49 |
| 249 | Figure 5.14 | Differential map of $dJ/\Omega$ from model built in Section 5.8.1 and profiles<br>250 provided directly from authors. (Top) Differential from Segue1. (bottom)<br>251 Differential from Coma Berenices. Note that their scales are not the same.<br>252 Segue1 shows the deepest discrepancies which is congruent with its large<br>253 uncertainties. Both models show anuli where unique models become apparent. . . . .   | 50 |

|     |   |    |
|-----|---|----|
| 254 | Figure 5.15 HAWC limits for Coma Berenices (top) and Segue1 (bottom) for two different<br>255 map sets. Blue lines are limits calculated on maps with poor model repre-<br>256 sentation. Orange lines are limits calculated on spatial profiles provided by<br>257 the authors of [45]. Black line is the ratio of the poor spatial model limits to<br>258 the corrected spatial models. The left y-axis measures $\langle \sigma v \rangle$ for the blue and<br>259 orange lines. The right y-axis measures the ratio and is unitless. . . . .  | 51 |
| 260 | Figure 5.16 Comparisons between the $J$ -factors versus the angular radius for the com-<br>261 putation of $J$ factors from Ref. [55] ( $\mathcal{GS}$ set in Table 5.1) in blue and for<br>262 the computation from Ref. [49, 57] ( $\mathcal{B}$ set in Tab. 5.1) in orange. The solid<br>263 lines represent the central value of the $J$ -factors while the shaded regions<br>264 correspond to the $1\sigma$ standard deviation. . . . .   | 53 |
| 265 | Figure 5.17 Comparisons between the $J$ -factors versus the angular radius for the computa-<br>266 tion of $J$ factors from Ref. [55] ( $\mathcal{GS}$ set in Tab. 5.1) in blue and for the<br>267 computation from Ref. [49, 57] ( $\mathcal{B}$ set in Tab. 5.1) in orange. The solid<br>268 lines represent the central value of the $J$ -factors while the shaded regions<br>269 correspond to the $1\sigma$ standard deviation. . . . .  | 54 |
| 270 | Figure 6.1 Spectral hypotheses from PPPC [44] and HDM [65] for DM annihilation:<br>$\chi\chi \rightarrow W^-W^+$ . Solid lines are spectral models with EW corrections from the<br>271 PPPC. Dash-dot lines are spectral models from HDM. Red lines are models<br>272 for $M_\chi = 1$ TeV. Blue lines represent models for $M_\chi = 100$ TeV. . . . .   | 59 |
| 274 | Figure 6.2 Photon spectra for $\chi\chi \rightarrow \gamma\gamma$ (left) and $\chi\chi \rightarrow ZZ$ (right) after Gaussian<br>275 convolution of line features. Both spectra have $\delta$ -features at photon energies<br>276 equal to the DM mass. Bluer lines are annihilation spectra with lower DM<br>277 mass. Redder lines are spectra from larger DM mass. All spectral models are<br>278 sourced from the Heavy Dark Matter models [65]. Axes are drawn roughly<br>279 according to the energy sensitivity of HAWC. . . . .   | 60 |
| 280 | Figure 6.3 $\frac{dJ}{d\Omega}$ maps for Coma Berenices, Draco, Segue1, and Sextans. Columns are<br>281 divided for the $\pm 1\sigma$ uncertainties in $dJ/d\Omega$ around the mean value from $\mathcal{LS}$<br>282 [66]. Origin is centered on the specific dwarf spheroidal galaxies (dSph). $\theta$<br>283 and $\phi$ axes are the angular separation from the center of the dwarf. Profiles<br>284 are truncated at $1^\circ$ and flattened beyond. . . . .   | 62 |
| 285 | Figure 6.4 Infographic on how jobs and DM computation was organized in Section 5.3.<br>286 Jobs were built for each permutation of CHANS and SOURCES shown by the<br>287 left block in the figure. Each job, which took on the order 2 hrs to compute,<br>288 had the following work flow: 1. Import HAWC analysis software, 2 min to<br>289 run. 2. Load HAWC count maps, 5 min to run. 3. Load HAWC energy and<br>290 spatial resolutions, 4 min. 5. Load DM spatial source templates and spectral<br>291 models, less than 1 s. 6. Perform likelihood fit on data and model, about 8<br>292 min per DM mass. 7. Write results to file, less than 1s. . . . . | 64 |

|     |             |  |    |
|-----|-------------|--|----|
| 293 | Figure 6.5  | Graphic of Gustafson parallel coding pattern. $f_s$ is the fraction of a program,<br>in time, spent on serial computation. $f_p$ is the fraction of computing time<br>that is parallelizable. $T_p$ is the total time for a parallel program to run. $T_1$ is<br>the total time for a parallel program to run if only 1 processor is allocated.<br>$P_N$ is the $N$ -th processor where it's row is the computation the processor<br>performs. The Gustafson pattern is most similar to what is implemented for<br>this analysis. Figure is pulled from [68]. . . . .  | 65 |
| 300 | Figure 6.6  | Task chart for one multithreaded job developed for this project. Green blocks<br>indicate a shared resource across the threads AND computation performed<br>serially. Red blocks indicate functional parallel processing within each thread.<br>3 threads are represented here, yet many more can be employed during the<br>full analysis. Jobs are defined by the SOURCE as these require unique maps<br>to be loaded into the likelihood estimator. The $m_\chi$ , CHAN, and $\langle\sigma v\rangle$ variables<br>are entered into the thread pool and allocated as evenly as possible across the<br>threads. . . . .   | 67 |
| 308 | Figure 6.7  | HAWC upper limits at 95% confidence level on $\langle\sigma v\rangle$ versus $m_\chi$ for $\chi\chi \rightarrow b\bar{b}, t\bar{t}, u\bar{u}, d\bar{d}, s\bar{s}, c\bar{c}, gg, W^+W^-$ , and $hh$ . Limits are with $\mathcal{LS}$ $J$ -factors<br>[66]. The solid line represents the observed combined limit. Dashed lines<br>represent limits from individual dSphs. . . . .   | 70 |
| 312 | Figure 6.8  | HAWC upper limits at 95% confidence level on $\langle\sigma v\rangle$ versus $m_\chi$ for $\chi\chi \rightarrow \nu_e\bar{\nu}_e, \nu_\mu\bar{\nu}_\mu, \nu_\tau\bar{\nu}_\tau, e\bar{e}, \mu\bar{\mu}, \tau\bar{\tau}, \gamma\gamma$ and $ZZ$ . Limits use $\mathcal{LS}$ $J$ -factors [66]. The<br>solid line represents the observed combined limit. Dashed lines represent<br>limits from individual dSphs. . . . .  | 71 |
| 316 | Figure 6.9  | HAWC TS values for best fit $\langle\sigma v\rangle$ versus $m_\chi$ for SM annihilation channels:<br>$\chi\chi \rightarrow b\bar{b}, t\bar{t}, u\bar{u}, d\bar{d}, s\bar{s}, c\bar{c}, gg, W^+W^-$ , and $hh$ . Limits use $\mathcal{LS}$ $J$ -factors.<br>The solid black line shows the combined best fit TS values. The colored,<br>dashed lines are the TS values from each dSph. . . . .   | 72 |
| 320 | Figure 6.10 | HAWC TS values for best fit $\langle\sigma v\rangle$ versus $m_\chi$ for SM annihilation channels:<br>$\chi\chi \rightarrow \nu_e\bar{\nu}_e, \nu_\mu\bar{\nu}_\mu, \nu_\tau\bar{\nu}_\tau, e\bar{e}, \mu\bar{\mu}, \tau\bar{\tau}, \gamma\gamma$ and $ZZ$ . Limits use $\mathcal{LS}$ $J$ -factors.<br>The solid black line shows the combined best fit TS values. The colored,<br>dashed lines are the TS values from each dSph. . . . .   | 73 |
| 324 | Figure 6.11 | Comparison of HAWC limits from this analysis to Glory Duck (Fig. 5.5)<br>for 3 dSphs and 3 DM annihilation channels: $b\bar{b}, \tau\bar{\tau}$ , and $e\bar{e}$ . Each sector<br>shows the 95% confidence limit from Glory Duck (blue line) and this analysis<br>(orange line) in the top plot. The lower plot features the ratio in log scale of<br>Glory Duck to this analysis in a red solid line. Horizontal dashed lines are<br>for ratios of 1.0 (black) and $\sqrt{2}$ (blue). Ratios larger than 1.0 are for limits<br>smaller, or stricter, than Glory Duck. Ratios larger than $\sqrt{2}$ indicates limits<br>are stricter than a simple doubling of the Glory Duck data. . . . . | 75 |

|     |             |  |    |
|-----|-------------|--|----|
| 332 | Figure 7.1  | Neutrino spectra at production (left panels) and after oscillation at Earth<br>333 (right panels). Blue, orange, and green lines are the $\nu_e$ , $\nu_\mu$ , and $\nu_\tau$ spectra<br>334 respectively. Top panels show the spectra in $\frac{dN}{dE}$ . Lower panels plot the flavor<br>335 ratio to $\nu_e + \nu_\mu + \nu_\tau$ . SM annihilation channels $b\bar{b}$ , $\tau\bar{\tau}$ , and $\nu_\mu\bar{\nu}_\mu$ are shown<br>336 for $M_\chi = 1$ PeV, TeV, and EeV. . . . .   | 80 |
| 337 | Figure 7.2  | Signal recovery for 100 TeV DM annihilation into $\nu_\mu\bar{\nu}_\mu$ for a source at Dec<br>338 = 16.06°. $n_{\text{inj}}$ is the number of injected signal events in simulation. $n_s$ is<br>339 the number of reconstructed signal events from the simulation. Although<br>340 the uncertainties are small and tight, the reconstructed $n_s$ are systematically<br>341 underestimated. . . . .   | 81 |
| 342 | Figure 7.3  | Top left panel shows the two kernels overlayed the original spectrum from<br>343 Charon. delta I is the difference in the integral of the peaks with respect to the<br>344 original spectrum. The vertical red line indicated where the original neutrino<br>345 line is maximized. Lower right shows the signal recovers of the DM model<br>346 using the Gaussian kernel with parameters enumerated above. . . . .   | 82 |
| 347 | Figure 7.4  | Example spline that failed the fit. Failed splined are corrected on a case by<br>348 case basis unless the SM channel has a systematic problem fitting the splines.<br>349 In this case, I made a bookkeeping error and loaded the incorrected neutrino<br>350 flavor . . . . .  | 84 |
| 351 | Figure 7.5  | Summary of input spectral models that were smoothed with Gaussian kernel.<br>352 Spectral models are for $\chi\chi \rightarrow e\bar{e}$ , $\mu\bar{\mu}\tau\bar{\tau}$ , $\nu_e\bar{\nu}_e$ , $\nu_\mu\bar{\nu}_\mu$ , and $\nu_\tau\bar{\nu}_\tau$ . These spectra<br>353 are the composite ( $\nu_\mu + \nu_\tau$ ) of neutrino flavors. Every spectral model used for<br>354 this analysis is featured as a colored solid line. Bluer lines are for lower DM<br>355 mass spectral models. DM masses range from 681 GeV to 100 PeV. HDM<br>356 [65], $\chi$ arov [69], and Photospline [71] are used to generate these spectra.<br>357 Energy (x-axis) was chosen to roughly represent the energy sensitivity of NST. . | 85 |
| 358 | Figure 7.6  | Test statistic (TS) distributions for Segue 1 and $\chi\chi \rightarrow b\bar{b}$ . Each subplot,<br>359 except the final, is the TS distribution for a specific DM mass listed in the<br>360 subplot. Orange dashed lines are the traces for a $\chi^2$ distribution with 1 degree<br>361 of freedom. $\epsilon[\cdot]$ is the fraction of trials smaller than the bracketed value. The<br>362 final subplot plots the all DM spectral models, similar to Fig. 7.5, used as<br>363 input for the TS distributions. . . . .  | 90 |
| 364 | Figure 7.7  | Same as Fig. 7.6 for Segue 1 $\chi\chi \rightarrow \tau\bar{\tau}$ . . . . .   | 91 |
| 365 | Figure 7.8  | Same as Fig. 7.6 for Segue 1 $\chi\chi \rightarrow \nu_\mu\bar{\nu}_\mu$ . . . . .   | 92 |
| 366 | Figure 7.9  | Same as Fig. 7.6 for Ursa Major II 1 $\chi\chi \rightarrow b\bar{b}$ . . . . .   | 93 |
| 367 | Figure 7.10 | Same as Fig. 7.6 for Ursa Major II 1 $\chi\chi \rightarrow \tau\bar{\tau}$ . . . . .   | 94 |

|     |   |     |
|-----|---|-----|
| 368 | Figure 7.11 Same as Fig. 7.6 for Ursa Major II 1 $\chi\chi \rightarrow \nu_\mu\bar{\nu}_\mu$ . . . . .  | 95  |
| 369 | Figure 7.12 Same as Fig. 7.6 for 15, $\mathcal{GS}$ $J$ -factor, stacked sources and $\chi\chi \rightarrow b\bar{b}$ . . . . .  | 96  |
| 370 | Figure 7.13 Same as Fig. 7.6 for 15, $\mathcal{GS}$ $J$ -factor, stacked sources and $\chi\chi \rightarrow t\bar{t}$ . . . . .  | 97  |
| 371 | Figure 7.14 Same as Fig. 7.6 for 15, $\mathcal{GS}$ $J$ -factor, stacked sources and $\chi\chi \rightarrow u\bar{u}$ . . . . .  | 98  |
| 372 | Figure 7.15 Same as Fig. 7.6 for 15, $\mathcal{GS}$ $J$ -factor, stacked sources and $\chi\chi \rightarrow d\bar{d}$ . . . . .  | 99  |
| 373 | Figure 7.16 Same as Fig. 7.6 for 15, $\mathcal{GS}$ $J$ -factor, stacked sources and $\chi\chi \rightarrow e\bar{e}$ . . . . .  | 100 |
| 374 | Figure 7.17 Same as Fig. 7.6 for 15, $\mathcal{GS}$ $J$ -factor, stacked sources and $\chi\chi \rightarrow \mu\bar{\mu}$ . . . . .  | 101 |
| 375 | Figure 7.18 Same as Fig. 7.6 for 15, $\mathcal{GS}$ $J$ -factor, stacked sources and $\chi\chi \rightarrow \tau\bar{\tau}$ . . . . .  | 102 |
| 376 | Figure 7.19 Same as Fig. 7.6 for 15, $\mathcal{GS}$ $J$ -factor, stacked sources and $\chi\chi \rightarrow W^+W^-$ . . . . .  | 103 |
| 377 | Figure 7.20 Same as Fig. 7.6 for 15, $\mathcal{GS}$ $J$ -factor, stacked sources and $\chi\chi \rightarrow ZZ$ . . . . .  | 104 |
| 378 | Figure 7.21 Same as Fig. 7.6 for 15, $\mathcal{GS}$ $J$ -factor, stacked sources and $\chi\chi \rightarrow \nu_e\bar{\nu}_e$ . . . . .  | 105 |
| 379 | Figure 7.22 Same as Fig. 7.6 for 15, $\mathcal{GS}$ $J$ -factor, stacked sources and $\chi\chi \rightarrow \nu_\mu\bar{\nu}_\mu$ . . . . .  | 106 |
| 380 | Figure 7.23 Signal Recovery study for an analysis with 15 stacked sources using the $\mathcal{GS}$ $J$ -factors [45]. Each panel block represents 14 studies for DM mass ranging between 1 TeV and 20 PeV and one annihilation channel. Top panel block is for $\chi\chi \rightarrow b\bar{b}$ . Bottom panel block is for $\chi\chi \rightarrow t\bar{t}$ . Each panel block features every spectral model used as input in the bottom-right subpanel. The remaining panels show $N_{inj}$ as the number of signal events injected into background simulation. Whereas, $N_s$ is the number of signal events recovered from analyzing the injected simulation. Blue line represents the median values of 100 simulations. Light blue bands show the $1\sigma$ statistical uncertainty around the median. . . . . | 107 |
| 390 | Figure 7.24 Same as Fig. 7.23 but for $\chi\chi \rightarrow \nu_\mu\bar{\nu}_\mu$ . . . . .   | 108 |
| 391 | Figure 7.25 Words. I predict Icecube Sensitivities weeee . . . . .  | 109 |
| 392 | Figure 7.26 Words. I predict Icecube Sensitivities weeee . . . . .  | 110 |
| 393 | Figure A.1 Sister figure to Figure 5.3. Sources in the first row from left to right: Bootes I, Canes Venatici I, II. In second row: Draco, Hercules, Leo I. In the first row: Leo II, Leo IV, Sextans. In the final row: Ursa Major I, Ursa Major II. . . . .   | 112 |

|     |   |   |     |
|-----|---|---|-----|
| 396 | Figure B.1 Sister figure to Figure 6.2 for remaining SM primary annihilation channels<br>397<br>398<br>399                              | studied for this thesis. These did not require any post generation smoothing<br>and so are directly pulled from [65] with a binning scheme most helpful for a<br>HAWC analysis.   | 113 |
| 400 | Figure B.2 <b>TODO: fill this out</b>   | 123   |     |
| 401 | Figure B.3 <b>TODO: fill this out</b>   | 124   |     |
| 402 | Figure B.4 <b>TODO: fill this out</b>   | 125   |     |
| 403 | Figure C.1 Current status of spline tables according to constraints defined by Tab. 7.1.<br>404<br>405<br>406<br>407                    | Green splines are splines that passed under the GOOD tolerance. Yellow<br>are splines that are OK. Red are splines that FAIL. All yellow splines were<br>inspected individually before running the analysis. Splines were made for the<br>$\mu$ (PID 14; top panel) flavor and $\tau$ (PID 16; bottom panel). | 129 |
| 408 | Figure C.2 <b>TODO: Fill this out eventually. I think I want all the plots generated<br/>409 first[NEEDS A SOURCE][FACT CHECK THIS]</b> | 130   |     |

**LIST OF ABBREVIATIONS**

- 411 **MSU** Michigan State University  
412 **LANL** Los Alamos National Laboratory  
413 **DM** Dark Matter  
414 **SM** Standard Model  
415 **HAWC** High Altitude Water Cherenkov Observatory  
416 **dSph** Dwarf Spheroidal Galaxy

## CHAPTER 1

### INTRODUCTION

418 Is the text not rendering right? Ah ok it knows im basically drafting the doc still

## CHAPTER 2

419

### DARK MATTER IN THE COSMOS

420 **2.1 Introduction**

421 The dark matter problem can be summarized in part by the following thought experiment.

422 Let us say you are the teacher for an elementary school classroom. You take them on a field  
423 trip to your local science museum and among the exhibits is one for mass and weight. The exhibit  
424 has a gigantic scale, and you come up with a fun problem for your class.

425 You ask your class, "What is the total weight of the classroom? Give your best estimation to  
426 me in 30 minutes, and then we'll check your guess on the scale. If your guess is within 10% of the  
427 right answer, we will stop for ice cream on the way back."

428 The students are ecstatic to hear this, and they get to work. The solution is some variation of  
429 the following strategy. The students should give each other their weight or best guess if they do  
430 not know. Then, all they must do is add each student's weight and get a grand total for the class.

431 The measurement on the giant scale should show the true weight of the class. When comparing  
432 the measured weight to your estimation, multiply the measurement by  $1.0 \pm 0.1$  to get the  $\pm 10\%$   
433 tolerances for your estimation.

434 Two of your students, Sandra and Mario, return to you with a solution.

435 They say, "We weren't sure of everyone's weight. We used 65 lbs. for the people we didn't  
436 know and added everyone who does know. There are 30 of us, and we got 2,000 lbs.! That's a ton!"

437 You estimated 1,900 lbs. assuming the average weight of a student in your class was 60 lbs.  
438 So, you are pleased with Sandra's and Mario's answer. You instruct your students to all gather on  
439 the giant scale and read off the weight together. To all your surprise, the scale reads *10,000 lbs.*!  
440 10,000 is significantly more than a 10% error from 2,000. In fact, it is approximately 5 times more  
441 massive than either your or your students' estimates. You think to yourself and conclude there  
442 must be something wrong with the scale. You ask an employee to check the scale and verify it is  
443 well calibrated. They confirm that the scale is in working order. You weigh a couple of students  
444 individually to assess that the scale is well calibrated. Sandra weighs 59 lbs., and Mario weighs

445 62 lbs., typical weights for their age. You then weigh each student individually and see that their  
446 weights individually do not deviate greatly from 60 lbs. So, where does all the extra weight come  
447 from?

448 This thought experiment serves as an analogy to the Dark Matter problem. The important  
449 substitution to make however is to replace the students with stars and the classroom with a galaxy,  
450 say the Milky Way. Individually the mass of stars is well measured and defined with the Sun as our  
451 nearest test case. However, when we set out to measure the mass of a collection of stars as large as  
452 galaxies, our well-motivated estimation is wildly incorrect. There simply is no way to account for  
453 this discrepancy except without some unseen, or dark, contribution to mass and matter in galaxies.  
454 I set out in my thesis to narrow the possibilities of what this Dark Matter could be.

455 This chapter is organized like the following... **TODO: Text should look like ... Chapter x has**  
456 **blah blah blah.**

## 457 2.2 Dark Matter Basics

458 Presently, a more compelling theory of cosmology that includes Dark Matter (DM) in order  
459 to explain a variety of observations is  $\Lambda$  Cold Dark Matter, or  $\Lambda$ CDM. I present the evidence  
460 supporting  $\Lambda$ CDM in Section 2.3 yet discuss the conclusions of the  $\Lambda$ CDM model here. According  
461 to  $\Lambda$ CDM fit to observations on the Cosmic Microwave Background (CMB), DM is 26.8% of the  
462 universe's current energy budget. Baryonic matter, stuff like atoms, gas, and stars, contributes to  
463 4.9% of the universe's current energy budget [1, 2, 3].

464 DM is dark; it does not interact readily with light at any wavelength. DM also does not interact  
465 noticeably with the other standard model forces (Strong and Weak) at a rate that is readily observed  
466 [3]. DM is cold, which is to say that the average velocity of DM is below relativistic speeds [1].  
467 'Hot' DM would not likely manifest the dense structures we observe like galaxies, and instead  
468 would produce much more diffuse galaxies than what is observed [3, 1]. DM is old; it played a  
469 critical role in the formation of the universe and the structures within it [1, 2].

470 Observations of DM have so far been only gravitational. The parameter space available to what  
471 DM could be therefore is extremely broad. The broad DM parameter space is iteratively tested in

472 DM searches by supposing a hypothesis that has not yet been ruled out and performing observations  
473 to test them. When the observations yield a null result, the parameter space is constrained further.  
474 I present some approaches for DM searches in Section 2.4.

475 **2.3 Evidence for Dark Matter**

476 Dark Matter (DM) has been a looming problem in physics for almost 100 years. Anomalies  
477 have been observed by astrophysicists in galactic dynamics as early as 1933 when Fritz Zwicky  
478 noticed unusually large velocity dispersion in the Coma cluster. Zwicky's measurement was the  
479 first recorded to use the Virial theorem to measure the mass fraction of visible and invisible matter  
480 in celestial bodies [4]. From Zwicky in [5], "*If this would be confirmed, we would get the surprising*  
481 *result that dark matter is present in much greater amount than luminous matter.*" Zwicky's and  
482 others' observation did not instigate a crisis in astrophysics because the measurements did not  
483 entirely conflict with their understanding of galaxies [4]. In 1978, Rubin, Ford, and Norbert  
484 measured rotation curves for ten spiral galaxies [6]. Rubin et al.'s 1978 publication presented a  
485 major challenge to the conventional understanding of galaxies that could no longer be dismissed by  
486 measurement uncertainties. Evidence has been mounting ever since for this exotic form of matter.  
487 The following subsections provide three compelling pieces of evidence in support of the existence  
488 of DM.

489 **2.3.1 First Clues: Stellar Velocities**

490 Zwicky, and later Rubin, measured the stellar velocities of various galaxies to estimate their  
491 virial mass. The Virial Theorem upon which these observations are interpreted is written as

$$2T + V = 0. \quad (2.1)$$

492 Where  $T$  is the kinetic energy and  $V$  is the potential energy in a self-gravitating system. The  
493 classical Newton's law of gravity from stars and gas was used for gravitational potential modeled in  
494 the observed galaxies:

$$V = -\frac{1}{2} \sum_i \sum_{j \neq i} \frac{m_i m_j}{r_{ij}}. \quad (2.2)$$

495 Zwicky et al. measured just the velocities of stars apparent in optical wavelengths [5]. Rubin et al.  
 496 added by measuring the velocity of the hydrogen gas via the 21 cm emission line of Hydrogen [6].  
 497 The velocities of the stars and gas are used to infer the total mass of galaxies and galaxy clusters  
 498 via Equation (2.1). An inferred mass is obtained from the luminosity of the selected sources. The  
 499 two inferences are compared to each other as a luminosity to mass ratio which typically yielded [1]

$$\frac{M}{L} \sim 400 \frac{M_{\odot}}{L_{\odot}} \quad (2.3)$$

500  $M_{\odot}$  and  $L_{\odot}$  referring to stellar mass and stellar luminosity, respectively. These ratios clearly indicate  
 501 a discrepancy in apparent light and mass from stars and gas and their velocities.

502 Rubin et al. [6] demonstrated that the discrepancy was unlikely to be an underestimation of  
 503 the mass of the stars and gas. The inferred "dark" mass was up to 5 times more than the luminous  
 504 mass. This dark mass also needed to extend well beyond the extent of the luminous matter.

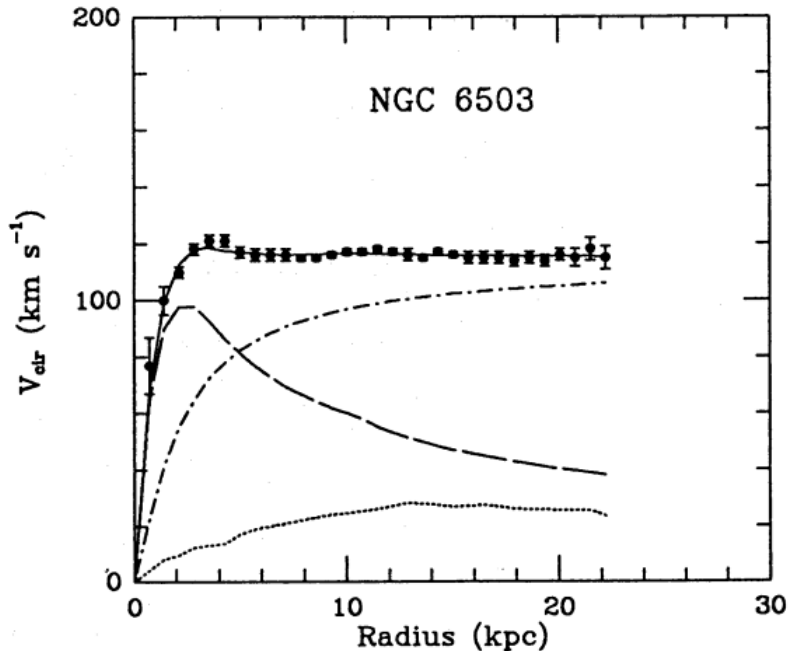


Figure 2.1 Rotation curve fit to NGC 6503 from [7]. Dashed line is the contribution from visible matter. Dotted curves are from gas. Dash-dot curves are from dark matter (DM). Solid line is the composite contribution from all matter and DM sources. Data are indicated with bold dots with error bars. Data agree strongly with a matter + DM composite prediction.

505 Figure 2.1 features one of many rotation curves plotted from the stellar velocities within galaxies.

506 The measured rotation curves mostly feature a flattening of velocities at higher radius which is not  
507 expected if the gravity was only coming from gas and luminous matter. The extension of the  
508 flat velocity region also indicates that the DM is distributed far from the center of the galaxy.  
509 Modern velocity measurements include significantly larger objects, galactic clusters, and smaller  
510 objects, dwarf galaxies. Yet, measurements along this regime are leveraging the Virial theorem  
511 with Newtonian potential energies. We know Newtonian gravity is not a comprehensive description  
512 of gravity. New observational techniques have been developed since 1978, and those are discussed  
513 in the following sections.

### 514 **2.3.2 Evidence for Dark Matter: Gravitational Lensing**

515 Modern evidence for dark matter comes from new avenues beyond stellar velocities. Grav-  
516 itational lensing from DM is a new channel from general relativity. General relativity predicts  
517 aberrations in light caused by massive objects. In recent decades we have been able to measure the  
518 lensing effects from compact objects and DM halos. Figure 2.2 shows how different massive ob-  
519 jects change the final image of a faraway galaxy resulting from gravitational lensing. Gravitational  
520 lensing developed our understanding of dark matter in two important ways.

521 Gravitational lensing provides additional compelling evidence for DM. The observation of two  
522 merging galactic clusters in 2006, shown in Figure 2.3, provided a compelling argument for DM  
523 outside the Standard Model. These clusters merged recently in astrophysical time scales. Galaxies  
524 and star cluster have mostly passed by each other as the likelihood of their collision is low. Therefore,  
525 these massive objects will mostly track the highest mass, dark and/or baryonic, density. Yet, the  
526 intergalactic gas is responsible for the majority of the baryonic mass in the systems [4]. These gas  
527 bodies will not phase through and will heat up as they collide together. The hot gas is located via  
528 x-ray emission from the cluster. Two observations of the clusters were performed independently of  
529 each other.

530 The first was the lensing of light around the galaxies due to their gravitational influences.  
531 When celestial bodies are large enough, the gravity they exert bends space and time itself. The  
532 warped space-time lenses light and will deflect in an analogous way to how glass lenses will bend

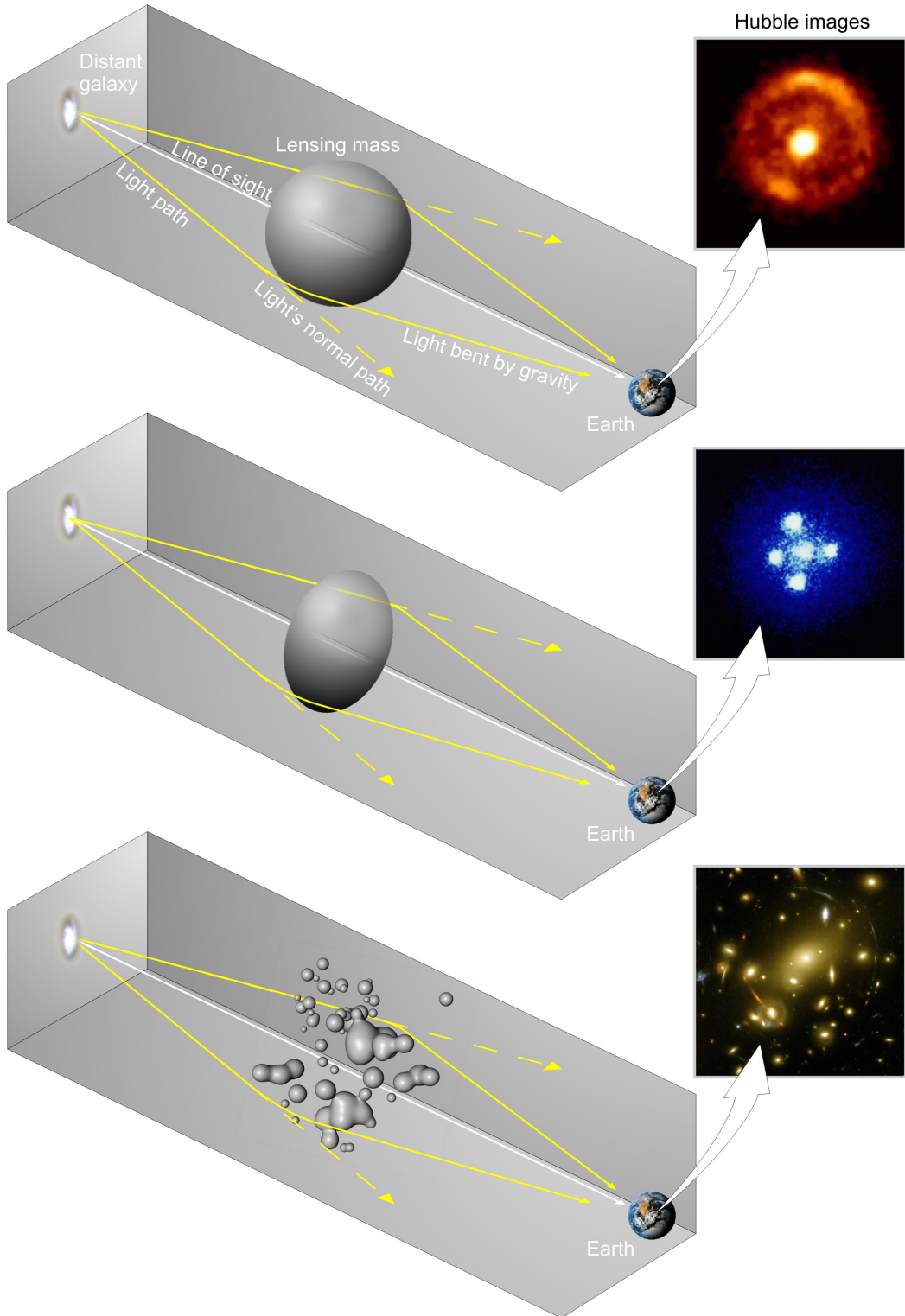


Figure 2.2 Light from distant galaxy is bent in unique ways depending on the distribution of mass between the galaxy and Earth. Yellow dashed lines indicate where the light would have gone if the matter were not present [8].

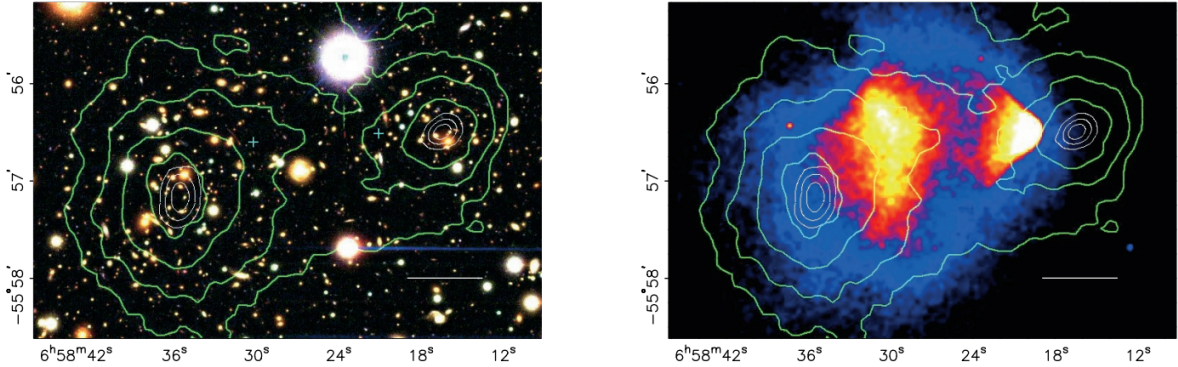


Figure 2.3 (left) Optical image of galactic cluster 1E0657-558. (right) X-ray image of the cluster with redder meaning hotter and higher baryon density. (both) Green contours are reconstruction of gravity contours from weak lensing. White rings are the best fit mass maxima at 68.3%, 95.5%, and 99.7% confidence. The matter maxima of the clusters are clearly separated from x-ray maxima. [9]

533 light, see Figure 2.2. With a sufficient understanding of light sources behind a massive object, we  
 534 can reconstruct the contours of the gravitational lenses. The gradient of the contours shown in  
 535 Figure 2.3 then indicates how dense the matter is and where it is.

536 The x-ray emission can then be observed from the clusters. Since these galaxies are mostly gas  
 537 and are merging, then the gas should be getting hotter. If they are merging, the x-ray emissions  
 538 should be the strongest where the gas is mostly moving through each other. Hence, X-ray emission  
 539 maps out where the gas is in the merging galaxy cluster.

540 The lensing and x-ray observations were done on the Bullet cluster featured on Figure 2.3.  
 541 The x-ray emissions do not align with the gravitational contours from lensing. The incongruence  
 542 in mass density and baryon density suggests that there is a lot of matter somewhere that does  
 543 not interact with light. Moreover, this dark matter cannot be baryonic [9]. The Bullet Cluster  
 544 measurement did not really tell us what DM is exactly, but it did give the clue that DM also does  
 545 not interact with itself very strongly. If DM did interact strongly with itself, then it would have been  
 546 more aligned with the x-ray emission [9]. There have been follow-up studies of galaxy clusters with  
 547 similar results. The Bullet Cluster and others like it provide a persuasive case against something  
 548 possibly amiss in our gravitational theories.

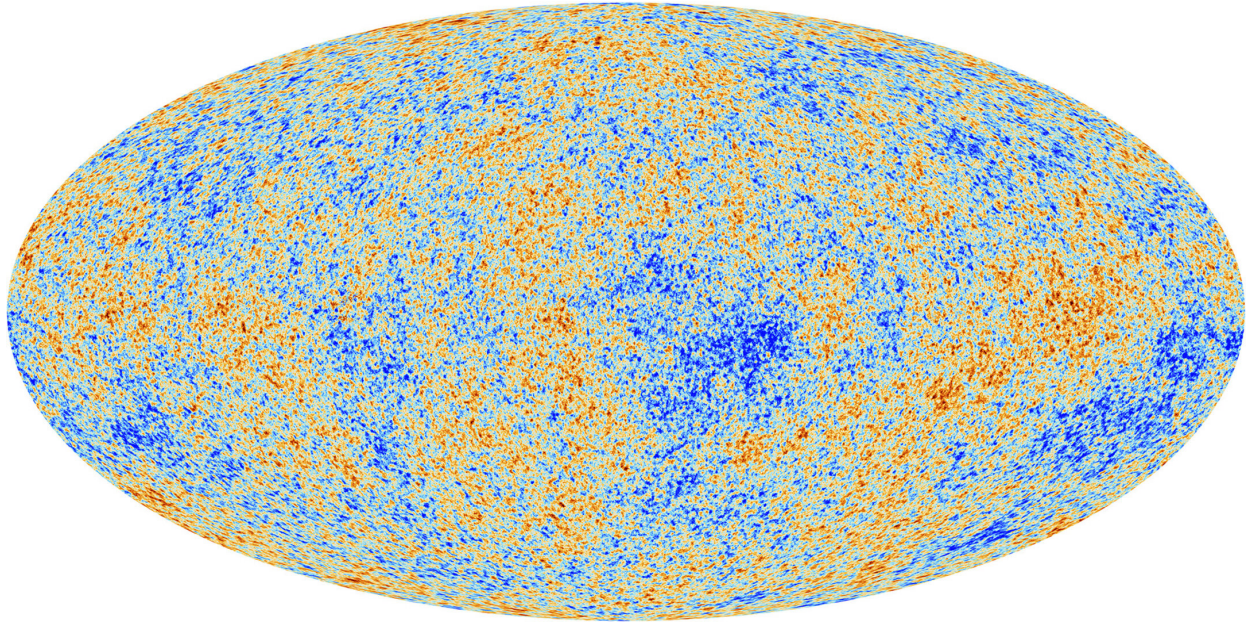


Figure 2.4 Plank CMB sky. Sky map features small variations in temperature in primordial light. These anisotropies are used to make inferences about the universe’s energy budget and developmental history. [10]

549     **2.3.3 Evidence for Dark Matter: Cosmic Microwave Background**

550     The Cosmic Microwave Background (CMB) is the primordial light from the early universe  
551     when Hydrogen atoms formed from the free electron and proton soup in the early universe. The  
552     CMB is the earliest light we can observe; released when the universe was about 380,000 years old.  
553     Then we look at how the simulated universes look like compared to what we see. Figure 2.4 is the  
554     most recent CMB image from the Plank satellite after subtracting the average value and masking the  
555     galactic plane [10]. Redder regions indicate a slightly hotter region in the CMB, and blue indicates  
556     colder. The intensity variations are on the order of 1 in 1000 with respect to the average value.

557     The Cosmic Microwave Background shows that the universe had DM in it from an incredibly  
558     early stage. To measure the DM, Dark Energy, and matter fractions of the universe from the CMB,  
559     the image is analyzed into a power spectrum, which shows the amplitude of the fluctuations as  
560     a function of spherical multipole moments.  $\Lambda$ CDM provides the best fit to the power spectra of  
561     the CMB as shown in Figure 2.5. The CMB power spectrum is quite sensitive to the fraction  
562     of each energy contribution in the early universe. Low  $l$  modes are dominated by variations  
563     in gravitational potential. Intermediate  $l$  emerge from oscillations in photon-baryon fluid from

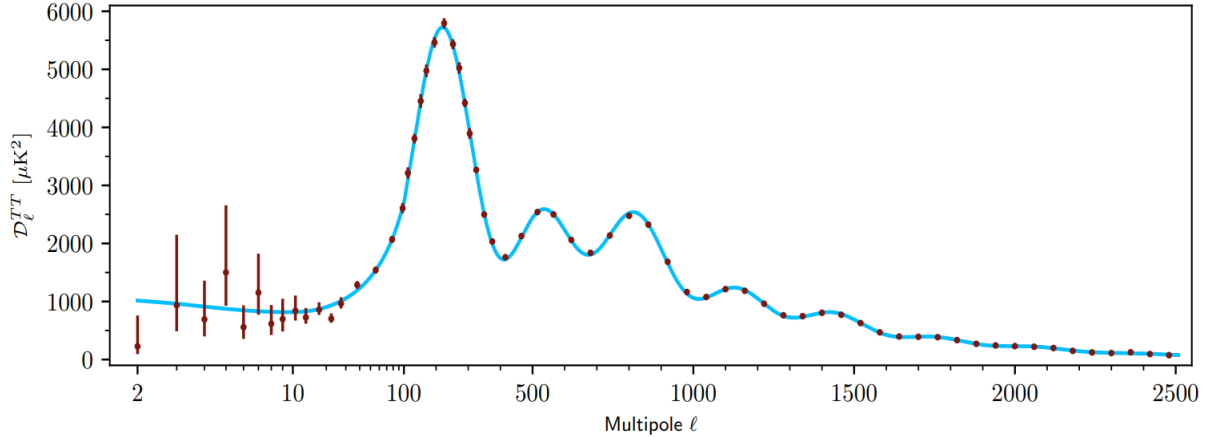


Figure 2.5 Observed Cosmic Microwave Background power spectrum as a function of multipole moment from Plank [10]. Blue line is best fit model from  $\Lambda$ CDM. Red points and lines are data and error, respectively.

564 competing baryon pressures and gravity. High  $l$  is a damped region from the diffusion of photons  
 565 during electron-proton recombination. [1]

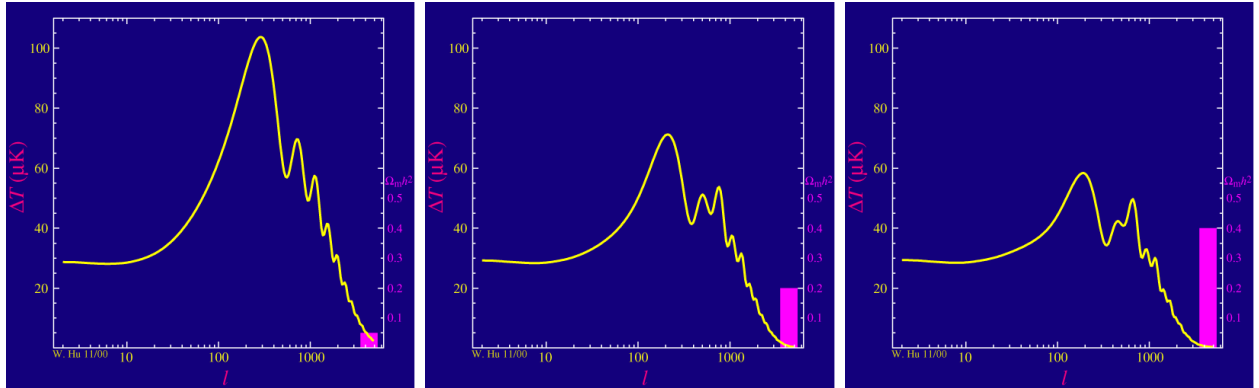


Figure 2.6 Predicted power spectra of CMB for different  $\Omega_m h^2$  values for fixed baryon density from [11]. (left) Low  $\Omega_m h^2$  increases the prominence of first and second peaks. (middle)  $\Omega_m h^2$  is most similar to the observed power spectrum. The second and third peaks are similar in height. (right)  $\Omega_m h^2$  is large which suppresses the first peak and raises the prominence of the third peak.

566 The harmonics would look quite different for a universe with less DM. Figure 2.6 demonstrates  
 567 the effect  $\Omega_m h^2$  has on the expected power spectrum for fixed baryon matter density. [11] Sweeping  
 568  $\Omega_m h^2$  in this way clearly shows the effect dark matter has on the CMB power spectrum. The  
 569 observations fit well with the  $\Lambda$ CDM model, and the derived fractions are as follows. The matter  
 570 fraction:  $\Omega_m = 0.3153$ ; and the baryon fraction:  $\Omega_b = 0.04936$  [10]. Plank's observations also  
 571 provide a measure of the Hubble constant,  $H_0$ .  $H_0$  especially has seen a growing tension in the

572 past decade that continues to deepened with observations from instruments like the James Webb  
573 Telescope [12, 13]. As Hubble tensions deepen, we may find that perhaps  $\Lambda$ **CDM**, despite its  
574 successes, is missing some critical physics.

575 Overall, the Newtonian motion of stars in galaxies, weak lensing from galactic clusters, and  
576 power spectra from primordial light form a compelling body of research in favor of dark matter.  
577 It takes another leap of theory and experimentation to make observations of DM that are non-  
578 gravitational in nature. In Section 2.3, the evidence for DM implies strongly that the DM is matter  
579 and not a lost parameter in the gravitational fields between massive objects. Finally, if we take one  
580 axiom: that this matter has quantum behavior, such as being described by some Bohr wavelength  
581 and abiding by some fermion or boson statistics; then we arrive at particle dark matter. One particle  
582 DM hypothesis is the Weakly Interacting Massive Particle (WIMP). This DM candidate theory is  
583 discussed further in the next section and is the focus of this thesis.

584 **2.4 Searching for Dark Matter: Particle DM**

585 Section 2.4 shows the Standard Model of particle physics and is currently the most accurate  
586 model for the dynamics of fundamental particles like electrons and photons. The current status  
587 of the SM does not have a viable DM candidate. When looking at the standard model, we can  
588 immediately exclude any charged particle because charged particles interact strongly with light.  
589 Specifically, this will rule out the following charged, fundamental particles:  $e, \mu, \tau, W, u, d, s, c, t, b$   
590 and their corresponding antiparticles. Recalling from Section 2.2 that DM must be long-lived and  
591 stable over the age of the universe which excludes all SM particles with decay half-lives at or shorter  
592 than the age of the universe. The lifetime constraint additionally eliminates the  $Z$  and  $H$  bosons.  
593 Finally, the candidate DM needs to be somewhat massive. Recall from Section 2.2 that DM is cold  
594 or not relativistic through the universe. This eliminates the remaining SM particles:  $\nu_{e,\mu,\tau}, g, \gamma$  as  
595 DM candidates. Because there are no DM candidates within the SM, the DM problem strongly  
596 hints to physics beyond the SM (BSM).

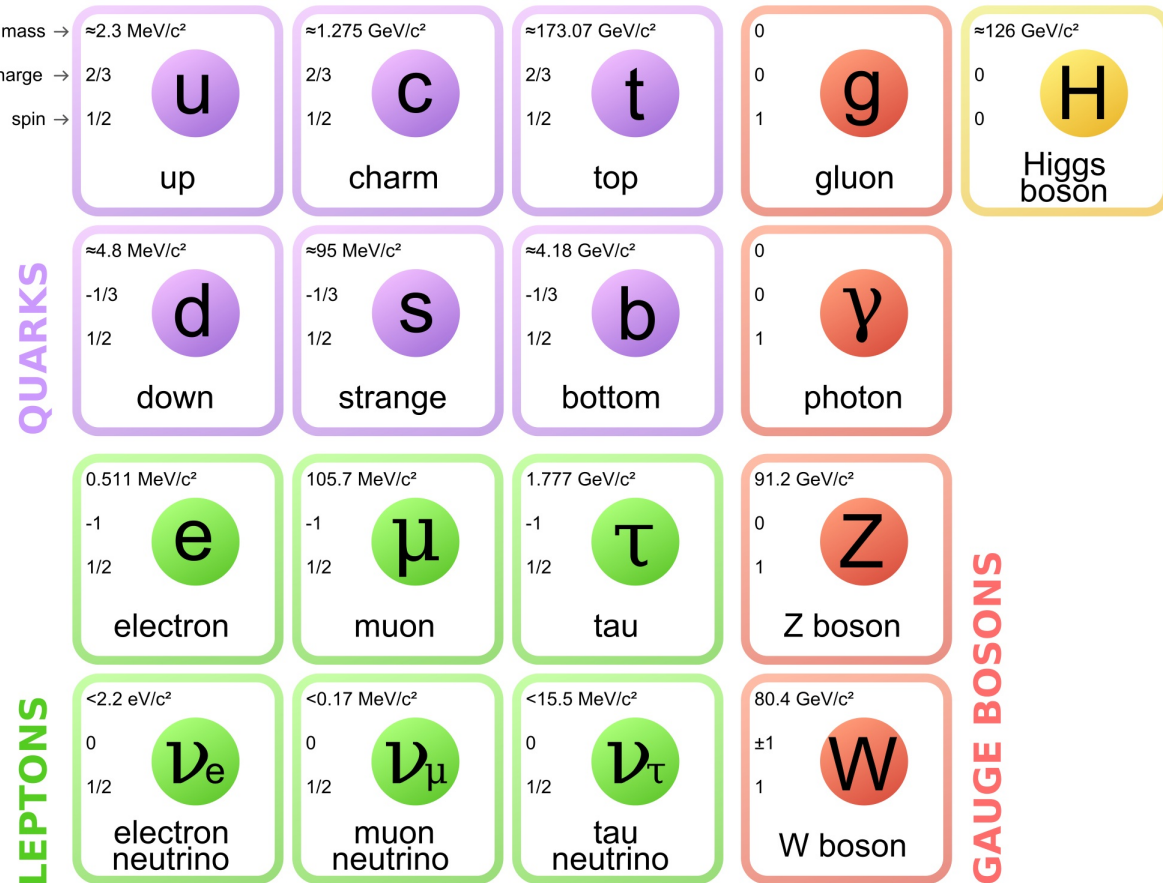


Figure 2.7 The Standard Model (SM) of particle physics. Figure taken from <http://www.quantumdiaries.org/2014/03/14/the-standard-model-a-beautiful-but-flawed-theory/>

### 597 2.4.1 Shake it, Break it, Make it

598 When considering DM that couples in some way with the SM, the interactions are roughly  
 599 demonstrated by interaction demonstrated in Figure 2.8. The figure is a simplified Feynman  
 600 diagram where the arrow of time represents the interaction modes of: **Shake it, Break it, Make it**.

601 **Shake it** refers to the direct detection of dark matter. Direct detection interactions start with  
 602 a free DM particle and an SM particle. The DM and SM interact via elastic or inelastic collision  
 603 and recoil away from each other. The DM remains in the dark sector and imparts some momentum  
 604 onto the SM particle. The hope is that the momentum imparted onto the SM particle is sufficiently  
 605 high enough to pick up with extremely sensitive instruments. Because we cannot create the DM in  
 606 the lab, a direct detection experiment must wait until DM is incident on the detector. Most direct  
 607 detection experiments are therefore placed in low-background environments with inert detection

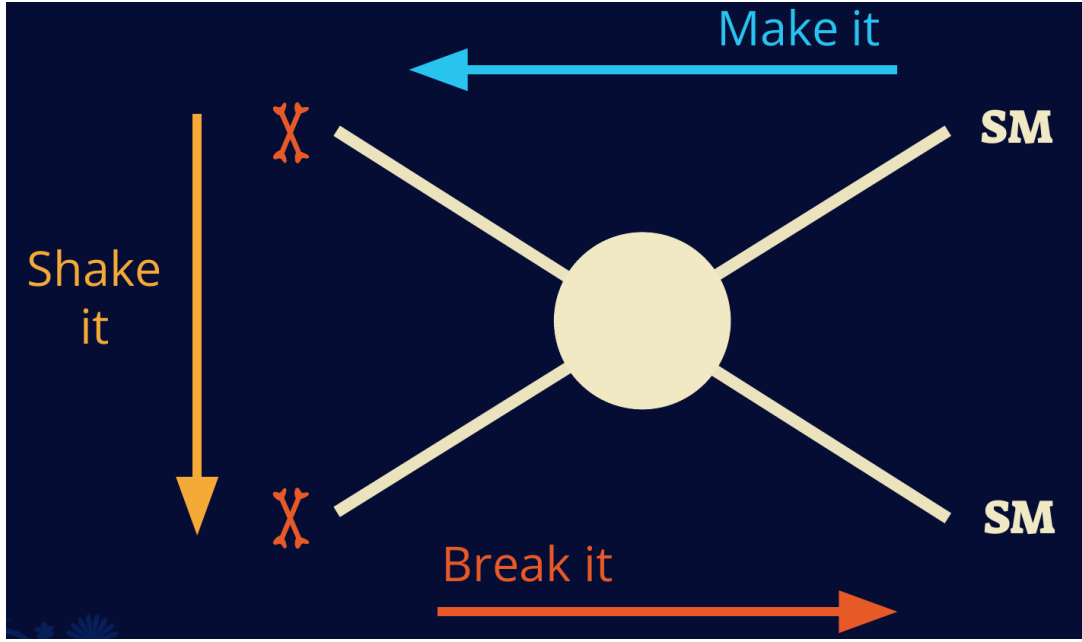


Figure 2.8 Simplified Feynman diagram demonstrating different ways DM can interact with SM particles. The 'X's refer to the DM particles whereas the SM refer to fundamental particles in the SM. The large circle in the center indicates the vertex of interaction and is purposely left vague. The colored arrows refer to different directions of time as well as their respective labels. The arrows indicate the initial and final state of the DM -SM interaction in time.

608 media like the noble gas Xenon. [14]

609 **Make it** refers to the production of DM from SM initial states. The experiment starts with  
 610 particles in the SM. These SM particles are accelerated to incredibly high energies and then collide  
 611 with each other. In the confluence of energy, DM hopefully emerges as a byproduct of the SM  
 612 annihilation. Often it is the collider experiments that are energetic enough to hypothetically produce  
 613 DM. These experiments include the world-wide collaborations ATLAS and CMS at CERN where  
 614 proton collide together at extreme energies. The DM searches, however, are complex. DM likely  
 615 does not interact with the detectors and lives long enough to escape the detection apparatus of  
 616 CERN's colliders. This means any DM production experiment searches for an excess of events  
 617 with missing momentum or energy in the events. An example event with missing transverse  
 618 momentum is shown in Figure 2.9. The missing momentum with no particle tracks implies a  
 619 neutral particle carried the energy out of the detector. However, there are other neutral particles  
 620 in the SM, like neutrons or neutrinos, so any analysis has to account for SM signatures of missing

621 momentum. [15]

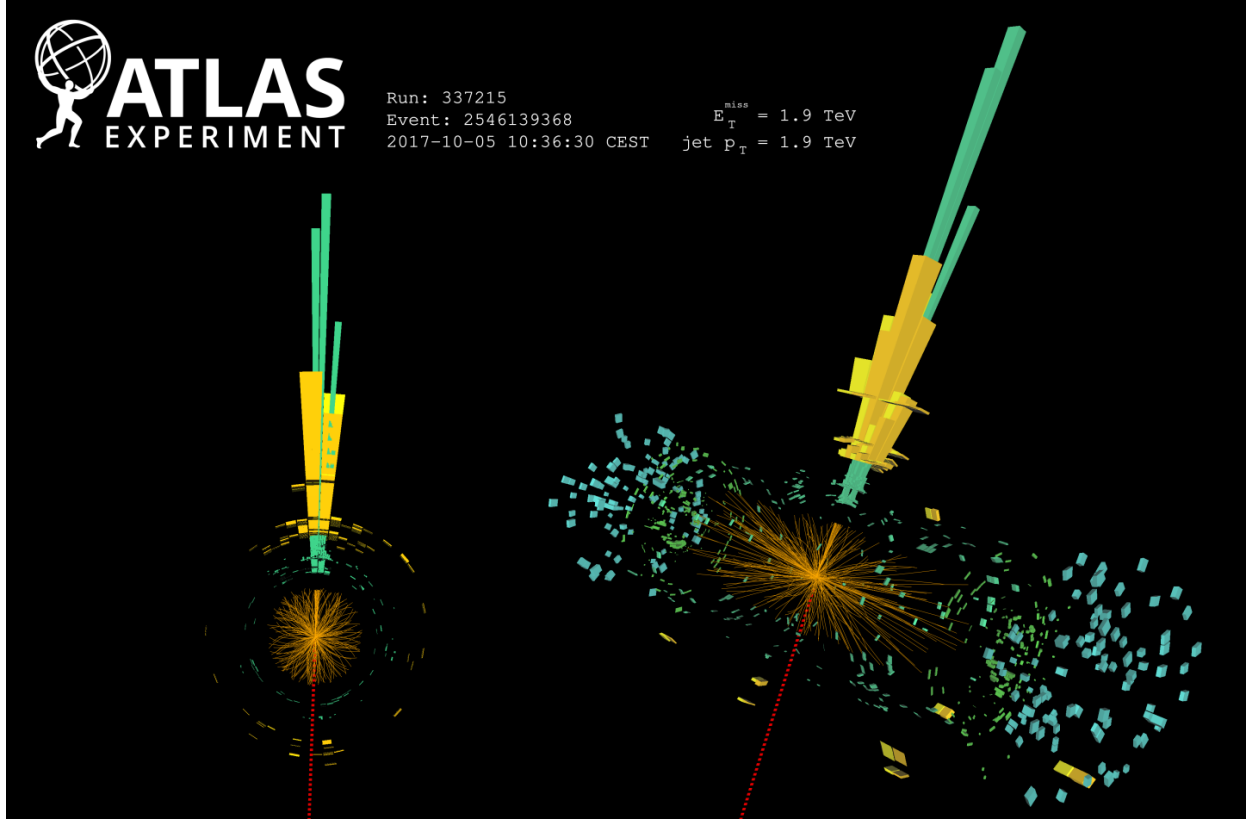


Figure 2.9 A single jet event in ATLAS detector from 2017 [16]. Jet momentum was observed to be 1.9 TeV. Missing transverse momentum was observed to be 1.9 TeV compared to the initial transverse momentum of the event was 0. Implied MET is traced by a red dashed line in event display.

#### 622 2.4.2 Break it: Standard Model Signatures of Dark Matter through Indirect Searches

623 **Break it** refers to the creation of SM particles from the dark sector, and it is the primary focus  
624 of this thesis. The interaction begins with DM or in the dark sector. The hypothesis is that this  
625 DM will either annihilate with itself or decay and produce an SM byproduct. This method is  
626 often referred to as the Indirect Detection of DM because we have no lab to directly control or  
627 manipulate the DM. Therefore, most indirect DM searches are performed using observations of  
628 known DM densities among the astrophysical sources. The strength is that we have the whole of the  
629 universe and its 13.6-billion-year lifespan to use as a detector and particle accelerator. Additionally,  
630 locations of dark matter are well cataloged since it was astrophysical observations that presented

631 the problem of DM in the first place.

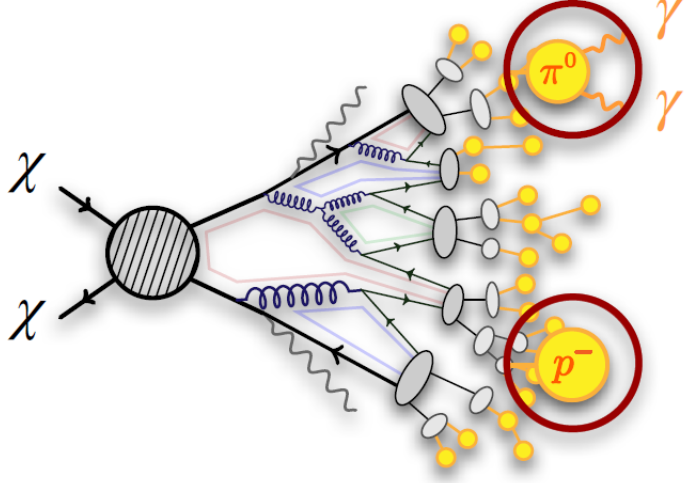


Figure 2.10 More detailed pseudo-Feynman diagram of particle cascade from dark matter annihilation into 2 quarks. The quarks hadronize and down to stable particles like  $\gamma$  or the anti-proton ( $p^-$ ). Diagram pulled from ICRC 2021 presentation on DM annihilation search [17].

632 However, anything can happen in the universe. There are many difficult to deconvolve back-  
633 grounds when searching for DM. One prominent example is the galactic center. We know the  
634 galactic center has a large DM content because of stellar kinematics in our Milky Way and DM halo  
635 simulations. Yet, any signal from the galactic center is challenging to parse apart from the extreme  
636 environment of our supermassive black hole, unresolved sources, and diffuse emission from the  
637 interstellar medium [18]. Despite the challenges, any DM model that yields evidence in the other  
638 two observation methods, **Shake it or Make it** must be corroborated with indirect observations of  
639 the known DM sources. Without corroborating evidence, DM observation in the lab is hard-pressed  
640 to demonstrate that it is the model contributing to the DM seen at the universal scale.

641 In the case of WIMP DM, signals are described in terms of primary SM particles produced  
642 from DM decay or annihilation. The SM initial state particles are then simulated down to stable  
643 final states such as the  $\gamma$ ,  $\nu$ ,  $p$ , or  $e$  which can traverse galactic lengths to reach Earth.

644 Figure 2.10 shows the quagmire of SM particles that emerges from SM initial states that are not  
645 stable [17]. There are many SM particles with varying energies that can be produced in such an

646 interaction. For any arbitrary DM source and stable SM particle, the SM flux from DM annihilating  
 647 to a neutral particle in the SM,  $\phi$ , from a region in the sky is described by the following.

$$\frac{d\Phi_\phi}{dE_\phi} = \frac{\langle\sigma v\rangle}{8\pi m_\chi^2} \frac{dN_\phi}{dE_\phi} \times \int_{\text{source}} d\Omega \int_{l.o.s} \rho_\chi^2 dl(r, \theta') \quad (2.4)$$

648 In Equation (7.1),  $\langle\sigma v\rangle$  is the velocity-weighted annihilation cross-section of DM to the SM.  $m_\chi$   
 649 refers to the mass of DM, noted with Greek letter  $\chi$ .  $\frac{dN_\phi}{dE_\phi}$  is the N particle flux weighted by the  
 650 particle energy. An example is provided in Figure 2.11 for the  $\gamma$  final state. The integrated terms  
 651 are performed over the solid angle,  $d\Omega$ , and line of sight, l.o.s.  $\rho$  is the density of DM for a  
 652 location  $(r, \theta')$  in the sky. The terms left of the ' $\times$ ' are often referred to as the particle physics  
 653 component. The terms on the right are referred to as the astrophysical component. For decaying  
 654 DM, the equation changes to...

$$\frac{d\Phi_\phi}{dE_\phi} = \frac{1}{4\pi\tau m_\chi} \frac{dN_\phi}{dE_\phi} \times \int_{\text{source}} d\Omega \int_{l.o.s} \rho_\chi dl(r, \theta') \quad (2.5)$$

655 In Equation (2.5),  $\tau$  is the decay lifetime of the DM. Just as in Equation (7.1), the left and right  
 656 terms are the particle physics and the astrophysical components respectively. The integrated  
 657 astrophysical component of Equation (7.1) is often called the J-Factor. Whereas the integrated  
 658 astrophysical component of Equation (2.5) is often called the D-Factor.

659     Exact DM  $\text{DM} \rightarrow \text{SM SM}$  branching ratios are not known, so it is usually assumed to go 100%  
 660 into an SM particle/anti-particle. Additionally, when a DM annihilation or decay produces one of  
 661 the neutral, long-lived SM particles ( $\nu$  or  $\gamma$ ), the particle is traced back to a DM source. For DM  
 662 above GeV energies, there are very few SM processes that can produce particles with such a high  
 663 energy. Seeing such a signal would almost certainly be an indication of the presence of dark matter.  
 664 Fortunately, the universe provides us with the largest volume and lifetime ever for a particle physics  
 665 experiment.

## 666 2.5 Sources for Indirect Dark Matter Searches

667     The first detection of DM relied on optical observations. Since then, we have developed new  
 668 techniques to find DM dense regions. As described in Section 2.3.1, many DM dense regions were  
 669 through observing galactic rotation curves. Our Milky Way galaxy is among DM dense regions

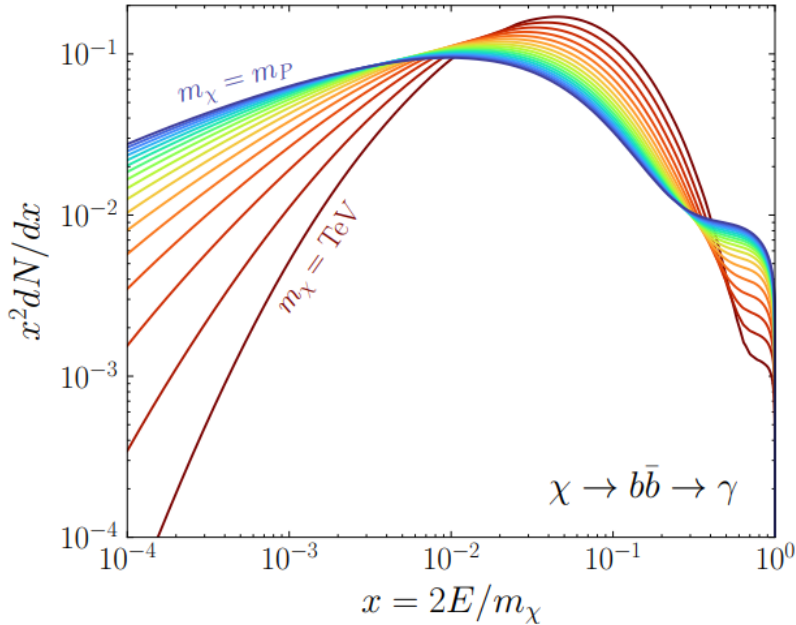


Figure 2.11 Dark Matter (DM) decay spectrum for  $b\bar{b}$  initial state and  $\gamma$  final state. Redder spectra are for larger DM masses. Bluer spectra are light DM masses.  $x$  is a unitless factor defined as the ratio of the mass of DM,  $m_\chi$ , and the final state particle energy  $E_\gamma$ . Figure from [19].

discovered, and it is the largest nearby DM dense region to look at. Additionally, the DM halo surrounding the Milky Way is clumpy [18]. There are regions in the DM halo of the Milky Way that have more DM than others that have captured gas over time. These sub-halos were dense enough collapse gas and form stars. These apparent sub galaxies are known as dwarf spheroidal galaxies and are the main sources studied in this thesis. Each source type comes with different trade-offs. Galactic Center studies will be very sensitive to the assumed distribution of DM. The central DM density can vary substantially as demonstrated in Figure 2.12. At distances close to the center of the galaxy, or small  $r$ , the differences in DM densities can be 3-4 orders of magnitude. Searches toward the galactic center will therefore be quite sensitive to the assumed DM distribution.

Searches toward Dwarf Spheroidal Galaxies (dSph's) suffer from uncertainties in the DM density less than the galactic center studies. This is mostly from their diminutive size being smaller than the angular resolution of most  $\gamma$ -ray observatories [18]. The DM content dSph's are typically determined with the Virial theorem, Equation (2.1), and are usually majority DM [18] in mass. DSph's tend to be ideal sources to look at for DM searches. Their environments are quiet with little

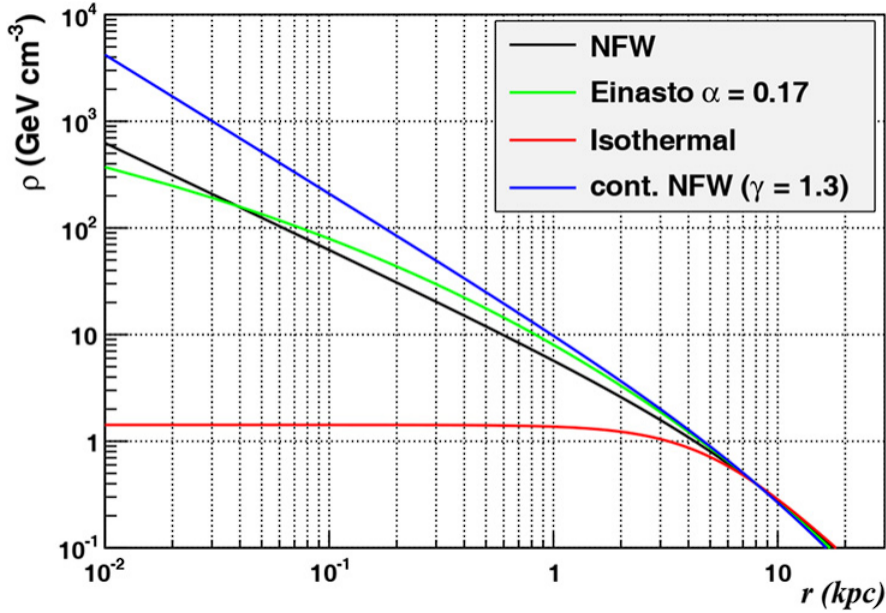


Figure 2.12 Different dark matter density profiles compared. Some models produce exceptionally large densities at small  $r$  [20].

684 astrophysical background. Unlike the galactic center, the most active components of dSph's are the  
 685 stars within them versus a violent accretion disc around a black hole. All this together means that  
 686 dSph's are among the best sources to look at for indirect DM searches. dSph's are the targets of  
 687 focus for this thesis.

## 688 2.6 Multi-Messenger Dark Matter

689 Astrophysics entered a new phase in the past few decades that leverages our increasing sensitivity  
 690 to SM channels and general relativity (GR). Up until the 21st century, astrophysical observations  
 691 were performed with photons ( $\gamma$ ) only. Astrophysics with this 'messenger' is fairly mature now.  
 692 Novel observations of the universe have since only adjusted the sensitivity of the wavelength of  
 693 light that is observed except at MeV energies. Gems like the CMB [10], and more have ultimately  
 694 been observations of different wavelengths of light. Multi-messenger astrophysics proposes using  
 695 other SM particles such the  $p^{+-}$ , or  $\nu$  or gravitation waves predicted by general relativity.

696 The experiment LIGO had a revolutionary discovery in 2016 with the first detection of a binary  
 697 black hole merger [21]. This opened the collective imagination to observing the universe through  
 698 gravitational waves. There has also been a surge of interest in the neutrino ( $\nu$ ) sector. IceCube

699 demonstrated that we are sensitive to neutrinos in regions that correlate with significant photon  
 700 emission like the galactic plane [22]. Neutrinos, like gravitational waves and light, travel mostly  
 701 unimpeded from their source to our observatories. This makes pointing to the originating source  
 702 of these messengers much easier than it is for cosmic rays which are deflected from their source by  
 703 magnetic fields.

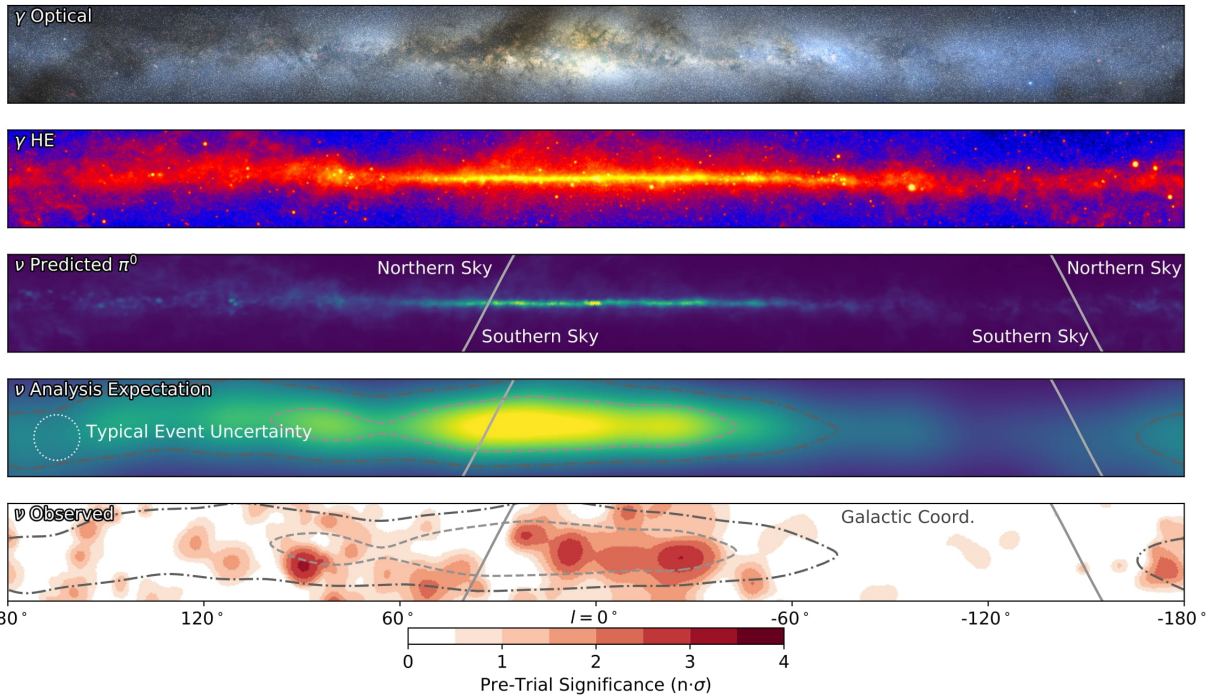


Figure 2.13 The Milky Way Galaxy in photons ( $\gamma$ ) and neutrinos ( $\nu$ ) [22]. The Galactic center is at  $l=0^\circ$  and is the brightest region in all panels. (top) An Optical color image of the Milky Way galaxy seen from Earth. Clouds of gas and dust obscure some light from stars. (2nd down) Integrated flux of  $\gamma$ -rays observed by the Fermi-LAT telescope [23]. (middle) Expected neutrino emission that corresponds with Fermi-LAT observations. (2nd up) Expected neutrino emission profile after considering detector systematics of IceCube. (bottom) Observed neutrino emission from region of the galactic plane. Substantial neutrino emission was detected.

704 The IceCube collaboration recently published a groundbreaking result of the Milky Way in  
 705 neutrinos. The recent result from IceCube, shown in Figure 2.13, proves that we can make  
 706 observations under different messenger regimes. The top two panels show the appearance of the  
 707 galactic plane to different wavelengths of light. Some sources are more apparent in some panels,  
 708 while others are not. This new channel is powerful because neutrinos are readily able to penetrate  
 709 through gas and dust in the Milky Way. This new image also refines our understanding of how high

710 energy particles are produced. For example, the fit to IceCube data prefers neutrino production  
 711 from the decay of  $\pi^0$  [22].

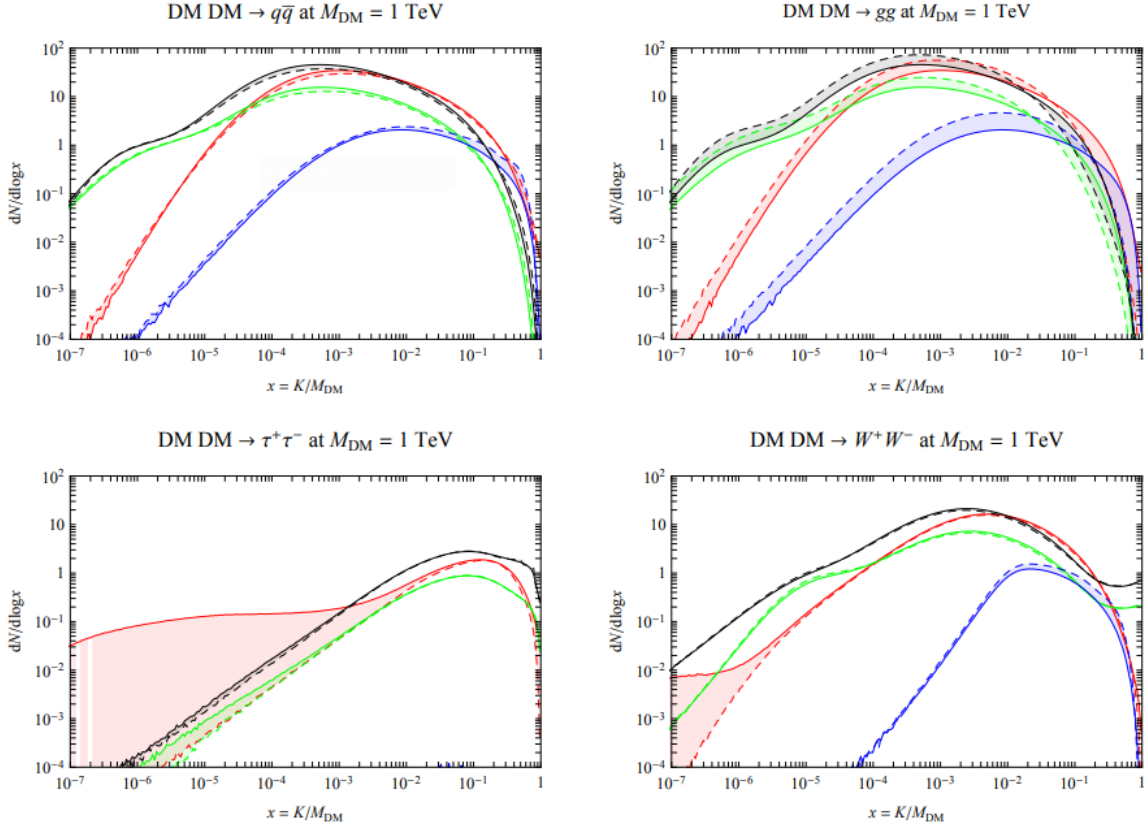


Figure 2.14 Dark Matter annihilation spectra for different final state particle and standard model annihilation channels [24]. Photons (red),  $e^\pm$  (green),  $\bar{p}$  (blue),  $\nu$  (black).

712 Exposing our observations to more cosmic messengers greatly increases our sensitivity to  
 713 rare processes. In the case of DM, Figure 2.14, there are many SM particles produced in DM  
 714 annihilation. Among the final state fluxes are gammas and neutrinos. Charged particles are also  
 715 produced however they would not likely make it to Earth since they will be deflected by magnetic  
 716 fields between the source and Earth. This means observatories that can see the neutral messengers  
 717 are especially good for DM searches and for combining data for a multi-messenger DM search.

## CHAPTER 3

718

### HIGH ALTITUDE WATER CHERENKOV (HAWC) OBSERVATORY

719 **3.1 The Detector**

720 **3.2 Events Reconstruction and Data Acquisition**

721 **3.2.1 G/H Discrimination**

722 **3.2.2 Angle**

723 **3.2.3 Energy**

724 **3.3 Remote Monitoring**

725 **3.3.1 ATHENA Database**

726 **3.3.2 HOMER**

727

## CHAPTER 4

### ICECUBE NEUTRINO OBSERVATORY

728 **4.1 The Detector**

729 **4.2 Events Reconstruction and Data Acquisition**

730 **4.2.1 Angle**

731 **4.2.2 Energy**

732 **4.3 Northern Test Site**

733 **4.3.1 PIgeon remote dark rate testing**

734 **4.3.2 Bulkhead Construction**

## CHAPTER 5

### GLORY DUCK: MULTI-WAVELENGTH SEARCH FOR DARK MATTTER ANNIHILATION TOWARDS DWARF SPHEROIDAL GALAXIES

#### 5.1 Introduction

The field of astrophysics now has several instruments and observatories sensitive to high energy gamma-rays. The energy sensitivity for the modern gamma-ray program spans many orders of magnitude. Figure 5.1 demonstrates these comparable sensitivities across energies for the five experiments: Fermi-LAT, HAWC, HESS, MAGIC, and VERITAS.

Each of the five experiments featured in Figure 5.1 have independently searched for DM annihilation from dwarf spheroidal galaxies (dSph) and set limits on annihilation cross-section of WIMPs. Intriguingly, there are regions of substantial overlap in their energy sensitivities. This clearly motivates an analysis that combines data from these five. Each experiment has unique gamma-ray detection methods and their weaknesses and strengths can be leveraged with each other. The HAWC gamma-ray observatory is extensively introduced in chapter 3, so it is not introduced here. A brief description of the remaining experiments are in the following paragraphs.

The Large Area Telescope (LAT) is a pair conversion telescope mounted on the NASA Fermi satellite in orbit  $\sim$ 550 km above the Earth [26]. LAT's field of view covers about 20% of the whole sky, and it sweeps the whole sky approximately every 3 hours. LAT's gamma-ray energy sensitivity ranges from 20 MeV up to 1 TeV. Previous DM searches towards dSphs using Fermi-LAT are published in [27] and [28].

The High Energy Spectroscopic System (HESS), Major Atmospheric Gamma Imaging Cherenkov (MAGIC), and Very Energetic Radiation Imaging Telescope Array System (VERITAS) are arrays of Imaging Atmospheric Cherenkov Telescopes (IACT). These telescopes observe the Cherenkov light emitted from gamma-ray showers in the Earth's atmosphere. The field of view for these telescopes is no larger than  $5^\circ$  with energy sensitivities ranging from 30 GeV up to 100 TeV [29, 30, 31]. IACTs are able to make precise observations in selected regions of the sky, however can only be operated in ideal dark conditions. HESS's observations of the dwarves

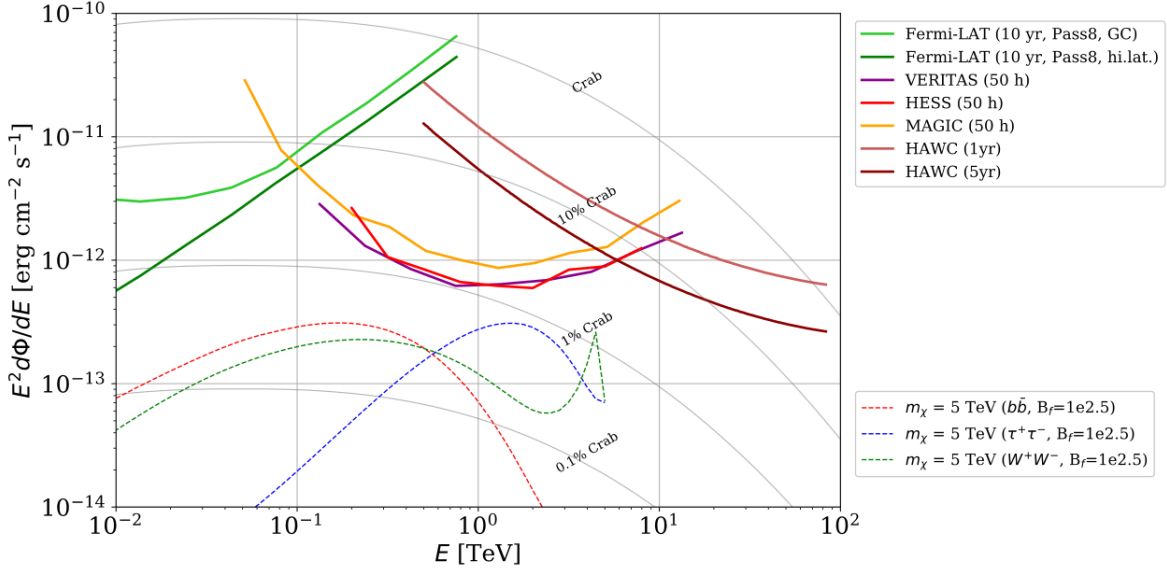


Figure 5.1 Sensitivities of five gamma-ray experiments compared to percentages of the Crab nebula’s emission and dark matter annihilation. Solid lines present estimated sensitivities to power law spectra [FACT CHECK THIS] for each experiment. Green lines are Fermi-LAT sensitivities where lighter green is the sensitivity to the galactic center and dark green is its sensitivity to higher declinations. Orange, red, and purple solid lines represent the MAGIC, HESS, and VERITAS 50 hour sensitivities respectively. The maroon and brown lines are the HAWC 1 year and 5 year sensitivities. Across four decades of gamma-ray energy, these experiments have similar sensitivities on the order  $10^{-12}$  erg  $\text{cm}^{-2}\text{s}^{-1}$ . The dotted lines are estimated dark matter fluxes assuming  $m_\chi = 5$  TeV DM annihilating to bottom quarks (red), tau leptons (blue), and W bosons (green). Faded gray lines outline percentage flux of the Crab nebula. Figure is an augmented version of [25]

761 Sculptor and Carina were between January 2008 and December 2009. HESS’s observations of  
 762 Coma Berenices were taken from 2010 to 2013, and Fornax was observed in 2010 [32, 33, 34].  
 763 MAGIC provided deep observations of Segue1 between 2011 and 2013 [35]. MAGIC also provides  
 764 data for three additional dwarves: Coma Berenices, Draco, and Ursa Major II where observations  
 765 were made in: January - June 2019 [36], March - September 2018 [36], and 2014 - 2016 [37]  
 766 respectively. VERITAS provided data for Boötes I, Draco, Segue 1, and Ursa Minor from 2009 to  
 767 2016 [38].

768 This chapter presents the Glory Duck analysis, the name given for the search for dark matter  
 769 annihilation from dSph by combining data from the five gamma-ray observatories: Fermi-LAT,  
 770 HAWC, HESS, MAGIC, and VERITAS. Specifically, the methods in analysis and modeling are  
 771 presented for the HAWC gamma-ray observatory. This work will be published in the Journal of

772 Cosmology and Astroparticle Physics and presented at the International Cosmic Ray Conference  
773 in 2019, 2021, and 2023 [39, 40, 41] and others.

774 **5.2 Dataset and Background**

775 This section enumerates the data analysis and background estimation methods used for HAWC's  
776 study of dSphs. Section 5.2.1 and Section 5.2.2 are most useful for fellow HAWC collaborators  
777 looking to replicate the Glory Duck analysis.

778 **5.2.1 Itemized HAWC files**

779 These files are only available withing HAWC's internal documentation and collaborators. They  
780 are not meant for public access, and are presented here so that HAWC collaborators can reproduce  
781 results accurately.

- 782 • Detector Response: `response_aerie_svn_27754_systematics_best_mc_test_noBr`  
783     `oadpulse\10pctlogchargesmearing_0.63qe_25kHzNoise_run5481_curvature`  
784     `0_index3.root`
- 785 • Data Map: `maps-20180119/liff/maptree_1024.root`
- 786 • Spectral Dictionary: `DM_CirrelliSpectrum_dict_gammas.npy`
- 787 • Analysis wiki: [https://private.hawc-observatory.org/wiki/index.php/Glory\\_Duck\\_Multi-Experiment\\_Dark\\_Matter\\_Search](https://private.hawc-observatory.org/wiki/index.php/Glory_Duck_Multi-Experiment_Dark_Matter_Search)

789 **5.2.2 Software Tools and Development**

790 This analysis was performed using HAL and 3ML [42, 43] in Python version 2. I built software  
791 to implement the *A Poor Particle Physicist Cookbook for Dark Matter Indirect Detection* (PPPC)  
792 [44] DM spectral model and dSphs spatial model from [45] for HAWC analysis. A NumPy version  
793 of this dictionary was made for both Py2 and Py3. The code base for creating this dictionary is  
794 linked on my GitLab sandbox:

- 795 • Py2: [Dictionary Generator \(Deprecated\)](#)

- 796 • Py3: [PPPC2Dict](#)

797     The analysis was performed using the  $f_{hit}$  framework as used and described in the HAWC Crab  
798 paper [42]. The Python2 NumPy dictionary file for gamma-ray final states is `dmCirSpecDict.npy`.  
799 The corresponding Python3 file is `DM_CirrelliSpectrum_dict_gammas.npy`. These files can  
800 also be used for decay channels and the PPPC describes how [44]. All other software used for data  
801 analysis, DM profile generation, and job submission to SLURM are also kept in my sandbox for  
802 [the Glory Duck](#) project.

803 **5.2.3 Data Set and Background Description**

804     The HAWC data maps used for this analysis contain 1017 days of data between runs 2104  
805 (2014-11-26) and 7476 (2017-12-20). They were generated from pass 4.0 reconstruction. The  
806 analysis is performed using the  $f_{hit}$  energy binning scheme with bins (1-9) similar to what was done  
807 for the Crab and previous HAWC dSph analysis [42, 46]. Bin 0 was excluded as it has substantial  
808 hadronic contamination and poor angular resolution.

809     This analysis was done on dSphs because of their large DM mass content relative to baryonic  
810 mass. We consider the following to estimate the background to this study.

- 811     • The dSphs' angular extent are small relative to HAWC's spatial resolution, so the analysis is  
812 not sensitive to large or small scale anisotropies.
- 813     • The dSphs used in this analysis are off the galactic plane and therefore not contaminated by  
814 diffuse emission from the galaxy.
- 815     • The dSphs are baryonically faint relative to their expected dark matter content and are not  
816 expected to contain high energy gamma-ray sources.

817     Therefor we make no additional assumptions on the background from our sources and use  
818 HAWC's standard direct integration method for background estimation [42]. The largest background  
819 under this consideration is from an isotropic flux of cosmic rays. The contamination of this hadronic  
820 flux is worse at lower energies where HAWC's gamma/hadron discrimination worse. It is possible

821 for gamma rays from DM annihilation to scatter in transit to HAWC via Inverse Compton Scattering  
822 (ICS). This was investigated and its impact on the flux is negligible. Supporting information on  
823 this is in Section 5.7.1

824 **5.3 Analysis**

825 The expected differential photon flux from DM-DM annihilation to standard model particles,  
826  $d\Phi_\gamma/dE_\gamma$ , over solid angle,  $\Omega$ , is described by the familiar equation.

$$\frac{d\Phi_\gamma}{dE_\gamma} = \frac{\langle\sigma v\rangle}{8\pi m_\chi^2} \frac{dN_\gamma}{dE_\gamma} \times \int_{\text{source}} d\Omega \int_{l.o.s} dl \rho_\chi^2 J(r, \theta') \quad (5.1)$$

827 Where  $\langle\sigma v\rangle$  is the velocity weighted annihilation cross-section.  $\frac{dN}{dE}$  is the expected differential  
828 number of photons produced at each energy per annihilation.  $m_\chi$  is the rest mass of the supposed  
829 DM particle.  $\rho_\chi$  is the DM density.  $J$  is the astrophysical J-factor and is defined as

$$J = \int d\Omega \int_{l.o.s} dl \rho_\chi^2(r, \theta') \quad (5.2)$$

830  $l$  is the distance to the source from Earth.  $r$  is the radial distance from the center of the source.  $\theta'$  is  
831 the half angle defining a cone containing the DM source. How each component is synthesized and  
832 considered for HAWC's analysis is presented in the following sections. Section 5.3.1 presents the  
833 particle physics model for DM annihilation. Section 5.3.2 presents the spatial distributions built  
834 for each dSph.

835 **5.3.1  $\frac{dN_\gamma}{dE_\gamma}$  - Particle Physics Component**

836 For these spectra, we import the PPPC with Electroweak (EW) corrections [44]. Public versions  
837 of the imported tables are provided by the [authors online](#). The spectrum is implemented as a model  
838 script in astromodels for 3ML. The EW corrections were previously not considered for HAWC and  
839 are significant for DM annihilating to EW coupled SM particles such as all leptons, and the  $\gamma$ ,  
840  $Z$ , and  $W$  bosons [46]. Figure 5.2 demonstrates the significance of EW corrections for W boson  
841 annihilation. Across EW SM channels, the gamma-ray spectra become harder than spectra without  
842 EW corrections. Tables from the PPPC were reformatted into Python NumPy dictionaries for  
843 collaboration-wide use. A class in astromodels was developed to include the EW correction from  
844 the PPPC and is aptly named `PPPCSpectra` within `DM_models.py`.

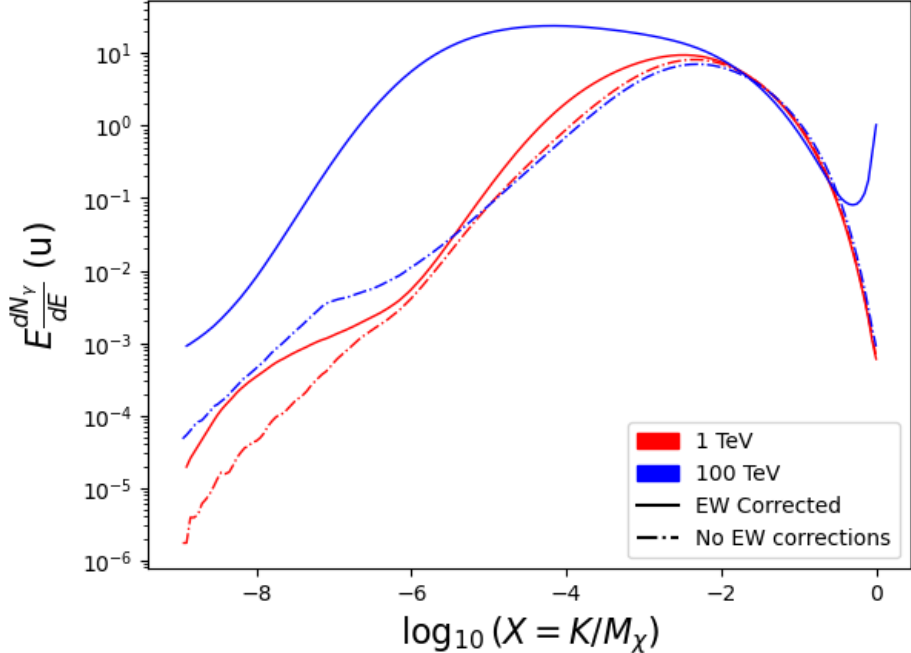


Figure 5.2 Effect of Electroweak (EW) corrections on expected DM annihilation spectrum for  $\chi\chi \rightarrow W^-W^+$ . Solid lines are spectral models that consider EW corrections. Dash-dot lines are spectral models without EW corrections. Red lines are models for  $M_\chi = 1$  TeV. Blue lines represent models for  $M_\chi = 100$  TeV. All models are sourced from the PPPC4DMID [44].

### 845 5.3.2 J- Astrophysical Component

846 The J-factor profiles for each source are imported from Geringer-Sameth (referred to with  $\mathcal{GS}$ )  
 847 [45].  $\mathcal{GS}$  fits the Zhao DM profile to the dSphs which has a DM density described as [47]

$$\rho(r) = \frac{\rho_0}{(r/R_s)^\gamma (1 + (r/R_s)^\alpha)^{(\beta-\gamma)}}. \quad (5.3)$$

848  $R_s$  is the scale radius and free parameter in the model.  $\gamma$  is the logarithmic slope in the region  
 849  $r \ll R_s$ .  $\beta$  is the logarithmic slope in the region  $r \gg R_s$ .  $\alpha$  is known as the sharpness of transition  
 850 where  $r \approx R_s$ . The classic Navarro-Frenk-White [48] (NFW) can be retrieved from Zhao by fixing  
 851  $(\alpha, \beta, \gamma) = (1, 3, 1)$ .

852  $\mathcal{GS}$  best fits were pulled from the publication as  $J(\theta)$ , where  $\theta$  is the angular separation from  
 853 the center of the source. HAWC requires maps in terms of  $\frac{dJ}{d\Omega}$ , so the conversion from the maps  
 854 was done in the following way...

855 First, convert the angular distances to solid angles

$$\Omega = 2 \cdot \pi(1 - \cos(\theta)) \quad (5.4)$$

856 which reduces with a small angle approximation to  $\pi\theta^2$ . Next, the central difference for both the  
857  $\Delta J$  and  $\Delta\Omega$  value were calculated from the discretized  $J(\theta)$  with the central difference stencil:

$$\Delta\phi_i = \phi_{i+1} - \phi_{i-1} \quad (5.5)$$

858 Where  $\phi$  is either  $\Omega$  or  $J$ . These were done separately in case the grid spacing in  $\theta$  was not uniform.  
859 Finally, these lists are divided so that we are left with an approximation of the  $dJ/d\Omega$  profile that  
860 is a function of  $\theta$ . Admittedly, this is an approximation method for the map which introduces small  
861 errors compared to the true profile estimate. This was checked as a systematic against the author's  
862 profiling of the spatial distribution and is documented in Section 5.8.1.

863 With  $\frac{dJ}{d\Omega}(\theta)$ , a map is generated, first by filling in the north-east quadrant of the map. This  
864 quadrant is then reflected twice, vertically then horizontally, to fill the full map. Maps are then  
865 normalized by dividing the discrete 2D integral of the map. The 2D integral was a simple height  
866 of bins, Newton's integral:

$$p^2 \cdot \sum_{i,j=0}^{N,M} \frac{dJ}{d\Omega}(\theta_{i,j}, \phi_{i,j}) \quad (5.6)$$

867 These maps are HEALpix maps with NSIDE 16384 and saved in the .fits format. The hyper fine  
868 resolution was selected to better preserve the total expected counts after integrating Eq. (7.1) with  
869 the detector response.

870 Another DM spatial distribution model from Bonnivard ( $\mathcal{B}$ ) [49] was used for the Glory Duck  
871 study. However, to save computational time, limits from  $\mathcal{GS}$  were scaled to  $\mathcal{B}$  instead of each  
872 experiment performing a full study a second time. How these models compare is demonstrated  
873 for each dSph in Figure 5.16 and Figure 5.17 Plots of these maps are provided for each source  
874 in chapter A Examples of the two most impactful dSphs derived from  $\mathcal{GS}$ , Segue1 and Coma  
875 Berenices are featured in Figure 5.3

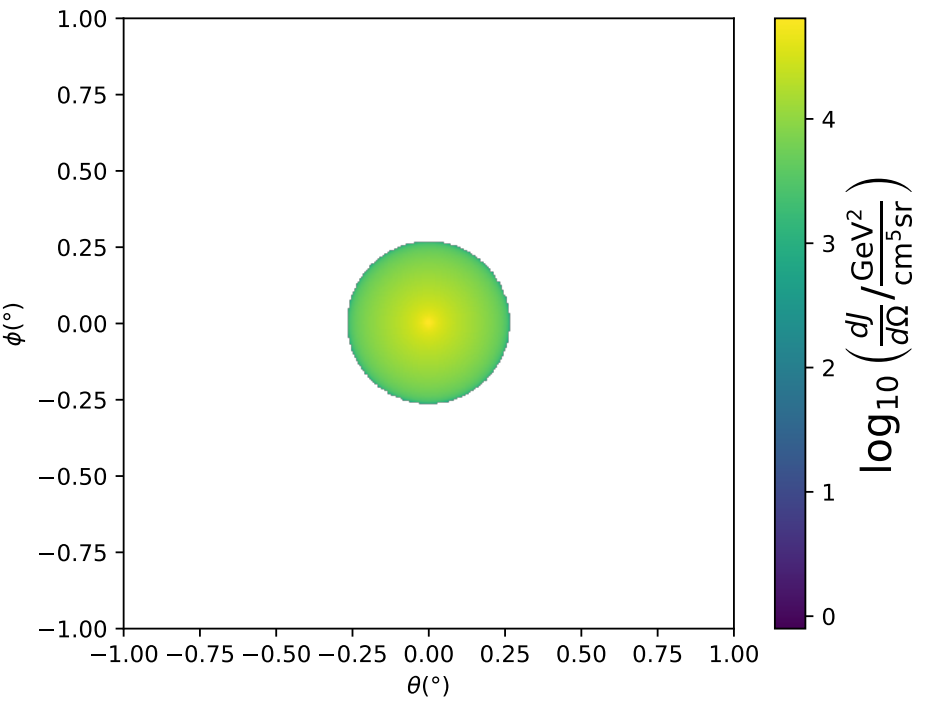
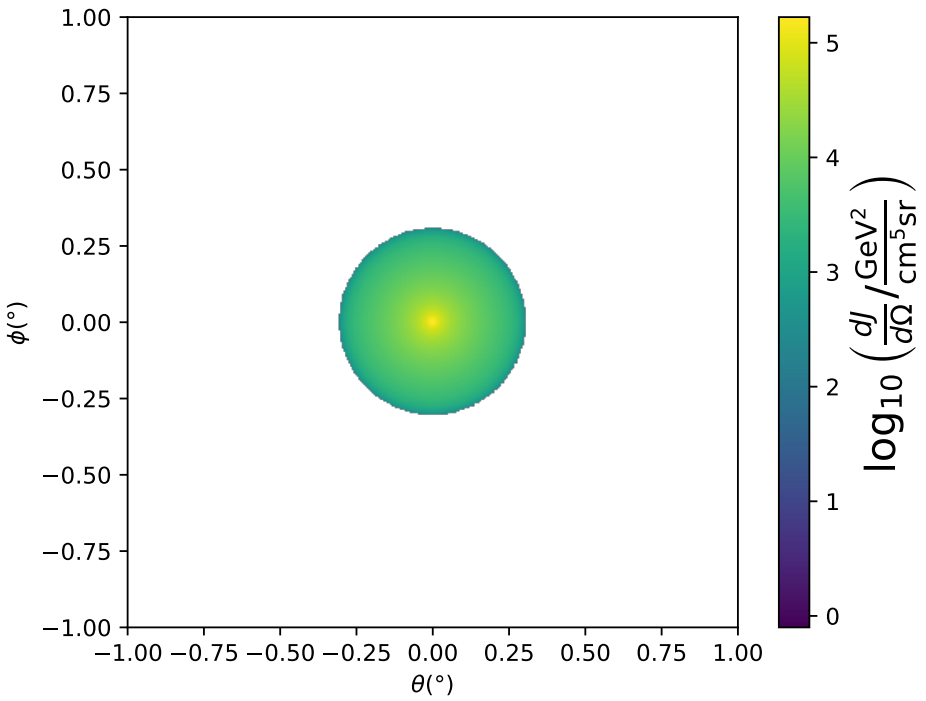


Figure 5.3  $\frac{dJ}{d\Omega}$  maps for Segue1 (top) and Coma Berenices (bottom). Origin is centered on the specific dwarf spheroidal galaxies (dSph). X and Y axes are the angular separation from the center of the dwarf. Profile is truncated at the scale radius. Plots of the remaining 11 dSph HAWC studied are linked in Fig. A.1.

876 **5.3.3 Source Selection and Annihilation Channels**

877 We use many of the dSphs presented in HAWC’s previous dSph DM search [46]. HAWC’s  
878 sources for Glory Duck include Boötes I, Coma Berenices, Canes Venatici I + II, Draco, Hercules,  
879 Leo I, II, + IV, Segue 1, Sextans, and Ursa Major I + II. A full description of all sources used  
880 in Glory Duck is found in Table 5.1. Triangulum II was excluded from the Glory Duck analysis  
881 because of large uncertainties in its  $J$  factor. Ursa Minor was excluded from HAWC’s contribution  
882 to the combination because the source extension model extended Ursa Minor beyond HAWC’s field  
883 of view. Ursa Minor was not expected to contribute significantly to the combined limit, so work  
884 was not invested in a solution to include Ursa Minor.

885 This analysis improves on the previous HAWC dSph paper [46] in the following ways. Pre-  
886 viously, the dSphs were treated and implemented as point sources. For this analysis, dSphs are  
887 modeled and treated as extended source. The impact of this change with respect to the upper limit  
888 is source dependent and is explored in Section 5.7.2. Previously, the particle physics model used for  
889 gamma-ray spectra from DM annihilation did not have EW corrections where the PPPC includes  
890 them. Finally, the gamma-ray ray dataset is much larger. The study performed here analyzes over  
891 1000 days of data compared to 507.

892 The SM annihilation channels probed for the Glory Duck combination include  $b\bar{b}$ ,  $e\bar{e}$ ,  $\mu\bar{\mu}$ ,  $\tau\bar{\tau}$ ,  
893  $t\bar{t}$ ,  $W^+W^-$ , and  $ZZ$ . A summary of all sources, with a description of each experiments’ sensitivity  
894 to the source, is provided in Table 5.2.

895 **5.4 Likelihood Methods**

896 **5.4.1 HAWC Likelihood**

897 For every analysis bin in energy,  $f_{hit}$  bins (1-9), and location, we can expect  $N$  signal events and  
898  $B$  background events. The expected number of excess signal events from dark matter annihilation,  
899  $S$ , is estimated by convolving Equation (7.1) with HAWC’s energy response and pixel point spread  
900 functions. I then compute the test statistic (TS) with the log-likelihood ratio test,

$$TS_{max} = -2 \ln \left( \frac{\mathcal{L}_0}{\mathcal{L}^{max}} \right) \quad (5.7)$$

Table 5.1 Summary of the relevant properties of the dSphs used in the present work. Column 1 lists the dSphs. Columns 2 and 3 present their heliocentric distance and galactic coordinates, respectively. Columns 4 and 5 report the  $J$ -factors of each source given from the  $\mathcal{GS}$  and  $\mathcal{B}$  independent studies and their estimated  $\pm 1\sigma$  uncertainties. The values  $\log_{10} J$  ( $\mathcal{GS}$  set) [45] correspond to the mean  $J$ -factor values for a source extension truncated at the outermost observed star. The values  $\log_{10} J$  ( $\mathcal{B}$  set) [49] are provided for a source extension at the tidal radius of each dSph. **Bolded sources are within HAWC's field of view and provided to the Glory Duck analysis.**

| Name                     | Distance<br>(kpc) | $l, b$<br>( $^{\circ}$ ) | $\log_{10} J$ ( $\mathcal{GS}$ set)<br>$\log_{10}(\text{GeV}^2\text{cm}^{-5}\text{sr})$ | $\log_{10} J$ ( $\mathcal{B}$ set)<br>$\log_{10}(\text{GeV}^2\text{cm}^{-5}\text{sr})$ |
|--------------------------|-------------------|--------------------------|---|--|
| <b>Boötes I</b>          | 66                | 358.08, 69.62            | $18.24^{+0.40}_{-0.37}$   | $18.85^{+1.10}_{-0.61}$  |
| <b>Canes Venatici I</b>  | 218               | 74.31, 79.82             | $17.44^{+0.37}_{-0.28}$   | $17.63^{+0.50}_{-0.20}$  |
| <b>Canes Venatici II</b> | 160               | 113.58, 82.70            | $17.65^{+0.45}_{-0.43}$   | $18.67^{+1.54}_{-0.97}$  |
| Carina                   | 105               | 260.11, -22.22           | $17.92^{+0.19}_{-0.11}$   | $18.02^{+0.36}_{-0.15}$  |
| <b>Coma Berenices</b>    | 44                | 241.89, 83.61            | $19.02^{+0.37}_{-0.41}$   | $20.13^{+1.56}_{-1.08}$  |
| <b>Draco</b>             | 76                | 86.37, 34.72             | $19.05^{+0.22}_{-0.21}$   | $19.42^{+0.92}_{-0.47}$  |
| Fornax                   | 147               | 237.10, -65.65           | $17.84^{+0.11}_{-0.06}$   | $17.85^{+0.11}_{-0.08}$  |
| <b>Hercules</b>          | 132               | 28.73, 36.87             | $16.86^{+0.74}_{-0.68}$   | $17.70^{+1.08}_{-0.73}$  |
| <b>Leo I</b>             | 254               | 225.99, 49.11            | $17.84^{+0.20}_{-0.16}$   | $17.93^{+0.65}_{-0.25}$  |
| <b>Leo II</b>            | 233               | 220.17, 67.23            | $17.97^{+0.20}_{-0.18}$   | $18.11^{+0.71}_{-0.25}$  |
| <b>Leo IV</b>            | 154               | 265.44, 56.51            | $16.32^{+1.06}_{-1.70}$   | $16.36^{+1.44}_{-1.65}$  |
| Leo V                    | 178               | 261.86, 58.54            | $16.37^{+0.94}_{-0.87}$   | $16.30^{+1.33}_{-1.16}$  |
| Leo T                    | 417               | 214.85, 43.66            | $17.11^{+0.44}_{-0.39}$   | $17.67^{+1.01}_{-0.56}$  |
| Sculptor                 | 86                | 287.53, -83.16           | $18.57^{+0.07}_{-0.05}$   | $18.63^{+0.14}_{-0.08}$  |
| <b>Segue I</b>           | 23                | 220.48, 50.43            | $19.36^{+0.32}_{-0.35}$   | $17.52^{+2.54}_{-2.65}$  |
| Segue II                 | 35                | 149.43, -38.14           | $16.21^{+1.06}_{-0.98}$   | $19.50^{+1.82}_{-1.48}$  |
| <b>Sextans</b>           | 86                | 243.50, 42.27            | $17.92^{+0.35}_{-0.29}$   | $18.04^{+0.50}_{-0.28}$  |
| <b>Ursa Major I</b>      | 97                | 159.43, 54.41            | $17.87^{+0.56}_{-0.33}$   | $18.84^{+0.97}_{-0.43}$  |
| <b>Ursa Major II</b>     | 32                | 152.46, 37.44            | $19.42^{+0.44}_{-0.42}$   | $20.60^{+1.46}_{-0.95}$  |
| Ursa Minor               | 76                | 104.97, 44.80            | $18.95^{+0.26}_{-0.18}$   | $19.08^{+0.21}_{-0.13}$  |

Table 5.2 Summary of dSph observations by each experiment used in this work. A ‘-’ indicates the experiment did not observe the dSph for this study. For Fermi-LAT, the exposure at 1 GeV is given. For HAWC,  $|\Delta\theta|$  is the absolute difference between the source declination and HAWC latitude. HAWC is more sensitive to sources with smaller  $|\Delta\theta|$ . For IACTs, we show the zenith angle range, the total exposure, the energy range, the angular radius  $\theta$  of the signal or ON region, the ratio of exposures between the background-control (OFF) and signal (ON) regions ( $\tau$ ), and the significance of gamma-ray excess in standard deviations,  $\sigma$ .

| Source name       | Fermi-LAT                       | HAWC                          | H.E.S.S, MAGIC, VERITAS |                     |              |                    |                       |        |                  |
|-------------------|---------------------------------|-------------------------------|-------------------------|---------------------|--------------|--------------------|-----------------------|--------|------------------|
|                   | Exposure ( $10^{11}$ s m $^2$ ) | $ \Delta\theta $ ( $^\circ$ ) | IACT                    | Zenith ( $^\circ$ ) | Exposure (h) | Energy range (GeV) | $\theta$ ( $^\circ$ ) | $\tau$ | $S$ ( $\sigma$ ) |
| Boötes I          | 2.6                             | 4.5                           | VERITAS                 | 15 – 30             | 14.0         | 100–41000          | 0.10                  | 8.6    | -1.0             |
| Canes Venatici I  | 2.9                             | 14.6                          | –                       | –                   | –            | –                  | –                     | –      | –                |
| Canes Venatici II | 2.9                             | 15.3                          | –                       | –                   | –            | –                  | –                     | –      | –                |
| Carina            | 3.1                             | –                             | H.E.S.S.                | 27 – 46             | 23.7         | 310 – 70000        | 0.10                  | 18.0   | -0.3             |
| Coma Berenices    | 2.7                             | 4.9                           | H.E.S.S.                | 47 – 49             | 11.4         | 550 – 70000        | 0.10                  | 14.4   | -0.4             |
|                   |                                 |                               | MAGIC                   | 5 – 37              | 49.5         | 60 – 10000         | 0.17                  | 1.0    | –                |
|                   |                                 |                               | MAGIC                   | 29 – 45             | 52.1         | 70 – 10000         | 0.22                  | 1.0    | –                |
| Draco             | 3.8                             | 38.1                          | VERITAS                 | 25 – 40             | 49.8         | 120 – 70000        | 0.10                  | 9.0    | -1.0             |
| Fornax            | 2.7                             | –                             | H.E.S.S.                | 11 – 25             | 6.8          | 230 – 70000        | 0.10                  | 45.5   | -1.5             |
| Hercules          | 2.8                             | 6.3                           | –                       | –                   | –            | –                  | –                     | –      | –                |
| Leo I             | 2.5                             | 6.7                           | –                       | –                   | –            | –                  | –                     | –      | –                |
| Leo II            | 2.6                             | 3.1                           | –                       | –                   | –            | –                  | –                     | –      | –                |
| Leo IV            | 2.4                             | 19.5                          | –                       | –                   | –            | –                  | –                     | –      | –                |
| Leo V             | 2.4                             | –                             | –                       | –                   | –            | –                  | –                     | –      | –                |
| Leo T             | 2.6                             | –                             | –                       | –                   | –            | –                  | –                     | –      | –                |
| Sculptor          | 2.7                             | –                             | H.E.S.S.                | 10 – 46             | 11.8         | 200 – 70000        | 0.10                  | 19.8   | -2.2             |
| Segue I           | 2.5                             | 2.9                           | MAGIC                   | 13 – 37             | 158.0        | 60 – 10000         | 0.12                  | 1.0    | -0.5             |
|                   |                                 |                               | VERITAS                 | 15 – 35             | 92.0         | 80 – 50000         | 0.10                  | 7.6    | 0.7              |
| Segue II          | 2.7                             | –                             | –                       | –                   | –            | –                  | –                     | –      | –                |
| Sextans           | 2.4                             | 20.6                          | –                       | –                   | –            | –                  | –                     | –      | –                |
| Ursa Major I      | 3.4                             | 32.9                          | –                       | –                   | –            | –                  | –                     | –      | –                |
| Ursa Major II     | 4.0                             | 44.1                          | MAGIC                   | 35 – 45             | 94.8         | 120 – 10000        | 0.30                  | 1.0    | -2.1             |
| Ursa Minor        | 4.1                             | –                             | VERITAS                 | 35 – 45             | 60.4         | 160 – 93000        | 0.10                  | 8.4    | -0.1             |

901 where  $\mathcal{L}_0$  is the null hypothesis, or no DM emission, likelihood.  $\mathcal{L}^{\max}$  is the best fit signal  
 902 hypothesis where  $\langle\sigma v\rangle$  maximizes the likelihood. We calculate the likelihood of each source and  
 903 model, assuming events are Poisson distributed, with

$$\mathcal{L} = \prod_i \frac{(B_i + S_i)^{N_i} e^{-(B_i + S_i)}}{N_i!} \quad (5.8)$$

905 where  $S_i$  is the sum of expected number of signal counts.  $B_i$  is the number of background counts  
 906 observed.  $N_i$  is the total number of counts.

907 I also calculate an upper limit on  $\langle\sigma v\rangle$  by calculating the 95% confidence level (CL). For the  
 908 CL, we define a parameter,  $TS_{95}$ , as

$$TS_{95} \equiv \sum_{\text{bins}} \left[ 2N \ln \left( 1 + \frac{\epsilon S_{\text{ref}}}{B} \right) - 2\epsilon S_{\text{ref}} \right] \quad (5.9)$$

909 where the expected signal counts from a dSph is scaled by  $\epsilon$ .  $S_{\text{ref}}$  is the expected number of excess  
 910 counts in a bin from DM emission from a dSph with a corresponding annihilation cross-section,  
 911  $\langle\sigma v\rangle$ . We scan  $\epsilon$  such that

$$2.71 = TS_{\max} - TS_{95} \quad (5.10)$$

912 HAWC's exclusive results are provided in Section 5.5.

### 913 5.4.2 Glory Duck Joint Likelihood

914 The joint likelihood for the 5-experiment combination was done similarly as Section 5.4.1. We  
 915 calculate upper limits on  $\langle\sigma v\rangle$  from the TS, Eq. (5.7), and define the likelihood ratio more generally

$$\lambda(\langle\sigma v\rangle | \mathcal{D}_{\text{dSphs}}) = \frac{\mathcal{L}(\langle\sigma v\rangle; \hat{\nu} | \mathcal{D}_{\text{dSphs}})}{\mathcal{L}(\widehat{\langle\sigma v\rangle}; \hat{\nu} | \mathcal{D}_{\text{dSphs}})} \quad (5.11)$$

916  $\mathcal{D}_{\text{dSphs}}$  is the totality of observations across experiments and dSphs.  $\nu$  are the nuisance parameters  
 917 which are the  $J$  factors in this study.  $\widehat{\langle\sigma v\rangle}$  and  $\hat{\nu}$  are the respective estimate that maximize  $\mathcal{L}$   
 918 globally. Finally,  $\hat{\nu}$  is the set of nuisance parameters that maximize  $\mathcal{L}$  for a fixed value of  $\langle\sigma v\rangle$ .

919 The *complete* joint likelihood,  $\mathcal{L}$  that encompasses all observations from all instruments and  
 920 dSphs can be factorized into *partial* functions for each dSph  $l$  (with  $\mathcal{L}_{\text{dSph},l}$ ) and its  $J$  factor ( $\mathcal{J}_l$ ):

$$\mathcal{L}(\langle\sigma v\rangle; \nu | \mathcal{D}_{\text{dSphs}}) = \prod_{l=1}^{N_{\text{dSphs}}} \mathcal{L}_{\text{dSph},l}(\langle\sigma v\rangle; J_l, \nu_l | \mathcal{D}_l) \times \mathcal{J}_l(J_l | J_{l,\text{obs}}, \sigma_{\log J_l}). \quad (5.12)$$

921 For this study,  $N_{\text{dSphs}} = 20$  is the number of dSphs studied.  $\mathcal{D}_l$  are the gamma-ray observations  
 922 of dSph,  $l$ .  $\nu_l$  are the nuisance parameters modifying the gamma-ray observations of dSph,  $l$ ,  
 923 but excludes  $\mathcal{J}_l$ .  $\mathcal{J}_l$  is the  $J$  factor for dSph,  $l$ , as defined in Equation (5.2), and it is a nuisance  
 924 parameter whose value is unknown.  $\log_{10} J_{l,\text{obs}}$  and  $\sigma_{\log J_l}$  are obtained by fitting a log-normal  
 925 function of  $J_{l,\text{obs}}$  to the posterior distribution of  $J_l$  [50].  $\log_{10} J_{l,\text{obs}}$  and  $\sigma_{\log J_l}$  values are provided  
 926 in Table 5.1. The term  $\mathcal{J}_l$  constraining  $J_l$  is written as:

$$\mathcal{J}_l(J_l | J_{l,\text{obs}}, \sigma_{\log J_l}) = \frac{1}{\ln(10)J_{l,\text{obs}}\sqrt{2\pi}\sigma_{\log J_l}} \exp\left(-\frac{(\log_{10} J_l - \log_{10} J_{l,\text{obs}})^2}{2\sigma_{\log J_l}^2}\right). \quad (5.13)$$

927 Both the  $\mathcal{GS}$  and  $\mathcal{B}$ , displayed in Table 5.1, sets of  $J$  factors are used in this analysis. Equation (5.13)  
 928 is also normalized, so it can also be interpreted as a probability density function (PDF) for  $J_{l,\text{obs}}$ .  
 929 From Equation (7.1), we can also see that  $\langle\sigma v\rangle$  and  $J_l$  are degenerate when computing  $\mathcal{L}_{\text{dSph},l}$ .  
 930 Therefore, as noted in [51], it is sufficient to compute  $\mathcal{L}_{\text{dSph},l}$  versus  $\langle\sigma v\rangle$  for a fixed value of  $J_l$ .  
 931 We used  $J_{l,\text{obs}}(\mathcal{GS})$  reported in Tab. 5.1, in order to perform the profile of  $\mathcal{L}$  with respect to  $J_l$ .  
 932 The degeneracy implies that for any  $J'_l \neq J_{l,\text{obs}}$  (in practice in our case we used  $J'_l = J_{l,\text{obs}}(\mathcal{B})$  to  
 933 compute results from a different set of  $J$  factors):

$$\mathcal{L}_{\text{dSph},l}(\langle\sigma v\rangle; J'_l, \nu_l | \mathcal{D}_l) = \mathcal{L}_{\text{dSph},l}\left(\frac{J'_l}{J_{l,\text{obs}}} \langle\sigma v\rangle; J_{l,\text{obs}}, \nu_l | \mathcal{D}_l\right), \quad (5.14)$$

934 which is a straightforward rescaling operation that reduces the computational needs of the profiling  
 935 operation since:

$$\mathcal{L}(\langle\sigma v\rangle; \hat{\nu} | \mathcal{D}_{\text{dSphs}}) = \prod_{l=1}^{N_{\text{dSphs}}} \max_{J_l} \left[ \mathcal{L}_{\text{dSph},l}(\langle\sigma v\rangle; J_l, \hat{\nu}_l | \mathcal{D}_l) \times \mathcal{J}_l(J_l | J_{l,\text{obs}}, \sigma_{\log J_l}) \right]. \quad (5.15)$$

936 In addition, Eq. (5.14) enables the combination of data from different gamma-ray instruments and  
 937 observed dSphs via tabulated values of  $\mathcal{L}_{\text{dSph},l}$ , or equivalently of  $\lambda$  from Eq. (5.11) as was done in  
 938 this work, versus  $\langle\sigma v\rangle$ .  $\mathcal{L}_{\text{dSph},l}$  is computed for a fixed value of  $J_l$  and profiled with respect to all  
 939 instrumental nuisance parameters  $\nu_l$ , these nuisance parameters are discussed in more detail below.  
 940 These values are produced by each detector independently and therefore there is no need to share  
 941 sensitive low-level information used to produce them, such as event lists. Figure 5.4 illustrates the  
 942 multi-instrument combination technique used in this study with a comparison of the upper limit

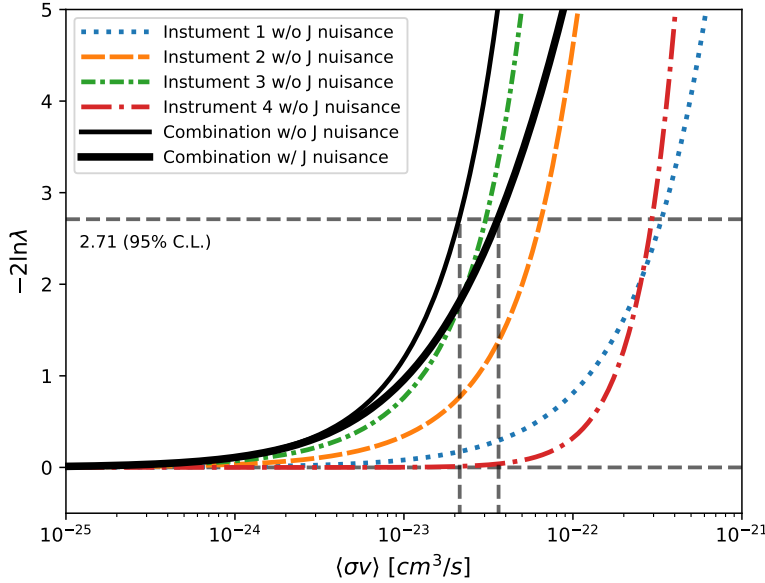


Figure 5.4 Illustration of the combination technique showing a comparison between  $-2 \ln \lambda$  provided by four instruments (colored lines) from the observation of the same dSph without any  $J$  nuisance and their sum, *i.e.* the resulting combined likelihood (thin black line). According to the test statistics of Equation (5.7), the intersection of the likelihood profiles with the line  $-2 \ln \lambda = 2.71$  indicates the 95% C.L. upper limit on  $\langle\sigma v\rangle$ . The combined likelihood (thin black line) shows a smaller value of upper limit on  $\langle\sigma v\rangle$  than those derived by individual instruments. We also show how the uncertainties on the  $J$  factor effects the combined likelihood and degrade the upper limit on  $\langle\sigma v\rangle$  (thick black line). All likelihood profiles are normalized so that the global minimum  $\widehat{\langle\sigma v\rangle}$  is 0. We note that each profile depends on the observational conditions in which a target object was observed. The sensitivity of a given instrument can be degraded and the upper limits less constraining if the observations are performed in non-optimal conditions such as a high zenith angle or a short exposure time.

943 on  $\langle\sigma v\rangle$  obtained from the combination of the observations of four experiments towards one dSph  
 944 versus the upper limit from individual instruments. It also shows graphically the effect of the  
 945  $J$ -factor uncertainty on the combined observations.

946 The *partial* joint likelihood function for gamma-ray observations of each dSph ( $\mathcal{L}_{dSph,l}$ ) is  
 947 written as the product of the likelihood terms describing the  $N_{exp,l}$  observations performed with  
 948 any of our observatories:

$$\mathcal{L}_{dSph,l} (\langle\sigma v\rangle; J_l, \nu_l | \mathcal{D}_l) = \prod_{k=1}^{N_{exp,l}} \mathcal{L}_{lk} (\langle\sigma v\rangle; J_l, \nu_{lk} | \mathcal{D}_{lk}), \quad (5.16)$$

949 where each  $\mathcal{L}_{lk}$  term refers to an observation of the  $l$ -th dSph with associated  $k$ -th instrument

950 responses.  $N_{\text{exp},l}$  varies from dSph to dSph and can be inferred from Table 5.2.

951     Each collaboration separately analyzes their data for  $\mathcal{D}_{lk}$  corresponding to dSph  $l$  and gamma-  
952     ray detector  $k$ , using as many common assumptions as possible in the analysis. HAWC's treatment  
953     was described earlier in Section 5.4.1 whereas the specifics of the remaining experiments is left to  
954     the publication. We compute the values for the likelihood functions  $\mathcal{L}_{lk}$  (see Eq. (5.16)) for a fixed  
955     value of  $J_l$  and profile over the rest of the nuisance parameters  $\nu_{lk}$ . Then, values of  $\lambda$  from Eq. (5.11)  
956     are computed as a function of  $\langle \sigma v \rangle$ , and shared using a common format. Results are computed for  
957     seven annihilation channels,  $W^+W^-$ ,  $ZZ$ ,  $b\bar{b}$ ,  $t\bar{t}$ ,  $e^+e^-$ ,  $\mu^+\mu^-$ , and  $\tau^+\tau^-$  over 62  $m_\chi$  values between  
958     5 GeV and 100 TeV provided in [44]. The  $\langle \sigma v \rangle$  range is defined between  $10^{-28}$  and  $10^{-18} \text{cm}^3 \cdot \text{s}^{-1}$ ,  
959     with 1001 logarithmically spaced values. The likelihood combination, i.e. Equation (5.12), and  
960     profile over the  $J$ -factor to compute the profile likelihood ratio  $\lambda$ , Equation (5.11), are carried out  
961     with two different public analysis software packages, namely `gLike` [52] and `LklCom` [53], that  
962     provide the same results [54].

963     As mentioned previously, each experiment computes the  $\mathcal{L}_{lk}$  from Equation (5.11) differently.  
964     The remainder of this section highlights the differences in this calculation across the experiments.  
965     Four experiments, namely *Fermi*-LAT, H.E.S.S., HAWC and MAGIC, use a binned likelihood to  
966     compute the  $\mathcal{L}_{lk}$ . For these experiments, for each observation  $\mathcal{D}_{lk}$  of a given dSph  $l$  carried out  
967     using a given gamma-ray detector  $k$ , the binned likelihood function is:

$$\mathcal{L}_{lk} (\langle \sigma v \rangle; J_l, \nu_{lk} | \mathcal{D}_{lk}) = \prod_{i=1}^{N_E} \prod_{j=1}^{N_P} \left[ \mathcal{P}(s_{lk,ij}(\langle \sigma v \rangle, J_l, \nu_{lk}) + b_{lk,ij}(\nu_{lk}) | N_{lk,ij}) \right] \times \mathcal{L}_{lk,\nu} (\nu_{lk} | \mathcal{D}_{\nu_{lk}}) \quad (5.17)$$

968     where  $N_E$  and  $N_P$  are the number of considered bins in reconstructed energy and arrival direction,  
969     respectively;  $\mathcal{P}$  represents a Poisson PDF for the number of gamma-ray candidate events  $N_{lk,ij}$   
970     observed in the  $i$ -th bin in energy and  $j$ -th bin in arrival direction, when the expected number is  
971     the sum of the expected mean number of signal events  $s_{ij}$  (produced by DM annihilation) and of  
972     background events  $b_{ij}$ ;  $\mathcal{L}_{lk,\nu}$  is the likelihood term for the extra  $\nu_{lk}$  nuisance parameters that vary  
973     from one instrument  $k$  to another. The expected counts for signal events  $s_{ij}$  for a given dSph  $l$  and

974 detector  $k$  is given by:

$$s_{ij}(\langle\sigma\nu\rangle, J) = \int_{E'_{\min,i}}^{E'_{\max,i}} dE' \int_{P'_{\min,j}}^{P'_{\max,j}} d\Omega' \int_0^\infty dE \int_{\Delta\Omega_{tot}} d\Omega \int_0^{T_{\text{obs}}} dt \frac{d^2\Phi(\langle\sigma\nu\rangle, J)}{dEd\Omega} \text{IRF}(E', P' | E, P, t) \quad (5.18)$$

975 where  $E'$  and  $E$  are the reconstructed and true energies,  $P'$  and  $P$  the reconstructed and true  
976 arrival directions;  $E'_{\min,i}$ ,  $P'_{\min,j}$ ,  $E'_{\max,i}$ , and  $P'_{\max,j}$  are their lower and upper limits of the  $i$ -th  
977 energy bin and the  $j$ -th arrival direction bin;  $T_{\text{obs}}$  is the (dead-time corrected) total observation  
978 time;  $t$  is the time along the observations;  $d^2\Phi/dEd\Omega$  is the DM flux in the source region (see  
979 Equation (7.1)); and  $\text{IRF}(E', P' | E, P, t)$  is the IRF, which can be factorized as the product of the  
980 effective collection area of the detector  $A_{\text{eff}}(E, P, t)$ , the PDFs for the energy estimator  $f_E(E' | E, t)$ ,  
981 and arrival direction  $f_P(P' | E, P, t)$  estimators. Note that for Fermi-LAT, HAWC, MAGIC, and  
982 VERITAS the effect of the finite angular resolution is taken into account through the convolution  
983 of  $d\Phi/dEd\Omega$  with  $f_P$  in Equation (5.18), whereas in the cases of H.E.S.S.  $f_P$  is approximated by a  
984 delta function. This approximation has been made in order to maintain compatibility of the result  
985 with what has been previously published. The difference introduced by this approximation is  $< 5\%$   
986 for all considered dSphs. A more comprehensive review of the differences between the analyses of  
987 different instruments can be found in [25].

## 988 5.5 HAWC Results

989 13 of the 20 dSphs considered for the Glory Duck analysis are within HAWC's field of view.  
990 These dSph are analyzed for emission from DM annihilation according to the likelihood method  
991 described in Section 5.4. The 13 likelihood profiles are then stacked to synthesize a combined  
992 limit on the dark matter cross-section,  $\langle\sigma\nu\rangle$ . This combination is done for the 7 SM annihilation  
993 channels used in the Glory Duck analysis. Figure 5.5 shows the combined limit for all annihilation  
994 channels with HAWC only observations. We also perform 300 studies of Poisson trials on the  
995 background. These trials are used to produce HAWC sensitivities with  $\pm 1\sigma$  and  $\pm 2\sigma$  uncertainty  
996 bands which were shared with the other collaborators for combination. The results on fitting to  
997 HAWC's Poisson trials of the DM hypothesis is shown in Figure 5.7 for all the DM annihilation  
998 channels studied for Glory Duck.

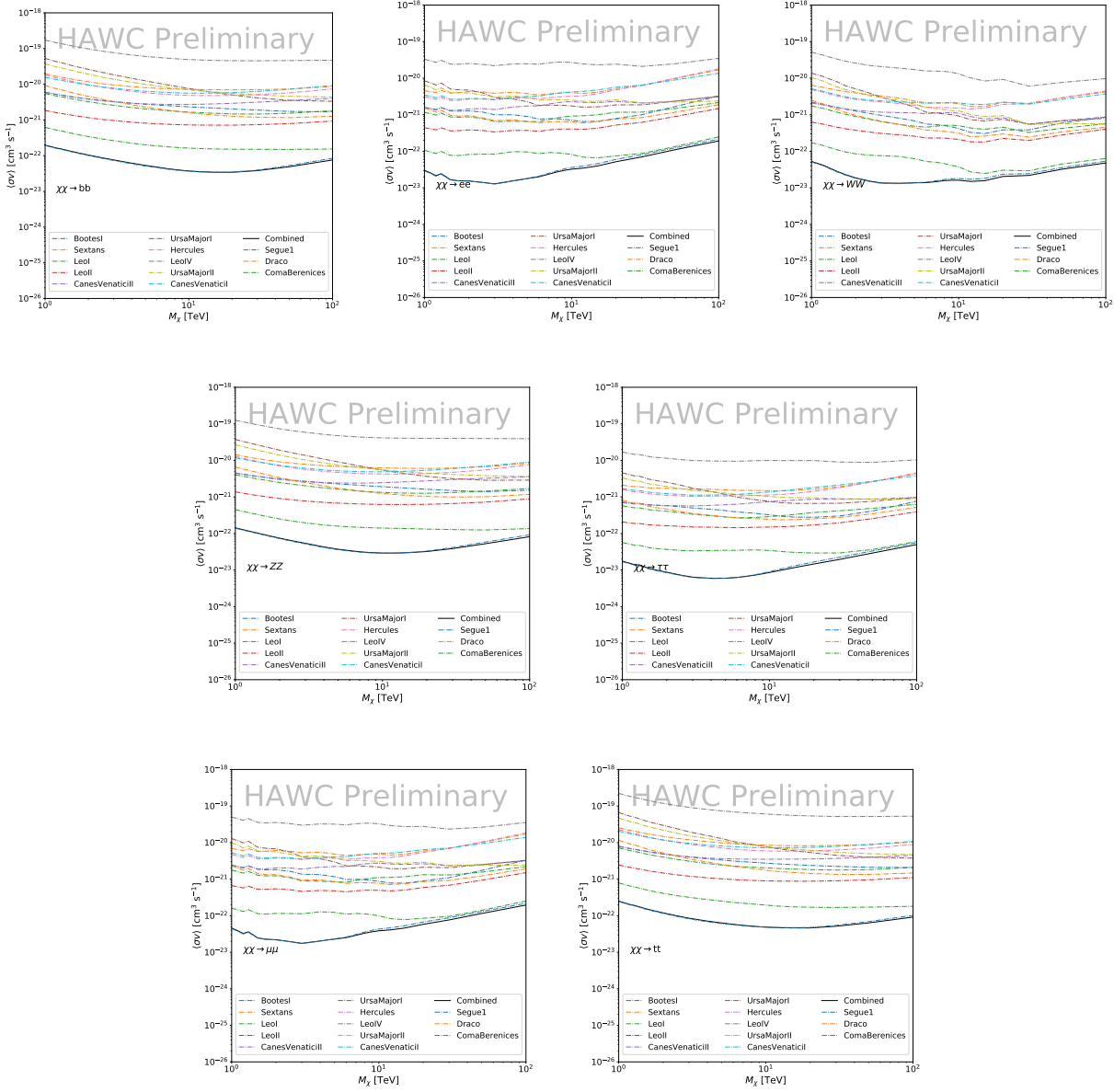


Figure 5.5

999      No DM was found in HAWC observations. HAWC's limits are dominated by the dSphs Segue1  
1000     and Coma Berenices. The remaining 11 dSphs do not contribute significantly to the limit because  
1001     they are at high zenith and/or have much smaller  $J$  factors. Even though some remaining dSphs  
1002     have large  $J$  factors, they are towards the edge of HAWC's field of view where HAWC analysis is  
1003     less sensitive.

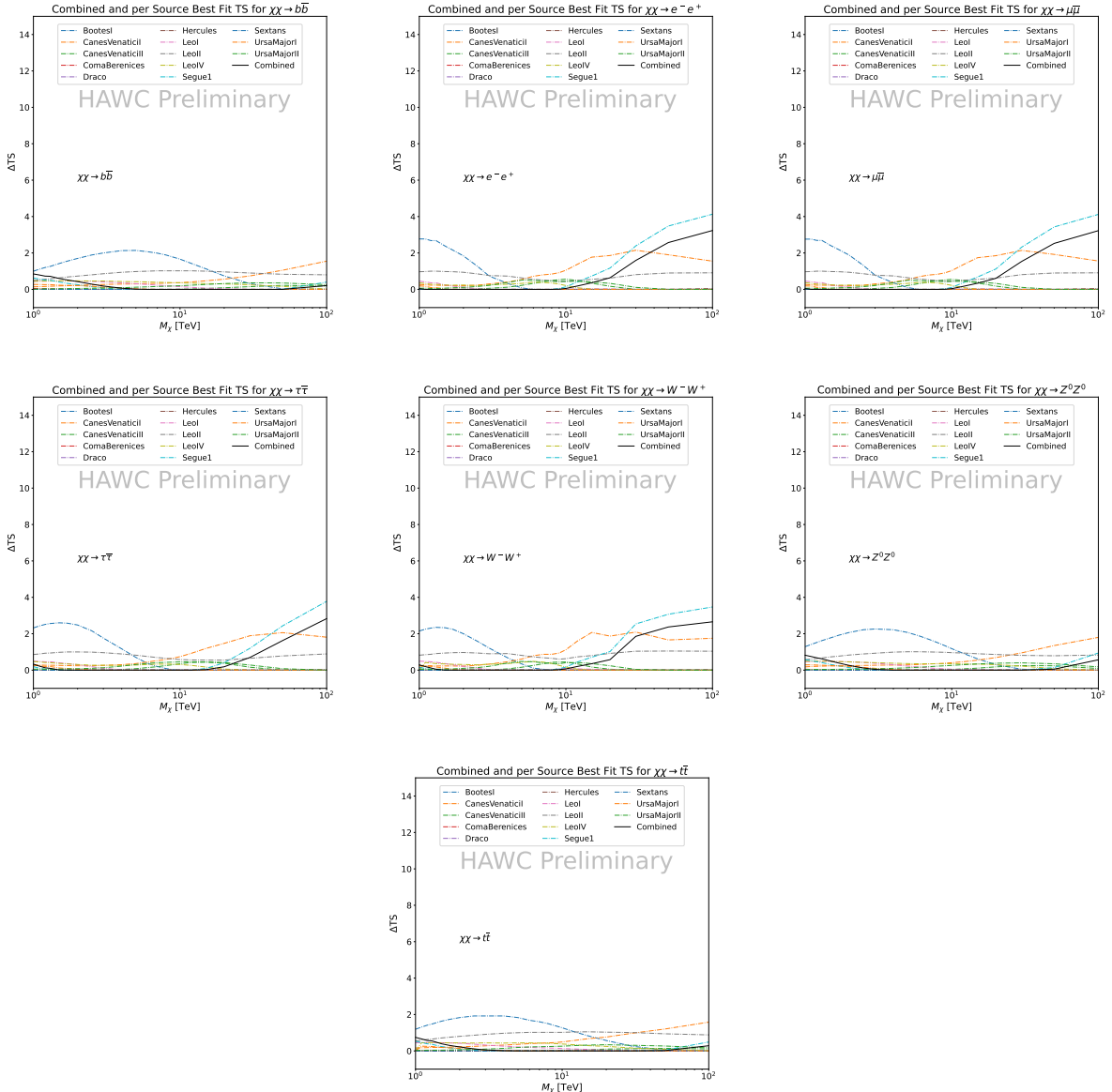


Figure 5.6 HAWC TS values for best fit  $\langle\sigma v\rangle$  versus  $m_\chi$  for seven SM annihilation channels with  $J$  factors from  $\mathcal{GS}$ . The solid black line shows the combined best fit TS values. The colored, dashed lines are the TS values for each of the 13 sources HAWC studied.

## 1004 5.6 Glory Duck Combined Results

1005 The crux of this analysis is that HAWC's results are combined with 4 other gamma-ray observa-  
 1006 tories: Fermi-LAT, H.E.S.S., MAGIC, and VERITAS. No significant DM emission was observed  
 1007 by any of the five instruments. We present the upper limits on  $\langle\sigma v\rangle$  assuming seven independent  
 1008 DM self annihilation channels, namely  $W^+W^-$ ,  $Z^+Z^-$ ,  $b\bar{b}$ ,  $t\bar{t}$ ,  $e^+e^-$ ,  $\mu^+\mu^-$ , and  $\tau^+\tau^-$ . The 68%

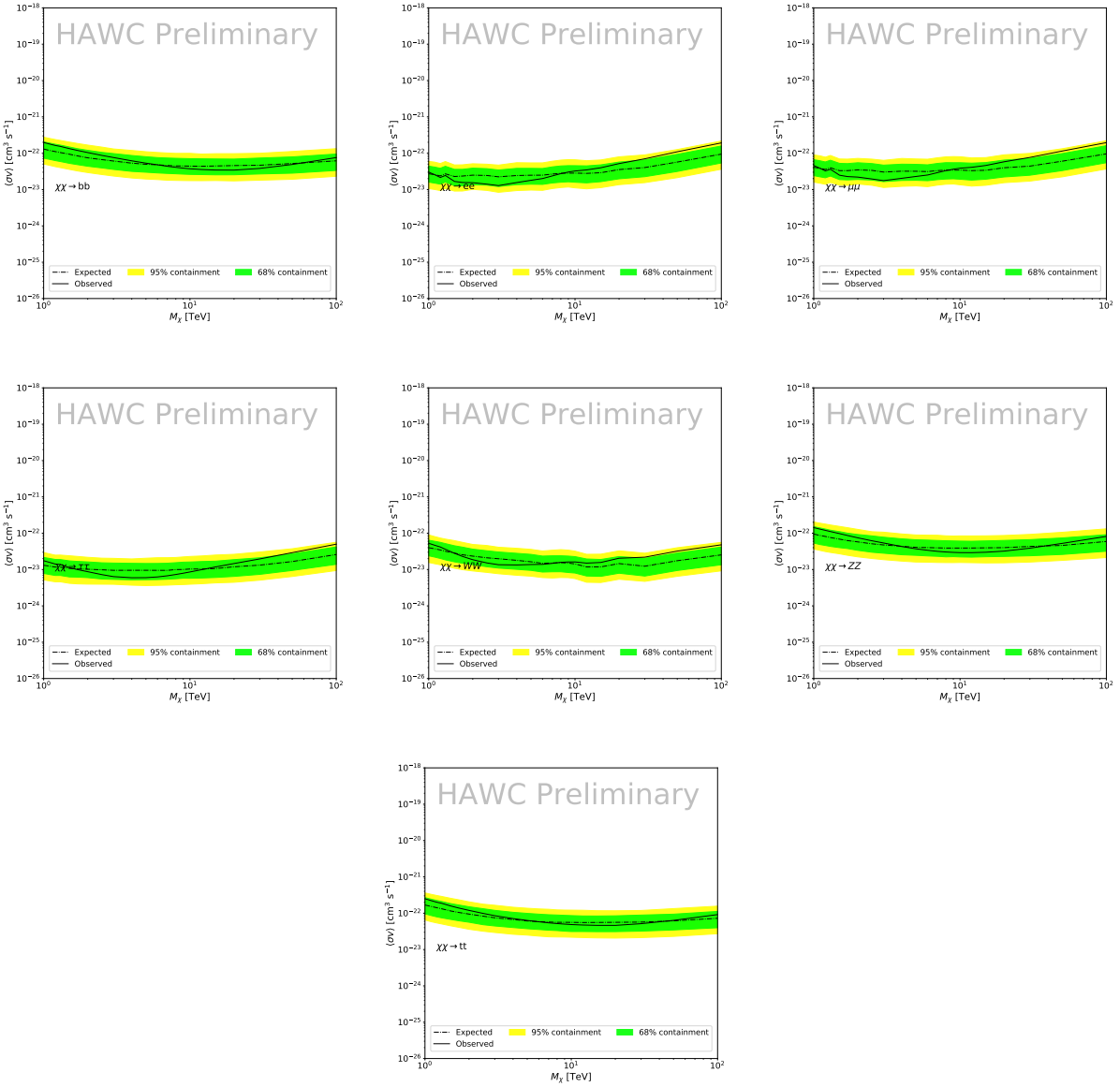


Figure 5.7 HAWC Brazil bands at 95% confidence level on  $\langle\sigma v\rangle$  versus DM mass for seven annihilation channels with  $J$ -factors from  $\mathcal{GS}$  [55]. The solid line represents the combined limit from 13 dSphs. The dashed line is the expected limit. The green band is the 68% containment. The yellow band is the 95% containment.

1009 and 95% containment bands are produced from 300 Poisson realizations of the null hypothesis  
 1010 corresponding to each of the combined datasets. These 300 realizations are combined identically  
 1011 to dSph observations. The containment bands and the median are extracted from the distribution  
 1012 of resulting limits on the null hypothesis. These 300 realizations are obtained either by fast simu-  
 1013 lations of the OFF observations, for H.E.S.S., MAGIC, VERITAS, and HAWC, or taken from real

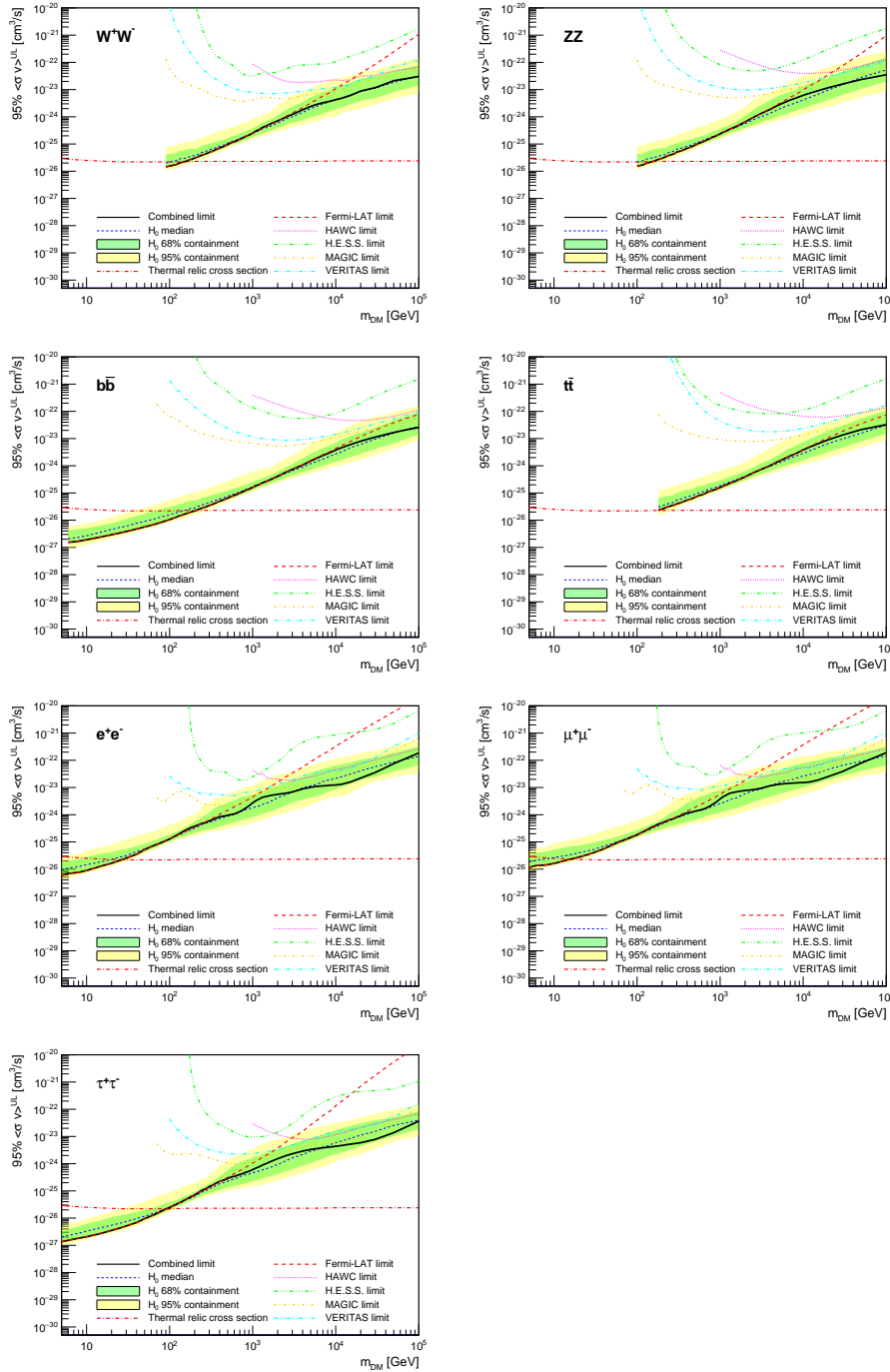


Figure 5.8 Upper limits at 95% confidence level on  $\langle\sigma v\rangle$  in function of the DM mass for eight annihilation channels, using the set of  $J$  factors from Ref. [55] ( $\mathcal{GS}$  set in Table 5.1). The black solid line represents the observed combined limit, the black dashed line is the median of the null hypothesis corresponding to the expected limit, while the green and yellow bands show the 68% and 95% containment bands. Combined upper limits for each individual detector are also indicated as solid, colored lines. The value of the thermal relic cross-section in function of the DM mass is given as the red dotted-dashed line [56].

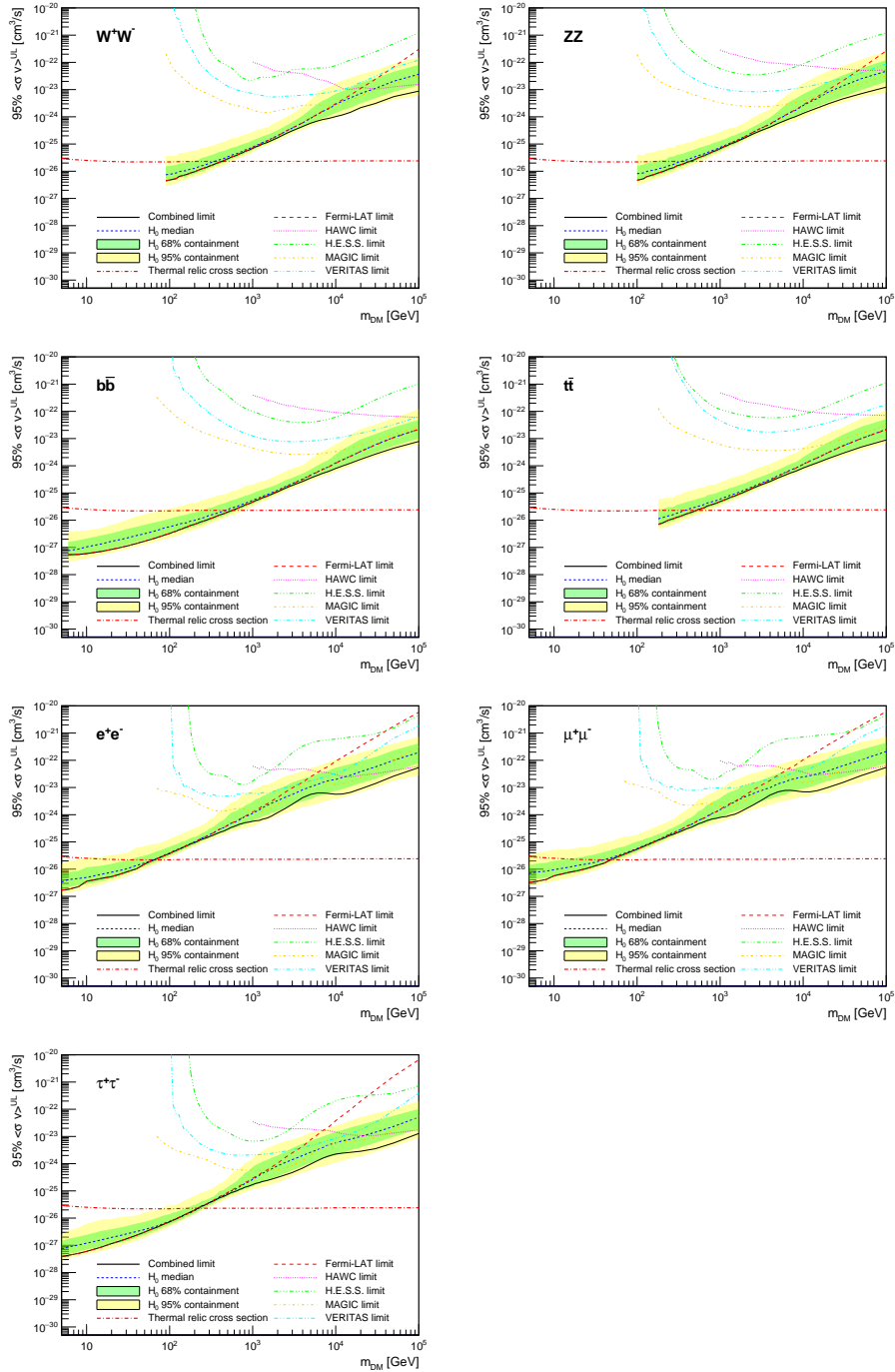


Figure 5.9 Same as Fig. 5.8, using the set of  $J$  factors from Ref. [49, 57] ( $\mathcal{B}$  set in Table 5.1).

1014 observations of empty fields of view in the case of Fermi-LAT [50, 58, 59].

1015 The obtained limits are shown in Figure 5.8 for the  $\mathcal{GS}$  set of  $J$ -factors [55] and in Figure 5.9  
 1016 for the  $\mathcal{B}$  set of  $J$ -factors [49, 57]. The combined limits are presented with their 68% and 95%  
 1017 containment bands, and are expected to be close to the median limit when no signal is present.

1018 We observe agreement with the null hypothesis for all channels, within  $2\sigma$  standard deviations,  
1019 between the observed limits and the expectations given by the median limits. Limits obtained from  
1020 each detector are also indicated in the figures, where limits for all dSphs observed by the specific  
1021 instrument have been combined.

1022 Below  $\sim 300$  GeV, the *Fermi*-LAT dominates the DM limits for all annihilation channels. From  
1023  $\sim 300$  GeV to  $\sim 2$  TeV, *Fermi*-LAT continues to dominate for the hadronic and bosonic DM channels,  
1024 yet the IACTs (H.E.S.S., MAGIC, and VERITAS) and *Fermi*-LAT all contribute to the limit for  
1025 leptonic DM channels. For DM masses between  $\sim 2$  TeV to  $\sim 10$  TeV, the IACTs dominate leptonic  
1026 DM annihilation channels, whereas both the *Fermi*-LAT and the IACTs dominate bosonic and  
1027 hadronic DM annihilation channels. From  $\sim 10$  TeV to  $\sim 100$  TeV, both the IACTs and HAWC  
1028 contribute significantly to the leptonic DM limit. For hadronic and bosonic DM, the IACTs and  
1029 *Fermi*-LAT both contribute strongly.

1030 We notice that the limits computed using the  $\mathcal{B}$  set of  $J$ -factor are always better compared to the  
1031 ones calculated with the  $\mathcal{GS}$  set. For the  $W^+W^-$ ,  $Z^+Z^-$ ,  $b\bar{b}$ , and  $t\bar{t}$  channels, the ratio between the  
1032 limits computed with the two sets of  $J$ -factor is varying between a factor of  $\sim 3$  and  $\sim 5$  depending  
1033 on the energy, with the largest ratio around 10 TeV. For the channels  $e^+e^-$ ,  $\mu^+\mu^-$ , and  $\tau^+\tau^-$ , the  
1034 ratio lies between  $\sim 2$  to  $\sim 6$ , being maximum around 1 TeV. Examining Figure 5.16 and Figure 5.17  
1035 in Section 5.8, these differences are explained by the fact that the  $\mathcal{B}$  set provides higher  $J$ -factors  
1036 for the majority of the studied dSphs, with the notable exception of Segue I. The variation on the  
1037 ratio of the limits for the two sets is due to different dSph dominating the limits depending on the  
1038 energy. One set,  $\mathcal{B}$ , pushes the range of which thermal cross-section which can be excluded to  
1039 higher mass. This comparison demonstrates the magnitude of systematic uncertainties associated  
1040 with the choice of the  $J$ -factor calculation. The  $\mathcal{GS}$  and  $\mathcal{B}$  sets present a difference in the limits for  
1041 all channels of about This difference is explained, see Figure 5.16 and Figure 5.17, by the fact that  
1042 the  $\mathcal{B}$  set provides higher  $J$ -factors for all dSph except for Segue I.

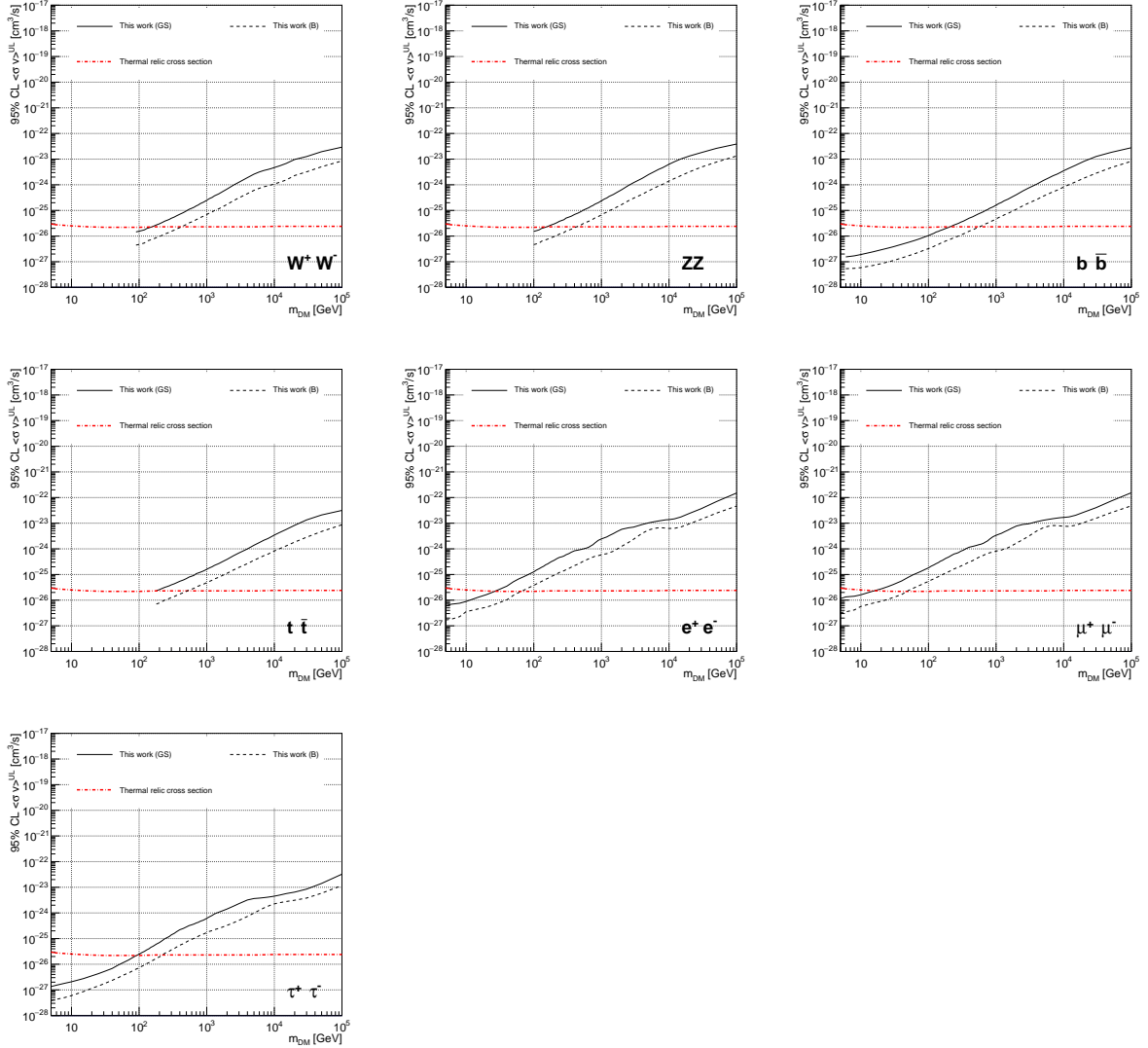


Figure 5.10 Comparisons of the combined limits at 95% confidence level for each of the eight annihilation channels when using the  $J$  factors from Ref. [55] ( $\mathcal{GS}$  set in Table 5.1), plain lines, and the  $J$  factor from Ref. [49, 57] ( $\mathcal{B}$  set in Table 5.1), dashed lines. The cross-section given by the thermal relic is also indicated [56].

## 1043 5.7 HAWC Systematics

### 1044 5.7.1 Inverse Compton Scattering

1045 The DM-DM annihilation channels produce many high energy electrons regardless of the  
 1046 primary annihilation channel. These high energy electrons can produce high energy gamma-rays  
 1047 through Inverse Compton Scattering (ICS). If this effect is strong, it would change the morphology  
 1048 of the source and increase the total expected gamma-ray counts from any source. The PPPC [44]

1049 provides tools in Mathematica for calculating the impact of ICS for an arbitrary location in the  
1050 sky for a specified annihilation channel. We calculated the change in gamma-ray counts for DM  
1051 annihilation to primary  $e\bar{e}$  for RA and Dec corresponding to Segue1 and Coma Berenices. These  
1052 dSphs were chosen because they are the strongest contributors to the limit.  $e\bar{e}$  was selected because  
1053 it would have the largest number of high energy electrons. The effect was found to be on the order  
1054 of  $10^{-7}$  on the gamma-ray spectrum. As a result, this systematic is not considered in our analysis.

### 1055 **5.7.2 Point Source Versus Extended Source Limits**

1056 The previous DM search toward dSph approximated the dSphs as point sources [46]. In  
1057 this analysis, the dSphs are implemented as extended with J-factor distributions following those  
1058 produced by [55]. The resolution of the cited map is much finer than HAWC's angular resolution.  
1059 The vast majority of the J-factor distribution is represented on the central HAWC pixel of the dSph  
1060 spatial map. However, the neighboring 8 pixels are not negligible and contribute to our limit.

1061 Figure 5.11 shows a substantial improvement to the limit for Segue1. Fig. 5.12 however showed  
1062 identical limits. These disparities are best explained by the relative difference in their J-Factors.  
1063 Both dSphs pass almost overhead the HAWC detector, however Segue1 has the larger J-Factor  
1064 between the two. Adjacent pixels to the central pixel will therefore contribute to the limits. This is  
1065 the case for other dSph that are closer to the zenith of the HAWC detector.

1066 Comparison plots for all sources and the combined limit can be found in the sandbox for the  
1067 Glory Duck project.

### 1068 **5.7.3 Impact of Pointing Systematic**

1069 During the analysis it was discovered that directional reconstruction of gamma-rays had a  
1070 systematic bias at large zenith angles. Slides describing this systematic can be found [here](#). Shown  
1071 on the presentation is dependence on the pointing systematic on declination. New spatial profiles  
1072 were generated for every dSph and limits were computed for the adjusted declination.

1073 Section 5.7.3 demonstrates the impact of this systematic for all DM annihilation channels  
1074 studied by HAWC. The impact is a tiny improvement, yet mostly identical, to the combined limits.

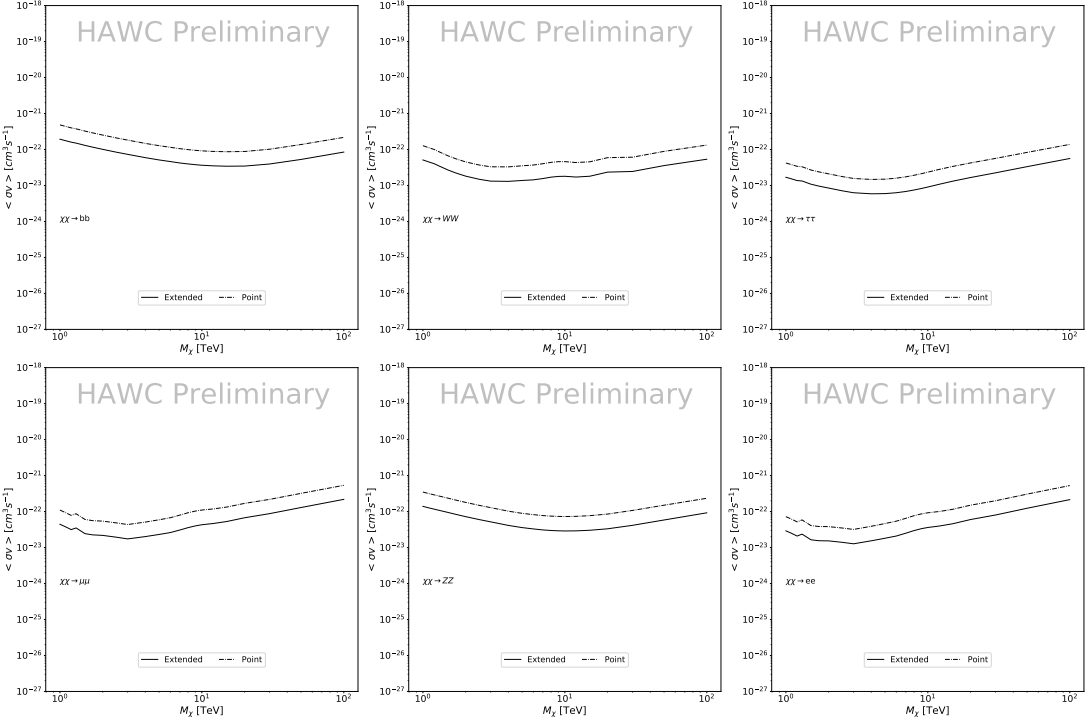


Figure 5.11 Comparisons of the combined limits at 95% confidence level for a point source analysis and extended source using [55]  $\mathcal{GS}$  J-factor distributions and PPPC [44] annihilation spectra. Shown are the limits for Segue1 which will have the most significant impact on the combined limit. 6 of the 7 DM annihilation channels are shown. Solid lines are extended source studies. Dashed lines are point source studies. Overall, the extended source analysis improves the limit by a factor of 2.

## 1075 5.8 J-factor distributions

### 1076 5.8.1 Numerical integration of $\mathcal{GS}$ maps

1077 It was discovered well after the HAWC analysis was completed that the published tables from  
 1078  $\mathcal{GS}$  [45] quoted median  $J$ -factors were computed in a non-trivial manner. The assumption myself  
 1079 and collaborators had been that the published tables represented the  $J$ -factor as a function of  $\theta$  for  
 1080 the best global fit model on a per-source basis. However, this is not the case. Instead, what is  
 1081 published are the best fit model for each dwarf that only considers stars up to the angular separation  
 1082  $\theta$ . Therefore, the model is changing for each value of  $\theta$  for each dwarf. Yet, the introduced features  
 1083 from unique models at each  $\theta$  are much smaller than the angular resolution of HAWC. It is not  
 1084 expected for these effects to impact the limits and TS greatly as a result.

1085 Median  $J$ -factor model profiles were provided by the authors. New maps were generated

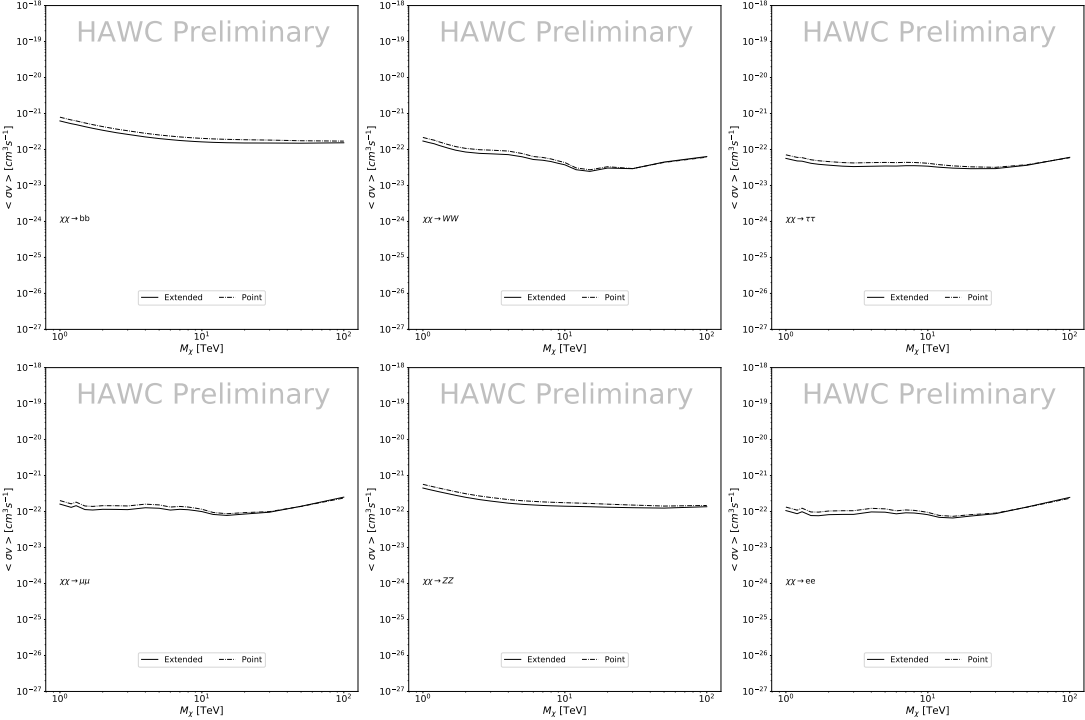


Figure 5.12 Same as Fig. 5.11 on Coma Berenices. This dSph also contributes significantly to the limit. The limits are identical in this case.

1086 and analyzed for Segue1 and Coma Berenices. Figure 5.14 shows the differential between maps  
 1087 generated with the method from Section 5.8.1 and from the authors of [45]. These maps were  
 1088 reanalyzed for all SM DM annihilation channels. Upper limits for these channels are shown in  
 1089 Figure 5.15

1090 From Figure 5.15, we can see that the impact of these model difference was no substantial.  
 1091 The observed impact was a fractional effect which is much smaller than the impact from selecting  
 1092 another DM spatial distribution model as was shown in Figure 5.10.

1093 **5.8.2  $\mathcal{GS}$  Versus  $\mathcal{B}$  spatial models**

1094 We show in this appendix a comparison between the  $J$ -factors computed by Geringer-Sameth  
 1095 *et al.* [55] (the  $\mathcal{GS}$  set) and the ones computed by Bonnivard *et al.* [49, 57] (the  $\mathcal{B}$  set). The  
 1096  $\mathcal{GS}$   $J$ -factors are computed through a Jeans analysis of the kinematic stellar data of the selected  
 1097 dSphs, assuming a dynamic equilibrium and a spherical symmetry for the dSphs. They adopted  
 1098 the generalized DM density distribution, known as Zhao-Hernquist, introduced by [47], carrying

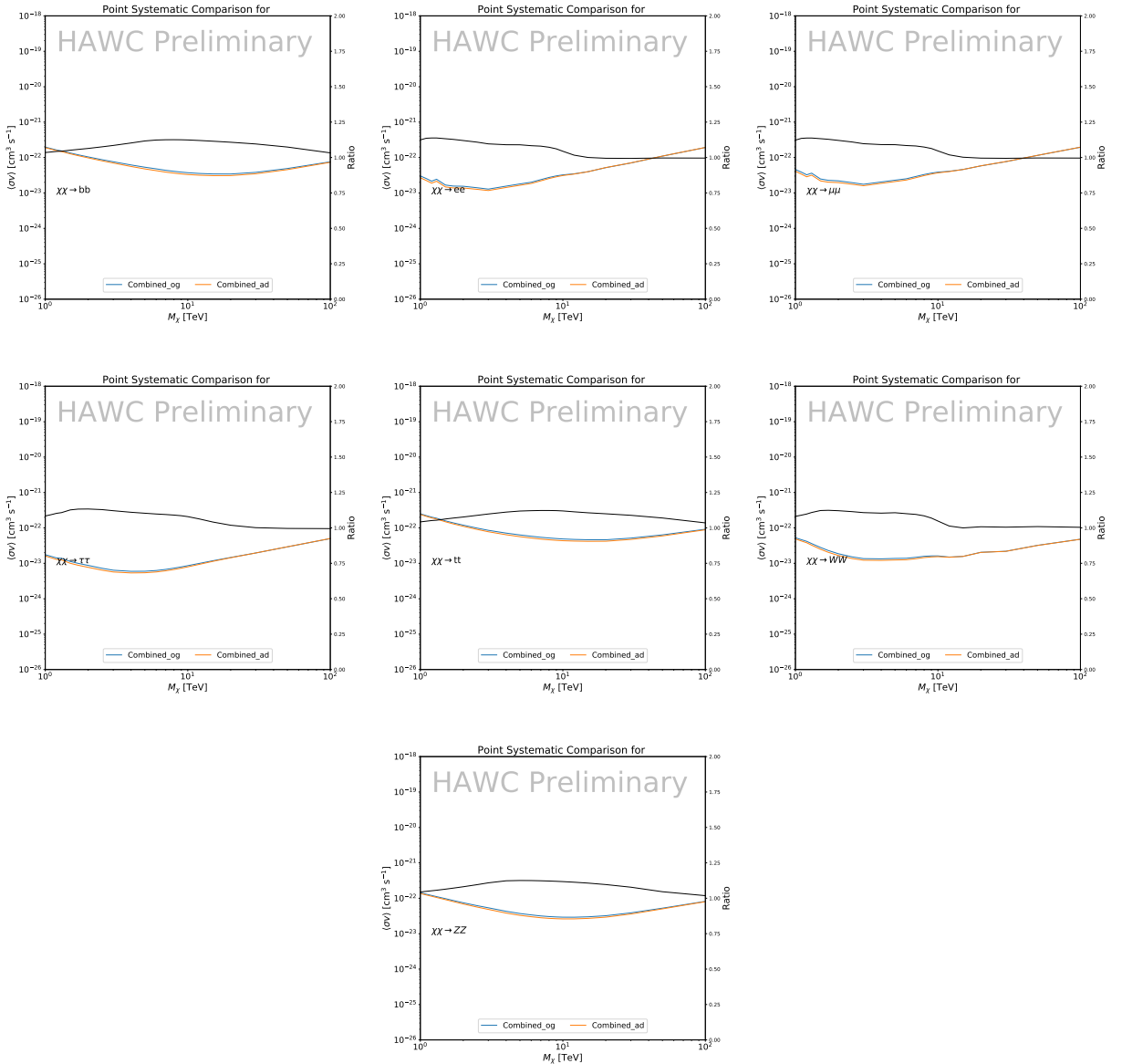


Figure 5.13 Comparison of combined limits when correcting for HAWC's pointing systematic. All DM annihilation channels are shown. The solid black line is the ratio between published limit to the declination corrected limit. The blue solid line or "Combined\_og" represented the limits computed for Glory Duck. The solid orange line or "Combined\_ad" represented the limits computed after correcting for the pointing systematic.

1099 three additional index parameters to describe the inner and outer slopes, and the break of the  
 1100 density profile. Such a profile parametrization allows the reduction of the theoretical bias from  
 1101 the choice of a specific radial dependency on the kinematic data. In other words, the increase of  
 1102 free parameters with the use of the Zhao-Hernquist profile allows a better description of the mass

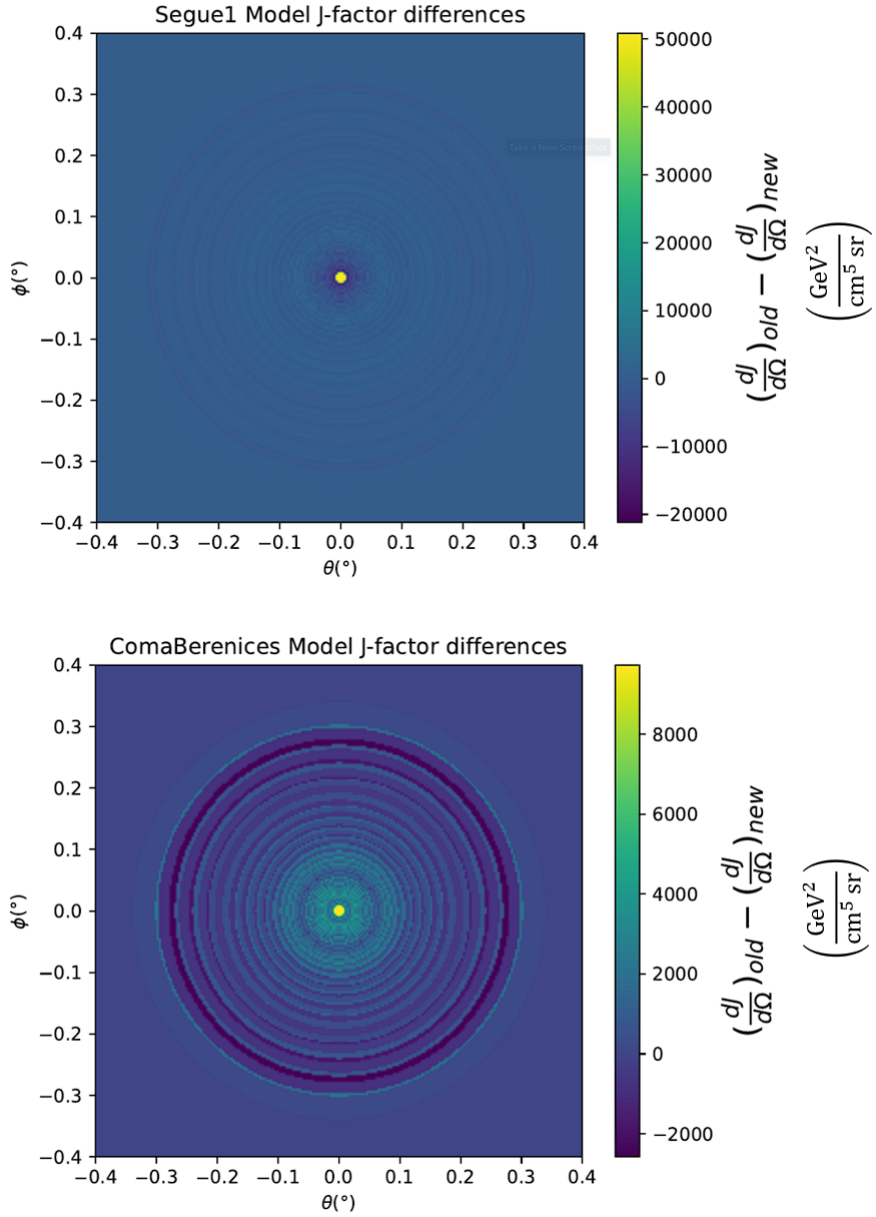


Figure 5.14 Differential map of  $dJ/\Omega$  from model built in Section 5.8.1 and profiles provided directly from authors. (Top) Differential from Segue1. (bottom) Differential from Coma Berenices. Note that their scales are not the same. Segue1 shows the deepest discrepancies which is congruent with its large uncertainties. Both models show anuli where unique models become apparent.

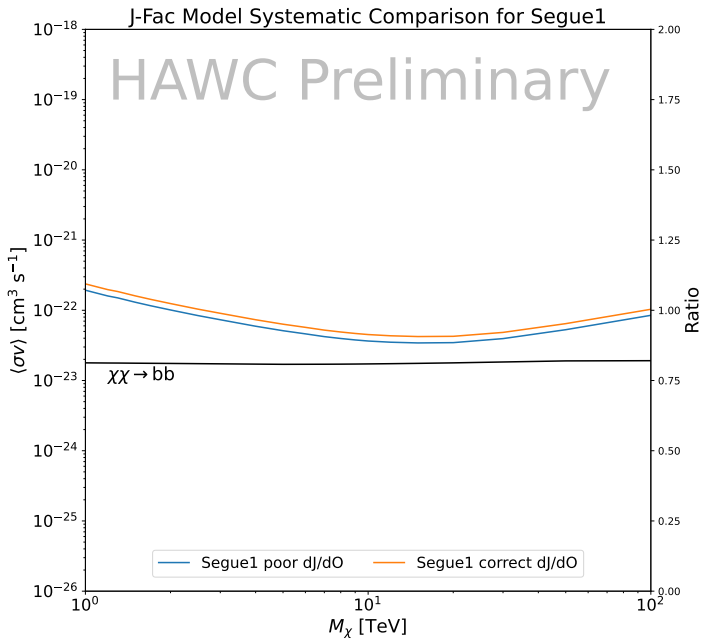
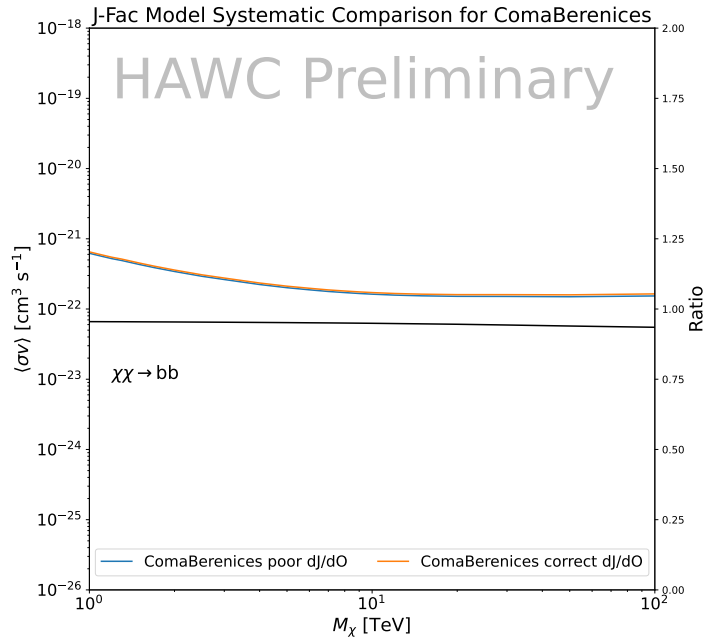


Figure 5.15 HAWC limits for Coma Berenices (top) and Segue1 (bottom) for two different map sets. Blue lines are limits calculated on maps with poor model representation. Orange lines are limits calculated on spatial profiles provided by the authors of [45]. Black line is the ratio of the poor spatial model limits to the corrected spatial models. The left y-axis measures  $\langle \sigma v \rangle$  for the blue and orange lines. The right y-axis measures the ratio and is unitless.

1103 density distribution of dark matter.

1104 In addition, a constant velocity anisotropy profile and a Plummer light profile [60] for the stellar  
1105 distribution were assumed. The velocity anisotropy profile depends on the radial and tangential  
1106 velocity dispersion. However, its determination remains challenging since only the line-of-sight  
1107 velocity dispersion can be derived from velocity measurements. Therefore, the parametrization of  
1108 the anisotropy profile is obtained from simulated halos (see [61] for more details). They provide the  
1109 values of the  $J$ -factors of regions extending to various angular radius up to the outermost member  
1110 star.

1111 The  $\mathcal{B}$   $J$ -factors were computed through a Jeans analysis taking into account the systematic  
1112 uncertainties induced by the DM profile parametrization, the radial velocity anisotropy profile, and  
1113 the triaxiality of the halo of the dwarf galaxies. They performed a more complete study of the dSph  
1114 kinematics and dynamics than  $\mathcal{GS}$  for the determination of the  $J$ -factor. Conservative values of the  
1115  $J$ -factors where obtained using an Einasto DM density profile [62], a realistic anisotropy profile  
1116 known as the Baes & Van Hese profile [63] which takes into account that the inner regions can be  
1117 significantly non-isotropic, and a Zhao-Hernquist light profile [47].

1118 For both sets,  $J$ -factor values are provided for all dSphs as a function of the radius of the  
1119 integration region [55, 49, 57]. Table 5.1 shows the heliocentric distance and Galactic coordinates  
1120 of the twenty dSphs, together with the two sets of  $J$ -factor values integrated up to the outermost  
1121 observed star for  $\mathcal{GS}$  and the tidal radius for  $\mathcal{B}$ . Both  $J$ -factor sets were derived through a Jeans  
1122 analysis based on the same kinematic data, except for Draco where the measurements of [64] have  
1123 been adopted in the computation of the  $\mathcal{B}$  value. The computations for producing the  $\mathcal{GS}$  and  $\mathcal{B}$   
1124 samples differ in the choice of the DM density, velocity anisotropy, and light profiles, for which the  
1125 set  $\mathcal{B}$  takes into account some sources of systematic uncertainties.

1126 Figure 5.16 and Figure 5.17 show the comparisons for the  $J$ -factor versus the angular radius  
1127 for each of the 20 dSphs used in this study. The uncertainties provided by the authors are also  
1128 indicated in the figures. For the  $\mathcal{GS}$  set, the computation stops at the angular radius corresponding  
1129 to the outermost observed star, while for the  $\mathcal{B}$  set, the computation stops at the angular radius

1130 corresponding to the tidal radius.

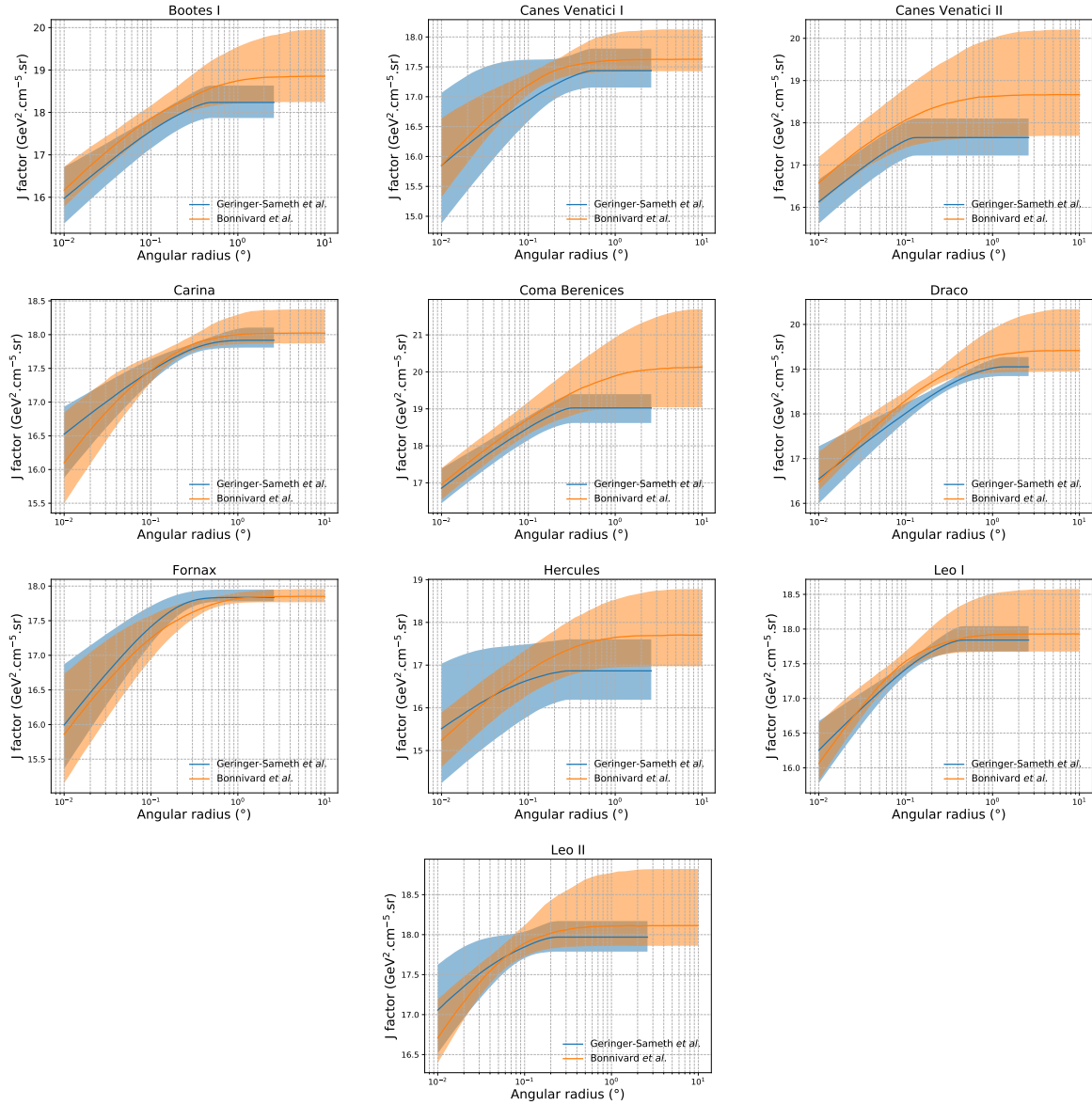


Figure 5.16 Comparisons between the  $J$ -factors versus the angular radius for the computation of  $J$  factors from Ref. [55] ( $\mathcal{GS}$  set in Table 5.1) in blue and for the computation from Ref. [49, 57] ( $\mathcal{B}$  set in Tab. 5.1) in orange. The solid lines represent the central value of the  $J$ -factors while the shaded regions correspond to the  $1\sigma$  standard deviation.

## 1131 5.9 Discussion and Conclusions

1132 In this multi-instrument analysis, we have used observations of 20 dSphs from the gamma-ray  
 1133 telescopes Fermi-LAT, H.E.S.S., MAGIC, VERITAS, and HAWC to perform a collective DM  
 1134 search annihilation signals. The data were combined across sources and detectors to significantly

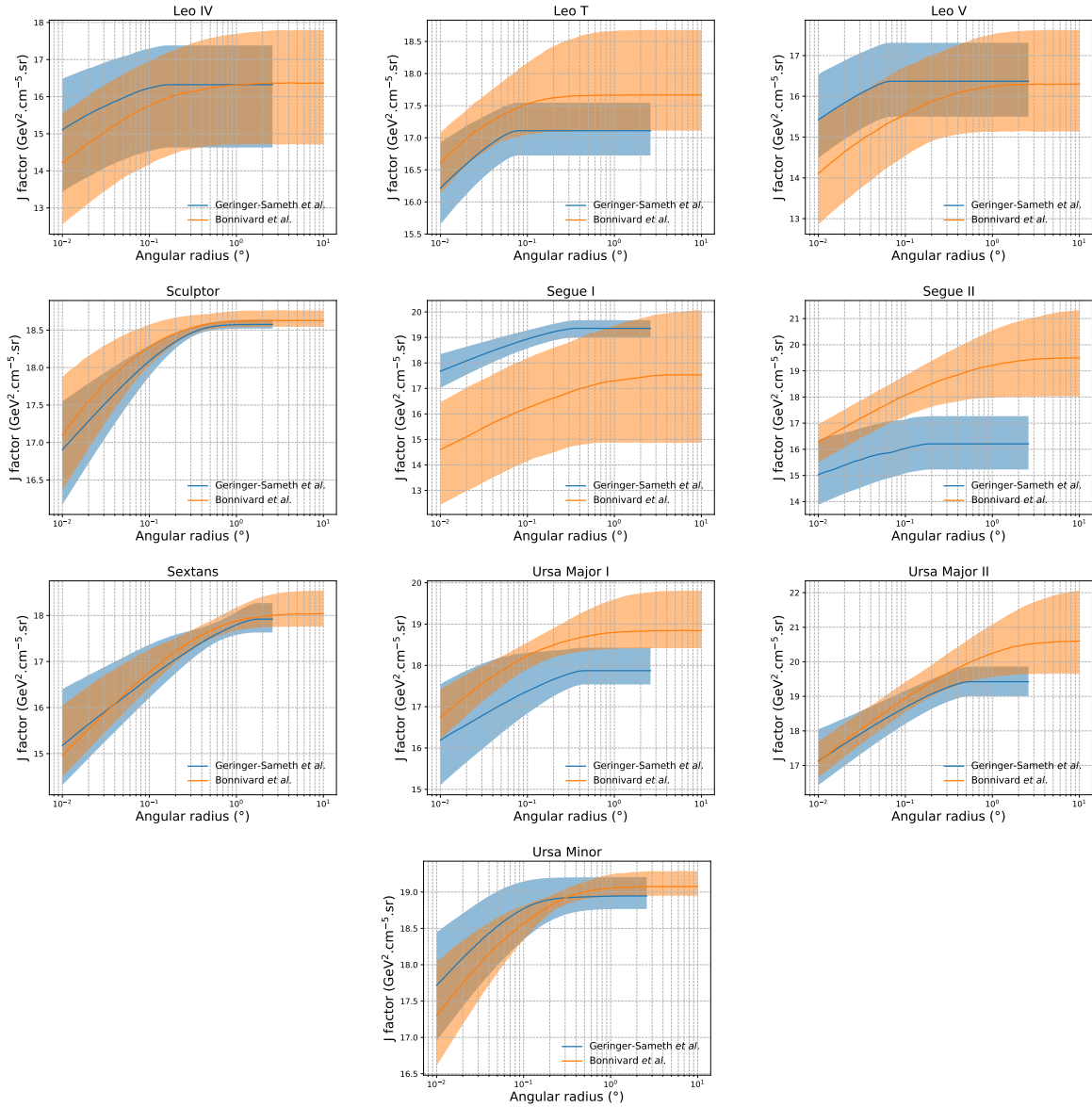


Figure 5.17 Comparisons between the  $J$ -factors versus the angular radius for the computation of  $J$  factors from Ref. [55] ( $\mathcal{GS}$  set in Tab. 5.1) in blue and for the computation from Ref. [49, 57] ( $\mathcal{B}$  set in Tab. 5.1) in orange. The solid lines represent the central value of the  $J$ -factors while the shaded regions correspond to the  $1\sigma$  standard deviation.

increase the sensitivity of the search. We have observed no significant deviation from the null, no DM hypothesis, and so present our results in terms of upper limits on the annihilation cross-section for seven potential DM annihilation channels.

Fermi-LAT brings the most stringent constraints for continuum channels below approximately 1 TeV. The remaining detectors dominate at higher energies. Overall, for multi-TeV DM mass,

1140 the combined DM constraints from all five telescopes are 2-3 times stronger than any individual  
1141 telescope for multi-TeV DM.

1142 Derived from observations of many dSphs, our results produce robust limits given the DM  
1143 content of the dSphs is relatively well constrained. The obtained limits span the largest mass  
1144 range of any WIMP DM search. Our combined analysis improves the sensitivity over previously  
1145 published results from each detector which produces the most stringent limits on DM annihilation  
1146 from dSphs. These results are based on deep exposures of the most promising known dSphs with  
1147 the currently most sensitive gamma-ray instruments. Therefore, our results constitute a legacy of  
1148 a generation of gamma-ray instruments on WIMP DM searches towards dSphs. Our results will  
1149 remain the reference in the field until a new generation of more sensitive gamma-ray instruments  
1150 begin operations, or until new dSphs with higher  $J$ -factors are discovered.

1151 This analysis serves as a proof of concept for future multi-instrument and multi-messenger  
1152 combination analyses. With this collaborative effort, we have managed to sample over four orders  
1153 in magnitude in gamma-ray energies with distinct observational techniques. Determining the nature  
1154 of DM continues to be an elusive and difficult problem. Larger datasets with diverse measurement  
1155 techniques could be essential to tackling the DM problem. A future collaboration using similar  
1156 techniques as the ones described in this paper could grow even beyond gamma rays. The models we  
1157 used for this study include annihilation channels with neutrinos in the final state. Advanced studies  
1158 could aim to merge our results with those from neutrino observatories with large data sets. Efforts  
1159 are already underway to add data from the IceCube, ANTARES, and KM3NeT observatories to  
1160 these gamma-ray results.

1161 From this work, a selection of the best candidates for observations, according to the latest  
1162 knowledge on stellar dynamics and modelling techniques for the derivation of the  $J$ -factors on  
1163 the potential dSphs targets, is highly desirable at the time that new experiments are starting their  
1164 dark matter programs using dSphs. Given the systematic uncertainty inherent to the derivation of  
1165 the  $J$ -factors, an informed observational strategy would be to select both objects with the highest  
1166  $J$ -factors that could lead to DM signal detection, and objects with robust  $J$ -factor predictions, i.e.

1167 with kinematic measurements on many bright stars, which would strengthen the DM interpretation  
1168 reliability of the observation outcome.

1169 This analysis combines data from multiple telescopes to produce strong constraints on astro-  
1170 physical objects. From this perspective, these methods can be applied beyond just DM searches.  
1171 Almost every astrophysical study can benefit from multi-telescope, multi-wavelength gamma-ray  
1172 studies. We have enabled these telescopes to study the cosmos with greater precision and detail.  
1173 Many astrophysical searches can benefit from multi-instrument gamma-ray studies, for which our  
1174 analysis lays the foundation.

## CHAPTER 6

### MULTITHREADING HAWC ANALYSES FOR DARK MATTER SEARCHES

#### 6.1 Introduction

HAWC's current software suite, plugins to 3ML and HAL [54, 42], do not fully utilize computational advancements of recent decades. Said advancements include the proliferation of Graphical Processing Units (GPUs), and multithreading on multicore processors. The analysis described in chapter 5 took up to 3 months of wall time waiting for the full gambit of data analysis and simulation of background to compute. Additionally, with the updated 2D energy binning scheme,  $f_{\text{hit}}$  and Neural Network (NN), the time needed to compute expected to grow. Although excessive computing time was, in part, from an intense use of a shared computing cluster, it was evident that there was room for improvement. In HAWC's next generation dSph DM search, I decided to develop codes that would utilize the multicore processors on modern high performance computing clusters. The results of this work are featured in this chapter and brought a human timing improvement to computation that scales approximately as  $1/N$  where  $N$  is the number of threads.

#### 6.2 Dataset and Background

This section enumerates the data and background methods used for HAWC's multithreaded study of dSphs. Section 6.2.1 and Section 6.2.2 are most useful for fellow HAWC collaborators looking to replicate a multithreaded dSph DM search.

##### 6.2.1 Itemized HAWC files

These files are only available within HAWC's internal documentation and collaborators. They are not meant for public access, and are presented here so that HAWC collaborators can reproduce results accurately.

- Detector Resolution: `refit-Pass5-Final-NN-detRes-zenith-dependent.root`
- Data Map: `Pass5-Final-NN-maptree-ch103-ch1349-zenith-dependent.root`
- Spectral Dictionary: `HDMspectra_dict_gamma.npy`

1199 **6.2.2 Software Tools and Development**

1200 This analysis was performed using HAL and 3ML [42, 43] in Python3. I built software  
1201 in collaboration with Michael Martin and Letrell Harris to implement the *Dark Matter Spectra*  
1202 *from the Electroweak to the Planck Scale* (HDM) [65] and dSphs spatial model from [66] for  
1203 HAWC analysis. A NumPy dictionary of HDM, `HDMspectra_dict_gamma.npy`, was made for  
1204 portability within the collaboration. These dictionaries were generated from the [git repository](#) [65].  
1205 The analysis was performed using the Neural Network energy estimator for Pass 5.F. A description  
1206 of this estimator was provided in chapter 3. [TODO: Define a subsection when it's written](#), and its  
1207 key, relevant improvements are an improved energy estimation and improved sensitivities at higher  
1208 zenith angles. All other software used for data analysis, DM profile generation, and job submission  
1209 to SLURM are also kept in my sandbox in the [Dark Matter HAWC](#) project. The above repository  
1210 also incorporates the model inputs used previously in Glory Duck, described in chapter 5, so Glory  
1211 Duck remains compatible with modern software.

1212 **6.2.3 Data Set and Background Description**

1213 The HAWC data maps used for this analysis contain 2565 days of data between runs 2104 and  
1214 7476. They were generated from pass 5.f reconstruction. The analysis is performed using the NN  
1215 energy estimator with bin list:

1216 `B1C0Ea, B1C0Eb, B1C0Ec, B1C0Ed, B1C0Ee, B2C0Ea, B2C0Eb, B2C0Ec, B2C0Ed, B2C0Ee,`  
1217 `B3C0Ea, B3C0Eb, B3C0Ec, B3C0Ed, B3C0Ee, B3C0Ef, B4C0Eb, B4C0Ec, B4C0Ed, B4C0Ee,`  
1218 `B4C0Ef, B5C0Ec, B5C0Ed, B5C0Ee, B5C0Ef, B5C0Eg, B6C0Ed, B6C0Ee, B6C0Ef, B6C0Eg,`  
1219 `B6C0Eh, B7C0Ee, B7C0Ef, B7C0Eg, B7C0Eh, B7C0Ei, B8C0Ee, B8C0Ef, B8C0Eg, B8C0Eh,`  
1220 `B8C0Ei, B8C0Ej, B9C0Ef, B9C0Eg, B9C0Eh, B9C0Ei, B9C0Ej, B10C0Eg, B10C0Eh,`  
1221 `B10C0Ei, B10C0Ej, B10C0Ek, B10C0El`

1222 Bin 0 was excluded as it has substantial hadronic contamination and poor angular resolution.

1223 Background considerations and source selection was identical to Section 5.2.3, and no additional  
1224 arguments are provided here. Many of the HAWC systematics explored in Section 5.7 also apply

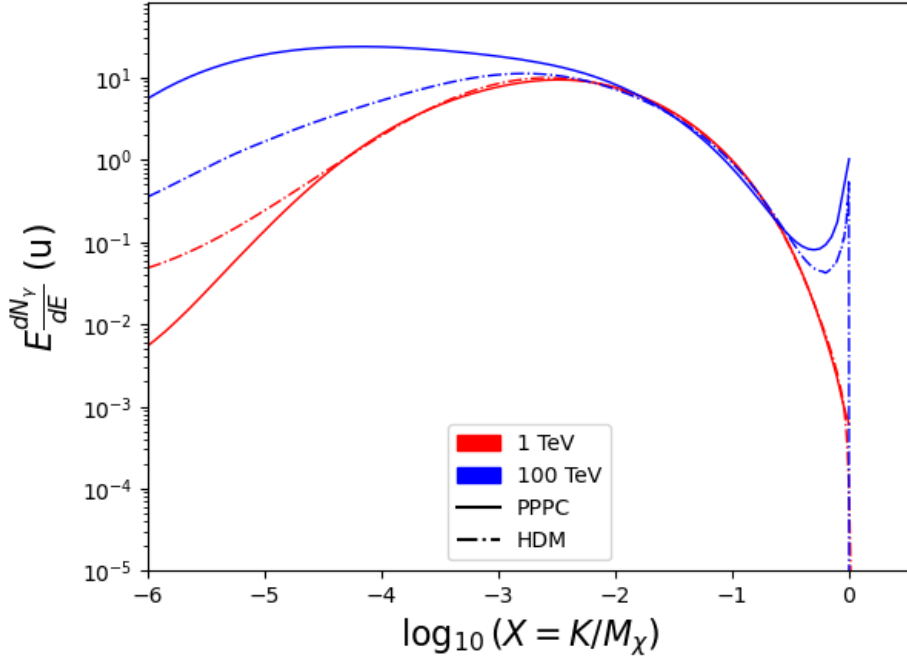


Figure 6.1 Spectral hypotheses from PPPC [44] and HDM [65] for DM annihilation:  $\chi\chi \rightarrow W^-W^+$ . Solid lines are spectral models with EW corrections from the PPPC. Dash-dot lines are spectral models from HDM. Red lines are models for  $M_\chi = 1$  TeV. Blue lines represent models for  $M_\chi = 100$  TeV.

1225 for this DM search and are not added upon here.

### 1226 6.3 Analysis

1227 The analysis and its systematics are almost identical to Section 5.3. Importantly, we use the  
 1228 same [TODO: fix this ref](#) Equation (7.1) and Equation (5.2) for estimating the gamma-ray flux at  
 1229 HAWC from our sources.

#### 1230 6.3.1 $\frac{dN_\gamma}{dE_\gamma}$ - Particle Physics Component

1231 For these spectra, we import HDM with Electroweak (EW) corrections and additional correc-  
 1232 tions for neutrinos above the EW scale [65]. The spectra are implemented as a model script in  
 1233 astromodels for 3ML. A comprehensive description of EW corrections and neutrino considerations  
 1234 are provided later in Sec. 8.

1235 Figure 6.1 demonstrates the impact of changes implemented in HDM on DM annihilation to W  
 1236 bosons. A class in astromodels was developed to include HDM and is aptly named `HDMspectra`  
 1237 within `DM_models.py`. The SM DM annihilation channels studied here are  $\chi\chi \rightarrow:$

1238       $e^+e^-$ ,  $\mu^+\mu^-$ ,  $\tau^+\tau^-$ ,  $b\bar{b}$ ,  $t\bar{t}$ ,  $gg$ ,  $W^+W^-$ ,  $ZZ$ ,  $c\bar{c}$ ,  $u\bar{u}$ ,  $d\bar{d}$ ,  $s\bar{s}$ ,  $\nu_e\bar{\nu}_e$ ,  $\nu_\mu\bar{\nu}_\mu$ ,  $\nu_\tau\bar{\nu}_\tau$ ,  $\gamma\gamma$ ,  $hh$ .

1239 For  $\gamma\gamma$  and  $ZZ$ , a substantial fraction of the signal photons are expected to have  $E_\gamma = m_\chi$  [65].  
 1240 This introduces  $\delta$ -function that is much narrower than the energy resolution of the HAWC detector.  
 1241 To ensure that this feature is not lost in the likelihood fits, the 'line' feature is convolved with a  
 1242 Gaussian kernel with a  $1\sigma$  width of  $0.05 \cdot m_\chi$  and total kernel window of  $\pm 4\sigma$ . This differs from  
 1243 HAWC's previous line study where 30% of HAWC's energy resolution was used for the kernel [67].  
 1244 The NN energy estimator's strength compared to  $f_{\text{hit}}$  at low gamma-ray energy enables narrower  
 1245 kernels [65].  $\chi\chi \rightarrow \gamma\gamma$  and  $ZZ$  spectral hypotheses are shown in Figure 6.2. We did not explore  
 1246 how well we reconstruct injected signal events for various kernels widths. This is a systematic  
 1247 that should be tested before publication to journal. Spectral models for the remaining annihilation  
 1248 channels are plotted for each  $m_\chi$  in Figure B.1.

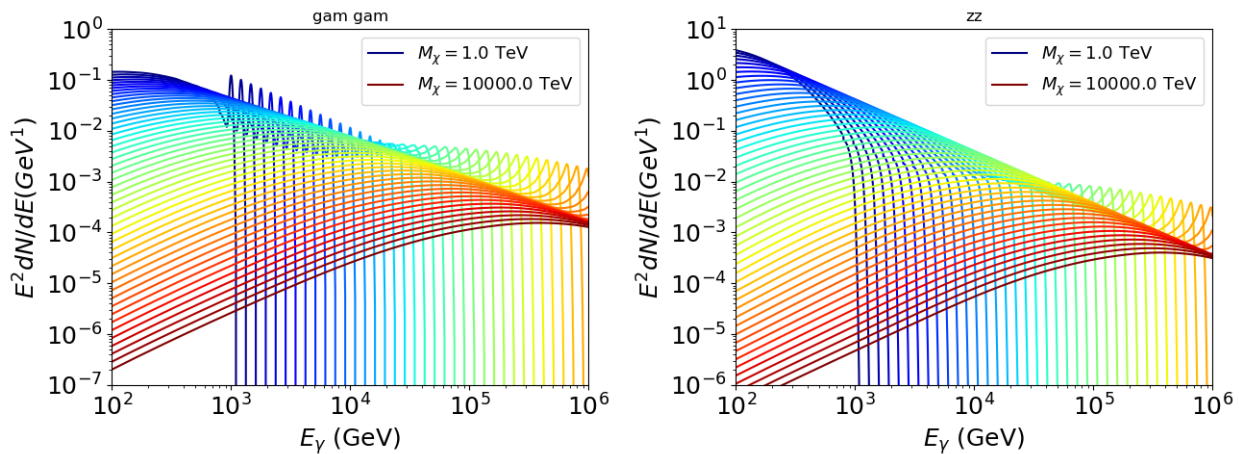


Figure 6.2 Photon spectra for  $\chi\chi \rightarrow \gamma\gamma$  (left) and  $\chi\chi \rightarrow ZZ$  (right) after Gaussian convolution of line features. Both spectra have  $\delta$ -features at photon energies equal to the DM mass. Bluer lines are annihilation spectra with lower DM mass. Redder lines are spectra from larger DM mass. All spectral models are sourced from the Heavy Dark Matter models [65]. Axes are drawn roughly according to the energy sensitivity of HAWC.

1249 **6.3.2 J Astrophysical Components**

1250 The J-factor profiles for each source are imported from Louis Strigari et al. (referred to with  
 1251  $\mathcal{LS}$ ) [66]. The  $\mathcal{LS}$  catalog fits a Navarro–Frenk–White (NFW) [48] spatial DM distributions to

1252 the dSphs which has a DM density of

$$\rho(r) = \frac{\rho_0}{\frac{r}{R_s} \left(1 + \frac{r}{R_s}\right)^2}. \quad (6.1)$$

1253  $\rho_0$  and the scale radius,  $R_s$  are free parameters fit for each dSph.  $r$  is the distance from the center  
1254 of the dSph.

1255 Profiles in  $\frac{dJ}{d\Omega}(\theta)$  up to an angular separation  $\theta = 0.5^\circ$  were provided directly from the authors.

1256 Map generation from these profiles were almost identical to Section 5.3.2 except that a higher order  
1257 trapezoidal integral was used for the normalization of the square, uniformly-spaced map:

$$p^2 \cdot \sum_{i=0}^N \sum_{j=0}^M w_{i,j} \frac{dJ}{d\Omega}(\theta_{i,j}, \phi_{i,j}) \quad (6.2)$$

1258  $p$  is the angular side of one pixel in the map.  $w_{i,j}$  is a weight assigned the following ways:

1259  $w_{i,j} = 1$  if  $(\theta_{i,j}, \phi_{i,j})$  is fully within the region of integration

1260  $w_{i,j} = 1/2$  if  $(\theta_{i,j}, \phi_{i,j})$  is on an edge of the region of integration

1261  $w_{i,j} = 1/4$  if  $(\theta_{i,j}, \phi_{i,j})$  is on a corner of the region of integration

1262 Figure 6.3 shows the median and  $\pm 1\sigma$  maps used as input for this DM annihilation study.

### 1263 6.3.3 Source Selection and Annihilation Channels

1264 HAWC's sources for this multithreaded analysis include Coma Berenices, Draco, Segue 1, and  
1265 Sextans.  $\mathcal{LS}$  observed up to 43 sources in its publication, however only 4 of the best fit profiles  
1266 were provided at the time this thesis was written. A full description of each source used in this  
1267 analysis is found in Table 6.1.

1268 This analysis improves on chapter 5 in the following ways. Previously, the particle physics  
1269 model used for gamma-ray spectra from DM annihilation was from the PPPC [44] which missed  
1270 important considerations relevant for the neutrino sector. HDM is used to account for this shortfall  
1271 [65]. HDM also models DM to the Planck scale which permits HAWC to probe PeV scale DM. For  
1272 this study, we sample DM masses: 1 TeV - 10 PeV with 6 mass bins per decade in DM mass. In

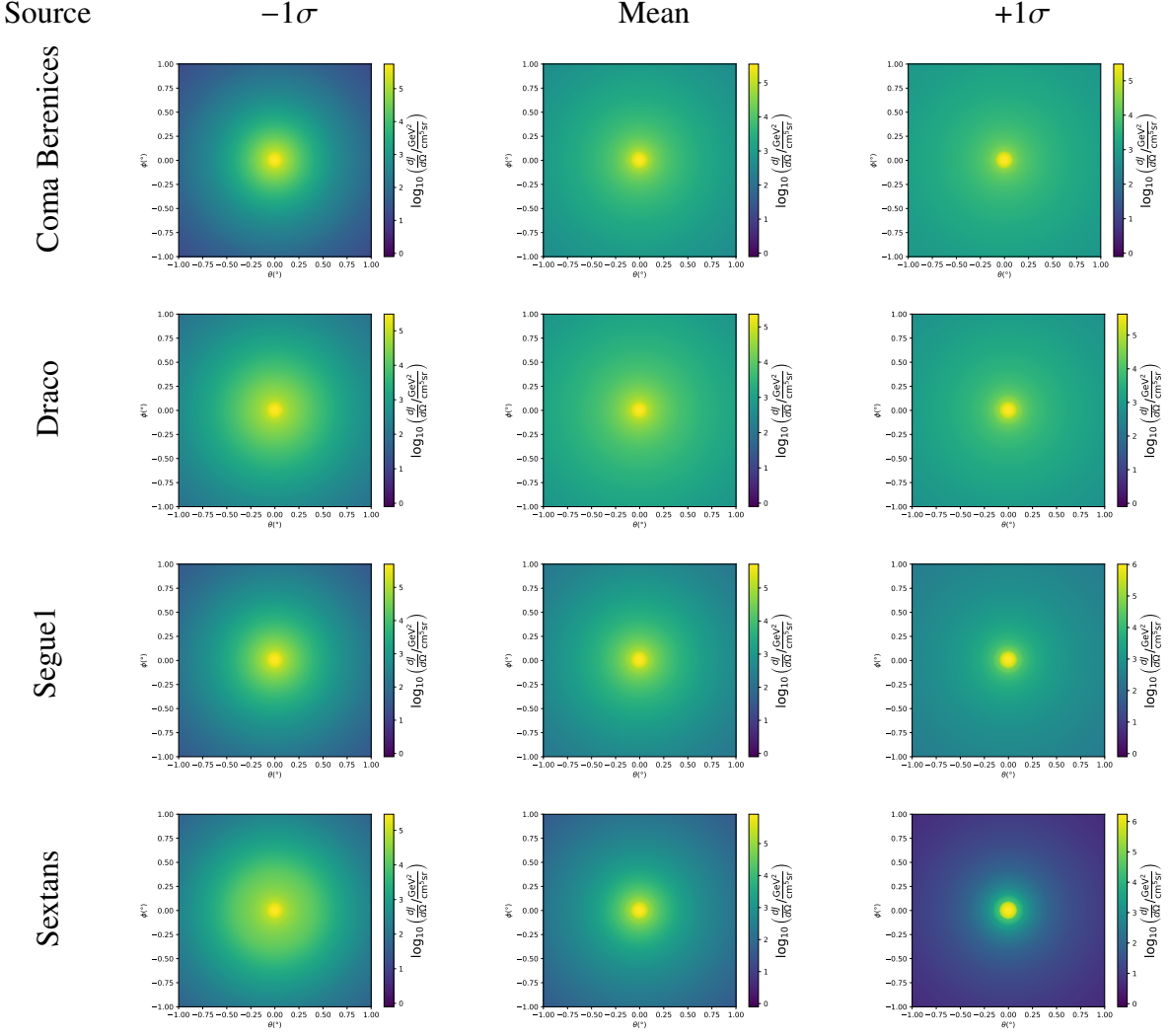


Figure 6.3  $\frac{dJ}{d\Omega}$  maps for Coma Berenices, Draco, Segue1, and Sextans. Columns are divided for the  $\pm 1\sigma$  uncertainties in  $dJ/d\Omega$  around the mean value from  $\mathcal{LS}$  [66]. Origin is centered on the specific dwarf spheroidal galaxies (dSph).  $\theta$  and  $\phi$  axes are the angular separation from the center of the dwarf. Profiles are truncated at  $1^\circ$  and flattened beyond.

1273 the case of line spectra ( $\chi\chi \rightarrow \gamma\gamma$ , or  $ZZ$ ), we double the mass binning to 12 DM mass bins per  
 1274 decade in DM mass.

1275  $\mathcal{LS}$  provides 25 sources within HAWC's field of view. Additionally, NFW [48] DM distributions  
 1276 have fewer parameters than Zhao [47], so  $\mathcal{LS}$  fits ultra-faint dwarves which expands the number of  
 1277 sources. However, all sources were not provided by the authors in time for the completion of this  
 1278 dissertation. Finally, the gamma-ray ray dataset is much larger. The study performed here analyzes  
 1279 2565 days of data compared to 1017 days analyzed in chapter 5.

1280 **6.4 Likelihood Methods**

1281 These are identical to Section 5.4.1 and no additional changes are made to the likelihood. Bins  
 1282 in this analysis are expanded to include HAWC’s NN energy estimator.

1283 **6.5 Computational Methods: Multithreading**

1284 Previously, as in Section 5.3, the likelihood was minimized for one model at a time. One model  
 1285 in this case representing a DM annihilation channel (CHAN), DM mass ( $m_\chi$ ), and dSph ((SOURCE)).  
 1286 In an effort to conserve human and CPU time, jobs submitted for high performance computing  
 1287 contained a list of  $m_\chi$  to iterate over for likelihood fitting. Jobs were then trivially parallelized  
 1288 for each permutation of the two lists: CHANS and SOURCES. The lists for CHANS and SOURCES are  
 1289 found in Section 6.3.1 and Table 6.1, respectively. Initially, 11  $m_\chi$  were serially sampled for one  
 1290 job defined by a [CHAN, SOURCE] tuple. Computing the likelihoods would take between 1.5 to 2 hrs,  
 1291 stochastically, for a job. We expect to compute likelihoods for data and 300 Poisson background  
 1292 trials. The estimated CPU time based on the above for all CHAN (N = 17) and SOURCE (M = 25)  
 1293 was estimated to 127,925 jobs. In total, 1,407,175 likelihood fits and profiles would be computed  
 1294 for the 11 mass bins we wished to study. The estimated CPU time ranged between 8k CPU days  
 1295 to 10k CPU days. Human time is more challenging to estimate as job allocation is stochastic and  
 1296 highly dependent on what other users are submitting. Yet, it is unlikely that all jobs would run  
 1297 simultaneously. Therefore, we can expect human time to be about as long as was seen in chapter 5

| Name           | Distance<br>(kpc) | $l, b$<br>( $^\circ$ ) | $\log_{10} J$ ( $\mathcal{LS}$ set)<br>$\log_{10}(\text{GeV}^2 \text{cm}^{-5} \text{sr})$ |
|----------------|-------------------|------------------------|---|
| Coma Berenices | 44                | 241.89, 83.61          | $19.00^{+0.36}_{-0.35}$   |
| Draco          | 76                | 86.37, 34.72           | $18.83^{+0.12}_{-0.12}$   |
| Segue I        | 23                | 220.48, 50.43          | $19.12^{+0.49}_{-0.58}$   |
| Sextans        | 86                | 243.50, 42.27          | $17.73^{+0.13}_{-0.12}$   |

Table 6.1 Summary of the relevant properties of the dSphs used in the present work. Column 1 lists the dSphs. Columns 2 and 3 present their heliocentric distance and galactic coordinates, respectively. Column 4 reports the  $J$ -factors of each source given from the  $\mathcal{LS}$  studies and estimated  $\pm 1\sigma$  uncertainties. The values  $\log_{10} J$  ( $\mathcal{LS}$  set) [66] correspond to the mean  $J$ -factor values for a source extension truncated at  $0.5^\circ$ .

1298 which was on the order of months to fully compute on a smaller analysis. A visual aid to describe  
 1299 how jobs were organized is provided in Figure 6.4.

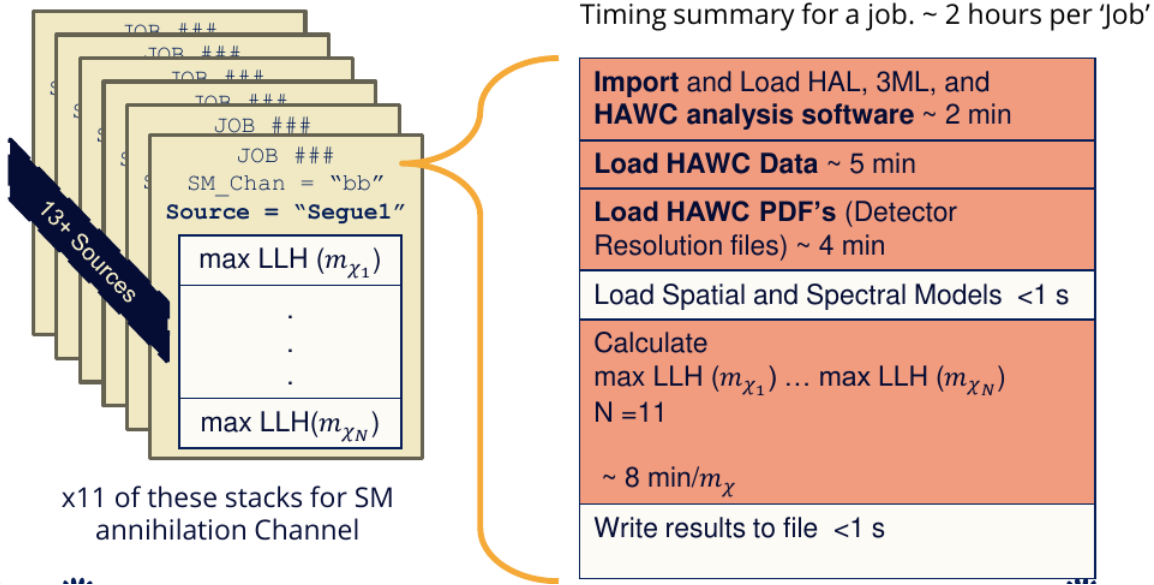


Figure 6.4 Infographic on how jobs and DM computation was organized in Section 5.3. Jobs were built for each permutation of CHANS and SOURCES shown by the left block in the figure. Each job, which took on the order 2 hrs to compute, had the following work flow: 1. Import HAWC analysis software, 2 min to run. 2. Load HAWC count maps, 5 min to run. 3. Load HAWC energy and spatial resolutions, 4 min. 5. Load DM spatial source templates and spectral models, less than 1 s. 6. Perform likelihood fit on data and model, about 8 min per DM mass. 7. Write results to file, less than 1s.

1300 The computational needs for this next generation DM analysis are extreme and is unlike other  
 1301 analyses performed on HAWC. It became clear that there was a lot to gain from optimizing how  
 1302 the likelihoods are computed. This section discusses how multi-threading was applied to solve and  
 1303 reduce HAWC's computing of likelihoods for large parameter spaces like in DM searches.

### 1304 6.5.1 Relevant Foundational Information

1305 The profiling of the likelihood for HAWC is done via gradient descent where the normalization  
 1306 of Equation (7.1) (linearly correlated with  $\langle \sigma v \rangle$ ) is rescaled in the descent. Additionally, we sample  
 1307 the likelihood space for a defined list of  $\langle \sigma v \rangle$ 's described in Section 5.4.2. The time to compute  
 1308 these values is not predictable or consistent because many variables can change across the full  
 1309 model-space. Comprehensively, these variables are:

1310     •  $m_\chi$  : DM rest mass  
 1311     • CHAN : DM annihilation channel in SM.  
 1312     • SOURCE : dSph. Involves a spatial template AND coordinate in HAWC data.  
 1313     •  $\langle\sigma v\rangle$ : Effectively the flux normalization and free parameter in the likelihood fit.  
 1314 Therefore, we develop an asynchronous, functional-parallel coding pattern. Asynchronous meaning  
 1315 the instructions within a function are independent and permitted to be out of sync with sibling  
 1316 computations. Functional-parallel meaning that instructions are the subject of parallelization  
 1317 rather than threading the likelihood computation. This is close to trivial parallelization seen in  
 1318 Figure 6.4 except that we seek to consolidate the loading stages (software, data, and detector  
 1319 resolution loading). Multiple asynchronous threads are expected to reduce total serial processing  
 1320 time and total overhead across the entire project in addition to saving human time.

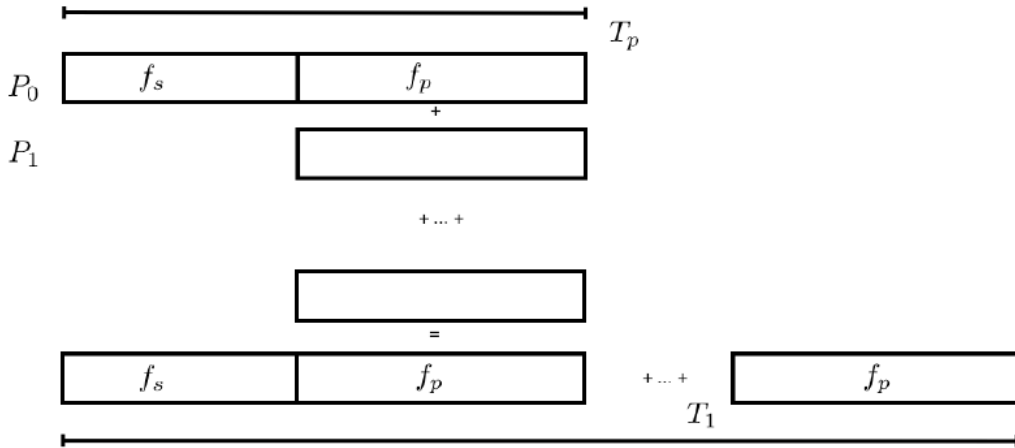


Figure 6.5 Graphic of Gustafson parallel coding pattern.  $f_s$  is the fraction of a program, in time, spent on serial computation.  $f_p$  is the fraction of computing time that is parallelizable.  $T_p$  is the total time for a parallel program to run.  $T_1$  is the total time for a parallel program to run if only 1 processor is allocated.  $P_N$  is the  $N$ -th processor where it's row is the computation the processor performs. The Gustafson pattern is most similar to what is implemented for this analysis. Figure is pulled from [68].

1321 We need a way to measure and compare the expected speedup and efficiency gain for this  
 1322 asynchronous coding pattern. I pull inspiration for timing measurement from [68] and use *Amdahl's*

1323 law with hybrid programming. Hybrid programming meaning that the computation is a mix of  
 1324 distributed and shared memory programming. If we assume the code is fully parallelizable over  $p$   
 1325 processors and  $c$  threads, the ideal speedup is simply  $pc$ , and ideal run-time is  $T_1/(pc)$ .  $T_1$  is the  
 1326 total time for a parallel program to run if only 1 processor is allocated. However, the coding pattern  
 1327 contains some amount of unavoidable serial computation, as shown in Figure 6.5. In our case, the  
 1328 run time,  $T_{p,c}$ , is estimated to be

$$T_{p,c} = \frac{T_1}{pc} (1 + F_s(c - 1)). \quad (6.3)$$

1329  $F_s$  is the fraction of CPU time dedicated to serial computation. The expected speedup,  $S_{p,c}$ , is

$$S_{p,c} \equiv \frac{T_1}{T_{p,c}} = \frac{pc}{1 + F_s(c - 1)}. \quad (6.4)$$

1330 From Equation (6.4), we can see that the speed-up scales with  $p/F_s$ . We are free to minimize  $F_s$   
 1331 asymptotically by enlarging the total models that are submitted to the thread pool, thereby shrinking  
 1332 the CPU fraction dedicated to serial operation. We are also free to define exactly how many threads  
 1333 and processors we utilize, yet eventually hit a hard cap at the hardware available on our computing  
 1334 cluster. HAWC uses Intel Xeon™processors with 48 cores and 96 threads. We see that a successful  
 1335 code will scale well as the expected speedup is inversely correlated with  $F_s$ . As the total number  
 1336 of models sampled grows, the speedup will also.

### 1337 6.5.2 Implementation

1338 The multithreaded code was written in Python3 and is documented in the `dark_matter_hawc`  
 1339 [repository](#) within the script named `mpu_analysis.py`. A version of the script as of April 25  
 1340 **TODO: make sure to update on this date** is also provided in Section B.2. It has many dependencies  
 1341 including the HAWC analysis software. Figure 6.6 displays the workflow of a job with 3 threads.  
 1342 Within a job, SOURCE is kept fixed and CHANS remains 17 elements long. More  $m_\chi$  are sampled  
 1343 from 11 bins up to 49 (for  $\gamma\gamma$  and ZZ) and 25 (for remaining CHANS) which amounts to 12 or 6  
 1344 mass bins per decade.  $m_\chi$  and CHANS are permuted into a 473 element list which is split evenly  
 1345 across N threads where N is [2, 8, 16]. For each  $m_\chi$ -CHAN tuple, 1001  $\langle\sigma v\rangle$  values are sampled in

Timing summary for a multi-threaded job.

|  |  |  |
|--|--|--|
| Import and Load HAL, 3ML, and <b>HAWC analysis software</b> ~ 2 min  |  |  |
| Load HAWC Data ~ 5 min   |  |  |
| Load HAWC PDF's (Detector Resolution files) ~ 4 min  |  |  |
| Load Spatial Model < 1s  |  |  |
| Load Spectra Models <1 s   | Load Spectra Models <1 s   | Load Spectra Models <1 s   |
| Calculate<br>max LLH (Chan_0, $m_{\chi_1}$ ) ...<br>max LLH (Chan_?, $m_{\chi_N}$ )<br>N = TOTAL/N_THREADS<br><br>~ 8 min/Spec_model | Calculate<br>max LLH (Chan_?, $m_{\chi_1}$ ) ...<br>max LLH (Chan_?, $m_{\chi_N}$ )<br>N = TOTAL/N_THREADS<br><br>~ 8 min/Spec_model | Calculate<br>max LLH (Chan_?, $m_{\chi_1}$ ) ...<br>max LLH (Chan_?, $m_{\chi_N}$ )<br>N = TOTAL/N_THREADS<br><br>~ 8 min/Spec_model |
| Write results to file <1 s   | Write results to file <1 s   | Write results to file <1 s   |
| Join Threads and terminate < 1s  |  |  |

Figure 6.6 Task chart for one multithreaded job developed for this project. Green blocks indicate a shared resource across the threads AND computation performed serially. Red blocks indicate functional parallel processing within each thread. 3 threads are represented here, yet many more can be employed during the full analysis. Jobs are defined by the SOURCE as these require unique maps to be loaded into the likelihood estimator. The  $m_{\chi}$ , CHAN, and  $\langle \sigma v \rangle$  variables are entered into the thread pool and allocated as evenly as possible across the threads.

- 1346 the likelihood, and the value of  $\langle \sigma v \rangle$  that maximizes the likelihood is found. Although rare, fits  
 1347 that failed are handled on a case by case basis.

### 1348 6.5.3 Performance

| M Tasks | $T_{p,c}$ (hr:min:s) |           |           |            |
|---------|----------------------|-----------|-----------|------------|
|         | $T_{1,1}$            | $T_{1,2}$ | $T_{1,8}$ | $T_{1,16}$ |
| 50      | 1:40:37.5            | 0:52:43.7 | 0:19:13.8 | 0:13:44.0  |
| 74      | 2:22:30.0            | 1:15:00.6 | 0:25:21.3 | 0:15:49.8  |
| 100     | (3:07:51.9)          | 1:40:10.5 | 0:30:44.4 | 0:20:01.4  |
| 200     | (6:02:20.6)          | -         | 1:00:32.0 | 0:30:35.0  |
| 473     | (13:58:40.3)         | -         | 2:01:41.4 | 1:07:53.2  |

Table 6.2 Timing summaries for analyses for serial and multithreaded processes. M tasks is the number of functional-parallel tasks ran for the computation.  $T_{p,c}$  is a single run time in hours:minutes:seconds for runs utilizing  $p$  nodes and  $c$  threads. Runs are run interactively on the same computer to maximize consistency. Empty entries are indicated with '-'. (·) entries are estimated entries extrapolated from data earlier in the column.

- 1349 We see a significant reduction to wall time needed for our dSph analyses to run. Table 6.2

1350 shows the timing summaries for analyses of different sizes and thread counts. Additionally, the  
 1351 efficiency gained when consolidating the serial loading of data is also apparent in our ability to  
 1352 study many more tasks in about the same amount of wall time as a smaller serial computation. Trials  
 1353 represented in the table were run on an AMD Opteron® processor 6344 with 48 cores, 2 threads per  
 1354 core; 2.6 GHz clock. This is not the same architecture used for analysis on the HAWC computing  
 1355 cluster however they are similar enough that results shown here are reasonably representative of  
 1356 computing on the HAWC computing cluster. I use Tab. 6.2 for the inferences and conclusions in  
 1357 the following paragraphs.

1358 First, we want to find  $T_s$ , the time of serial computation. From Fig. 6.5, the timing for our  
 1359 coding pattern can be written as

$$T_s + Mt_p = T_{1,1}^M. \quad (6.5)$$

1360  $M$  is the number of functional-parallel tasks (represented as column 1 of Tab. 6.2), and  $t_p$  is the  
 1361 average time to complete a single parallel task.  $T_{1,1}^M$  is the total time for a parallel program to run if  
 1362 only 1 processor is allocated for  $M$  parallel task. With two runs of different  $M$  ( $M_1$  and  $M_2$ ), we  
 1363 can use a system of equations to compute

$$T_s = 803.1\text{s} \text{ and } t_p = 104.6\text{s} \quad (6.6)$$

1364 Now, we have specific estimation for the fraction of serial computing time,  $F_s$ :

$$F_s = \frac{803.1}{803.1 + 104.6 \cdot M}. \quad (6.7)$$

1365 The maximum  $M$  for this study is 473 which evaluates to:  $F_s = 0.016$  or 1.6% of computing time.  
 1366 Table 6.3 shows the resulting speedups.

1367 We see a speedup that generally exceeds expectations from Eq. (6.4) for real trail runs. We also  
 1368 see that there are diminishing returns as the number of threads increases. For small jobs with large  $c$ ,  
 1369 both the expected and observed speedup are significantly smaller than  $c$ . One thing not considered  
 1370 in Eq. (6.4) is the time incurred via communication latency. Communication latency increases  
 1371 with the number of threads and contributes to diminishing returns. Additionally, these values are

| M Tasks | $F_s$    | $S_{1,2}$   | $S_{1,8}$   | $S_{1,16}$    |
|---------|----------|-------------|-------------|---------------|
| 50      | 1.33 E-1 | 1.90 [1.76] | 5.23 [4.14] | 6.35 [5.34]   |
| 74      | 9.40 E-2 | 1.90 [1.83] | 5.62 [4.82] | 9.00 [6.64]   |
| 100     | 7.13 E-2 | 1.88 [1.87] | 6.11 [5.34] | 9.38 [7.73]   |
| 200     | 3.70 E-2 | - [1.93]    | 5.98 [6.36] | 11.85 [10.29] |
| 473     | 1.60 E-2 | - [1.97]    | 6.89 [7.20] | 12.35 [12.91] |

Table 6.3 Speed up summaries for analyses for serial and multithreaded processes. M tasks is the number of functional-parallel tasks ran for the computation.  $S_{p,c}$  is a single speedup comparison for runs utilizing  $p$  nodes and  $c$  threads. [·] are the estimated speedups calculated from Tab. 6.2, Eq. (6.7), and Eq. (6.4). Empty entries are indicated with '-'.

1372 for single runs and do not consider the stochastic variation expected in a shared high performance  
 1373 computing resource. Therefor, these results are not strictly conclusive, yet demonstrate the merits  
 1374 of multi-threading. We see very clearly that there is a lot to gain, and this new coding pattern will  
 1375 expand HAWC's analysis capabilities.

## 1376 6.6 Analysis Results

1377 3 of the 43  $\mathcal{L}\mathcal{S}$  dSphs considered for the multithreaded analysis. These dSph are analyzed  
 1378 for emission from DM annihilation according to the likelihood method described in Section 5.4.  
 1379 The three likelihood profiles are then stacked to synthesize a combined limit on the dark matter  
 1380 annihilation cross-section,  $\langle\sigma v\rangle$ . This combination is done each of the 17 SM annihilation channels.  
 1381 Figure 6.7 and Fig. 6.8 show the combined limits for all annihilation channels with HAWC's  
 1382 observations. Test statistics of the best fit  $\langle\sigma v\rangle$  values for each  $m_\chi$  and CHAN are shown in Fig. 6.9  
 1383 and Fig. 6.10. We also compare these limits to HAWC's Glory Duck limits shown in Section 5.5.  
 1384 The comparison to Glory Duck are featured in Fig. 6.11 for all the DM annihilation channels studied  
 1385 for Glory Duck. A full comparison is provided in the appendix in Fig. B.2, Fig. B.3, and Fig. B.4.  
 1386 Here, we show updated limits for  $\chi\chi \rightarrow b\bar{b}, e\bar{e}, \mu\bar{\mu}, \tau\bar{\tau}, t\bar{t}, W^+W^-$ ,  $\gamma\gamma$  and  $ZZ$ . For the first time  
 1387 ever, we show limits for  $\chi\chi \rightarrow c\bar{c}, s\bar{s}, u\bar{u}, d\bar{d}, \nu_e\bar{\nu}_e, \nu_\mu\bar{\nu}_\mu, \nu_\tau\bar{\nu}_\tau, gg$ , and  $hh$ .

1388 No DM was found in HAWC observations. The largest excess found in HAWC data was for DM  
 1389 annihilating to  $W$ -bosons or  $\nu_e\bar{\nu}_e$  for  $m_\chi = 10$  TeV at significance  $2.11\sigma$  and  $2.14\sigma$  respectively.  
 1390 HAWC's limits and excesses are dominated by Segue1. Coma Berenices shows excesses at higher  
 1391 DM mass, yet no similar excesses were observed in Segue1 or Sextans. Sextans did not contribute

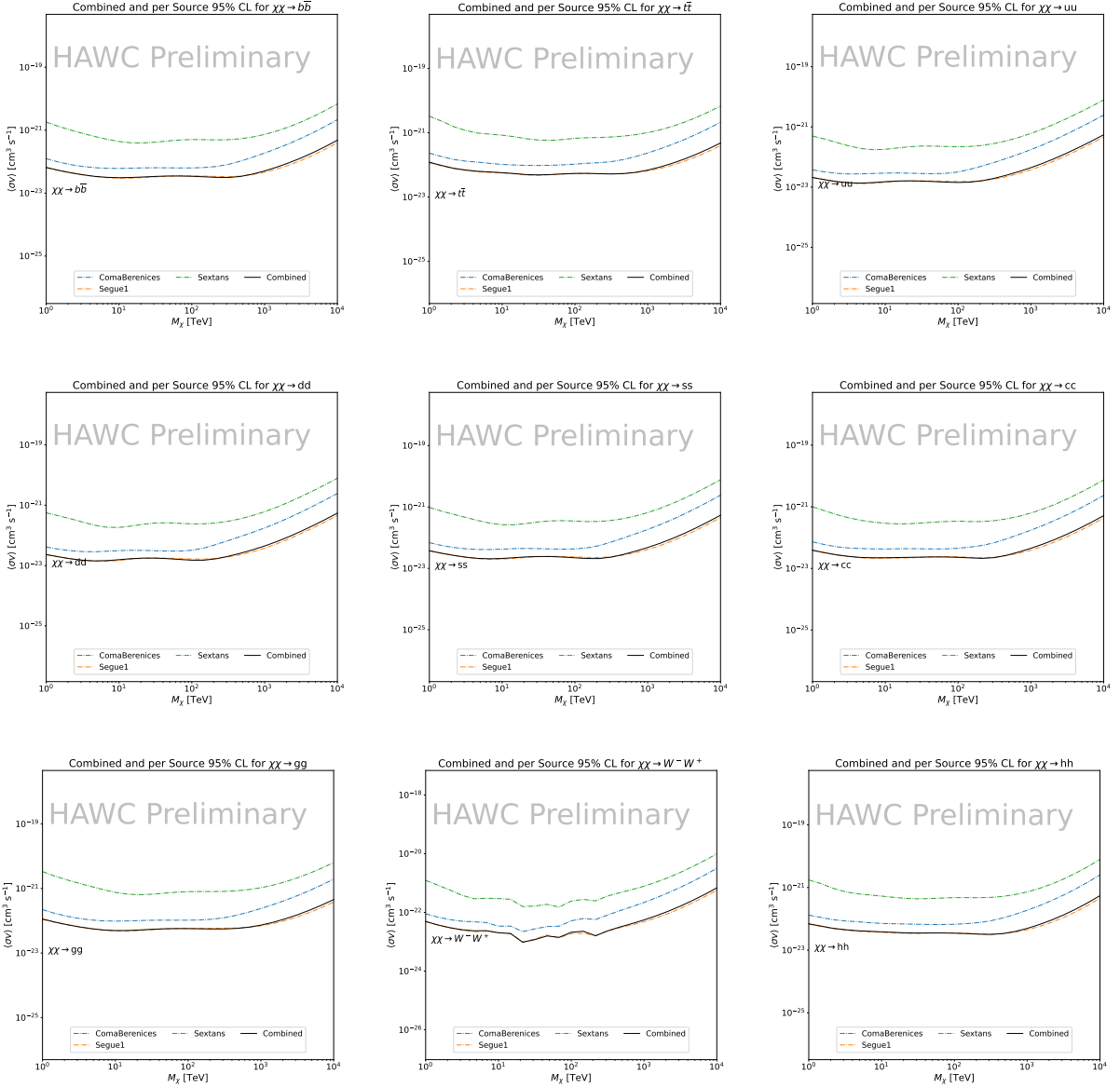


Figure 6.7 HAWC upper limits at 95% confidence level on  $\langle\sigma v\rangle$  versus  $m_\chi$  for  $\chi\chi \rightarrow b\bar{b}$ ,  $t\bar{t}$ ,  $u\bar{u}$ ,  $d\bar{d}$ ,  $s\bar{s}$ ,  $c\bar{c}$ ,  $gg$ ,  $W^+W^-$ , and  $hh$ . Limits are with  $\mathcal{L}\mathcal{S}$   $J$ -factors [66]. The solid line represents the observed combined limit. Dashed lines represent limits from individual dSphs.

1392 significantly to signal excesses or the combined limit as it is at high zenith. Draco was not included  
 1393 as the PDF of some of our analysis bins were wider than what is reasonable for a point source  
 1394 analysis. Draco is at a high zenith for HAWC, so the effort required to include it was not justified  
 1395 by the benefits.

1396 We did not generate background trials in time of writing this thesis. These are not shown and

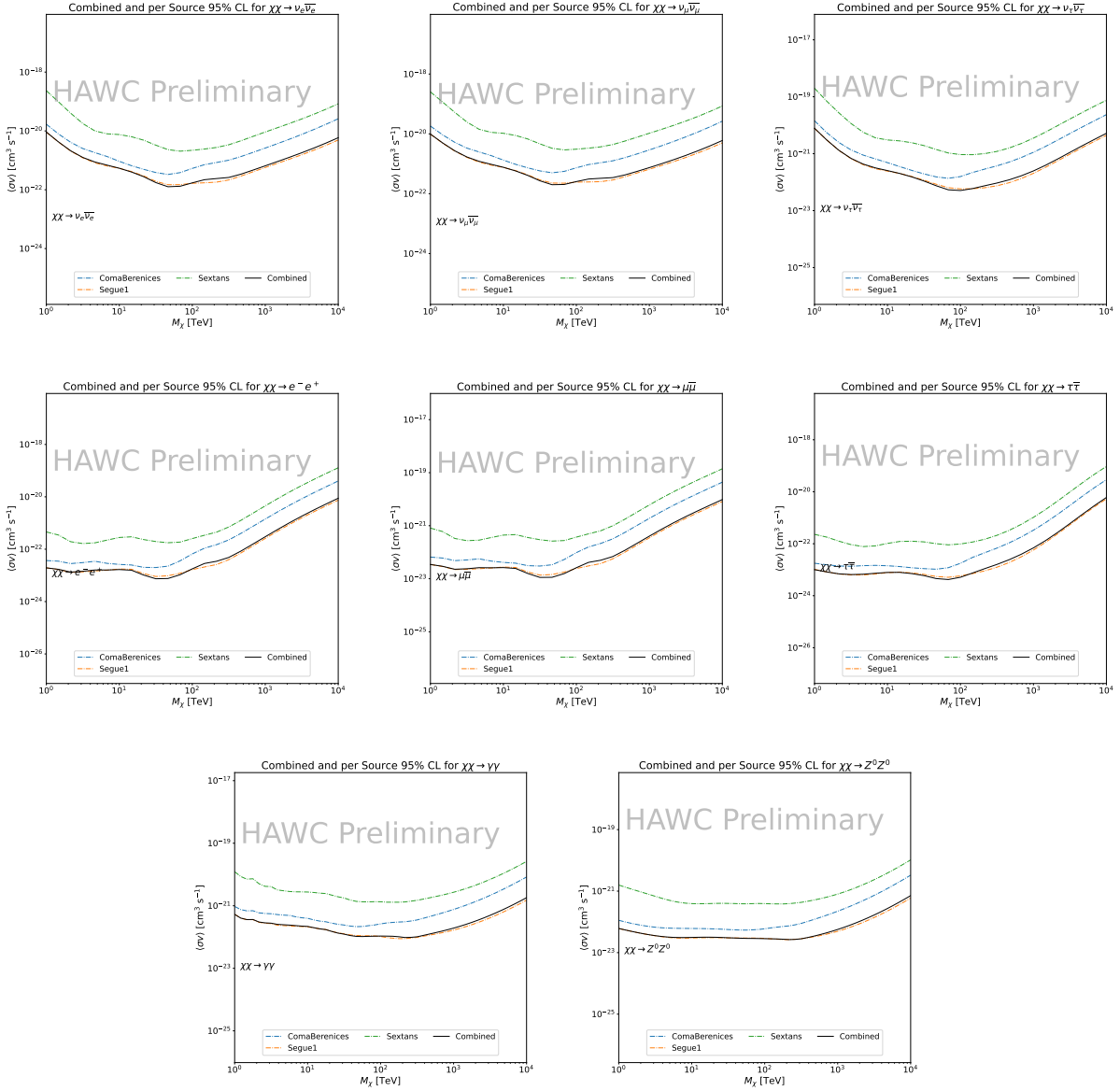


Figure 6.8 HAWC upper limits at 95% confidence level on  $\langle\sigma v\rangle$  versus  $m_\chi$  for  $\chi\chi \rightarrow \nu_e \bar{\nu}_e$ ,  $\nu_\mu \bar{\nu}_\mu$ ,  $\nu_\tau \bar{\nu}_\tau$ ,  $e \bar{e}$ ,  $\mu \bar{\mu}$ ,  $\tau \bar{\tau}$ ,  $\gamma\gamma$  and  $ZZ$ . Limits use  $\mathcal{L}S$   $J$ -factors [66]. The solid line represents the observed combined limit. Dashed lines represent limits from individual dSphs.

1397 are an immediate next step for this analysis before publication.

1398 When comparing these results to Section 5.5, we see an overall decrease to the confidence limit  
 1399 therefore improvement to HAWC's expected sensitivity. This improvement is generally stronger  
 1400 than a doubling of data, or a factor  $\sqrt{2}$  decrease. The comparison is somewhat complex and  
 1401 dependent on the dSph and SM annihilation channel. Figure 6.11 shows the comparisons of limits

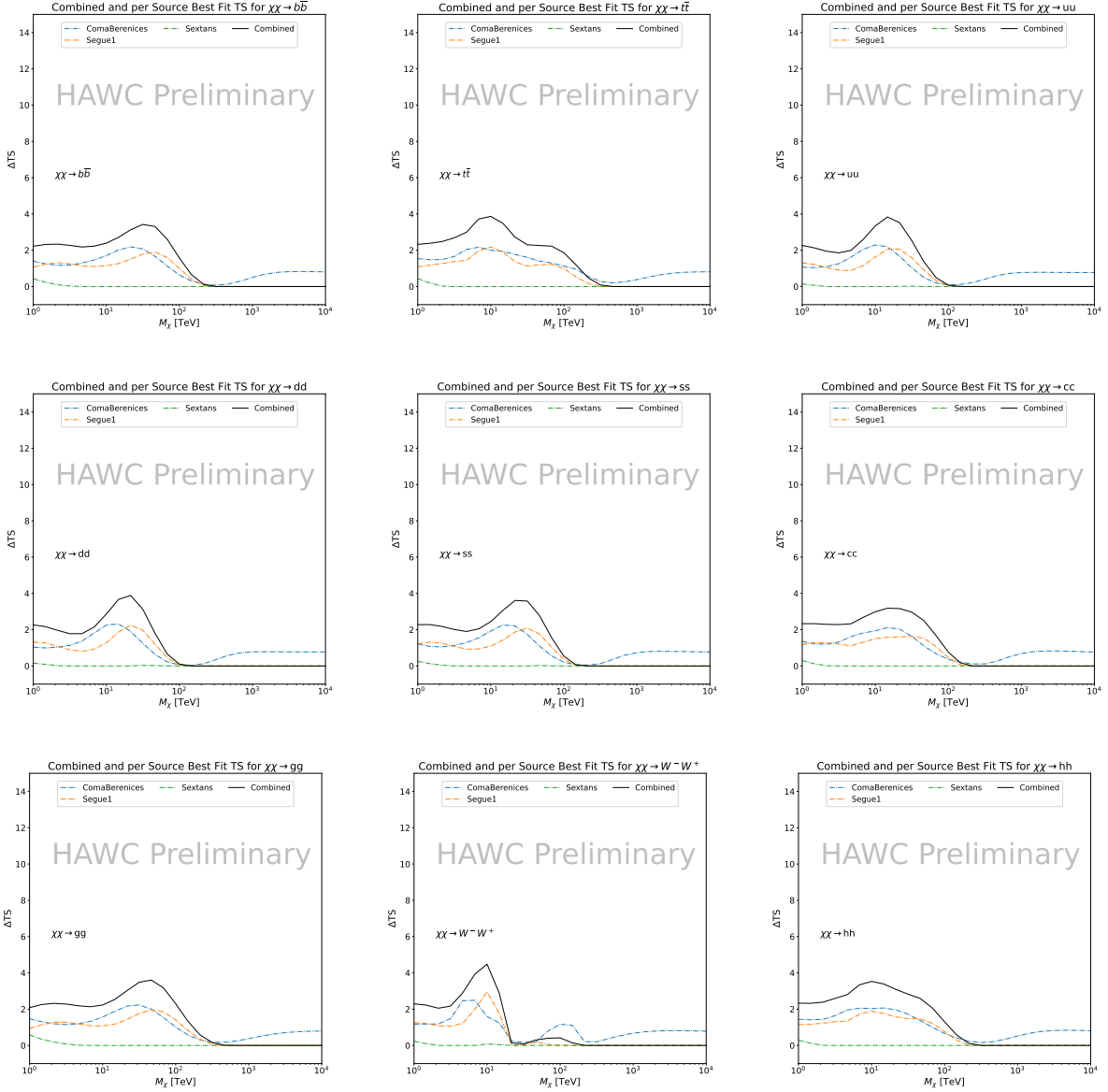


Figure 6.9 HAWC TS values for best fit  $\langle\sigma v\rangle$  versus  $m_\chi$  for SM annihilation channels:  $\chi\chi \rightarrow b\bar{b}$ ,  $t\bar{t}$ ,  $u\bar{u}$ ,  $d\bar{d}$ ,  $s\bar{s}$ ,  $c\bar{c}$ ,  $gg$ ,  $W^-W^+$ , and  $hh$ . Limits use  $\mathcal{LS}$   $J$ -factors. The solid black line shows the combined best fit TS values. The colored, dashed lines are the TS values from each dSph.

1402 calculated for this analysis and Glory Duck (Section 5.5). Segue 1 and Coma Berenices are low  
 1403 zenith where improvements to HAWC's analysis come only from energy estimation. Differences  
 1404 between these two are dominantly from their differences in  $J$ -factor, half-light radii of the dSphs,  
 1405 and the particle physics inputs. Substantial gains in HAWC's analysis methods (pass 5.F) were  
 1406 made at high zenith which is important for sources like Sextans. The HDM particle physics model

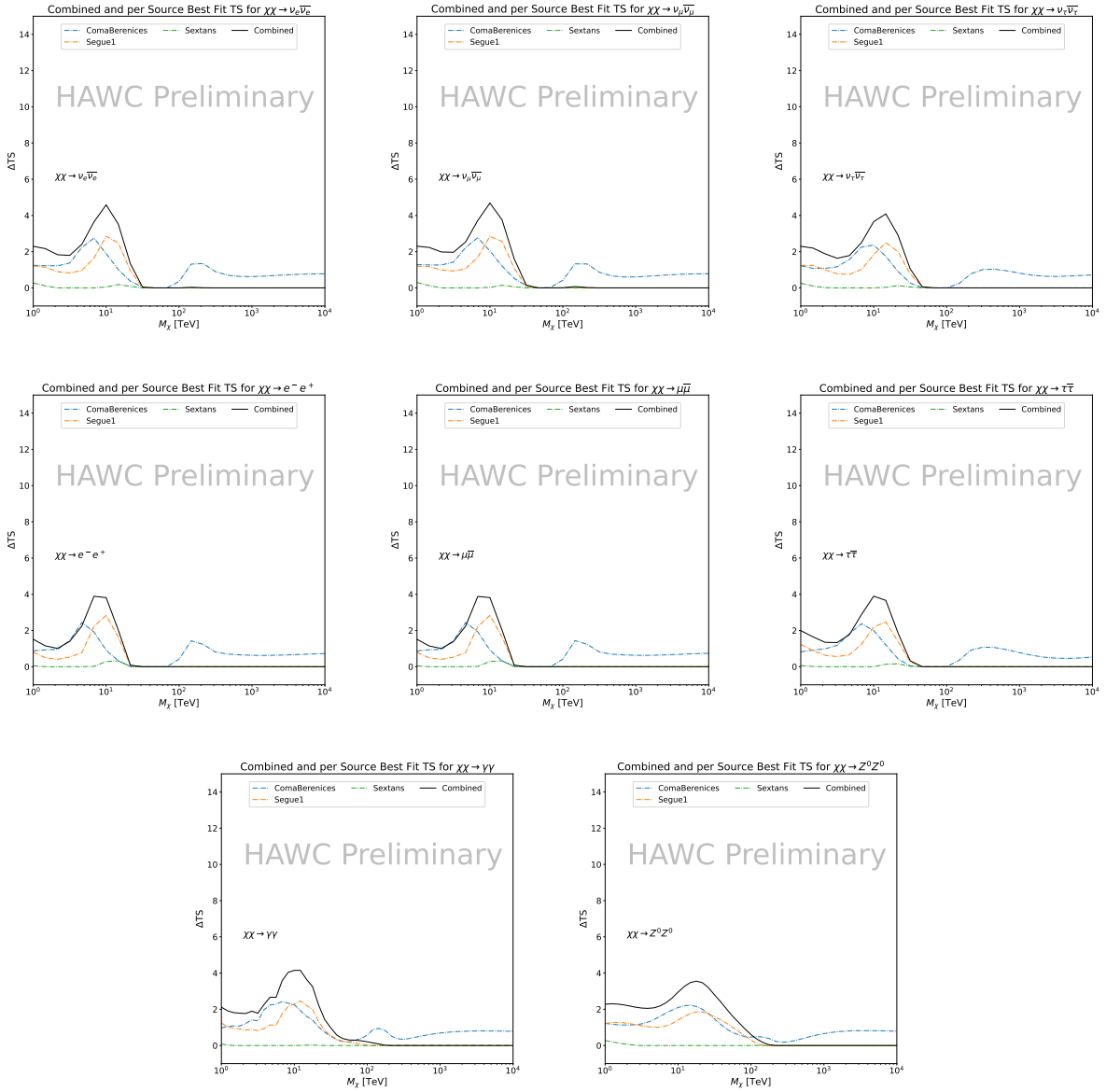


Figure 6.10 HAWC TS values for best fit  $\langle\sigma v\rangle$  versus  $m_\chi$  for SM annihilation channels:  $\chi\chi \rightarrow \nu_e \bar{\nu}_e$ ,  $\nu_\mu \bar{\nu}_\mu$ ,  $\nu_\tau \bar{\nu}_\tau$ ,  $e^- e^+$ ,  $\mu \bar{\mu}$ ,  $\tau \bar{\tau}$ ,  $\gamma\gamma$  and  $ZZ$ . Limits use  $\mathcal{LS}$   $J$ -factors. The solid black line shows the combined best fit TS values. The colored, dashed lines are the TS values from each dSph.

1407 produces almost identical spectra to the PPPC for  $\chi\chi \rightarrow e^- e^+$ . This channel can be used to  
 1408 compare limits between dSph spatial models. Overhead sources see minimal improvement to the  
 1409 limits, while high zenith sources see an order of magnitude improvement for all DM masses. Softer  
 1410 SM annihilation channels see broad improvements to the limit compared to harder channels.

1411 **6.7 Systematics**

1412     Systematics to this analysis are identical to what was performed earlier in Glory Duck, Sec-  
1413     tion 5.7. We are also sensitive to the choice in spatial template, and this was explored in Section 5.7.2  
1414     and Section 5.8.2.

1415 **6.8 Conclusion and Discussion**

1416     In this multithreaded analysis, we have used observations of 3 dSphs from HAWC to perform  
1417     a collective DM annihilation search towards dSphs. The data were combined across sources  
1418     to significantly increase the sensitivity of the search. Advanced computational techniques were  
1419     deployed to accelerate wall-time spent analyzing by an order of magnitude. We have observed  
1420     no significant deviation from the null, no DM hypothesis, and so present our results in terms of  
1421     upper limits on the velocity-weighted cross-section,  $\langle\sigma v\rangle$ , for seventeen potential DM annihilation  
1422     channels across four decades of DM mass.

1423     This analysis serves as a proof of concept for multithreaded HAWC analyses with large parameter  
1424     spaces. Larger datasets with fast techniques will be essential to tackling the DM problem. The  
1425     models we used for this study include annihilation channels with neutrinos in the final state.  
1426     Advanced studies could aim to merge our results with those from neutrino observatories with large  
1427     data sets.

1428     A full HAWC analysis will include systematic studies of the  $J$ -factor distributions. Additionally,  
1429     because of the timing reduction, the study can be doubled in size to include DM decay. We have not  
1430     yet received the remaining spatial profiles to the  $\mathcal{LS}$  catalog, and limits can be quickly computed  
1431     once these are received. Finally, statistical studies with Poisson variation of HAWC's background  
1432     are essential to a comprehensive understanding of our observed excesses.

Segue1

Coma Berenices

Sextans

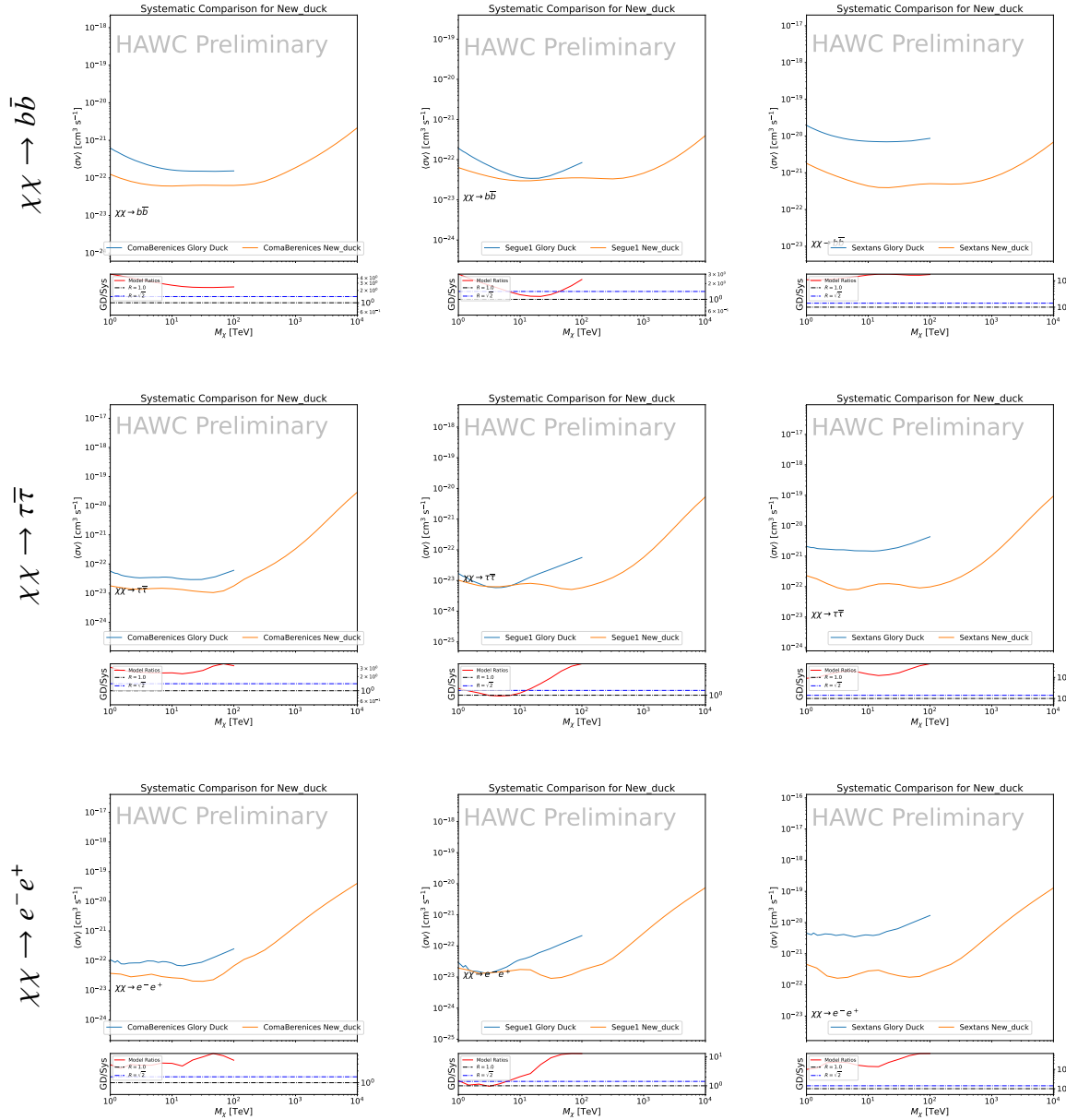


Figure 6.11 Comparison of HAWC limits from this analysis to Glory Duck (Fig. 5.5) for 3 dSphs and 3 DM annihilation channels:  $b\bar{b}$ ,  $\tau\bar{\tau}$ , and  $e^-e^+$ . Each sector shows the 95% confidence limit from Glory Duck (blue line) and this analysis (orange line) in the top plot. The lower plot features the ratio in log scale of Glory Duck to this analysis in a red solid line. Horizontal dashed lines are for ratios of 1.0 (black) and  $\sqrt{2}$  (blue). Ratios larger than 1.0 are for limits smaller, or stricter, than Glory Duck. Ratios larger than  $\sqrt{2}$  indicates limits are stricter than a simple doubling of the Glory Duck data.

## CHAPTER 7

### 1433 HEAVY DARK MATTER ANNIHILATION SEARCH WITH ICECUBE'S NORTH SKY 1434 TRACK DATA

#### 1435 7.1 Introduction

1436 Neutrinos are another astrophysical messenger than can travel long distances without interaction.  
1437 Uniquely, they interact less readily than photons especially above PeV energies. Neutrinos thereofre  
1438 provide another window through which we can perform dark matter searches. Neutrinos come in  
1439 three flabors and so this triples the multiplicity of the particles we are searching for.

1440 Icecube has not done a DM annihilation analysis towards dwarf galaxies for a while. **TODO:**  
1441 [cite 2013 paper](#). This is in spite of the potentially crucial sensitivity afforded from neutrino spectral  
1442 lines [TODO: cite dan hooper and neutrino lines](#). A lot has changed in IC3 since that last analysis (we  
1443 have more strings, we have much more sophisticated analysis methods, and the theory modeling  
1444 has made significant leaps.) Therefore it is time to finally do a DM search toward dSphs. The hope  
1445 is that by laying down the important statistical foundation as well, that this work can be meshed  
1446 with gamma-ray data. IceCube is sensitive to annihilating DM to the DM ranges above 1 TeV  
1447 and can produce competitive results relative to gamma ray observatories in spectral models that  
1448 produce sharp neutrino features. The goal of this analysis is to perform a DM annihilation search  
1449 using the new datasets NST. The search will only be towards dwarf spheroidal galaxies (dSph).  
1450 These sources are known for their low backgrounds and high DM contents. Since the dataset is  
1451 sensitive to the north and south, as many dSph as possible will be included. Additionally, with  
1452 annihilation, these sources can be treated as point sources with little loss to sensitivity or model  
1453 dependence on how the DM is distributed. DM masses from 500 GeV to 100 PeV are considered  
1454 for this analysis. All standard model annihilation channels available from the HDMspectra are  
1455 studied in this analysis.

1456 Additional work is done to extract the Likelihood profiles for each DM, source hypothesis so  
1457 that these data can be combined with gamma-ray observatories. This work is considered a separate  
1458 project as the statistical treatment is unique from many IceCube analyses. The wiki for [ the

1459 combined analysis] **TODO: instead point to chapter**This chapter presents the analysis work for  
1460 IC3 for DM searches toward dSphs. This section describes the various steps and features of the  
1461 analysis. It is structure first introduces the data and how it is treated, then systematic studies of the  
1462 dwarves individually. Finally, the stacked analysis and results are presented.

1463 **7.2 Dataset and Background**

1464 This section enumerates the data and background methods used for IceCube's study of dSphs.  
1465 Section 7.2.1 and Section 7.2.2 are most useful for fellow IceCube collaborators looking to replicate  
1466 this analysis.

1467 **7.2.1 Itemized IceCube files**

1468 These files are only available withing IceCube's internal documentation and collaborators. They  
1469 are not meant for public access, and are presented here so that IceCube collaborators can reproduce  
1470 results accurately.

- 1471 • Software Environment: CVMFS Py3-v4.1.1
- 1472 • Data Sample: Northern Tracks NY86v5p1
- 1473 • Analysis Software: csky ([nu\\_dark\\_matter](#))
- 1474 • Analysis wiki: [https://wiki.icecube.wisc.edu/index.php/Dark\\_Matter\\_Annihilation\\_Search\\_towards\\_dwarf\\_spheroidals\\_with\\_NST\\_and\\_DNN\\_Cascades](https://wiki.icecube.wisc.edu/index.php/Dark_Matter_Annihilation_Search_towards_dwarf_spheroidals_with_NST_and_DNN_Cascades)
- 1476 • Project repository

1477 **7.2.2 Software Tools and Development**

1478 This analysis was performed inside IceCube's CVMFS (3.4.1.1) software environment using  
1479 csky for likelihood calculations. Csky did not come with dark matter spectral models nor could  
1480 accomodate custom flux models. We developed these capacities for single source and stacked  
1481 source studies for this analysis. The analysis code is held in a separate repository from csky. The  
1482 [nu\\_dark\\_matter](#) branch of [csky](#) manages the input of custom dark matter spectra and accompanied

1483 DM astrophysical source then calculates likelihoods with a selected data sample. The [IceCube Dark](#)  
1484 [Matter dSph repository](#) manages the generation of spectral models for neutrinos, physics parameter  
1485 extraction from  $n_{\text{sig}}$ ,  $J$ -factor per source inputs, and bookkeeping for the large parameter space.  
1486 The project repository required a secondary software environment for neutrino oscillations. How  
1487 to launch and run those calculations are documented in the project repository and the Docker image  
1488 is additionally saved in Section C.1

1489 **7.2.3 Data Set and Background Description**

1490 For this analysis, I use the Northern Sky Tracks (NST) Sample (Version V005-P01). The sample  
1491 contains up-going track-like events, usually from  $\nu_\mu$  and  $\nu_\tau$  and has a superior angular resolution  
1492 compared to the cascade dataset. This sample covers 10.4 years of data (IC86\_2011-2021). The  
1493 accepted neutrino energy range used for the analysis is unique from most other IceCube searches  
1494 because DM spectra are very hard. The sampled energy range is  $1 < \log(E_\nu/\text{GeV}) < 9.51$  with  
1495 step size 0.125.

1496 The strength of a dwarf analysis is that there is no additional background consideration beyond  
1497 nominal, baseline background estimations. For NST, the nominal contribution comes from atmo-  
1498 spheric neutrinos and isotropic astrophysical neutrinos. We estimate the background by scrambling  
1499 NST data along Right Ascension.

1500 **7.3 Analysis**

1501 The expected differential neutrino flux from DM-DM annihilation to standard model particles,  
1502  $d\Phi_\nu/dE_\nu$ , over solid angle,  $\Omega$  is described by the familiar equation.

$$\frac{d\Phi_\nu}{dE_\nu} = \frac{\langle\sigma\nu\rangle}{8\pi m_\chi^2} \frac{dN_\nu}{dE_\nu} \times \int_{\text{source}} d\Omega \int_{l.o.s} \rho_\chi^2 dl(r, \theta') \quad (7.1)$$

1503 This is identical to past examples except that there are 3 neutrino flavors, so there are a corresponding  
1504 3 flux equations. Section 5.3 has a complete description of all the terms. Additionally, neutrinos  
1505 oscillate between flavors which needs to be considered for the expected neutrino flux at Earth.  
1506 Section 7.3.1 presents the particle physics model for DM annihilation. Section 7.3.2 presents the  
1507 spatial distributions built for each dSph.

1508 **7.3.1  $\frac{dN_\nu}{dE_\nu}$  - Particle Physics Component**

1509 Neutrino spectra from heavy dark matter annihilation were generated using HDMspectra [65]  
1510 and  $\chi$ arov [69]. HDMspectra simulates the decay and annihilation of heavy dark matter, for  
1511 different dark matter masses and SM primary annihilation channels. The simulation includes  
1512 electroweak radiative corrections and higher order loop corrections with quarks. This publication  
1513 also pushes the simulated DM mass to the Plank scale (1 EeV), however this study will not explore  
1514 that high.

1515 An important novel feature in the spectra is that neutrino line channels will be accompanied  
1516 with a low energy tail. Thus the earth will not fully attenuate a neutrino SM channel signal from  
1517 high declination sources where the neutrino flux must first traverse through the Earth. The SM  
1518 annihilation channels that feature lines include all leptonic channels. ( $\nu_{e,\mu,\tau}$ ,  $e$ ,  $\mu$ , and  $\tau$ ) We use  
1519  $\chi$ arov to propagate and oscillate the neutrinos from the source to Earth. Because these sources are  
1520 quite large in absolute terms, and also far (order 10 kpc or more), the resulting flavor spectra are  
1521 the averages of the transition probabilities [69]:

$$P(\nu_\alpha \rightarrow \nu_\beta) \approx \begin{bmatrix} 0.55 & 0.18 & 0.27 \\ 0.18 & 0.44 & 0.38 \\ 0.27 & 0.38 & 0.35 \end{bmatrix} \quad (7.2)$$

1522 When calculating the expected contribution to  $n_s$ , only  $\nu_\mu$ ,  $\nu_\tau$  are considered as NST's effective  
1523 area to  $\nu_e$  is essentially 0 [70]. With these consideration, the expected composite neutrino spectrum  
1524 is sum of the two flavors:  $\nu_\mu + \nu_\tau$ . The spectral tables are then converted to splines to condense  
1525 information, enable random sampling of the spectra, and enable faster computation times. The  
1526 spectral splines are finally implemented as a DM class in csky. Examples of the spectra before and  
1527 after propagation are shown in Fig. 7.1.

$M_\chi$ 

1 TeV

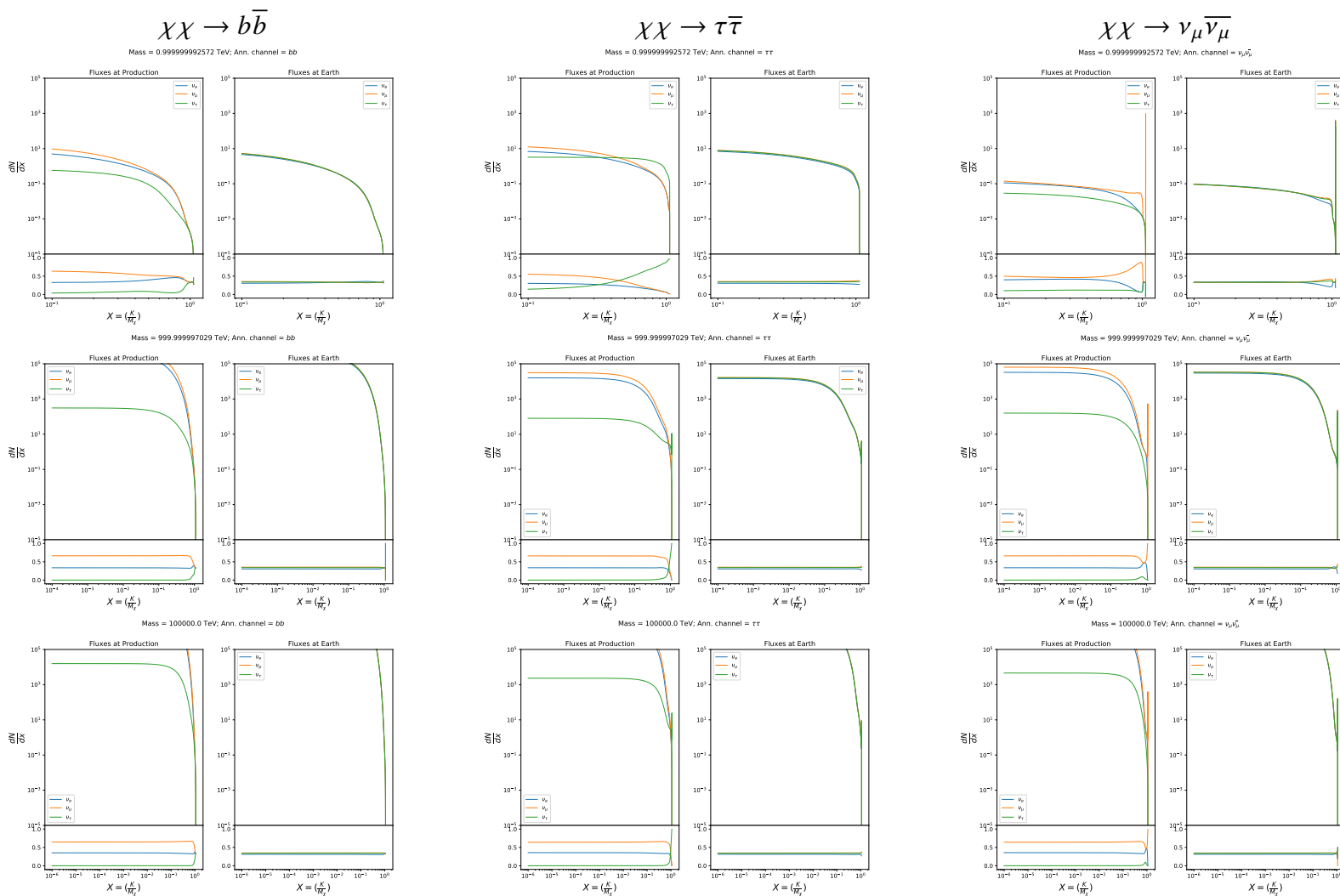


Figure 7.1 Neutrino spectra at production (left panels) and after oscillation at Earth (right panels). Blue, orange, and green lines are the  $\nu_e$ ,  $\nu_\mu$ , and  $\nu_\tau$  spectra respectively. Top panels show the spectra in  $\frac{dN}{dE}$ . Lower panels plot the flavor ratio to  $\nu_e + \nu_\mu + \nu_\tau$ . SM annihilation channels  $b\bar{b}$ ,  $\tau\bar{\tau}$ , and  $\nu_\mu\bar{\nu}_\mu$  are shown for  $M_\chi = 1 \text{ PeV}$ ,  $1 \text{ TeV}$ , and  $1 \text{ EeV}$ .

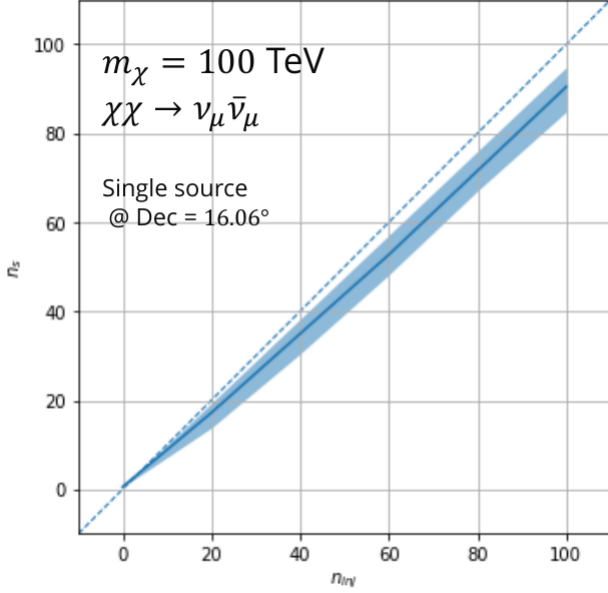


Figure 7.2 Signal recovery for 100 TeV DM annihilation into  $\nu_\mu \bar{\nu}_\mu$  for a source at Dec = 16.06°.  $n_{\text{inj}}$  is the number of injected signal events in simulation.  $n_s$  is the number of reconstructed signal events from the simulation. Although the uncertainties are small and tight, the reconstructed  $n_s$  are systematically underestimated.

### 7.3.1.1 Treatment of Neutrino Line Features

All leptonic DM annihilation channels  $\chi\chi \rightarrow [\nu_{e,\mu,\tau}, e, \mu, \tau]$  develop a prominent and narrow

spectral line feature. For all neutrino flavors, this line is visible and prominent in all mass models

studied for this analysis. For charged leptons, the feature only really shows up at the larger DM

mass models. Examples for lines in both neutrinos and charged leptons annihilation are provided

in Fig. 7.1. This line feature is so narrow relative the sampled energy range that the MC rarely

samples within the neutrino line. As a result, often the best fit to simulation of background will

always floor to TS = 0 and the signal recovery tends to be conservative.

To remedy this, a similar approach to the IceCube’s decay analysis [TODO: refer to Minjin’s](#)

[page](#). 2 kernels were tested (Gaussian, uniform (flat)) to smooth out the line feature. The widths

were tuned such that the signal recovery approached unity for DM mass 100 TeV to 1 PeV.

Additionally, the tuning was performed only for a source at declination 16.06 (Segue 1). This is

to avoid confusion loss in signal recovery from too narrow a line and from Earth’s attenuation of

high energy neutrinos. The convolution also needed to as close as possible preserve the integrated

counts of neutrinos. The optimized kernel window for all lines is summarized as:

- 1543 • Gaussian kernel w/ $2\sigma$  width =  $3.5E-3 \cdot m_\chi$
- 1544 • Minimum energy included in convolution =  $\text{MIN}[0.995 \cdot m_\chi, En(\nu_{line}) - 4\sigma]$
- 1545 • Maximum energy included in convolution =  $\text{MAX}[1.005 \cdot m_\chi, En(\nu_{line}) + 4\sigma]$

1546 where  $En(\nu_{line})$  is the neutrino energy where the neutrino line is at the maximum.

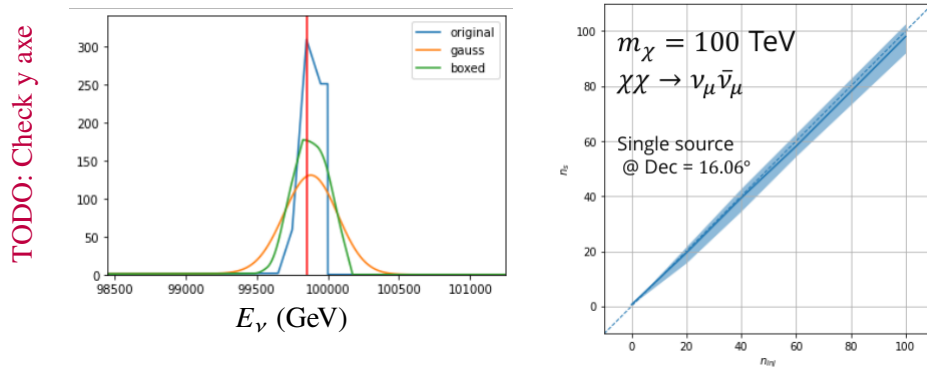


Figure 7.3 Top left panel shows the two kernels overlaid the original spectrum from Charon. delta I is the difference in the integral of the peaks with respect to the original spectrum. The vertical red line indicated where the original neutrino line is maximized. Lower right shows the signal recoveries of the DM model using the Gaussian kernel with parameters enumerated above.

1547 These parameters broadly improved the signal recovery of the line spectra. An example is  
1548 provided below. Signal recovery plots of the full analysis are provided much further down.

### 1549 7.3.1.2 Spline Fitting

1550 In an effort to reduce computational work, memory burden, and align with point source methods  
1551 used for NGC1068 and Seyfert analyses, spectral splines were created and adopted for estimating  
1552 the neutrino flux for the different annihilation. Software was written to generate, handle, and  
1553 calculate values on the splines. When using splines, one has to be careful of the goodness to fit.  
1554 There are critical caveats when testing the goodness to fit to MC generated above for all channels.

- 1555 • The splines must be Log10(\*) in Energy and dN/dE to account for the exponential nature of  
1556 the flux
- 1557 • The fidelity of the fit matters more at  $E_\nu \approx m_\chi$  where the model uncertainties are minimal  
1558 and physical considerations (like the cut-off) are most apparent.

- 1559 • The fidelity of the fit matters less at low  $E_\nu$  as the model uncertainties are large AND  
 1560 IceCube's sensitivity diminishes significantly below 500 GeV

- 1561 • Total integrated counts should be well preserved, however, the resolution of the MC is much  
 1562 higher than IceCube's energy resolution.

1563 – Meaning over several steps in E, the integral is preserved

1564 – the step size enters the cost function

1565 – Oscillating residuals, so long as they are very small and well centered, are not penalized  
 1566 as this gets averaged out.

1567 The resulting cost function to evaluate the goodness of fit was used to account for the above  
 1568 considerations.

$$e_i = x_i \cdot \left( \frac{dN_i}{dE_i} - 10^{\hat{e}_i} \right) \quad (7.3)$$

1569 Where  $\hat{e}_i$  is the spline estimator's value for  $x_i$ .  $x_i = E_{\nu_i}/m_\chi$ .  $\frac{dN_i}{dE_i}$  is the flux value from MC.

$$\text{err} = \sqrt{\frac{1}{x_{\max} - x_{\min}} \int_{x_{\min}}^{x_{\max}} e^2 dx} \quad (7.4)$$

1570 I then take the RMS of the error distribution and the resulting value (err) is used to evaluate  
 1571 the fidelity of the spectral spline. Each SM channel had different tolerances for 'err'. Channels  
 1572 with very hard cut-offs had looser tolerance for err because a lot of error would be generated from  
 1573 the cut-off being estimated to occur slightly early or late. Soft channels don't have this issue and  
 1574 therefore the tolerance is very strict. The table blow summarizes the tolerances for the SM channels.

1575

1576 The errors are then plotted in two ways. First, FAIL and OK are directly plotted with  $e_i$  as a  
 1577 function of x, and the full spline and MC. Second, a summary plot of all the splines is plotted and  
 1578 colors coded.

1579 Figure C.1 are the spline summaries and represent the current, up-to-date status of the splines.  
 1580 The goal broadly is to eliminate all red and inspect yellow.  $\nu_e$  is not considered in this analysis  
 1581 among the neutrino final states and so no work was done to converge the spline fits for this flavor.

| $\chi\chi \rightarrow$                   | GOOD   | OK             | FAIL   | Limits of err calc [ $X_{min}, X_{max}$ ]   |
|--|--------|----------------|--------|---|
| $Z^0 Z^0, W^+ W^-$                       | 1.0E-3 | 1.0E-3, 1.0E-2 | 1.0E-2 | MAX[100GeV/ $m_\chi$ , $10^{-6}$ ], 1.0   |
| $t\bar{t}, hh$                           | 1.0E-5 | 1.0E-5, 1.0E-4 | 1.0E-4 | MAX[100GeV/ $m_\chi$ , $10^{-6}$ ], 1.0   |
| $b\bar{b}, d\bar{d}, u\bar{u}$           | 9.0E-7 | 9.0E-7, 9.0E-6 | 9.0E-6 | MAX[100GeV/ $m_\chi$ , $10^{-6}$ ], 1.0   |
| $\nu\bar{\nu}_{e,\mu,\tau}$              | 1.0E-3 | 1.0E-3, 1.0E-2 | 1.0E-2 | MAX[100GeV/ $m_\chi$ , $10^{-6}$ ],<br>MIN[0.995, ( $E_n(\nu_{line}) - 4\sigma$ )/ $M_\chi$ ] |
| $e\bar{e}, \mu\bar{\mu}, \tau\bar{\tau}$ | 1.0E-3 | 1.0E-3, 1.0E-2 | 1.0E-2 | MAX[100GeV/ $m_\chi$ , $10^{-6}$ ],<br>MIN[0.995, ( $E_n(\nu_{line}) - 4\sigma$ )/ $M_\chi$ ] |

Table 7.1 TODO: fill me daddy

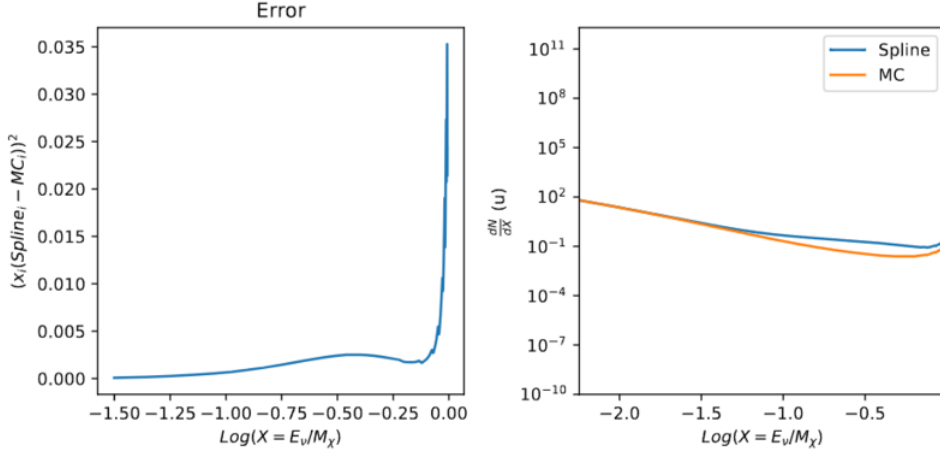


Figure 7.4 Example spline that failed the fit. Failed splined are corrected on a case by case basis unless the SM channel has a systematic problem fitting the splines. In this case, I made a bookkeeping error and loaded the incorrected neutrino flavor

1582 A Final inspection of the splines by eye was done to verify that the spline fitting did not introduce  
 1583 spurious features into the distribution that would corrupt the LLH fitting.

### 1584 7.3.1.3 Composite Neutrino Spectra

1585 With all of the previously mentioned pieces, we are ready to fully assemble a comprehensive  
 1586 description of the particle physics term  $dN/dE$  in Eq. (7.1).

$$\frac{dN_\nu}{dE_\nu} = \left( \frac{dN_{\nu_e}}{dE_{\nu_e}} + \frac{dN_{\nu_\mu}}{dE_{\nu_\mu}} + \frac{dN_{\nu_\tau}}{dE_{\nu_\tau}} \right)_{\text{src}} \cdot \mathbf{P}(\nu_\alpha \rightarrow \nu_\beta) \quad (7.5)$$

1587 Figure 7.5 shows the spectral models that required Gaussian smoothing, the leptonic annihilation  
 1588 channels. The remaining models where the only processing was the spline fitting are documented  
 1589 in the TODO: refer to apdxNotice that the different neutrino flavors are unique, especially in their  
 1590 low energy tails. Therefore, this analysis will be sensitive to DM annihilating to the distinct neutrino

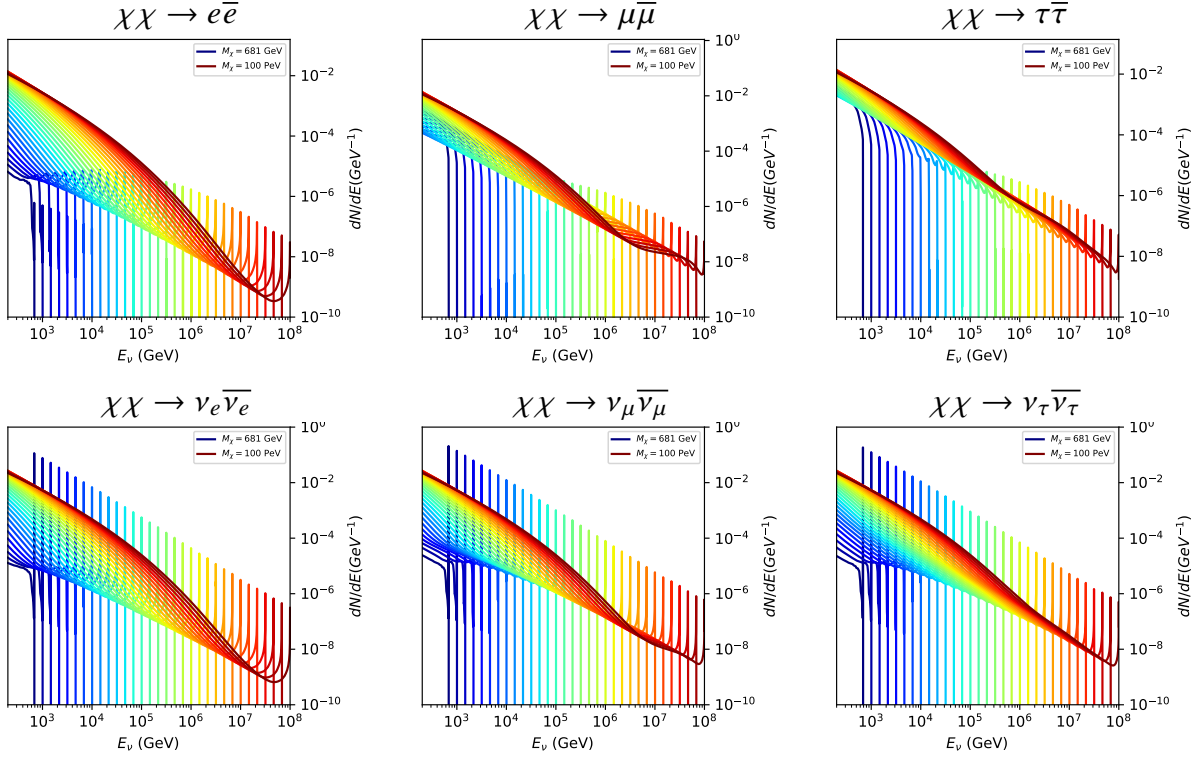


Figure 7.5 Summary of input spectral models that were smoothed with Gaussian kernel. Spectral models are for  $\chi\chi \rightarrow e\bar{e}$ ,  $\mu\bar{\mu}\tau\bar{\tau}$ ,  $\nu_e\bar{\nu}_e$ ,  $\nu_\mu\bar{\nu}_\mu$ , and  $\nu_\tau\bar{\nu}_\tau$ . These spectra are the composite ( $\nu_\mu + \nu_\tau$ ) of neutrino flavors. Every spectral model used for this analysis is featured as a colored solid line. Bluer lines are for lower DM mass spectral models. DM masses range from 681 GeV to 100 PeV. HDM [65],  $\chi$ arov [69], and Photospline [71] are used to generate these spectra. Energy (x-axis) was chosen to roughly represent the energy sensitivity of NST.

1591 flavors. All leptonic channels show prominent, hard features around  $E_\nu = m_\chi$ .

### 1592 7.3.2 J- Astrophysical Component

1593 The expected neutrino counts from a dwarf spheroidal galaxy depends also on the the 'astro-  
 1594 physical factor'. The value for this (in our specific case) J-factor for a target depends on its dark  
 1595 matter density distribution,  $\rho_\chi$  and how far it is  $l$ . For this analysis, we adopt the  $\mathcal{GS}$  model used  
 1596 in Sec. 5 for dSph from [45]. These models are based on a modified Navarro-Frenk-White (NFW)  
 1597 profile where the indices of the NFW (traditionally 1,3,1) are allowed to float. More specifically,  
 1598 these DM distributions are described using the Zhao profile. The Zhao profile is written as:

1599 where  $\theta$  is the angular distance from the center of the source. For the case annihilation, the  
 1600 source diameter, [<https://iopscience.iop.org/article/10.1088/0004-637X/801/2/74> here] defined as

1601 the  $2\theta_{\max}$ , of these dwarves is typically under  $1^\circ$  with the largest in the catalog, Fornax, extending  
 1602 to  $2.61^\circ$ . Fornax is not in the northern sky and the remaining sources are notably below this angular  
 1603 size. Therefore, the sources are treated as point sources because the typical source diameter is under  
 1604 1 degree. The J-factor used for the point source assumption is the total J emitted from  $\theta_{\max}$ . These  
 1605 values are enumerated in Geringer-Sameth 2015 and again in the table below with their coordinates.  
 1606 Coordinates are given in J200.0 equatorial coordinates. IceCube uses identical sources to Tab. 5.1  
 1607 except we analyze source with declinations above  $0.0$  degrees.

### 1608 7.3.3 Source Selection and Annihilation Channels

1609 We use all of the dSphs presented in IceCube's previous dSph DM search [70]. IceCube's  
 1610 sources for these simulation studies include Bootes I, Canes VenaticiI, Canes Venatici II, Coma  
 1611 Berenices, Draco, Hercules, Leo I, Leo II, Leo V, Leo T, Segue 1, Segue 2, Ursa Major I, Ursa Major  
 1612 II, and Ursa Minor. A full description of all sources used in Table 5.1. Sources with declinations  
 1613 less than  $0.0$  are excluded from this analysis.

1614 This analysis improves on the previous IceCube dSph paper [70] in the following ways. Pre-  
 1615 viously, the IceCube detector was not yet completed to the 86 string configuration. Many more  
 1616 dSphs will be observed, from 4 to 15. Previously, the particle physics model used for neutrino-ray  
 1617 spectra from DM annihilation did not have EW corrections where they are now included [65]. The  
 1618 spectral models also predict substantial differences between the neutrino flavors, so this analysis  
 1619 will be the first DM dwarf analysis to discriminate between primary neutrino flavors. The study  
 1620 performed here studies 10.4 years of data.

1621 The SM annihilation channels probed for this study include  $b\bar{b}$ ,  $t\bar{t}$ ,  $u\bar{u}$ ,  $d\bar{d}$ ,  $e\bar{e}$ ,  $\mu\bar{\mu}$ ,  $\tau\bar{\tau}$ ,  $ZZ$ ,  
 1622  $W^+W^-$ ,  $\nu_e\bar{\nu}_e$ ,  $\nu_\mu\bar{\nu}_\mu$ , and  $\nu_\tau\bar{\nu}_\tau$ .

### 1623 7.4 Likelihood Methods

1624 I use the Point-Source search likelihood which is widely used in IceCube analyses. The  
 1625 likelihood function is defined as the following:

$$L(n_s) = \prod_{i=1}^N \left[ \frac{n_s}{N} S_i + \left(1 - \frac{n_s}{N}\right) B_i \right] \quad (7.6)$$

1626 where  $i$  is an event index,  $S$  and  $B$  are the signal PDF and background PDF respectively. For a joint  
1627 analysis where the sources are stacked the likelihood is expanded in the simplified way:

$$L(n_s) = \prod_{i=1}^{N_{\text{sources}}} L_i(n_s) \quad (7.7)$$

1628 Where  $L_i$  is the likelihood from the  $i$ -th source in the stacked analysis. The test statistic definition  
1629 remains the same as Eq. (5.7)

## 1630 7.5 Background Simulation

1631 Before we look at data, we must first analyze background and signal injection to validate our  
1632 analysis. The following sections show the results of the likelihood fitting for a suite of background  
1633 trials for the DM models we set out to study in [TODO: refer to the section](#). We study the TS  
1634 distributions first for each source, then for the stacked analysis.

1635 The TS distributions are not expected to behave according to a chi-squared distribution with 1  
1636 degree of freedom. This is in large part due to the distinct spectral shapes demonstrated earlier.  
1637 These can vary significantly between DM mass and annihilation models. Therefore, Wilks' theorem  
1638 may not be applicable to the analysis. Instead, a critical value is defined from a large number of  
1639 background trials.

1640 I assume that TS values are physical:  $\text{TS} \geq 0$ .  $\eta$  denotes the fraction of positive TS values  
1641 above the threshold and written in the legend.  $\epsilon[x]$  indicate the fraction of events where  $\text{TS} < x$ .  
1642 For TS plots shown here, the decimal values of  $x$  are 1.0e-2 and 1.0e-3. The following plots show  
1643 the background TS distributions obtained from Segue1, a source with little Earth attenuation and  
1644 large J-factor, assuming that dark matter annihilates into  $b\bar{b}$ . I also show the 15 source stack TS  
1645 distributions with identical DM models.

### 1646 7.5.1 TS per Source

1647 Below I present the TS distributions for Segue1 and  $\chi\chi \rightarrow b\bar{b}$ . All remaining channels and  
1648 source TS panels are hosted on [TODO: Change this text, it will all be here](#).

1649 Although it was not expected, almost every distribution produced follows a chi2 distribution  
1650 with 1 degree of freedom. This is important for future assumptions made (in multi-messenger) and

1651 may justify statistical calculations assuming Wilk's theorem is valid.

1652     TODO: add text saying that you show: bb, numu, and tau??? specs for Seg1 and UMa2?

1653     **7.5.2 Stacked TS**

1654     The presentation of these plots are identical to the previous 'per Source' section. I use csky  
1655     source software to calculate the TS distributions. Bugs were found when implementing, however  
1656     were rectified. Warning to future users performing a stacked analysis with custom spectra. In  
1657     using the above, I am making the implicit assumption that the primary/only cause to a difference in  
1658     neutrino counts from the sources is accounted for through the J-factors. The J-factors are therefor  
1659     used as weights for the stacking where an individual source's weight is defined as:

1660     Each subplot, except the final, is the TS distribution for a specific DM mass listed in the subplot.  
1661     The final subplot plots the all DM spectral models used as input for the TS distribution calculations  
1662     with bluer lines indicating lower DM mass and redder indicating higher DM mass. Below is an  
1663     image of bb. The full resolution pdfs were provided in links above.

1664     **7.6 Signal Recovery**

1665     **7.6.1 Sensitivities**

1666     In IceCube, we usually define the 90% confidence level (CL), as the minimum number of signal  
1667     events ( $n_s$ ) required to have a Type I error rate smaller than 0.5 and Type II error rate of 0.1. Csky  
1668     performs the sweep to find  $n_s$  that satisfies the previous condition, and from  $n_s$  I use the following  
1669     equation

$$n_s = T_{live} \int_0^{\Delta\Omega} d\Omega \int_{E_{min}}^{E_{max}} dE_\nu A_{eff}(\hat{n}, E_\nu) \frac{d\Phi_\nu}{d\Omega dE_\nu}(\hat{n}, E_\nu), \quad (7.8)$$

1670     to extract the sensitivity on the dark matter annihilation cross-section.  $T_{live}$  is the detector  
1671     livetime,  $A_{eff}$  is the effective area of the detector, and  $E_{min}$ ,  $E_{max}$  are the minimum, maximum  
1672     energies of the expected neutrinos, respectively.

1673     Sensitivities are calculated for each source individually as if they were the only source and as  
1674     a stack. Example plots of these plots are shown below and organized by the single source/stacked  
1675     studies. Finally, I generated a plot with all hypotheses which is presented at the very end.

1676 **7.7 Systematics**

1677 Lol What Systematics. Beside signal recovery we don't have many additional studies for here.  
1678 The current analysis plan is to compare these sensitivities to another  $J$ -factor catalog such as  $\mathcal{LS}$   
1679 [66]. Additionally, we set out to perform a standard suite of IceCube systematic studies which  
1680 include: **TODO: THE BIG 4: ICE MODEL ETC**

1681 **7.8 Conclusions**

1682 We built many things for this analysis. We utilized advanced computing techniques like  
1683 parallel programming and spline fitting of particle physics Monte Carlo to greatly expand and  
1684 refine IceCube's sensitivity to DM annihilation from dSphs. We imported updated astrophysical  
1685 and particle physics models that better represent what we believe neutrino signals from DM  
1686 annihilation should look like. We, for the first time, build an analysis that is sensitivity to PeV DM  
1687 annihilation.

1688 When we compare to previous IceCube publications of dSphs [70], we see an order of magnitude  
1689 improvement to our sensitivity. This analysis has been working group approved within IceCube and  
1690 has begun the unblinding process. This processes did not complete in time for this dissertation.  
1691 Therefor we do not show data for this thesis and is the clear next step.

1692 The test statistic distributions in this analysis also demonstrate more characteristic behaviour  
1693 compared to previous DM analyses. With a 10 year dataset, we finally have enough statistics to  
1694 almost trivially combine with other photon observatories, such as HAWC. The first ground work for  
1695 a multi-messenger DM search is provided with concluding remarks in Sec. 8.

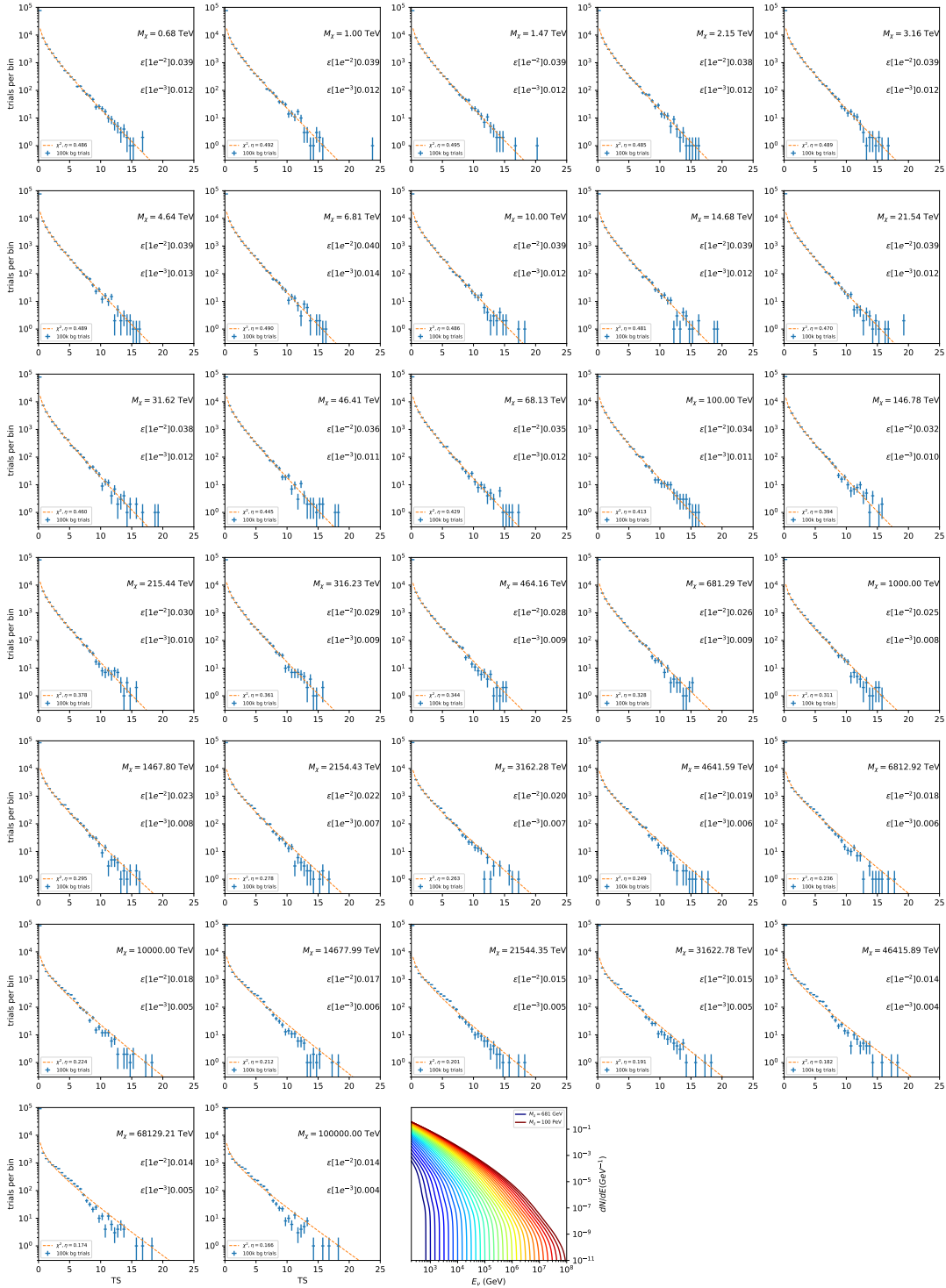


Figure 7.6 Test statistic (TS) distributions for Segue 1 and  $\chi\chi \rightarrow b\bar{b}$ . Each subplot, except the final, is the TS distribution for a specific DM mass listed in the subplot. Orange dashed lines are the traces for a  $\chi^2$  distribution with 1 degree of freedom.  $\epsilon[\cdot]$  is the fraction of trials smaller than the bracketed value. The final subplot plots the all DM spectral models, similar to Fig. 7.5, used as input for the TS distributions.

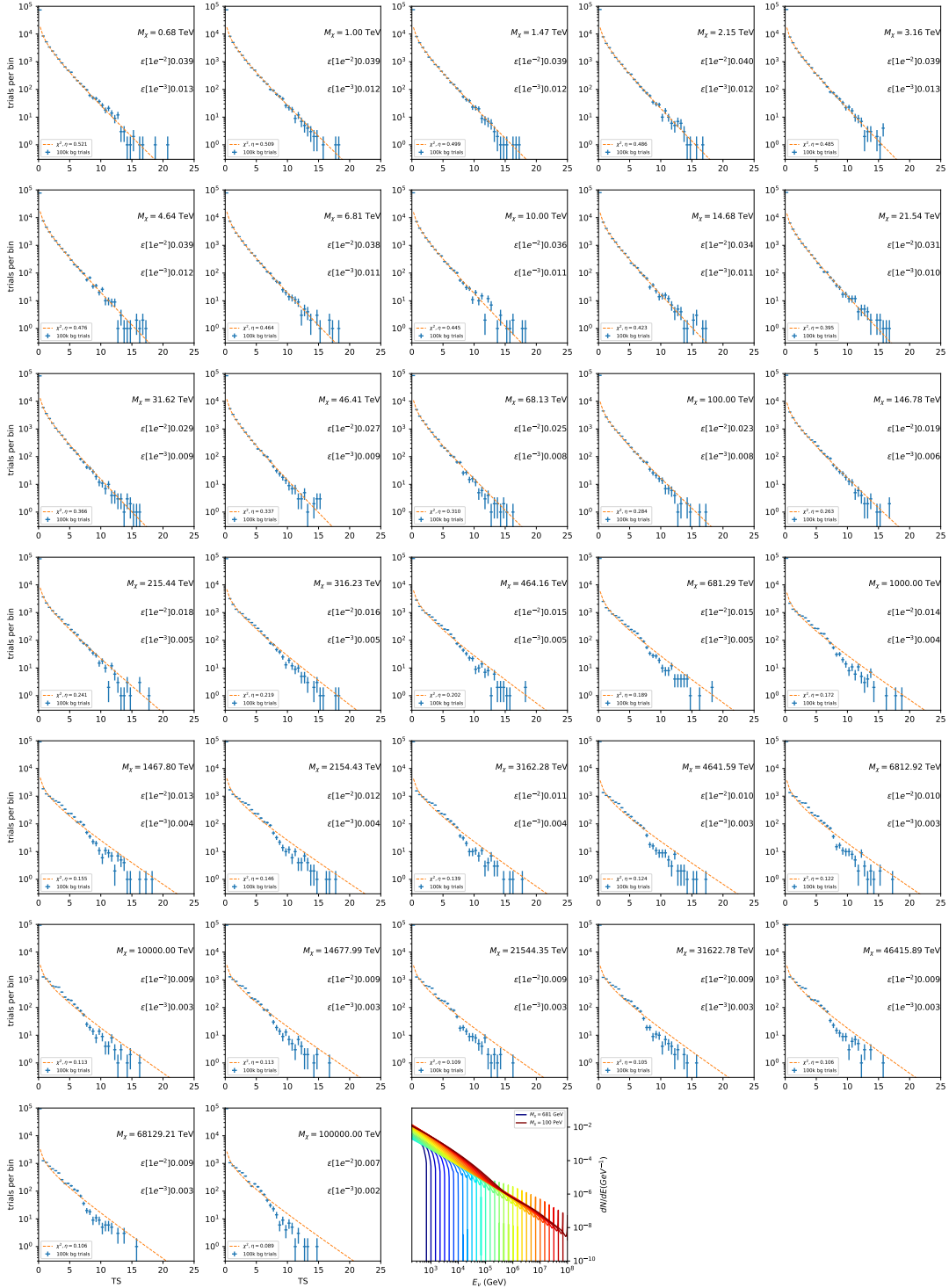


Figure 7.7 Same as Fig. 7.6 for Segue 1  $\chi\chi \rightarrow \tau\bar{\tau}$ .

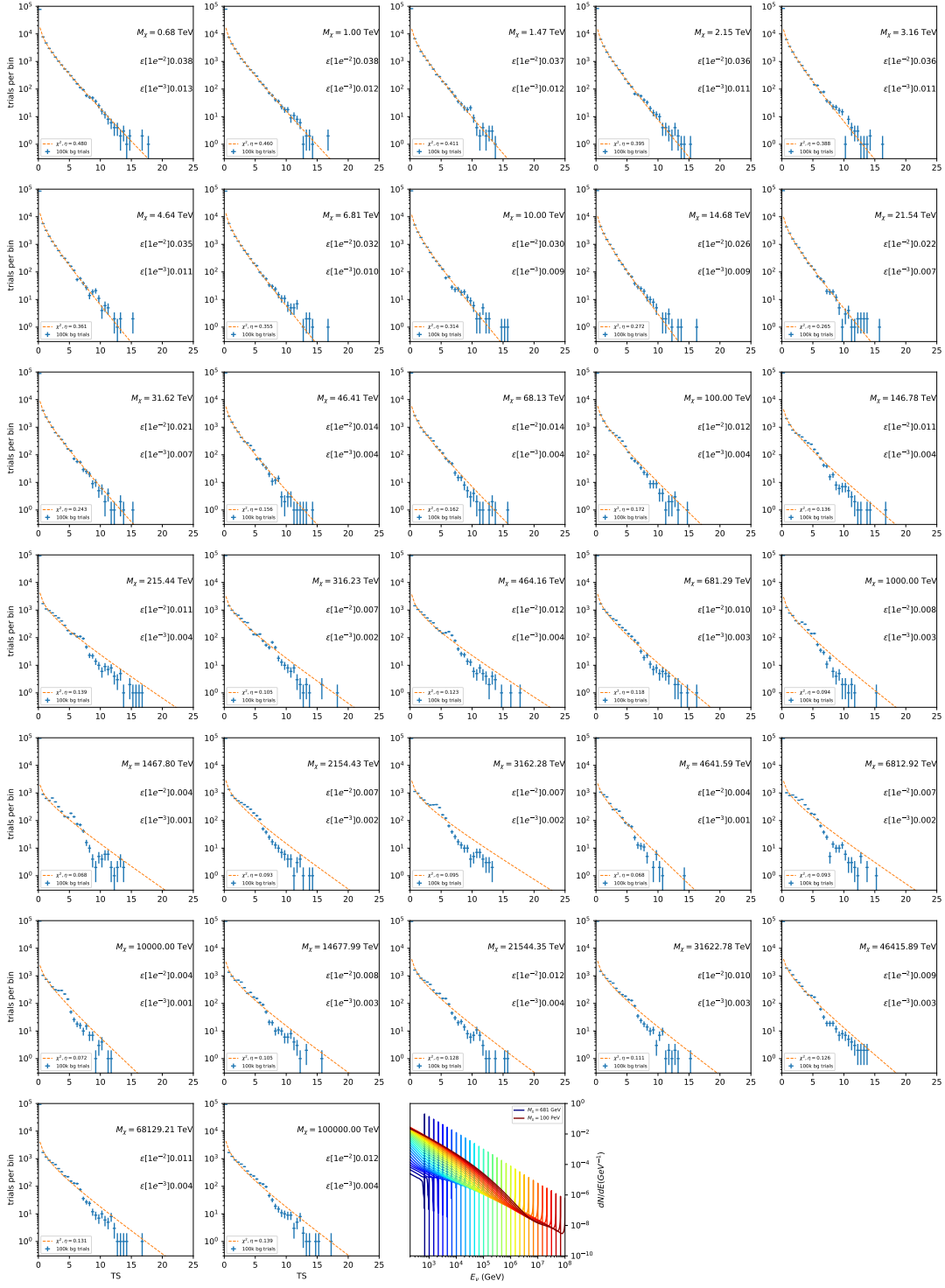


Figure 7.8 Same as Fig. 7.6 for Segue 1  $\chi\chi \rightarrow \nu_\mu\bar{\nu}_\mu$ .

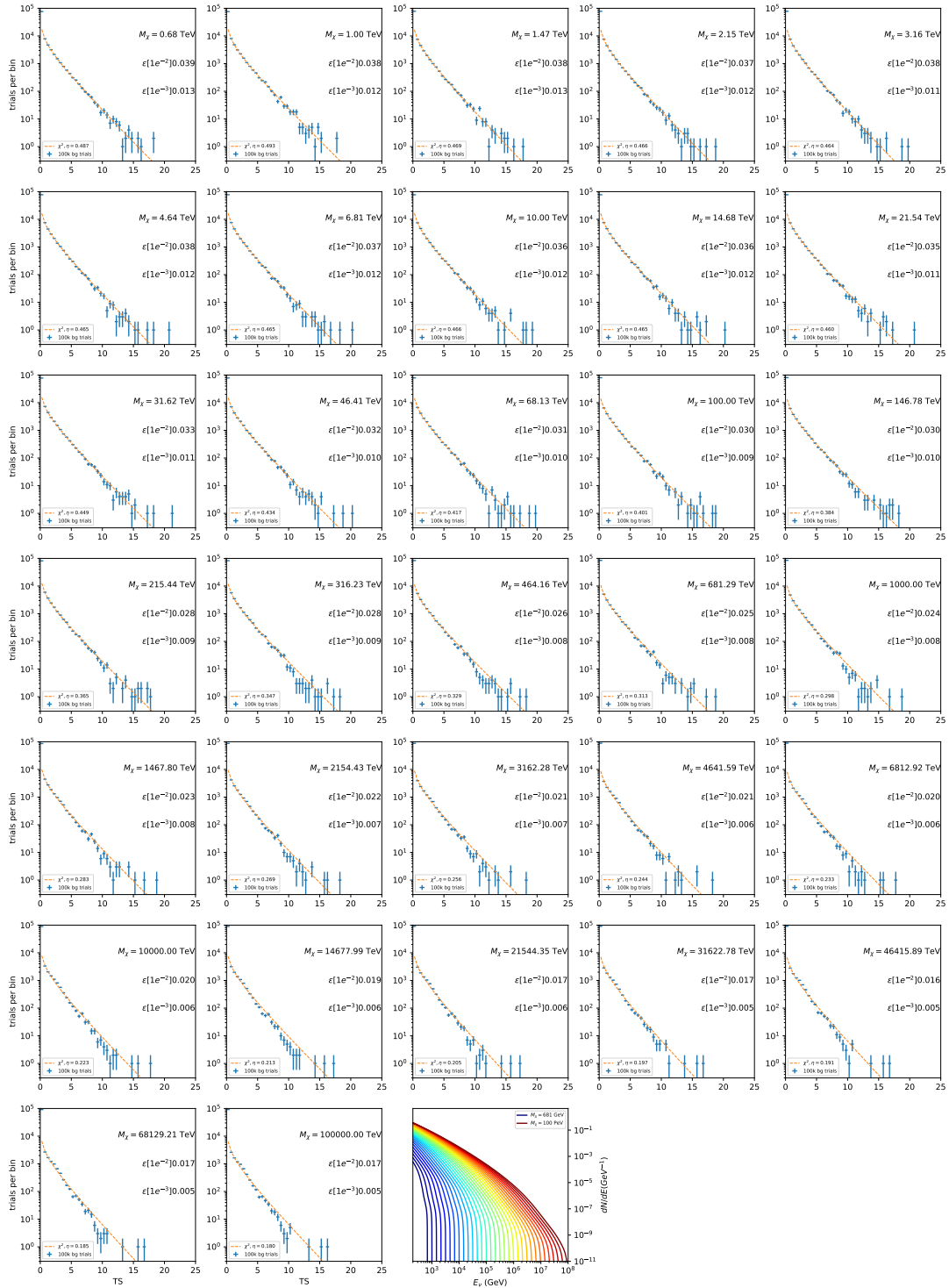


Figure 7.9 Same as Fig. 7.6 for Ursa Major II 1  $\chi\chi \rightarrow b\bar{b}$ .

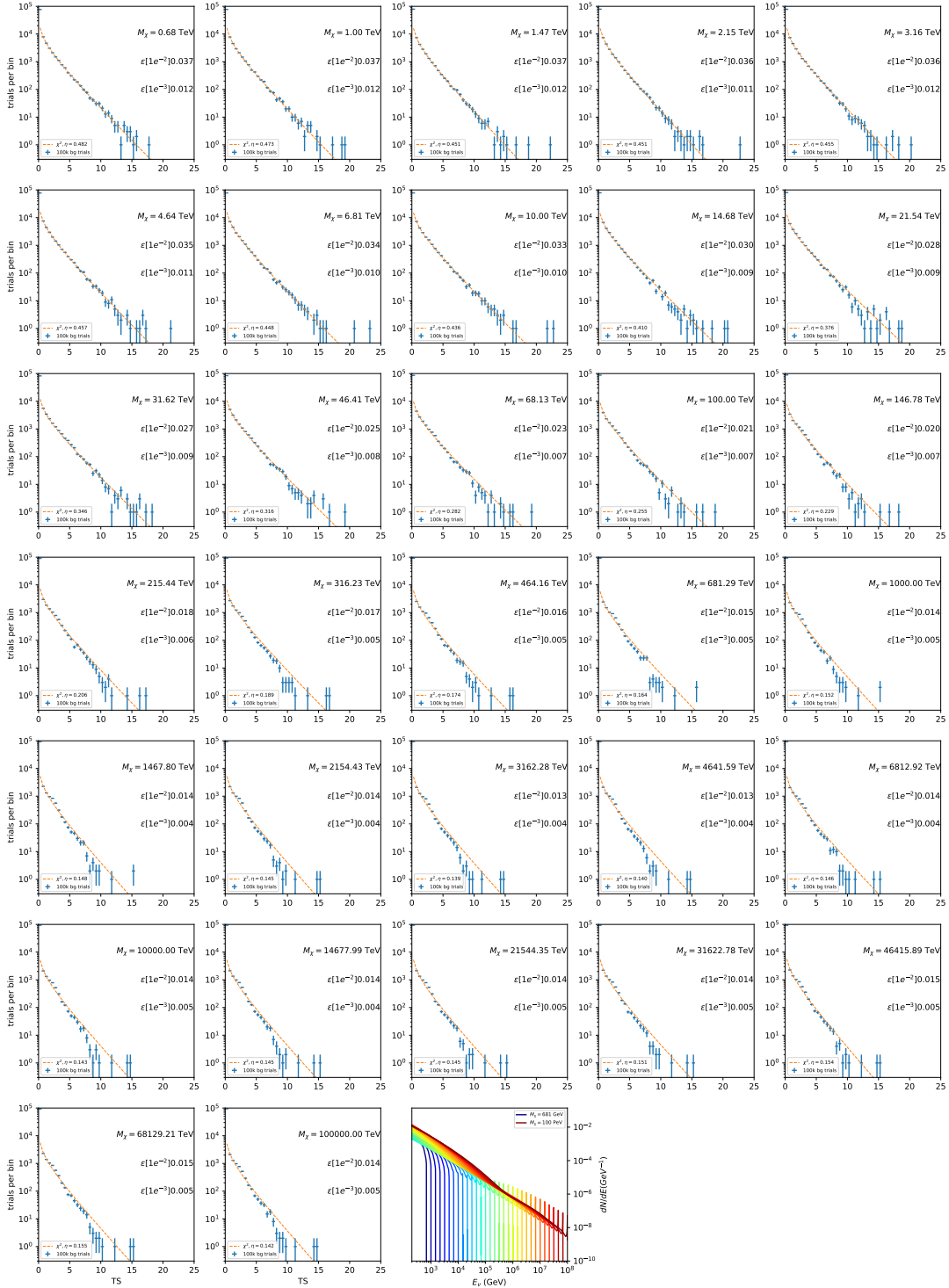


Figure 7.10 Same as Fig. 7.6 for Ursa Major II 1  $\chi\chi \rightarrow \tau\bar{\tau}$ .

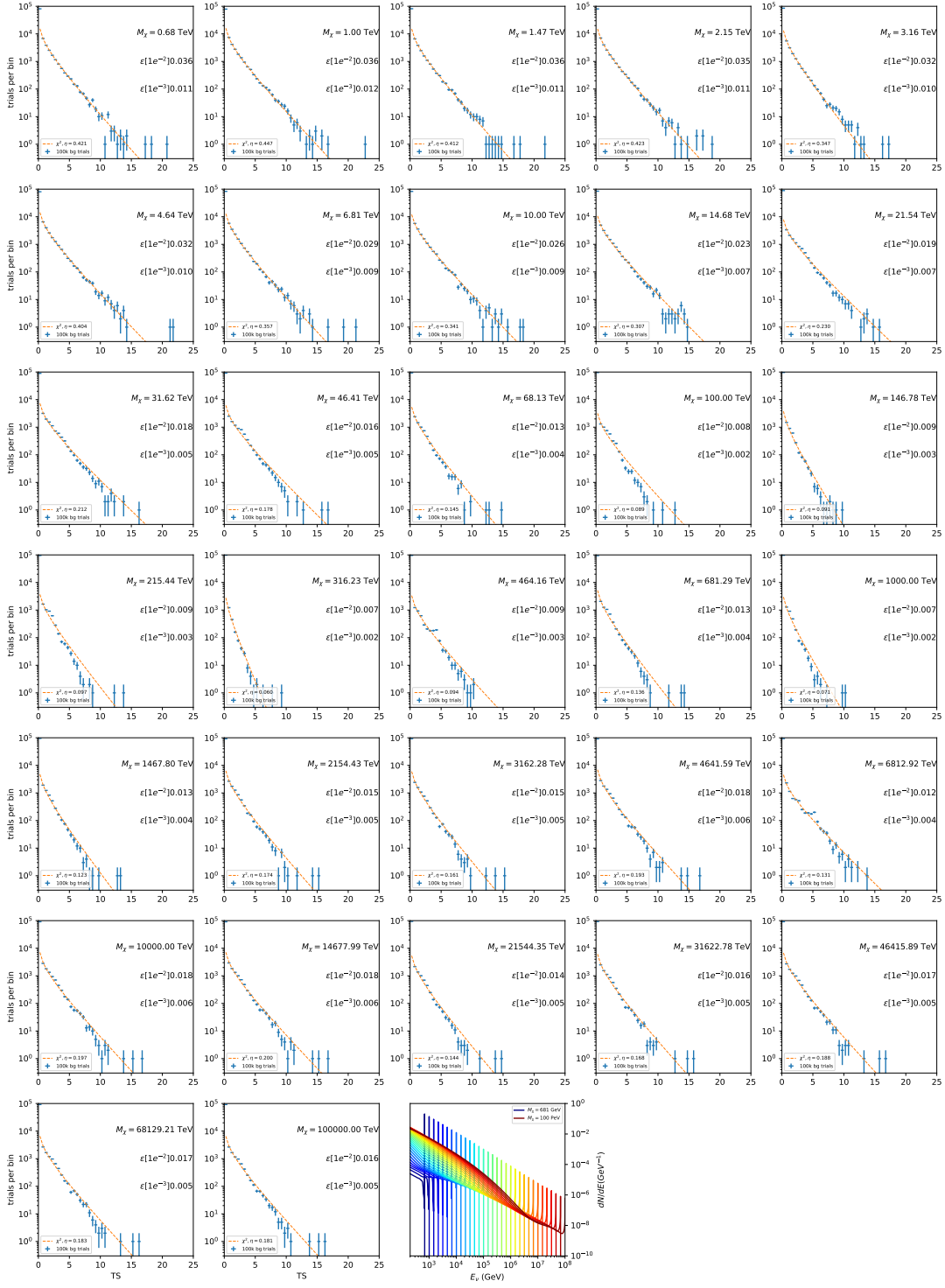


Figure 7.11 Same as Fig. 7.6 for Ursa Major II 1  $\chi\chi \rightarrow \nu_\mu\bar{\nu}_\mu$ .

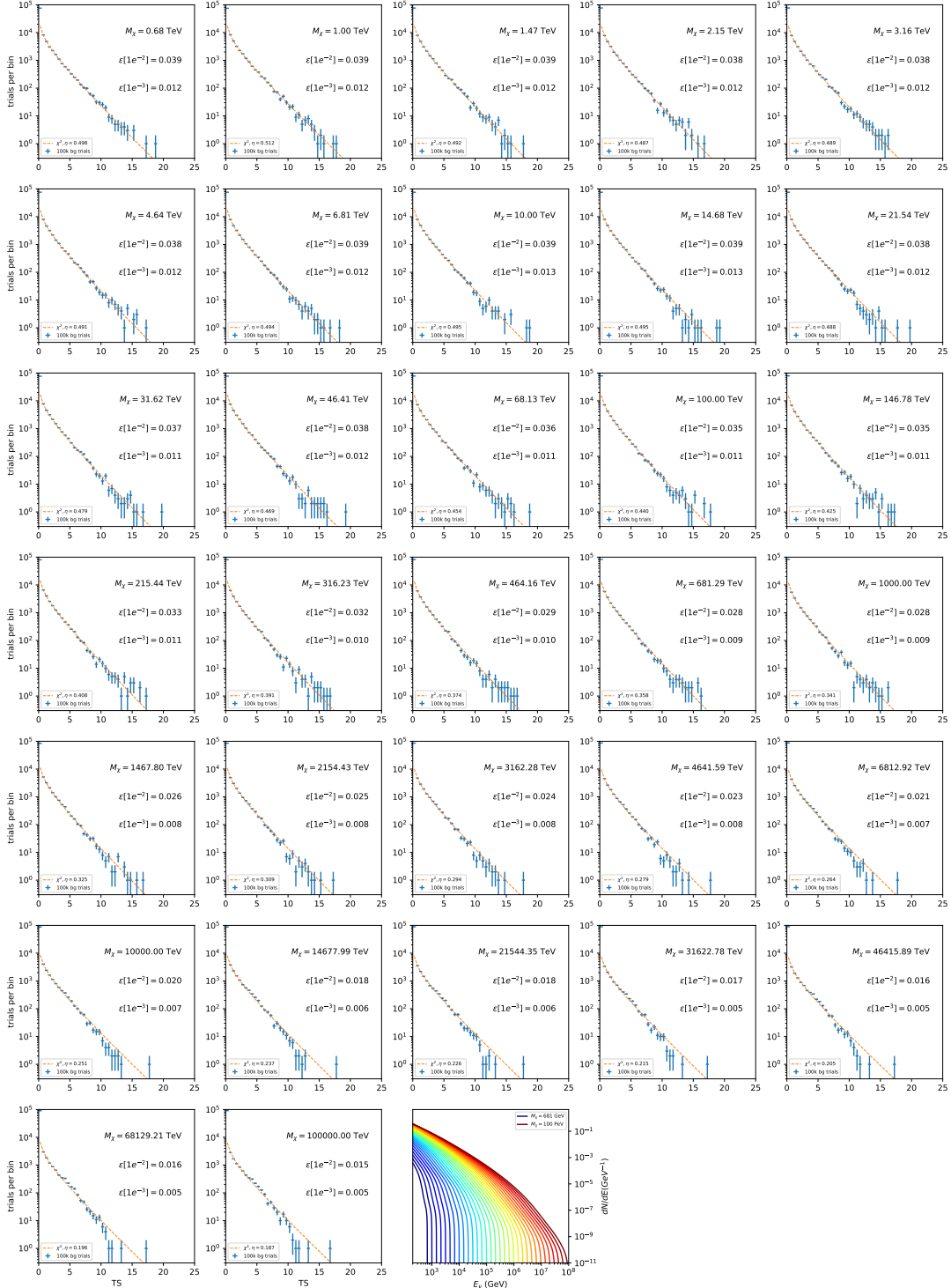


Figure 7.12 Same as Fig. 7.6 for 15,  $\mathcal{GS}$  J-factor, stacked sources and  $\chi\chi \rightarrow b\bar{b}$ .

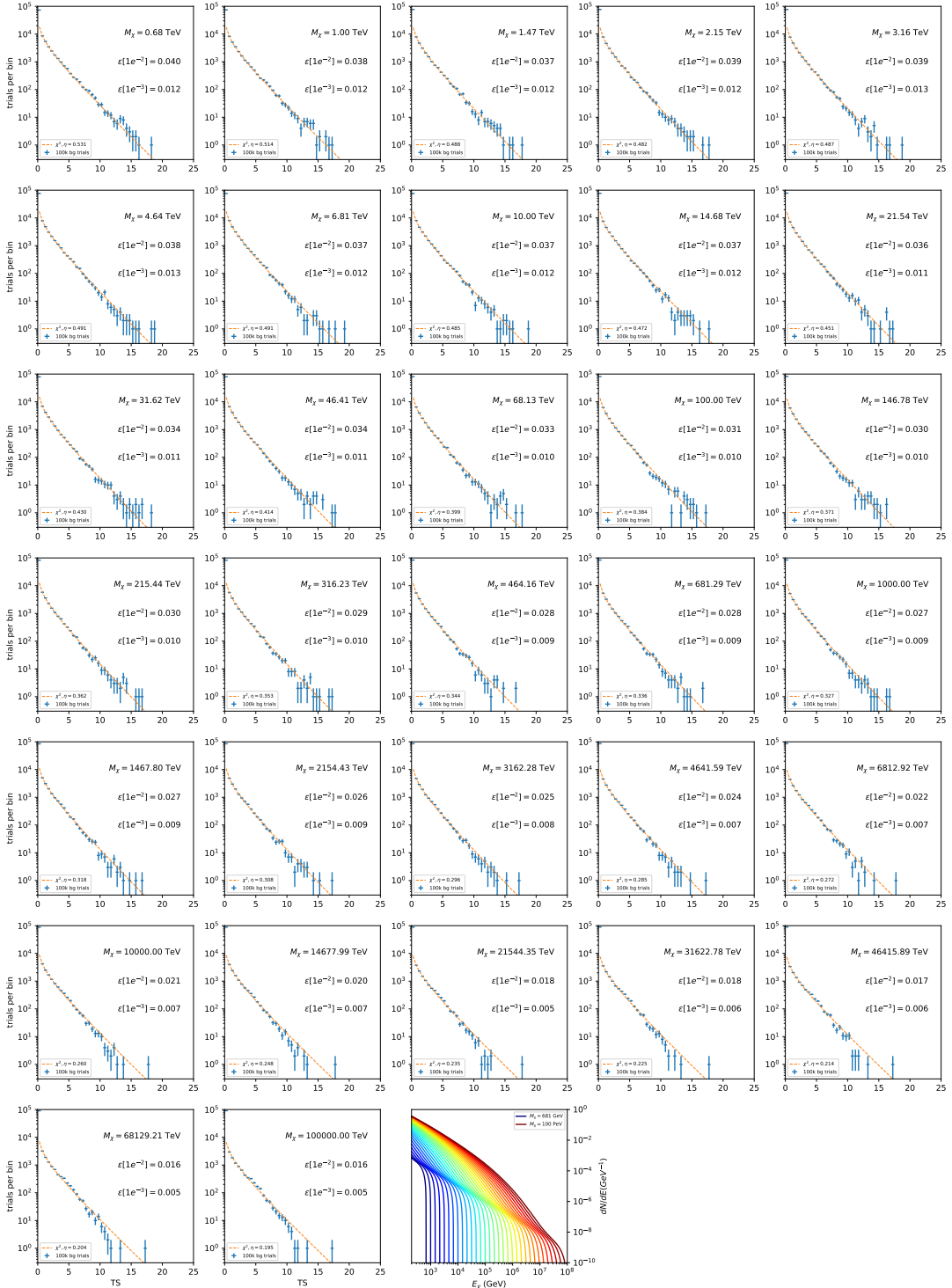


Figure 7.13 Same as Fig. 7.6 for 15,  $\mathcal{GS}$   $J$ -factor, stacked sources and  $\chi\chi \rightarrow t\bar{t}$ .

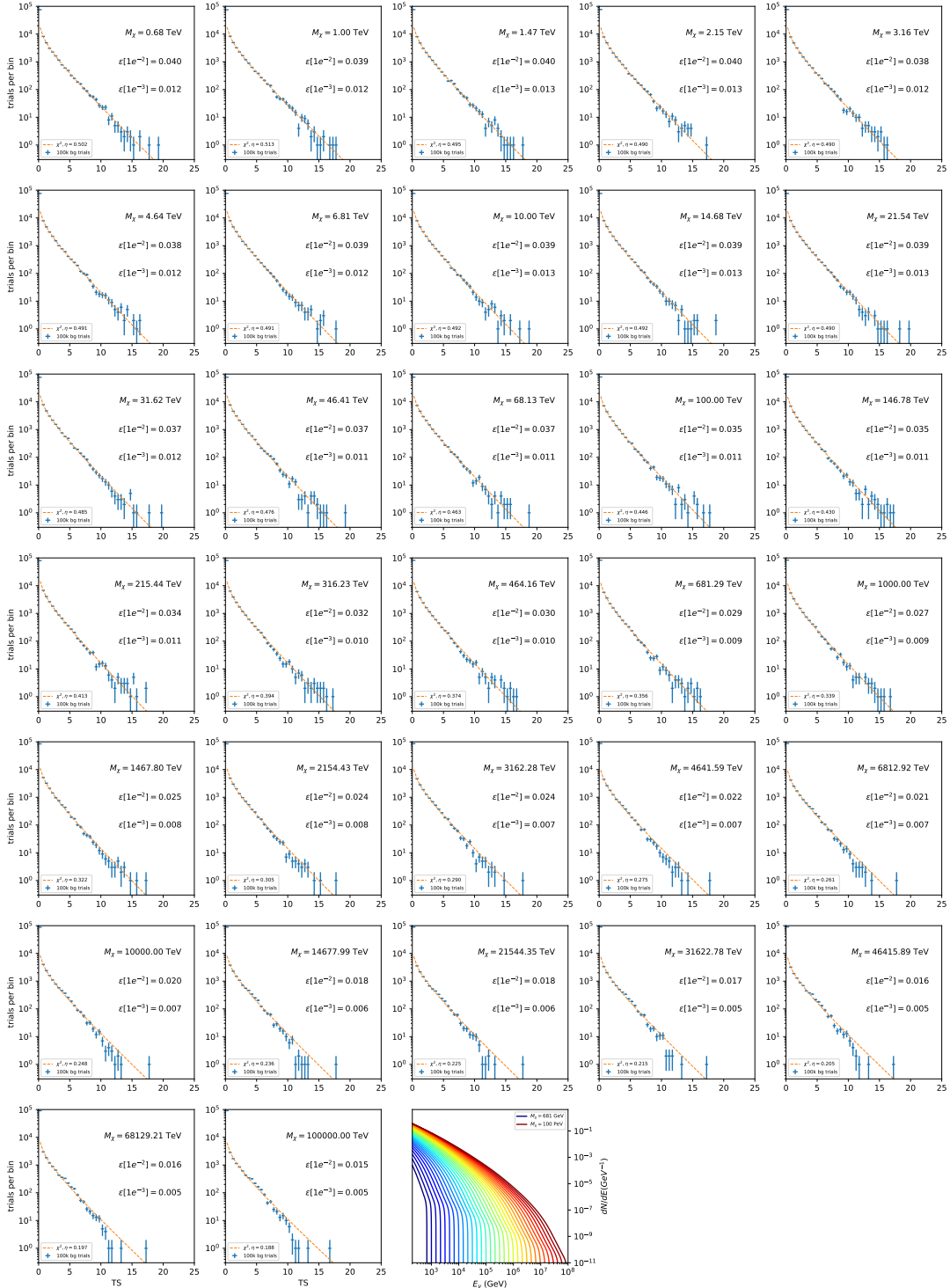


Figure 7.14 Same as Fig. 7.6 for 15,  $\mathcal{GS}$  J-factor, stacked sources and  $\chi\chi \rightarrow u\bar{u}$ .

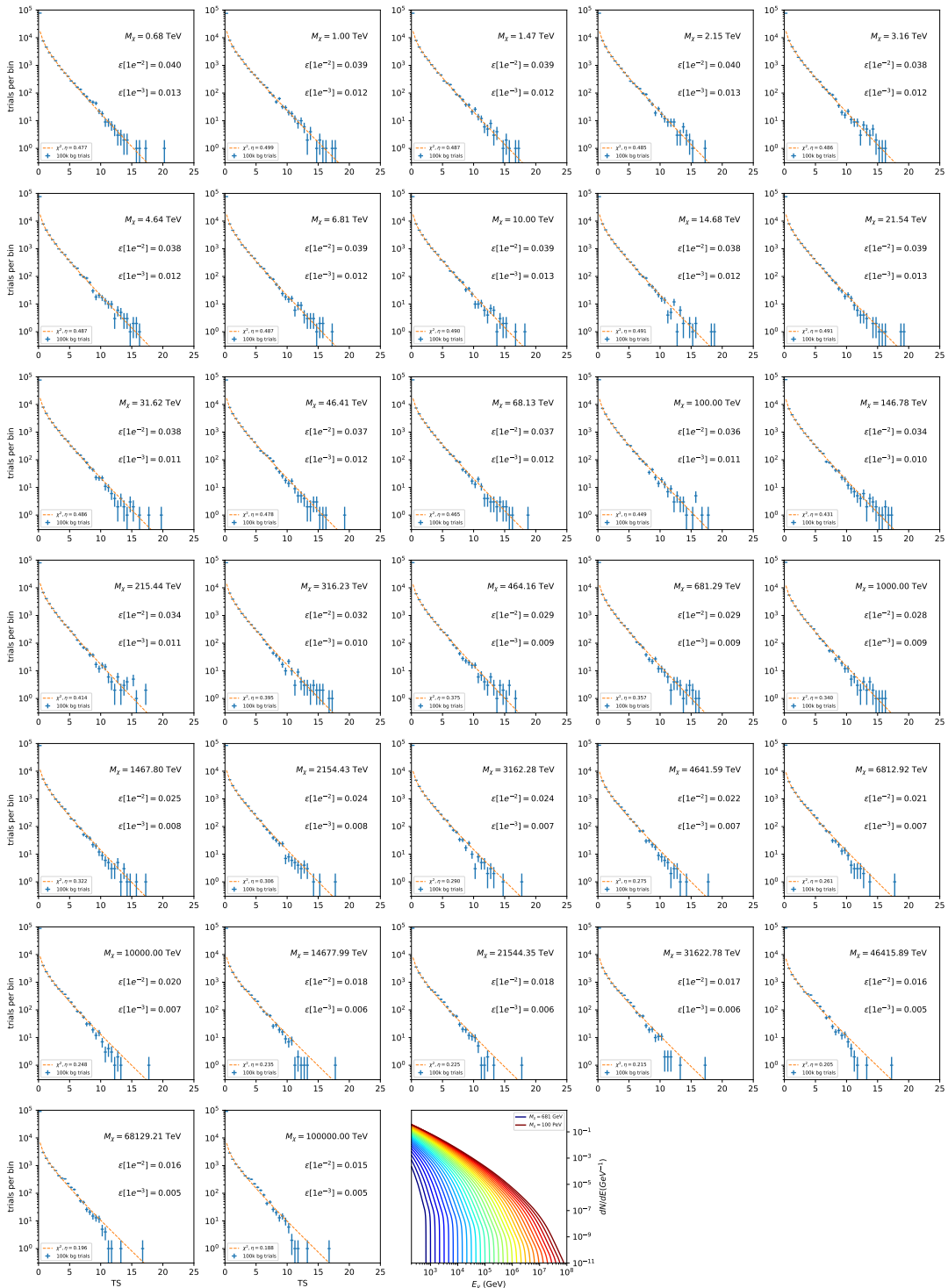


Figure 7.15 Same as Fig. 7.6 for 15,  $\mathcal{G}\mathcal{S}$  J-factor, stacked sources and  $\chi\chi \rightarrow d\bar{d}$ .

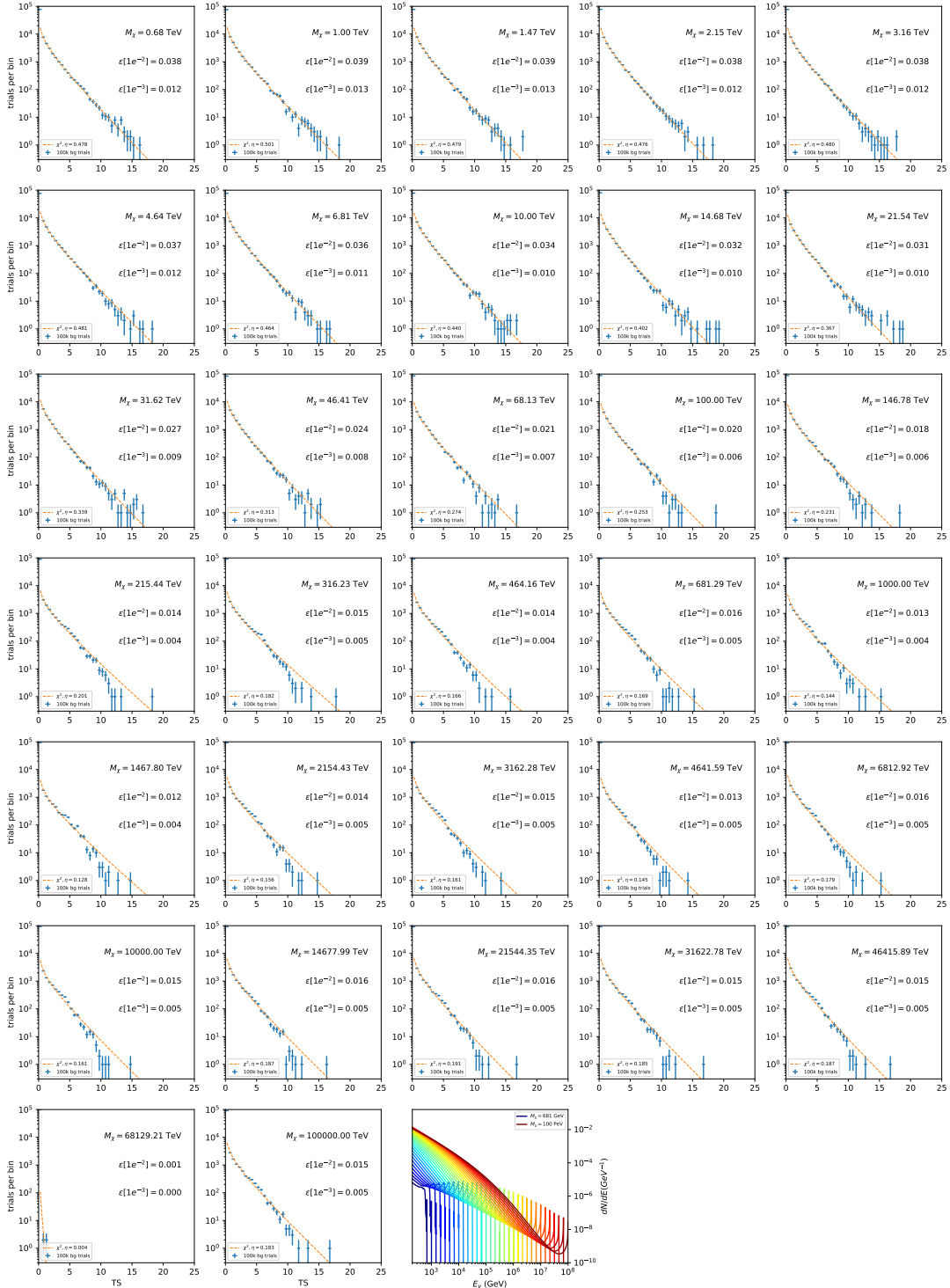


Figure 7.16 Same as Fig. 7.6 for 15,  $\mathcal{GS}$  J-factor, stacked sources and  $\chi\chi \rightarrow e\bar{e}$ .

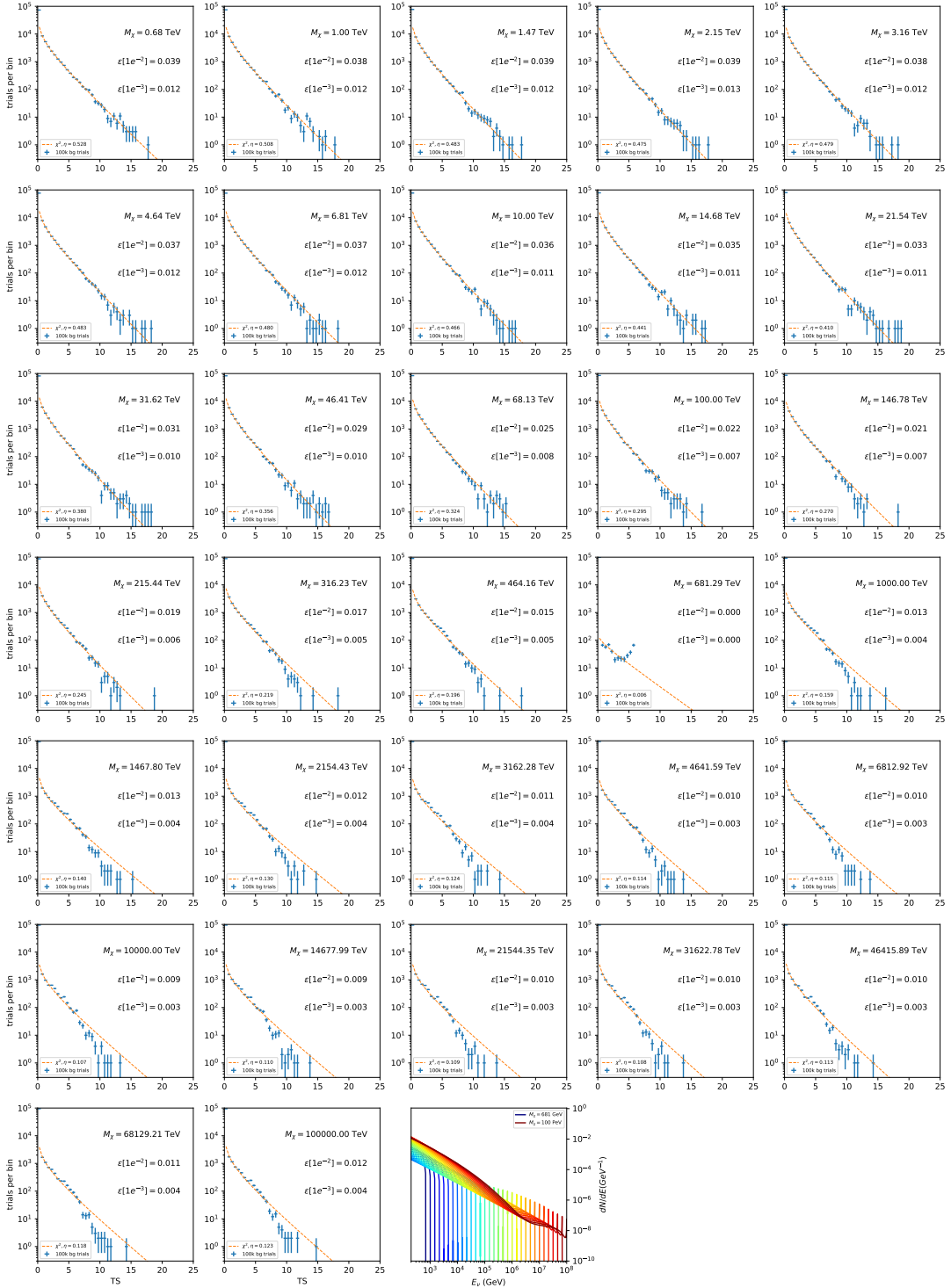


Figure 7.17 Same as Fig. 7.6 for 15,  $\mathcal{GS}$   $J$ -factor, stacked sources and  $\chi\chi \rightarrow \mu\bar{\mu}$ .

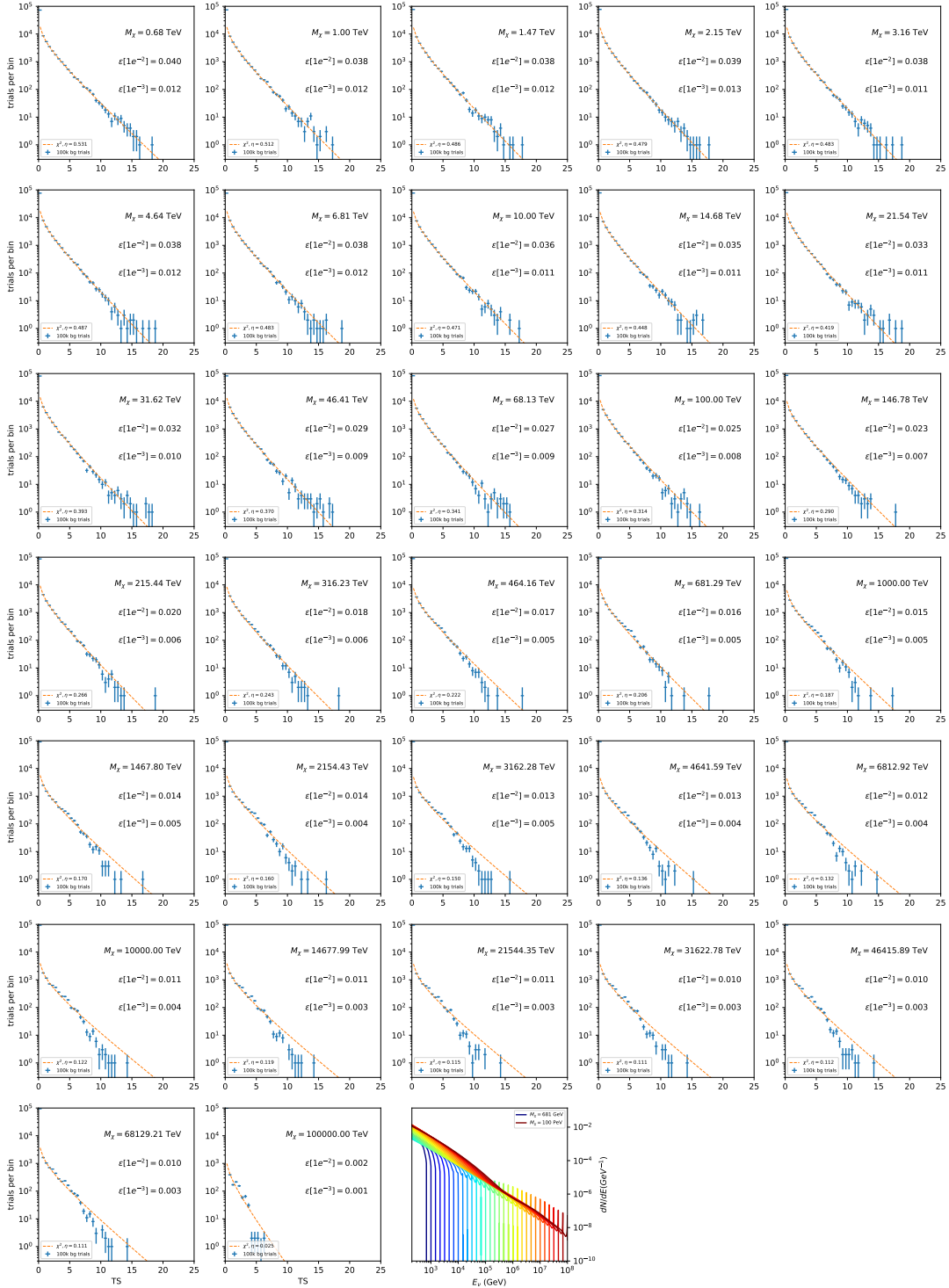


Figure 7.18 Same as Fig. 7.6 for 15,  $\mathcal{GS}$   $J$ -factor, stacked sources and  $\chi\chi \rightarrow \tau\bar{\tau}$ .

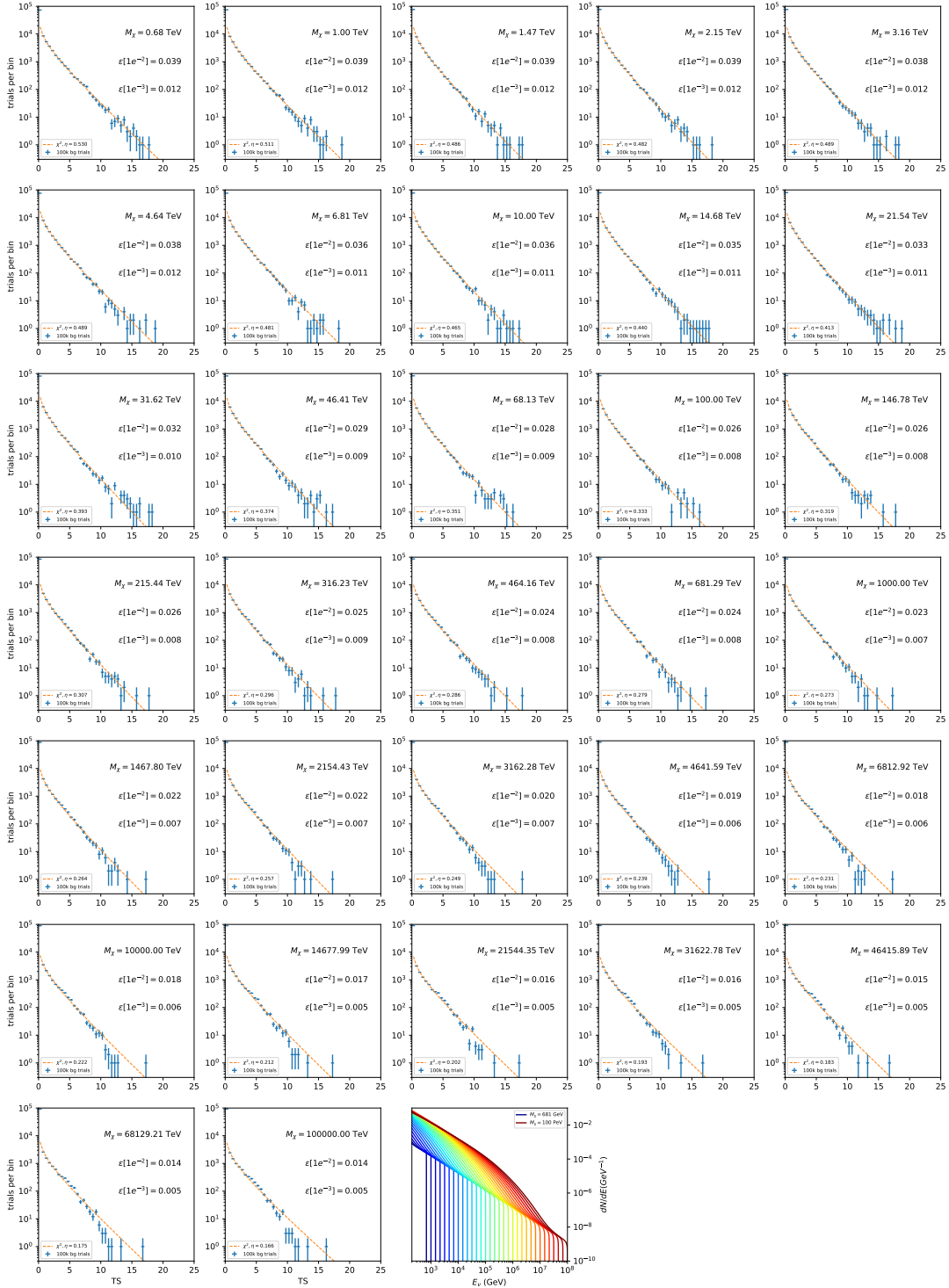


Figure 7.19 Same as Fig. 7.6 for 15, GS J-factor, stacked sources and  $\chi\chi \rightarrow W^+W^-$ .

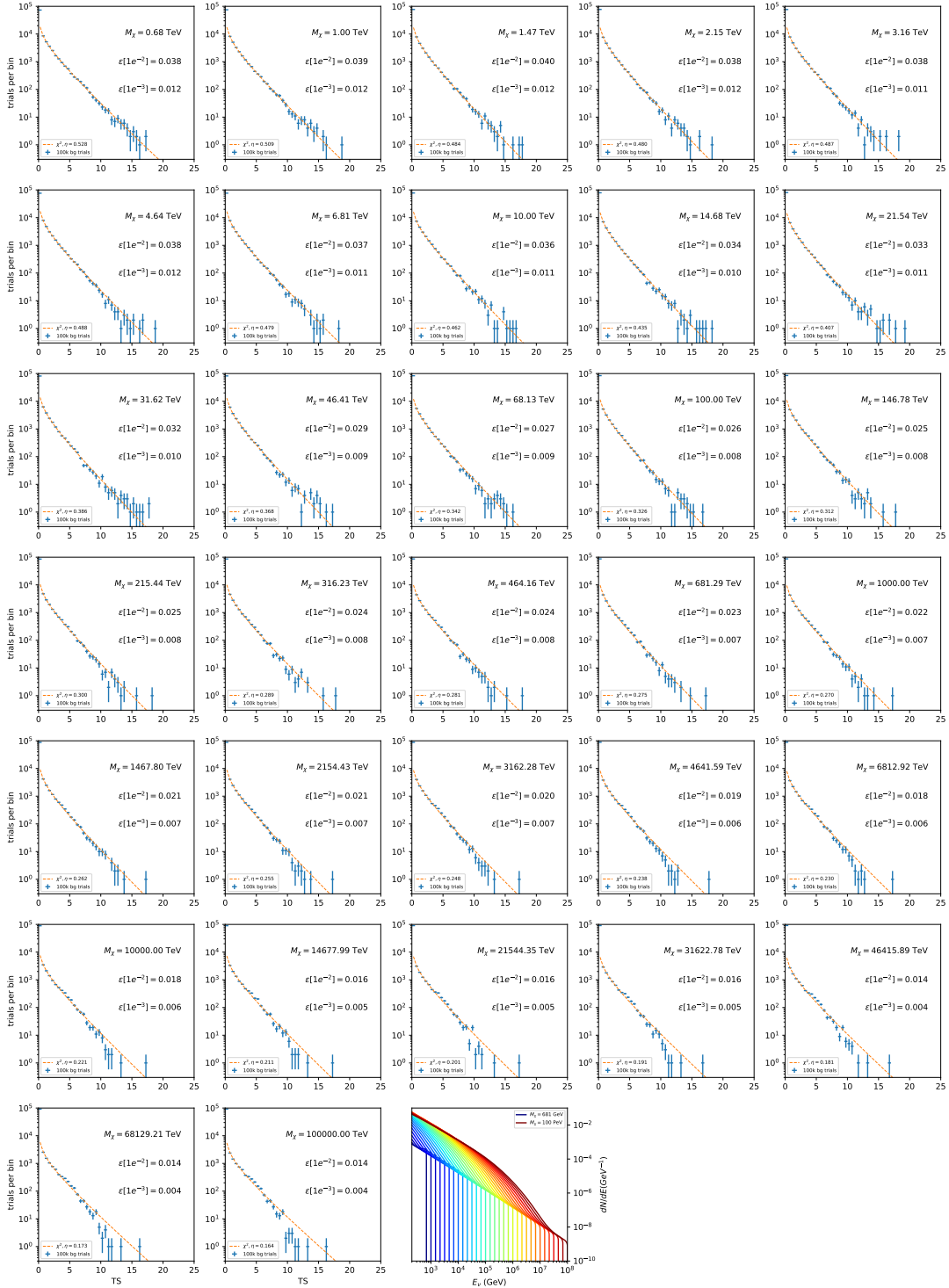


Figure 7.20 Same as Fig. 7.6 for 15,  $\mathcal{GS}$  J-factor, stacked sources and  $\chi\chi \rightarrow ZZ$ .

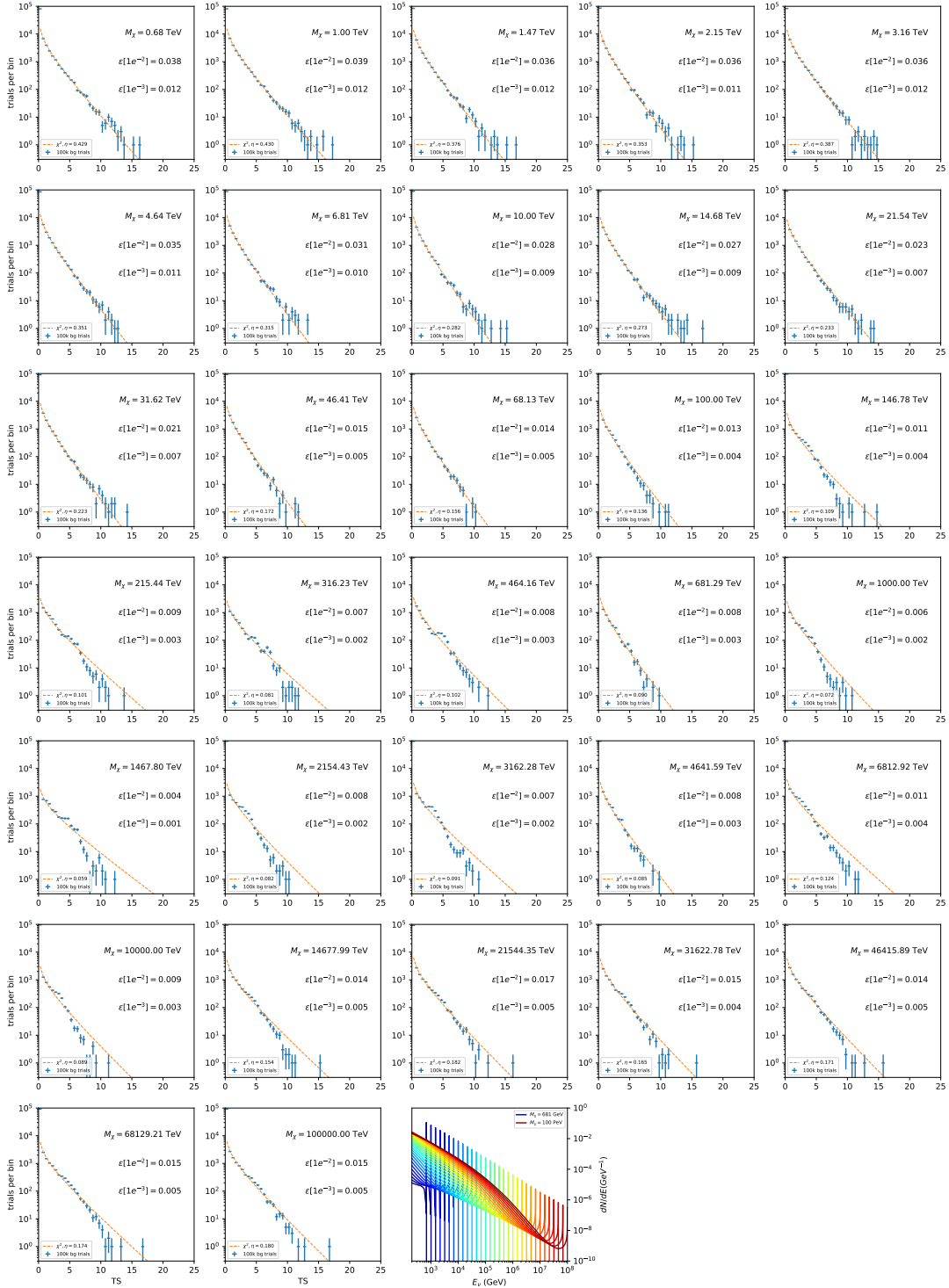


Figure 7.21 Same as Fig. 7.6 for 15,  $\mathcal{GS}$   $J$ -factor, stacked sources and  $\chi\chi \rightarrow \nu_e \bar{\nu}_e$ .

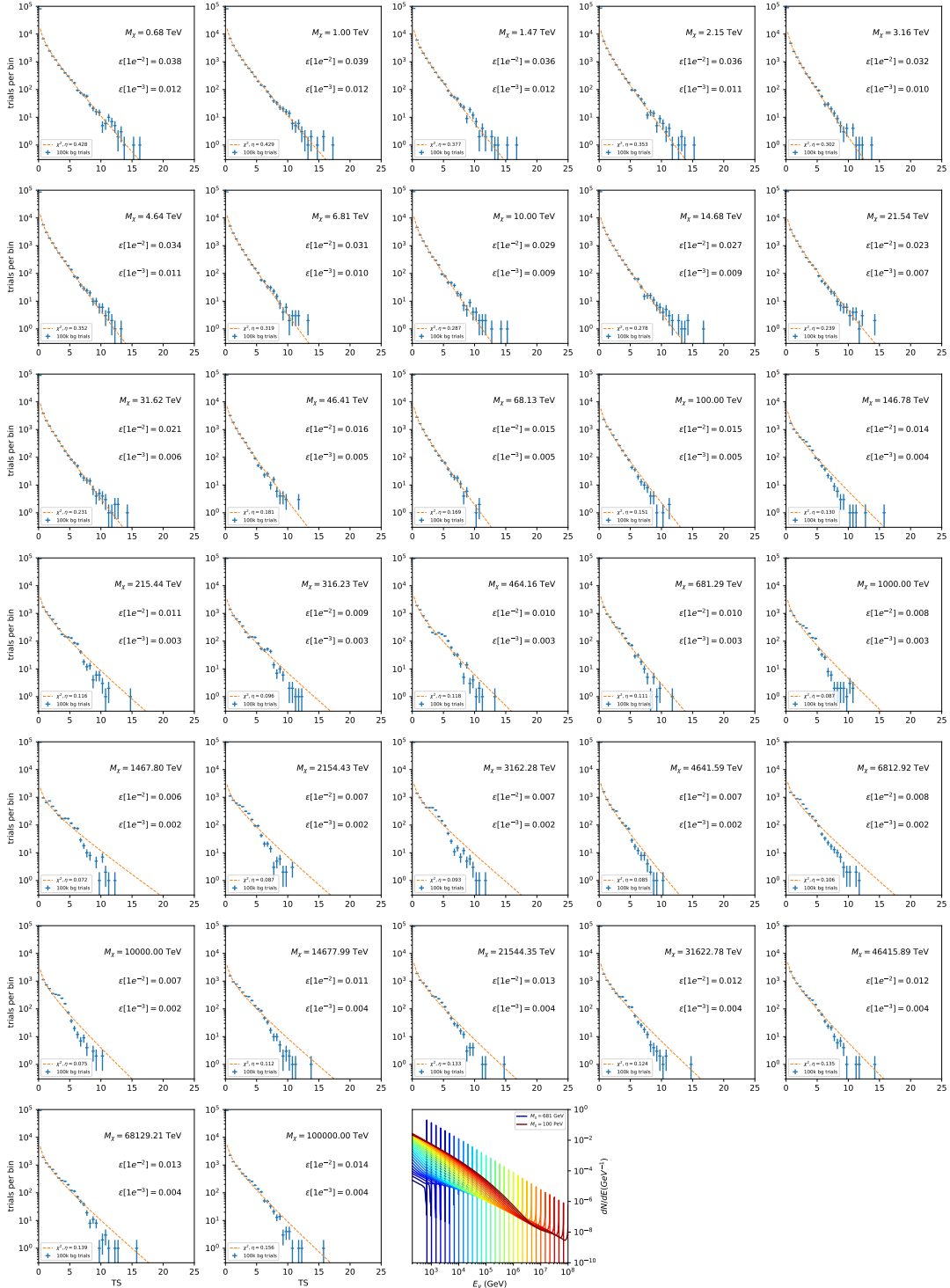


Figure 7.22 Same as Fig. 7.6 for 15, GS J-factor, stacked sources and  $\chi\chi \rightarrow \nu_\mu \bar{\nu}_\mu$ .

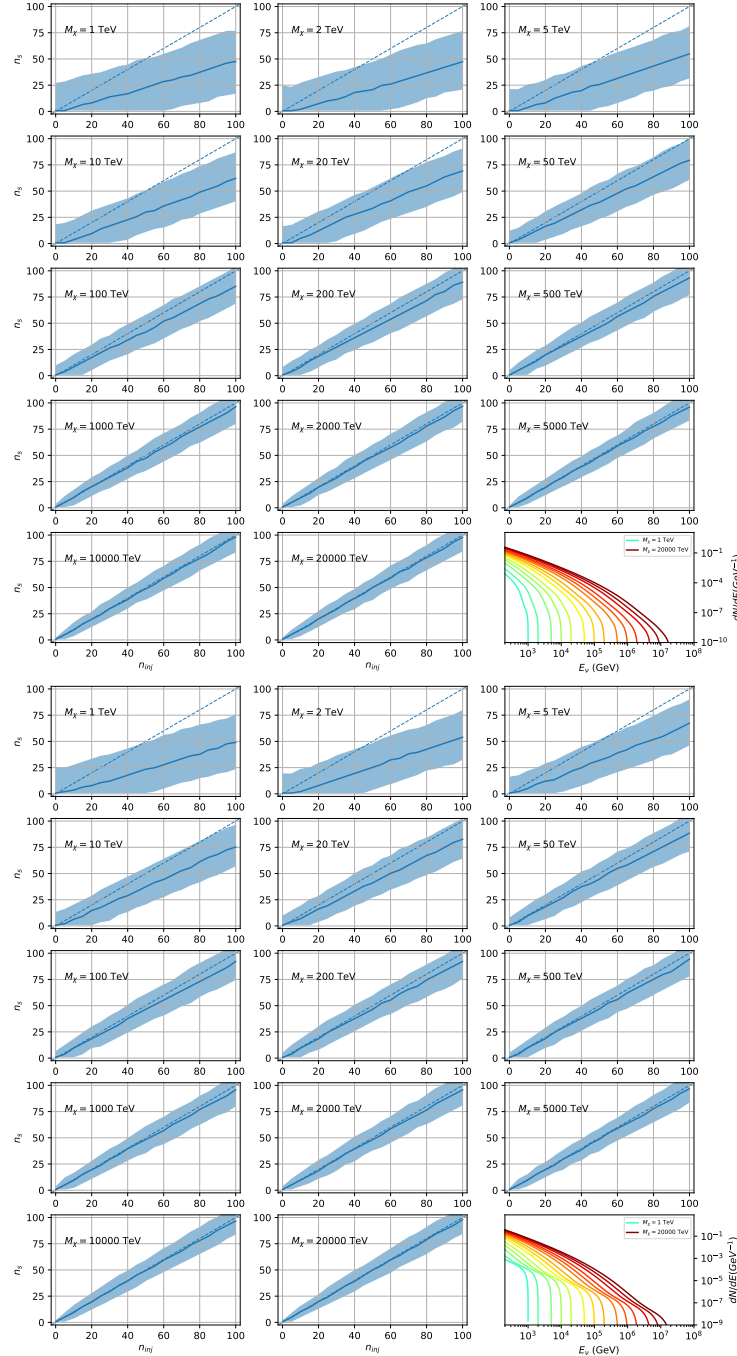


Figure 7.23 Signal Recovery study for an analysis with 15 stacked sources using the  $\mathcal{GS}$   $J$ -factors [45]. Each panel block represents 14 studies for DM mass ranging between 1 TeV and 20 PeV and one annihilation channel. Top panel block is for  $\chi\chi \rightarrow b\bar{b}$ . Bottom panel block is for  $\chi\chi \rightarrow t\bar{t}$ . Each panel block features every spectral model used as input in the bottom-right subpanel. The remaining panels show  $N_{inj}$  as the number of signal events injected into background simulation. Whereas,  $N_s$  is the number of signal events recovered from analyzing the injected simulation. Blue line represents the median values of 100 simulations. Light blue bands show the  $1\sigma$  statistical uncertainty around the median.

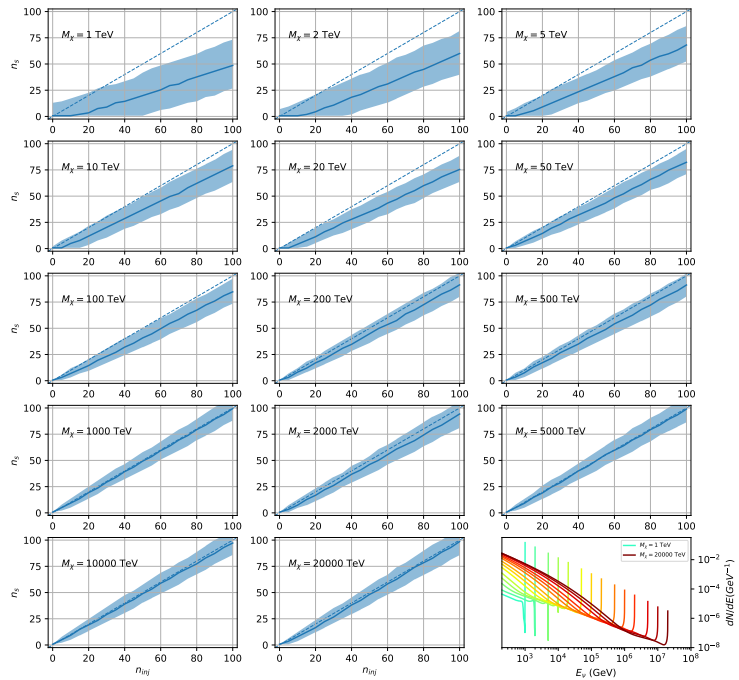


Figure 7.24 Same as Fig. 7.23 but for  $\chi\chi \rightarrow \nu_\mu\bar{\nu}_\mu$ .

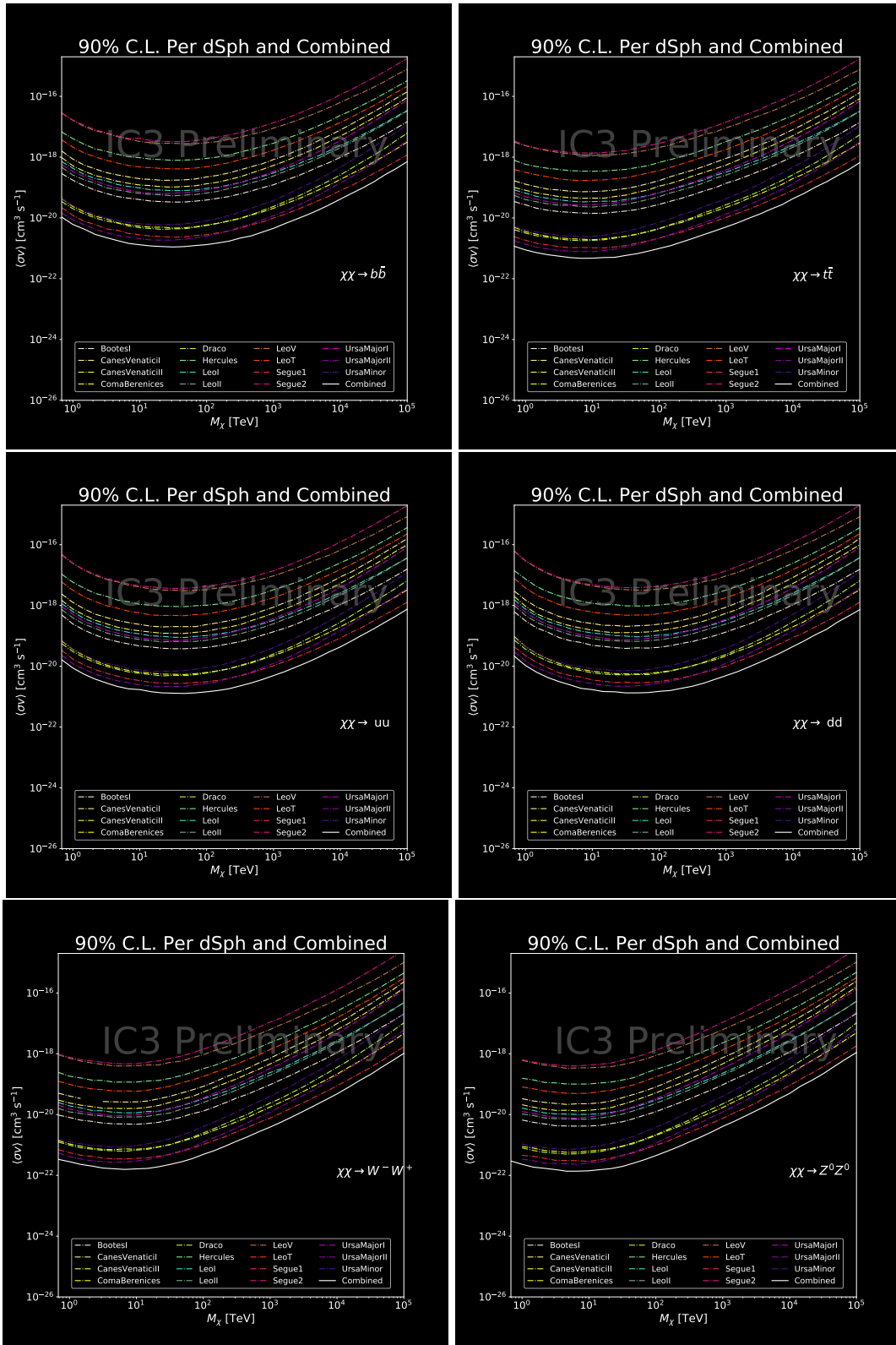


Figure 7.25 Words. I prent Icecibe Sensitivities weeee

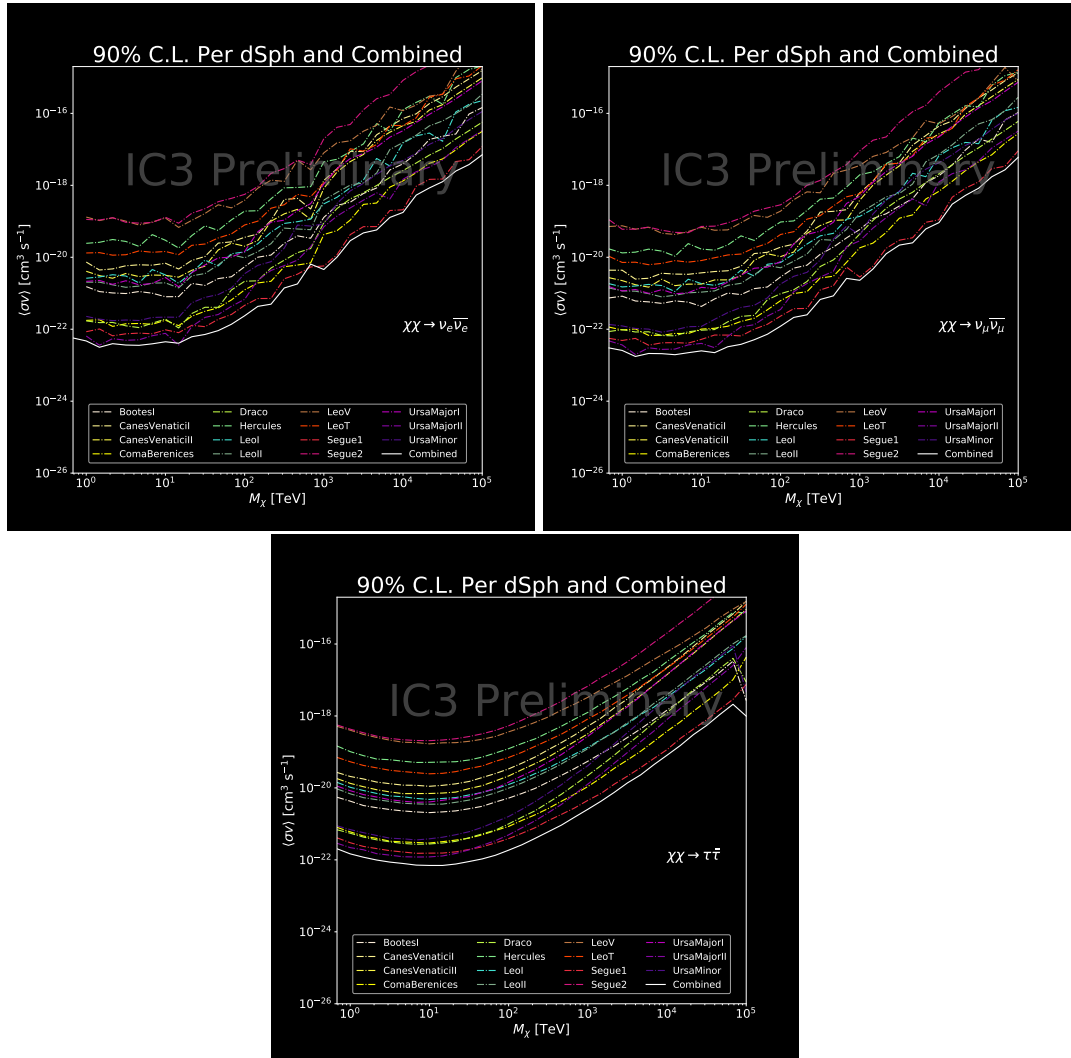


Figure 7.26 Words. I prent Icecibe Sensitivities weeee

1696

## **CHAPTER 8**

### **NU DUCK**

## MULTI-EXPERIMENT SUPPLEMENTARY FIGURES

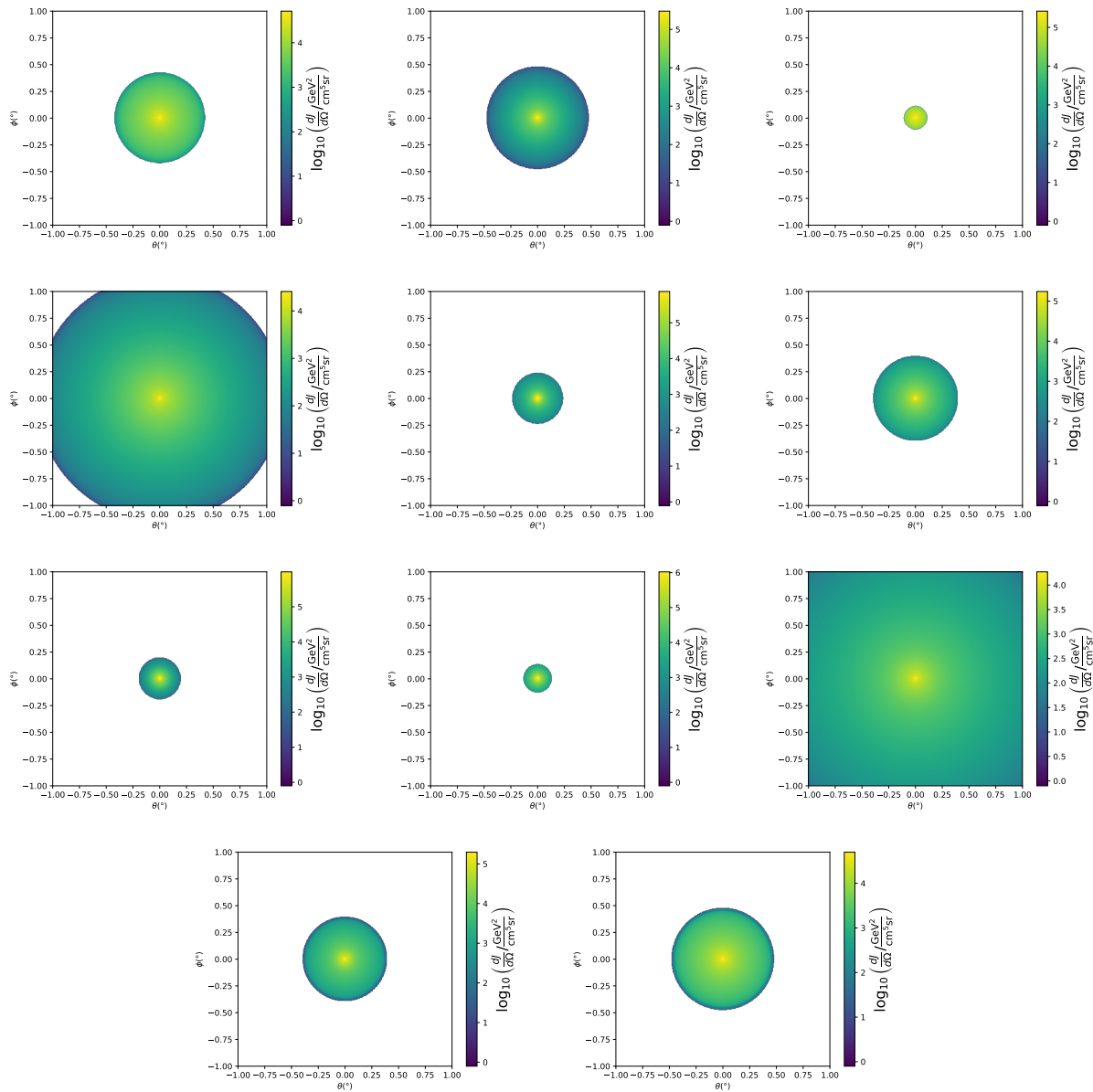


Figure A.1 Sister figure to Figure 5.3. Sources in the first row from left to right: Bootes I, Canes Venatici I, II. In second row: Draco, Hercules, Leo I. In the first row: Leo II, Leo IV, Sextans. In the final row: Ursa Major I, Ursa Major II.

## APPENDIX B

### 1698 MULTITHREADING DARK MATTER ANALYSES SUPPLEMENTARY MATERIAL

#### 1699 B.1 Remaining Spectral Models

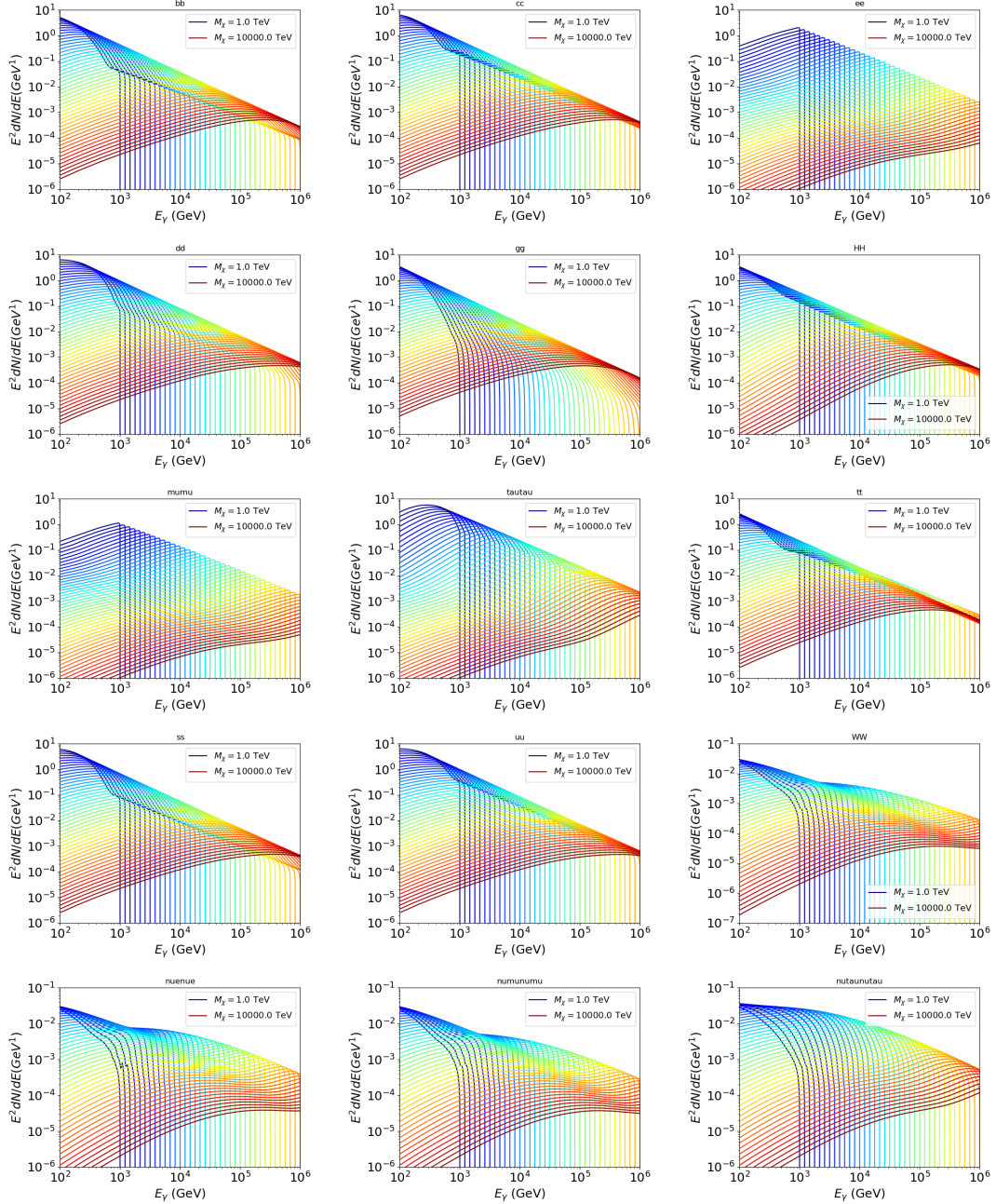


Figure B.1 Sister figure to Figure 6.2 for remaining SM primary annihilation channels studied for this thesis. These did not require any post generation smoothing and so are directly pulled from [65] with a binning scheme most helpful for a HAWC analysis.

## 1700 B.2 mpu\_analysis.py

```
17011 import warnings
17012 with warnings.catch_warnings():
17013     warnings.simplefilter("ignore")
17014 # Python base libraries
17015 import os
17016 import sys
17017 import time
17018 # Import general libraries with namespace
17019 import matplotlib
17020 # Necessary for computing on cluster
17021 matplotlib.use("agg")
17022 import numpy as np
17023 import multiprocessing as mp
17024 # Import HAWC software
17025 sys.path.insert(1, os.path.join(os.environ['HOME'], 'hawc_software', 'threeML-
17026     analysis-scripts', 'fitModel'))
17027 from analysis_modules import *
17028 from threeML import *
17029 from hawc_hal import HAL, HealpixConeROI
17030 from threeML.minimizer.minimization import FitFailed
17031 # Import Dark Matter HAWC Libraries
17032 import analysis_utils as au
17033 import spectra as spec
17034 import sources as srcs
17035
17036 #* READ ONLY PATHS This block will change eventually
17037 MASS_LIST = './plotting/studies/nd/masses.txt'
17038 CHAN_LIST = './plotting/studies/nd/chans.txt'
17039
17040 #* WRITE PATHS, default location is to scratch
17041 OUT_PATH = os.path.join(os.environ["SCRATCH"], os.environ["USER"], 'New_duck')
```

```

17321 print('Our out path is going to be {}'.format(OUT_PATH))
17332
17343 # Define parallel Function. Can also be run serially
17354 def some_mass_fit(sigVs, datalist, shape, dSph, jfactor, mass_chan,
17365                 progress=None, log_file='', queue=None, i_job=0):
17376
17387     if progress is None:
17398         progress = [0]
17409     else: # Create log files for each thread
17410         log_file = log_file.replace('.log', '_ThreadNo_')
17421         log_file = log_file + str(i_job) + ".log"
17432         sys.stdout = open(log_file, "w")
17443
17454     fits = []
17465
17476     try:
17487         for m_c in mass_chan:
17498             print(f'Mass chan tuple: {m_c}')
17509             mass = int(m_c[0])
17510             ch = m_c[1]
17521             # Build path to output files
17532             outPath = os.path.join(OUT_PATH, ch, dSph)
17543             au.ut.ensure_dir(outPath)
17554
17565             if progress[i_job] < 0:
17576                 # If the master gets a Keyboard interrupt, commit suicide.
17587                 break
17598
17609                 ### Start Model Building for DM mass and SM channel #####
17610                 spectrum = spec.DM_models.HDMSpectra()
17621                 spectrum.set_channel(ch)
17632
17643                 myDwarf = ExtendedSource(dSph, spatial_shape=shape,

```

```

17654                     spectral_shape=spectrum)

17655

17656     spectrum.J = jfactor * u.GeV**2 / u.cm**5
17657     spectrum.sigmav = 1e-24 * u.cm**3 / u.s
17658     spectrum.set_dm_mass(mass * u.GeV)

17659

17660     spectrum.sigmav.bounds = (1e-30, 1e-12)
17661     model = Model(myDwarf)
17662     ##### End model Building #####
17663

17664     jl = JointLikelihood(model, datalist, verbose=False)
17665

17666     try:
17667         result, lhdf = jl.fit(compute_covariance=False)
17668         ts = -2.* (jl.minus_log_like_profile(1e-30) - jl.
17669         _current_minimum)
17670
17671         # Also profile the LLH vs sv
17672         ll = jl.get_contours(spectrum.sigmav, sigVs[0],
17673                               sigVs[-1], len(sigVs),
17674                               progress=False, log=['False'])
17675
17676
17677         sigv_ll = au.ut.calc_95_from_profile(ll[0], ll[2])
17678
17679         # Write results to file
17680         outFileLL = outPath+f"/LL_{dSph}_{ch}_mass{int(mass)}_GD.txt"
17681         np.savetxt(outFileLL, (sigVs, ll[2]),
17682                     delimiter='\t', header='sigV\tLL\n')
17683
17684
17685         with open(outPath+f"/results_{dSph}_{ch}_mass{int(mass)}_GD.
17686         txt", "w") as results_file:
17687             results_file.write("mDM [GeV]\tsigV_95\tsigV_B.F.\n")
17688
17689             results_file.write("%i\t%.5E\t%.5E\t%.5E"%(mass, sigv_ll,
17690
17691                                         ts, result.value[0]))

```

```

17985         # End write to file
17996     except FitFailed: # Don't kill all threads if a fit fails
18007         print("Fit failed. Go back and calculate this spectral model
1801    later")
18028             fits.append((ch, mass, -1, -1))
18039             with open(log_file+'.fail', 'w') as f_file:
18040                 f_file.write(f'{ch}, {mass}\n')
18051
18062             progress[i_job] += 1
18073             matplotlib.pyplot.close() # Prevent leaky memory
18084
18095             fits.append((ch, mass, result.value[0], ts))
18106             progress[i_job] += 1
18117             matplotlib.pyplot.close()
18128     except KeyboardInterrupt:
18139         progress[i_job] = -1
18140
18151     fits = np.array(fits)
18162     if queue is None:
18173         return fits
18184     else:
18195         queue.put((i_job, fits))
18206
18217 def main(args):
18228     masses = np.loadtxt(MASS_LIST, dtype=int)
18239     chans = np.loadtxt(CHAN_LIST, delimiter=',', dtype=str)
18240     mass_chan = au.ut.permute_lists(chans, masses)
18251
18262     print(f"DM masses for this study are: {masses}")
18273     print(f"SM Channels for this study are XX -> {chans}")
18284     print(mass_chan)
18295
18306     # extract information from input argument

```

```

18317 dSph = args.dSph
18328 data_mngr = au.ut.Data_Selector('P5_NN_2D')
18339 dm_profile = srcts.Spatial_DM(args.catalog, dSph, args.sigma, args.decay)
18340
18351     ### Extract Source Information ####
18362 if dm_profile.get_dec() < -22.0 or dm_profile.get_dec() > 62.0:
18373     raise ValueError("HAWC can't see this source D: Exitting now...")
18384
18395 print(f'{dSph} information')
18406 print(f'jfac: {dm_profile.get_factor()}\tRA: {dm_profile.get_ra()}\tDec: {dm_profile.get_dec()}\n')
18427
18438 shape = SpatialTemplate_2D(fits_file=dm_profile.get_src_fits())
18449     ### Finish Extract Source Information ####
18450
18461     ### LOAD HAWC DATA ####
18472 roi = HealpixConeROI(data_radius=2.0, model_radius=8.0,
18483                         ra=dm_profile.get_ra(), dec=dm_profile.get_dec())
18494 bins = choose_bins.analysis_bins(args, dec=dm_profile.get_dec())
18505
18516 hawc = HAL(dSph, data_mngr.get_datmap(), data_mngr.get_detres(), roi)
18527 hawc.set_active_measurements(bin_list=bins)
18538 datalist = DataList(hawc)
18549     ### FINISH LOAD HAWC DATA ####
18550
18561 # set up SigV sampling. This sample is somewhat standardized
18572 sigVs = np.logspace(-28,-18, 1001, endpoint=True) # NOTE This will change
1858 whith HDM
18593
18604 if args.n_threads == 1:
18615     # No need to start || programming just iterate over the masses
18626 kw_arg = dict(sigVs=sigVs, datalist=datalist, shape=shape, dSph=dSph,
18637                 jfactor=dm_profile.get_factor(), mass_chan=mass_chan,

```

```

18648                 log_file=args.log)
18659             some_mass_fit(**kw_arg)
18660         else:
18671             # I Really want to suppress TQMD output
18682             from tqdm import tqdm
18693             from functools import partialmethod
18704             tqdm.__init__ = partialmethod(tqdm.__init__, disable=True)
18715
18726             x = np.array_split(mass_chan, args.n_threads)
18737             n_jobs = len(x)
18748
18759             print("Thread jobs summary by mass and SM channel")
18760             for xi in x:
18771                 print(f'{xi}')
18782
18793             queue = mp.Queue()
18804             progress = mp.Array('i', np.zeros(n_jobs, dtype=int))
18815
18826             # Define task pool that will be split amongsts threads
18837             kw_args = [dict(sigVs=sigVs, datalist=datalist, shape=shape,
18848                             dSph=dSph, jfactor=dm_profile.get_factor(),
18859                             mass_chan=mass_chan, progress=progress,
18860                             queue=queue, i_job=i, log_file=args.log)
18871                 for i, mass_chan in enumerate(x)]
18882
18893             # Define each process
18904             procs = [mp.Process(target=some_mass_fit, kwargs=kw_args[i]) \
18915                 for i in range(n_jobs)]
18926
18937             ### Start MASTER Thread only code block ###
18948             # Begin running all child threads
18959             for proc in procs: proc.start()
18960

```

```

18971     try:
18982         # In this case, the master does nothing except monitor progress of
1899      the threads
19003         # In an ideal world, the master thread also does some computation.
19014         n_complete = np.sum(progress)
19025         while_count = 0
19036
19047         while n_complete < len(mass_chan):
19058
19069             if np.any(np.asarray(progress) < 0):
19070                 # This was no threads are stranded when killing the script
19081                 raise KeyboardInterrupt()
19092             if while_count%1000 == 0:
19103                 print(f"{np.sum(progress)} of {len(mass_chan)} finished")
19114
19125             n_complete = np.sum(progress)
19136             time.sleep(.25)
19147             while_count += 1
19158
19169         except KeyboardInterrupt:
19170             # signal to jobs that it's time to stop
19181             for i in range(n_jobs):
19192                 progress[i] = -2
19203                 print('\nKeyboardInterrupt: terminating early.')
19214             ### End MASTER Thread only code block ####
19225
19236             fitss = [queue.get() for proc in procs]
19247             print(fitss)
19258             print(f'Thread statuses: {progress[:]}')
19269
19270             # putting results in a file
19281
19292             print("QUACK! All Done!")

```

```

19303
19314
19325 if __name__ == '__main__':
19336     import argparse
19347
19358     p = argparse.ArgumentParser(description="Run a DM annihilation analysis on
1936         a dwarf spheroidal for a specific SM channel for DM masses [1 TeV to 10
1937         PeV]")
19389
19390     # Dwarf spatial modeling arguements
19401     p.add_argument("-ds", "--dSph", type=str,
19412                     help="dwarf spheroidal galaxy to be studied", required=
1942 True)
19433     p.add_argument("-cat", "--catalog", type=str, choices=['GS15', 'LS20'],
19444                     default='LS20', help="source catalog used")
19455     p.add_argument("-sig", "--sigma", type=int, choices=[-1, 0, 1], default=0,
19466                     help="Spatial model uncertainty. 0 corresponds to the
1947 median. +/-1 correspond to the +/-1sigma uncertainty respectively.")
19487
19498     # Arguements for the energy estimators
19509     p.add_argument("-e", "--estimator", type=str,
19510                     choices=['P5_NHIT', 'P5_NN_2D'],
19521                     default="P5_NN_2D", required=False,
19532                     help="The energy estimator choice. Options are: P5_NHIT,
1954 P5_NN_2D. GP not supported (yet).")
19553     p.add_argument("--use-bins", default=None, nargs="*",
19564                     help="Bins to use for the analysis", dest="use_bins")
19575     p.add_argument('--select_bins_by_energy', default=None, nargs="*",
19586                     help="Does nothing. May fill in later once better
1959 understood")
19607     p.add_argument('--select_bins_by_fhit', default=None, nargs="*",
19618                     help="Also does nothing see above")
19629     p.add_argument( '-ex', "--exclude", default=None, nargs="*",

```

```

19630         help="Exclude Bins", dest="exclude")

19641

19652 # Computing and logging arguements.

19663 p.add_argument('-nt', '--n_threads', type=int, default=1,
19674                         help='Maximum number of threads spawned by script. Default
1968     is 4')

19695 p.add_argument('-log', '--log', type=str, required=True,
19706                         help='Name for log files. Especially needed for threads')

19717

19728 p.add_argument('--decay', action="store_true",
19739                         help='Set spectral DM hypothesis to decay')

19740

19751 args = p.parse_args()

19762 print(args.decay)

19773 if args.exclude is None: # default exclude bins 0 and 1
19784     args.exclude = ['B0C0Ea', 'B0C0Eb', 'B0C0Ec', 'B0C0Ed', 'B0C0Ee']

19795

19806 if args.decay: OUT_PATH += '_dec'
19817 else: OUT_PATH += '_ann'

19828

19839 OUT_PATH = OUT_PATH + '_' + args.catalog
19840 if args.sigma != 0: OUT_PATH += f'_{args.sigma}sig'

19851

19862 main(args)

```

1987 **B.3 Comparison with Glory Duck**

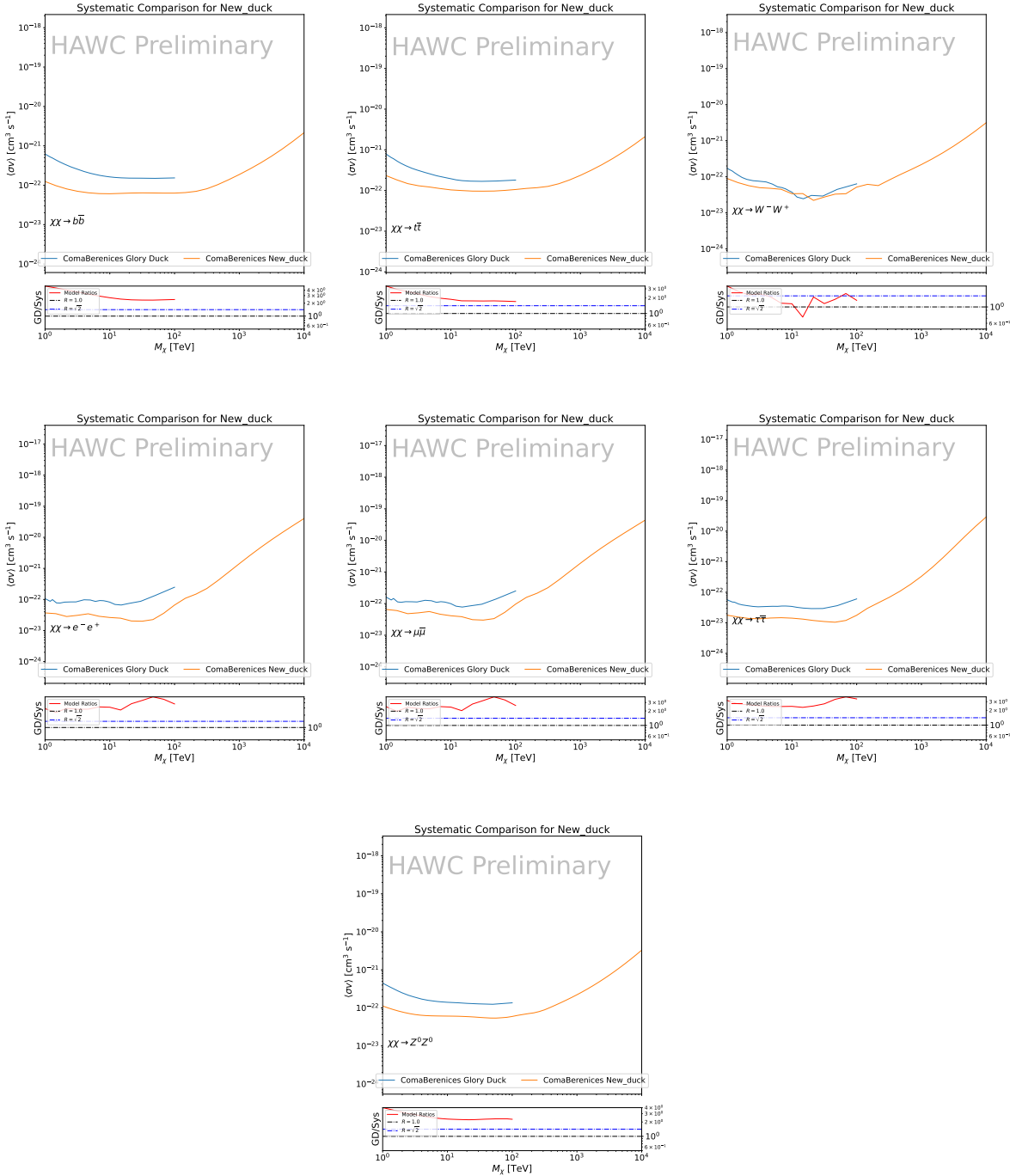


Figure B.2 TODO: fill this out

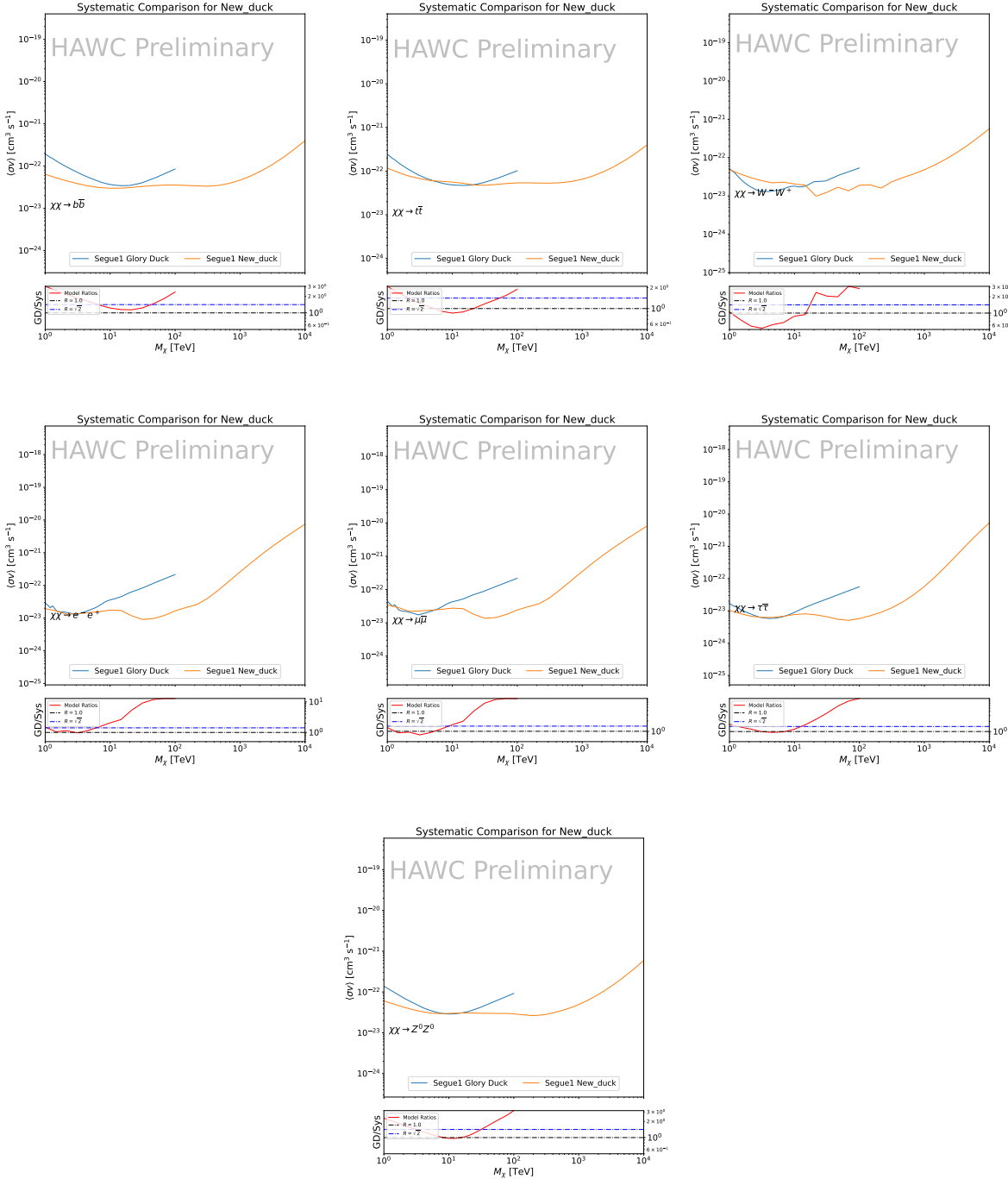


Figure B.3 TODO: fill this out

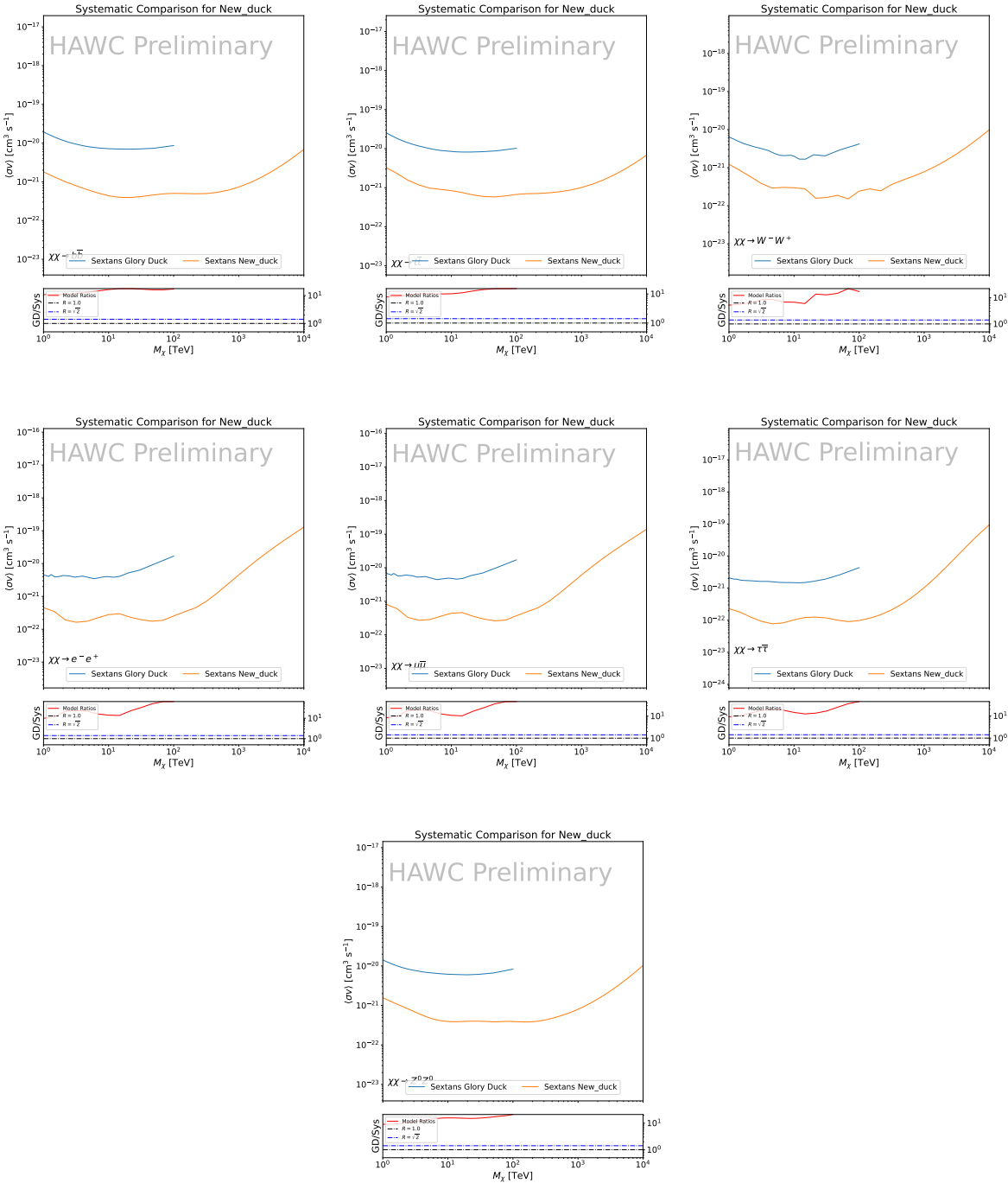


Figure B.4 TODO: fill this out

## APPENDIX C

### 1988 ICECUBE HEAVY DARK MATTER ANALYSIS SUPPLEMENTARY MATERIAL

#### 1989 C.1 Docker Image for Oscillating Neutrino Spectra

```
19901 FROM ubuntu:18.04
19912
19923 # Execute commands to install software packages
19934 RUN apt -y update
19945
19956   # Install utility programs
19967 RUN apt -y install vim wget git cmake
19978
19989 ARG DEBIAN_FRONTEND=noninteractive
19990
20001   # Install python
20012 RUN apt -y install python python-dev python-pip libjpeg-dev zlib1g-dev
20023
20034   # We need Python2 for installing Charon.
20045 RUN apt -y install python-numpy python-sympy python-matplotlib \
20056           python-sympy python-h5py python-astropy python-ipython
20067
20078   # Install dependencies of Charon : SQuIDS, NuSQuIDS
20089 RUN apt -y install libgsl-dev libgslcblas0 libgsl23 gsl-bin pkg-config
20090   # Install SQuIDS
20101 RUN mkdir /home/SQuIDS /home/SQuIDS_install
20112 WORKDIR /home/SQuIDS
20123 RUN git clone https://github.com/jsalvado/SQuIDS.git
20134 WORKDIR /home/SQuIDS/SQuIDS
20145 RUN git checkout 7ad9ba7c6ad06d1f0fa8418f937ebf1a403fef90
20156   # Before executing "make install" an environmental variable has to be set.
20167 ENV PKG_CONFIG_PATH=/home/SQuIDS/SQuIDS/lib
20178 RUN ./configure --prefix=../SQuIDS_install \
```

```

20189     && make
20190 RUN make install
20201
20212     # Set up an environmental varialbe that is required to install nuSQuIDS..
20223 ENV SQuIDS=/home/SQuIDS/SQuIDS
20234 ENV LD_LIBRARY_PATH=$SQuIDS/lib:$LD_LIBRARY_PATH
20245
20256     # Install NuSQuIDS
20267 RUN mkdir /home/nuSQuIDS
20278 WORKDIR /home/nuSQuIDS
20289 RUN git clone https://github.com/qrliu/nuSQuIDS.git
20290 WORKDIR /home/nuSQuIDS/nuSQuIDS
20301 RUN git checkout 072d8ef740e2fc7330f1fabaea94f0f4540c46f9
20312 RUN apt -y install libhdf5-dev hdf5-tools
20323 RUN apt -y install libboost1.65-all-dev
20334 RUN ./configure --with-squids=$SQuIDS --with-python-bindings --prefix=../
2034     nuSQuIDS_install \
20355     && make \
20366     && make install
20377
20388     # Set up an environmental variable for nuSQuIDS.
20399 ENV nuSQuIDS=/home/nuSQuIDS/nuSQuIDS
20400 ENV LD_LIBRARY_PATH=$nuSQuIDS/lib:$LD_LIBRARY_PATH
20411
20422     # Build the python bindings
20433 WORKDIR /home/nuSQuIDS/nuSQuIDS/resources/python/src
20444 RUN make
20455
20466     # Set up an environmental variable for the python bindings.
20477 ENV PYTHONPATH=$nuSQuIDS/resources/python/bindings/:$PYTHONPATH
20488
20499     # Install Charon in the /home/Charon/charon directory.
20500 RUN mkdir /home/Charon

```

```
20511 WORKDIR /home/Charon
20512 RUN git clone https://github.com/icecube/charon.git \
20513     && apt -y install unzip python-scipy
20514 WORKDIR charon
20515 RUN git checkout c531efe4e01dc364a60d1c83f950f04526ccd771
20516 RUN unzip ./charon/xsec/xsec.zip -d charon/xsec/ \
20517
20518 # Download neutrino spectra tables in the /home/Charon/charon/data directory
20519 .
20520     && mkdir ./charon/data
20521 WORKDIR ./charon/data
20522 RUN wget --no-check-certificate https://icecube.wisc.edu/~qliu/charon/
20523     SpectraEW.hdf5 \
20524     && wget --no-check-certificate https://icecube.wisc.edu/~qliu/charon/
20525     Spectra_PYTHIA.hdf5 \
20526     && wget --no-check-certificate https://icecube.wisc.edu/~qliu/charon/
20527     Spectra_noEW.hdf5
20528
20529 WORKDIR ../..
20530 RUN python setup.py install
20531 WORKDIR /home
```

2072 C.2 Spline Fitting Statuses

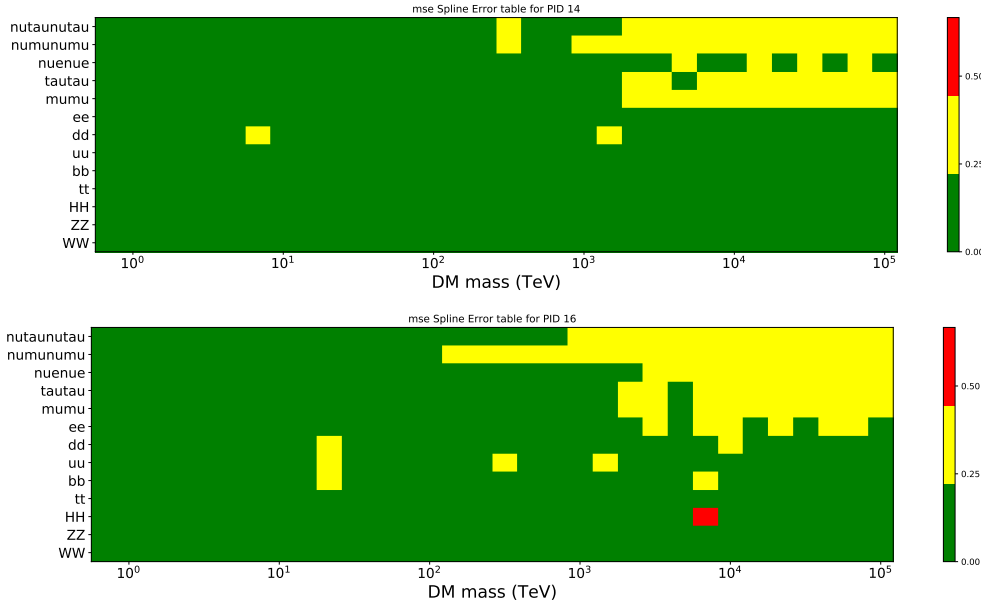


Figure C.1 Current status of spline tables according to constraints defined by Tab. 7.1. Green splines are splines that passed under the GOOD tolerance. Yellow are splines that are OK. Red are splines that FAIL. All yellow splines were inspected individually before running the analysis. Splines were made for the  $\mu$  (PID 14; top panel) flavor and  $\tau$  (PID 16; bottom panel).

2073 C.3 Segue 1 And Ursa Major II Signal Recovery



Figure C.2 TODO: Fill this out eventually. I think I want all the plots generated first[NEEDS A SOURCE][FACT CHECK THIS]

## BIBLIOGRAPHY

- [1] Anne M. Green. “Dark matter in astrophysics/cosmology”. In: *SciPost Phys. Lect. Notes* (2022), p. 37. doi: [10.21468/SciPostPhysLectNotes.37](https://doi.org/10.21468/SciPostPhysLectNotes.37). URL: <https://scipost.org/10.21468/SciPostPhysLectNotes.37>.
- [2] Bing-Lin Young. “A survey of dark matter and related topics in cosmology”. In: *Frontiers of Physics* 12 (Oct. 2016). doi: <https://doi.org/10.1007/s11467-016-0583-4>. URL: <https://doi.org/10.1007/s11467-016-0583-4>.
- [3] Gianfranco Bertone, Dan Hooper, and Joseph Silk. “Particle dark matter: evidence, candidates and constraints”. In: *Physics Reports* 405.5 (2005), pp. 279–390. issn: 0370-1573. doi: <https://doi.org/10.1016/j.physrep.2004.08.031>. URL: <https://www.sciencedirect.com/science/article/pii/S0370157304003515>.
- [4] Gianfranco Bertone and Dan Hooper. “History of dark matter”. In: *Rev. Mod. Phys.* 90 (4 Aug. 2018), p. 045002. doi: [10.1103/RevModPhys.90.045002](https://doi.org/10.1103/RevModPhys.90.045002). URL: <https://link.aps.org/doi/10.1103/RevModPhys.90.045002>.
- [5] Fritz Zwicky. “The Redshift of Extragalactic Nebulae”. In: *Helvetica Physica Acta* 6. (1933), pp. 110–127. doi: [10.5169/seals-110267](https://doi.org/10.5169/seals-110267).
- [6] Vera C. Rubin and Jr. Ford W. Kent. “Rotation of the Andromeda Nebula from a Spectroscopic Survey of Emission Regions”. In: *ApJ* 159 (Feb. 1970), p. 379. doi: [10.1086/150317](https://doi.org/10.1086/150317).
- [7] K. G. Begeman, A. H. Broeils, and R. H. Sanders. “Extended rotation curves of spiral galaxies: dark haloes and modified dynamics”. In: *Monthly Notices of the Royal Astronomical Society* 249.3 (Apr. 1991), pp. 523–537. issn: 0035-8711. doi: [10.1093/mnras/249.3.523](https://doi.org/10.1093/mnras/249.3.523). eprint: <https://academic.oup.com/mnras/article-pdf/249/3/523/18160929/mnras249-0523.pdf>. URL: <https://doi.org/10.1093/mnras/249.3.523>.
- [8] *Different types of gravitational lenses*. website. Feb. 2004. URL: <https://esahubble.org/images/heic0404b/>.
- [9] Douglas Clowe et al. “A Direct Empirical Proof of the Existence of Dark Matter”. In: *apjl* 648.2 (Sept. 2006), pp. L109–L113. doi: [10.1086/508162](https://doi.org/10.1086/508162). arXiv: [astro-ph/0608407 \[astro-ph\]](https://arxiv.org/abs/astro-ph/0608407).
- [10] Planck Collaboration and N. et. al. Aghanim. “Planck 2018 results I. Overview and the cosmological legacy of Planck”. In: *A&A* 641 (2020). doi: [10.1051/0004-6361/201833880](https://doi.org/10.1051/0004-6361/201833880). URL: <https://doi.org/10.1051/0004-6361/201833880>.
- [11] Wayne Hu. *Matter Density Animation*. web. 2024. URL: <http://background.uchicago.edu/~whu/animbut/anim2.html>.

- 2108 [12] Wenlong Yuan et al. “A First Look at Cepheids in a Type Ia Supernova Host with JWST”. in:  
2109     *The Astrophysical Journal Letters* 940.1 (Nov. 2022). doi: [10.3847/2041-8213/ac9b27](https://doi.org/10.3847/2041-8213/ac9b27).  
2110     URL: <https://dx.doi.org/10.3847/2041-8213/ac9b27>.
- 2111 [13] Wendy L. Freedman. “Measurements of the Hubble Constant: Tensions in Perspective”. In:  
2112     *The Astrophysical Journal* 919.1 (Sept. 2021), p. 16. doi: [10.3847/1538-4357/ac0e95](https://doi.org/10.3847/1538-4357/ac0e95).  
2113     URL: <https://dx.doi.org/10.3847/1538-4357/ac0e95>.
- 2114 [14] Jodi Cooley. “Dark Matter direct detection of classical WIMPs”. In: *SciPost Phys. Lect.*  
2115     *Notes* (2022), p. 55. doi: [10.21468/SciPostPhysLectNotes.55](https://doi.org/10.21468/SciPostPhysLectNotes.55). URL: <https://scipost.org/10.21468/SciPostPhysLectNotes.55>.
- 2117 [15] “Search for new phenomena in events with an energetic jet and missing transverse momentum  
2118     in  $pp$  collisions at  $\sqrt{s} = 13$  TeV with the ATLAS detector”. In: *Phys. Rev. D* 103  
2119     (11 July 2021), p. 112006. doi: [10.1103/PhysRevD.103.112006](https://doi.org/10.1103/PhysRevD.103.112006). URL: <https://link.aps.org/doi/10.1103/PhysRevD.103.112006>.
- 2121 [16] *Jetting into the dark side: a precision search for dark matter*. website. July 2020. URL:  
2122     <https://atlas.cern/updates/briefing/precision-search-dark-matter>.
- 2123 [17] Celine Armand et. al. “Combined dark matter searches towards dwarf spheroidal galaxies  
2124     with Fermi-LAT, HAWC, H.E.S.S., MAGIC, and VERITAS”. in: *Proceedings of Science*.  
2125     Vol. 395. Mar. 2022. doi: <https://doi.org/10.22323/1.395.0528>.
- 2126 [18] Tracy R. Slatyer. “Les Houches Lectures on Indirect Detection of Dark Matter”. In: *SciPost*  
2127     *Phys. Lect. Notes* (2022), p. 53. doi: [10.21468/SciPostPhysLectNotes.53](https://doi.org/10.21468/SciPostPhysLectNotes.53). URL:  
2128     <https://scipost.org/10.21468/SciPostPhysLectNotes.53>.
- 2129 [19] Christian W Bauer, Nicholas L. Rodd, and Bryan R. Webber. “Dark matter spectra from  
2130     the electroweak to the Planck scale”. In: *Journal of High Energy Physics* 2021.1029-8479  
2131     (June 2021). doi: [https://doi.org/10.1007/JHEP06\(2021\)121](https://doi.org/10.1007/JHEP06(2021)121).
- 2132 [20] Riccardo Catena and Piero Ullio. “A novel determination of the local dark matter density”.  
2133     In: *Journal of Cosmology and Astroparticle Physics* 2010.08 (Aug. 2010), p. 004. doi:  
2134     [10.1088/1475-7516/2010/08/004](https://doi.org/10.1088/1475-7516/2010/08/004). URL: <https://dx.doi.org/10.1088/1475-7516/2010/08/004>.
- 2136 [21] B. P. Abbott et al. “Observation of Gravitational Waves from a Binary Black Hole Merger”.  
2137     In: *Phys. Rev. Lett.* 116 (6 Feb. 2016), p. 061102. doi: [10.1103/PhysRevLett.116.061102](https://doi.org/10.1103/PhysRevLett.116.061102). URL: <https://link.aps.org/doi/10.1103/PhysRevLett.116.061102>.
- 2139 [22] R. Abbasi et. al. “Observation of high-energy neutrinos from the Galactic plane”. In: *Science*  
2140     380.6652 (June 2023), pp. 1338–1343.
- 2141 [23] NASA Goddard Space Flight Center. *Fermi’s 12-year view of the gamma-ray sky*. website.

- 2142 2022. URL: <https://svs.gsfc.nasa.gov/14090>.
- 2143 [24] Marco Cirelli et al. “PPPC 4 DM ID: a poor particle physicist cookbook for dark matter  
2144 indirect detection”. In: *Journal of Cosmology and Astroparticle Physics* 2011.03 (Mar.  
2145 2011), p. 051. doi: [10.1088/1475-7516/2011/03/051](https://doi.org/10.1088/1475-7516/2011/03/051). URL: <https://dx.doi.org/10.1088/1475-7516/2011/03/051>.
- 2147 [25] Javier Rico. “Gamma-Ray Dark Matter Searches in Milky Way Satellites—A Comparative  
2148 Review of Data Analysis Methods and Current Results”. In: *Galaxies* 8.1 (Mar. 2020), p. 25.  
2149 doi: [10.3390/galaxies8010025](https://doi.org/10.3390/galaxies8010025). arXiv: [2003.13482 \[astro-ph.HE\]](https://arxiv.org/abs/2003.13482).
- 2150 [26] W. B. Atwood et al. “The Large Area Telescope on the Fermi Gamma-Ray Space Telescope  
2151 Mission”. In: *apj* 697.2 (June 2009), pp. 1071–1102. doi: [10.1088/0004-637X/697/2/1071](https://doi.org/10.1088/0004-637X/697/2/1071). arXiv: [0902.1089 \[astro-ph.IM\]](https://arxiv.org/abs/0902.1089).
- 2153 [27] M. Ackermann et al. “Searching for Dark Matter Annihilation from Milky Way Dwarf  
2154 Spheroidal Galaxies with Six Years of Fermi Large Area Telescope Data”. In: *prl* 115.23,  
2155 231301 (Dec. 2015), p. 231301. doi: [10.1103/PhysRevLett.115.231301](https://doi.org/10.1103/PhysRevLett.115.231301). arXiv:  
2156 [1503.02641 \[astro-ph.HE\]](https://arxiv.org/abs/1503.02641).
- 2157 [28] Mattia Di Mauro, Martin Stref, and Francesca Calore. “Investigating the effect of Milky  
2158 Way dwarf spheroidal galaxies extension on dark matter searches with Fermi-LAT data”.  
2159 In: *Phys. Rev. D* 106 (12 Dec. 2022), p. 123032. doi: [10.1103/PhysRevD.106.123032](https://doi.org/10.1103/PhysRevD.106.123032).  
2160 URL: <https://link.aps.org/doi/10.1103/PhysRevD.106.123032>.
- 2161 [29] F. et al. Aharonian. “Observations of the Crab Nebula with H.E.S.S.”. In: *Astron. Astrophys.*  
2162 457 (2006), pp. 899–915. doi: [10.1051/0004-6361:20065351](https://doi.org/10.1051/0004-6361:20065351). arXiv: [astro-ph/0607333](https://arxiv.org/abs/astro-ph/0607333).
- 2164 [30] J. Albert et al. “VHE  $\gamma$ -Ray Observation of the Crab Nebula and its Pulsar with the MAGIC  
2165 Telescope”. In: *The Astrophysical Journal* 674.2 (Feb. 2008), p. 1037. doi: [10.1086/525270](https://doi.org/10.1086/525270). URL: <https://dx.doi.org/10.1086/525270>.
- 2167 [31] N. Park. “Performance of the VERITAS experiment”. In: *Proceedings, 34th International  
2168 Cosmic Ray Conference (ICRC2015): The Hague, The Netherlands, July, 30th July - 6th  
2169 August*. Vol. 34. 2015, p. 771. arXiv: [1508.07070 \[astro-ph.IM\]](https://arxiv.org/abs/1508.07070).
- 2170 [32] A. Abramowski et al. “H.E.S.S. constraints on Dark Matter annihilations towards the Sculptor  
2171 and Carina Dwarf Galaxies”. In: *Astropart. Phys.* 34 (2011), pp. 608–616. doi: [10.1016/j.astropartphys.2010.12.006](https://doi.org/10.1016/j.astropartphys.2010.12.006). arXiv: [1012.5602 \[astro-ph.HE\]](https://arxiv.org/abs/1012.5602).
- 2173 [33] A. Abramowski et al. “Search for dark matter annihilation signatures in H.E.S.S. observations  
2174 of Dwarf Spheroidal Galaxies”. In: *Phys. Rev. D* 90 (2014), p. 112012. doi: [10.1103/PhysRevD.90.112012](https://doi.org/10.1103/PhysRevD.90.112012). arXiv: [1410.2589 \[astro-ph.HE\]](https://arxiv.org/abs/1410.2589).

- 2176 [34] H. Abdalla et al. “Searches for gamma-ray lines and ‘pure WIMP’ spectra from Dark  
2177 Matter annihilations in dwarf galaxies with H.E.S.S”. in: *JCAP* 11 (2018), p. 037. doi:  
2178 [10.1088/1475-7516/2018/11/037](https://doi.org/10.1088/1475-7516/2018/11/037). arXiv: [1810.00995 \[astro-ph.HE\]](https://arxiv.org/abs/1810.00995).
- 2179 [35] J. Aleksić et al. “Optimized dark matter searches in deep observations of Segue 1 with  
2180 MAGIC”. in: *JCAP* 1402 (2014), p. 008. doi: [10.1088/1475-7516/2014/02/008](https://doi.org/10.1088/1475-7516/2014/02/008).  
2181 arXiv: [1312.1535 \[hep-ph\]](https://arxiv.org/abs/1312.1535).
- 2182 [36] V.A. Acciari et al. “Combined searches for dark matter in dwarf spheroidal galaxies observed  
2183 with the MAGIC telescopes, including new data from Coma Berenices and Draco”. In: *Physics of the Dark Universe* (2021), p. 100912. issn: 2212-6864. doi: <https://doi.org/10.1016/j.dark.2021.100912>. URL: <https://www.sciencedirect.com/science/article/pii/S2212686421001370>.
- 2187 [37] M. L. Ahnen et al. “Indirect dark matter searches in the dwarf satellite galaxy Ursa Major II  
2188 with the MAGIC Telescopes”. In: *JCAP* 1803.03 (2018), p. 009. doi: [10.1088/1475-7516/2018/03/009](https://doi.org/10.1088/1475-7516/2018/03/009). arXiv: [1712.03095 \[astro-ph.HE\]](https://arxiv.org/abs/1712.03095).
- 2190 [38] S. et al. Archambault. “Dark matter constraints from a joint analysis of dwarf Spheroidal  
2191 galaxy observations with VERITAS”. in: *prd* 95.8 (Apr. 2017). doi: [10.1103/PhysRevD.95.082001](https://doi.org/10.1103/PhysRevD.95.082001). arXiv: [1703.04937 \[astro-ph.HE\]](https://arxiv.org/abs/1703.04937).
- 2193 [39] Louise Oakes et al. “Combined Dark Matter searches towards dwarf spheroidal galaxies with  
2194 Fermi-LAT, HAWC, HESS, MAGIC and VERITAS”. in: *Proceedings of Science*. 2019.
- 2195 [40] Celine Armand et al. on behalf of the Fermi-LAT, HAWC, HESS, MAGIC, VERITAS.  
2196 “Combined Dark Matter searches towards dwarf spheroidal galaxies with Fermi-LAT,  
2197 HAWC, HESS, MAGIC and VERITAS”. in: *Proceedings of Science*. 2021.
- 2198 [41] Daniel Kerszberg et al. on behalf of the Fermi-LAT, HAWC, HESS, MAGIC, and VER-  
2199 TIAS collaborations. “Search for dark matter annihilation with a combined analysis of  
2200 dwarf spheroidal galaxies from Fermi-LAT, HAWC, H.E.S.S., MAGIC and VERITAS”. in:  
2201 *Proceedings of Science*. 2023.
- 2202 [42] A. U. Abeysekara et al. “Observation of the Crab Nebula with the HAWC Gamma-Ray  
2203 Observatory”. In: *The Astrophysical Journal* 843.1 (June 2017), p. 39. doi: [10.3847/1538-4357/aa7555](https://doi.org/10.3847/1538-4357/aa7555). URL: <https://doi.org/10.3847/1538-4357/aa7555>.
- 2205 [43] Giacomo Vianello et al. *The Multi-Mission Maximum Likelihood framework (3ML)*. 2015.  
2206 arXiv: [1507.08343 \[astro-ph.HE\]](https://arxiv.org/abs/1507.08343).
- 2207 [44] Marco Cirelli et al. “PPPC 4 DM ID: a poor particle physicist cookbook for dark matter  
2208 indirect detection”. In: *Journal of Cosmology and Astroparticle Physics* 2011.03 (Mar.  
2209 2011). issn: 1475-7516. doi: [10.1088/1475-7516/2011/03/051](https://doi.org/10.1088/1475-7516/2011/03/051). URL: <http://dx.doi.org/10.1088/1475-7516/2011/03/051>.

- 2211 [45] Alex Geringer-Sameth, Savvas M. Koushiappas, and Matthew Walker. “DWARF GALAXY  
2212 ANNIHILATION AND DECAY EMISSION PROFILES FOR DARK MATTER EXPERI-  
2213 MENTS”. In: *The Astrophysical Journal* 801.2 (Mar. 2015), p. 74. ISSN: 1538-4357. doi:  
2214 [10.1088/0004-637x/801/2/74](https://doi.org/10.1088/0004-637x/801/2/74). URL: <http://dx.doi.org/10.1088/0004-637X/801/2/74>.
- 2216 [46] A. Albert et al. “Dark Matter Limits from Dwarf Spheroidal Galaxies with the HAWC  
2217 Gamma-Ray Observatory”. In: *The Astrophysical Journal* 853.2 (Feb. 2018), p. 154. ISSN:  
2218 1538-4357. doi: [10.3847/1538-4357/aaa6d8](https://doi.org/10.3847/1538-4357/aaa6d8). URL: <http://dx.doi.org/10.3847/1538-4357/aaa6d8>.
- 2220 [47] HongSheng Zhao. “Analytical models for galactic nuclei”. In: *Mon. Not. Roy. Astron. Soc.*  
2221 278 (1996), pp. 488–496. doi: [10.1093/mnras/278.2.488](https://doi.org/10.1093/mnras/278.2.488). arXiv: [astro-ph/9509122](https://arxiv.org/abs/astro-ph/9509122)  
2222 [[astro-ph](#)].
- 2223 [48] Julio F. Navarro, Carlos S. Frenk, and Simon D. M. White. “The Structure of Cold Dark  
2224 Matter Halos”. In: *ApJ* 462 (May 1996), p. 563. doi: [10.1086/177173](https://doi.org/10.1086/177173). eprint:  
2225 [astro-ph/9508025](https://arxiv.org/abs/astro-ph/9508025) (astro-ph).
- 2226 [49] V. Bonnivard et al. “Spherical Jeans analysis for dark matter indirect detection in dwarf  
2227 spheroidal galaxies - Impact of physical parameters and triaxiality”. In: *Mon. Not. Roy.  
2228 Astron. Soc.* 446 (2015), pp. 3002–3021. doi: [10.1093/mnras/stu2296](https://doi.org/10.1093/mnras/stu2296). arXiv:  
2229 [1407.7822](https://arxiv.org/abs/1407.7822) [[astro-ph.HE](#)].
- 2230 [50] M. Ackermann et al. “Searching for Dark Matter Annihilation from Milky Way Dwarf  
2231 Spheroidal Galaxies with Six Years of Fermi Large Area Telescope Data”. In: *prl* 115.23,  
2232 231301 (Dec. 2015), p. 231301. doi: [10.1103/PhysRevLett.115.231301](https://doi.org/10.1103/PhysRevLett.115.231301). arXiv:  
2233 [1503.02641](https://arxiv.org/abs/1503.02641) [[astro-ph.HE](#)].
- 2234 [51] M. L. Ahnen et al. “Limits to Dark Matter Annihilation Cross-Section from a Combined  
2235 Analysis of MAGIC and Fermi-LAT Observations of Dwarf Satellite Galaxies”. In: *JCAP*  
2236 1602.02 (2016), p. 039. doi: [10.1088/1475-7516/2016/02/039](https://doi.org/10.1088/1475-7516/2016/02/039). arXiv: [1601.06590](https://arxiv.org/abs/1601.06590)  
2237 [[astro-ph.HE](#)].
- 2238 [52] Javier Rico et al. *gLike: numerical maximization of heterogeneous joint  
2239 likelihood functions of a common free parameter plus nuisance parameters*.  
2240 <https://doi.org/10.5281/zenodo.4601451>. Version v00.09.03. Mar. 2021. doi: [10.5281/zenodo.4601451](https://doi.org/10.5281/zenodo.4601451). URL: <https://doi.org/10.5281/zenodo.4601451>.
- 2242 [53] Tjark Miener and Daniel Nieto. *LklCom: Combining likelihoods from different experiments*.  
2243 <https://doi.org/10.5281/zenodo.4597500>. Version v0.5.3. Mar. 2021. doi: [10.5281/zenodo.4597500](https://doi.org/10.5281/zenodo.4597500). URL: <https://doi.org/10.5281/zenodo.4597500>.
- 2245 [54] T. Miener et al. “Open-source Analysis Tools for Multi-instrument Dark Matter Searches”.  
2246 In: *arXiv e-prints*, arXiv:2112.01818 (Dec. 2021), arXiv:2112.01818. arXiv: [2112.01818](https://arxiv.org/abs/2112.01818)

- 2247 [astro-ph.IM].
- 2248 [55] Alex Geringer-Sameth and Matthew Koushiappas Savvas M. and Walker. “Dwarf galaxy  
2249 annihilation and decay emission profiles for dark matter experiments”. In: *Astrophys.*  
2250 *J.* 801.2 (2015), p. 74. doi: [10.1088/0004-637X/801/2/74](https://doi.org/10.1088/0004-637X/801/2/74). arXiv: [1408.0002](https://arxiv.org/abs/1408.0002)  
2251 [astro-ph.CO].
- 2252 [56] Gianfranco Bertone, Dan Hooper, and Joseph Silk. “Particle dark matter: evidence, can-  
2253 didates and constraints”. In: *Physics Reports* 405.5-6 (Jan. 2005), pp. 279–390. ISSN:  
2254 0370-1573. doi: [10.1016/j.physrep.2004.08.031](https://doi.org/10.1016/j.physrep.2004.08.031). URL: <http://dx.doi.org/10.1016/j.physrep.2004.08.031>.
- 2255 [57] V. Bonnivard et al. “Dark matter annihilation and decay in dwarf spheroidal galaxies: The  
2256 classical and ultrafaint dSphs”. In: *Mon. Not. Roy. Astron. Soc.* 453.1 (2015), pp. 849–867.  
2257 doi: [10.1093/mnras/stv1601](https://doi.org/10.1093/mnras/stv1601). arXiv: [1504.02048](https://arxiv.org/abs/1504.02048) [astro-ph.HE].
- 2259 [58] A. et al. Albert. “Searching for Dark Matter Annihilation in Recently Discovered Milky Way  
2260 Satellites with Fermi-LAT”. in: *Astrophys. J.* 834.2 (2017), p. 110. doi: [10.3847/1538-4357/834/2/110](https://doi.org/10.3847/1538-4357/834/2/110). arXiv: [1611.03184](https://arxiv.org/abs/1611.03184) [astro-ph.HE].
- 2262 [59] Mattia Di Mauro and Martin Wolfgang Winkler. “Multimessenger constraints on the dark  
2263 matter interpretation of the Fermi-LAT Galactic Center excess”. In: *prd* 103.12, 123005  
2264 (June 2021), p. 123005. doi: [10.1103/PhysRevD.103.123005](https://doi.org/10.1103/PhysRevD.103.123005). arXiv: [2101.11027](https://arxiv.org/abs/2101.11027)  
2265 [astro-ph.HE].
- 2266 [60] H. C. Plummer. “On the Problem of Distribution in Globular Star Clusters: (Plate 8.)”  
2267 In: *Monthly Notices of the Royal Astronomical Society* 71.5 (Mar. 1911), pp. 460–470.  
2268 ISSN: 0035-8711. doi: [10.1093/mnras/71.5.460](https://doi.org/10.1093/mnras/71.5.460). eprint: <https://academic.oup.com/mnras/article-pdf/71/5/460/2937497/mnras71-0460.pdf>. URL:  
2269 <https://doi.org/10.1093/mnras/71.5.460>.
- 2270 [61] Daniel R. Hunter. “Derivation of the anisotropy profile, constraints on the local velocity  
2271 dispersion, and implications for direct detection”. In: *JCAP* 02 (2014), p. 023. doi:  
2272 [10.1088/1475-7516/2014/02/023](https://doi.org/10.1088/1475-7516/2014/02/023). arXiv: [1311.0256](https://arxiv.org/abs/1311.0256) [astro-ph.CO].
- 2274 [62] Barun Kumar Dhar and Liliya L. R. Williams. “Surface mass density of the Einasto family  
2275 of dark matter haloes: are they Sersic-like?” In: *Mon. Not. Roy. Astron. Soc.* (2010). doi:  
2276 [10.1111/j.1365-2966.2010.16446.x](https://doi.org/10.1111/j.1365-2966.2010.16446.x).
- 2277 [63] M. Baes and E. Van Hese. “Dynamical models with a general anisotropy profile”. In:  
2278 *Astron. Astrophys.* 471 (2007), p. 419. doi: [10.1051/0004-6361:20077672](https://doi.org/10.1051/0004-6361:20077672). arXiv:  
2279 [0705.4109](https://arxiv.org/abs/0705.4109) [astro-ph].
- 2280 [64] Matthew G. Walker, Edward W. Olszewski, and Mario Mateo. “Bayesian analysis of re-  
2281 solved stellar spectra: application to MMT/Hectochelle observations of the Draco dwarf

- 2282 spheroidal”. In: *mnras* 448.3 (Apr. 2015), pp. 2717–2732. doi: [10.1093/mnras/stv099](https://doi.org/10.1093/mnras/stv099).  
2283 arXiv: [1503.02589 \[astro-ph.GA\]](https://arxiv.org/abs/1503.02589).
- 2284 [65] Nicholas L. Rodd et al. “Dark matter spectra from the electroweak to the Planck scale”. In:  
2285 *J. High Energy Physics* 121.10.1007 (June 2021).
- 2286 [66] Pace, Andrew B and Strigari, Louis E. “Scaling relations for dark matter annihilation and  
2287 decay profiles in dwarf spheroidal galaxies”. In: *Monthly Notices of the Royal Astronomical  
2288 Society* 482.3 (Oct. 2018), pp. 3480–3496. ISSN: 0035-8711. doi: [10.1093/mnras/sty2839](https://doi.org/10.1093/mnras/sty2839).
- 2289 [67] Albert, A. et al. “Search for gamma-ray spectral lines from dark matter annihilation in  
2290 dwarf galaxies with the High-Altitude Water Cherenkov observatory”. In: *Phys. Rev. D* 101 (10 May 2020), p. 103001. doi: [10.1103/PhysRevD.101.103001](https://doi.org/10.1103/PhysRevD.101.103001). URL:  
2291 <https://link.aps.org/doi/10.1103/PhysRevD.101.103001>.
- 2292 [68] Victor Eijkhout and Edmund Show and Robert van de Geijn. *The Science of Computing.  
2293 The Art of High Performance Computing*. Vol. 3. Open Copy published under CC-BY 4.0  
2294 license, 2023, pp. 63–66.
- 2295 [69] Qinrui Liu and Jeffrey Lazar and Carlos A. Argüelles and Ali Kheirandish. “χaro: a tool  
2296 for neutrino flux generation from WIMPs”. In: *Journal of Cosmology and Astroparticle  
2297 Physics* 2020.10 (Oct. 2020), p. 043. doi: [10.1088/1475-7516/2020/10/043](https://doi.org/10.1088/1475-7516/2020/10/043). URL:  
2298 <https://dx.doi.org/10.1088/1475-7516/2020/10/043>.
- 2299 [70] Aartsen, M. et al. “IceCube search for dark matter annihilation in nearby galaxies and galaxy  
2300 clusters”. In: *Phys. Rev. D* 88 (12 Dec. 2013), p. 122001. doi: [10.1103/PhysRevD.88.122001](https://doi.org/10.1103/PhysRevD.88.122001). URL: <https://link.aps.org/doi/10.1103/PhysRevD.88.122001>.
- 2301 [71] Nathan Whitehorn and Jakob van Santen. *Photospline*. IceCube: GitHub.